SPHERICALLY CONFINED COLLOIDAL SUSPENSIONS OF HYDRODYNAMICALLY INTERACTING PARTICLES: A MODEL FOR INTRACELLULAR TRANSPORT.

A Dissertation

Presented to the Faculty of the Graduate School

of Cornell University

in Partial Fulfillment of the Requirements for the Degree of

Doctor of Philosophy

by

Christian Alberto Aponte Rivera

December 2017

SPHERICALLY CONFINED COLLOIDAL SUSPENSIONS OF HYDRODYNAMICALLY INTERACTING PARTICLES: A MODEL FOR INTRACELLULAR TRANSPORT.

Christian Alberto Aponte Rivera, Ph.D.

Cornell University 2017

The diffusion in and rheology of hydrodynamically interacting colloids confined by a spherical cavity via dynamic simulation is studied as a model for intracellular and other confined biophysical transport. The modeling of transport and rheology in such confined inhomogeneous soft materials requires an accurate description of the microscopic forces driving particle motion, such as entropic and hydrodynamic forces, and of particle interactions with nearby boundaries. Previous models of such micro-confined transport behavior had been limited primarily to a single particle inside a spherical cavity. Although attempts had been made prior to this work to extend such models to more than one confined particle, none had yet successfully accounted for the effects of hydrodynamics, owing to the difficulties of modeling many-body long-ranged interactions. To accurately model spherically confined suspensions, new far-field mobility functions are derived and, together with the appropriate near-field resistance functions, implemented in a Stokesian-dynamics like approach. The method fully accounts for all many-body far-field interactions and near-field interactions both between the particles themselves and between particles and the enclosing cavity. Utilizing the newly developed method, we study short- and long- time self-diffusion at equilibrium, with a focus on the dependence of the former on particle positions relative to the cavity, and of both on volume

fraction and size ratio. It is found that the cavity exerts qualitative changes in transport behavior, such as a position dependent and anisotropic short-time self-diffusivity and anisotropic long-time transport behavior. Such qualitative changes suggest that careful interpretation of experimental measurements in 3D confined suspensions requires accounting for such confinement induced behaviors. To elucidate the effects of confinement on inter-particle hydrodynamic interactions, the method is utilized to determine the concentrated mobility of particles in the spherically confined domain. Confinement is found to induce qualitative changes in the functional dependence of particle entrainment with inter-particle separation. For widely separated particles, the functional dependence on inter-particle separation can be predicted via a Green's function. How this behavior can be utilized to develop a more accurate framework for two-point microrheology measurements near confining boundaries is discussed.

BIOGRAPHICAL SKETCH

The author grew up in Arecibo, Puerto Rico. He studied chemical engineering at the University of Puerto Rico at Mayagüez, where he was introduced to the wonderful world of fluid mechanics by his teacher and mentor, Professor Carlos Rinaldi. During a research internship the summer of 2011, in which he worked in the group of Professor John Brady at the California Institute of Technology, he was introduced to colloidal hydrodynamics, and decided to pursue a doctoral degree in order to conduct research in this area. In 2012, he arrived at Cornell University, where he conducted the work presented in this dissertation under the guidance of his teacher and mentor, Professor Roseanna Zia. Next, he will be moving to Duke University, to conduct research on the exciting field of polymer physics, studying the dynamics and rheology of charged polymers.

To my wife and life partner, Andreea E. Mascan, and my daughter Argelia E. Aponte Mascan.

ACKNOWLEDGEMENTS

During my years as a graduate student I have been met with many challenges, and consider myself very fortunate to have had a wonderful group of mentors, colleagues, friends and family that have helped me through them. I am deeply grateful to my PhD adviser, Professor Roseanna Zia, who has taught me how to conduct research, write publications, be a mentor and a teacher to others, and supported my academic goals since my very first day of graduate school. I consider myself very fortunate to have such a talented, dedicated, and excellent scientist as a mentor, and know the lessons I learned as her advisee and the advice she has given me will have a lasting impact on my life and academic career.

I am very grateful to the members of my thesis committee, Professor Donald Koch and Brian Kirby, for serving in my thesis committee and for insightful discussions regarding my work and its applications. I am also very grateful to Professor Susan Daniel, who provided me with many opportunities to be of service to the Robert Frederick Smith School of Chemical and Biomolecular Engineering (CBE) at Cornell and has set such an excellent example of how professors can impact society through outreach and community involvement. During my time as a graduate student, I have been very fortunate to also have mentors outside of Cornell. I am very grateful to Professor Carlos Rinaldi, who introduced me to the field of fluid mechanics, has supported my academic goals and provided me with excellent advice since my time as an undergraduate student at the University of Puerto Rico at Mayagüez. My thanks also go to Professor Ubaldo Cordova-Figueroa, who has supported my academic goals since my time as an undergraduate student and with whom I have had many insightful discussion regarding science and academia.

I consider myself very fortunate to have had excellent colleagues both in and outside the Zia group. I am grateful to have shared many fun and interesting conversations with my officemate Benjamin Dolata, as well as my other fellow Zia group members: Henry Chu, Benjamin Landrum, Lilian Johnson, Nicholas Hoh, Ritesh Mohanty, Yu Su, Jialun 'Galen' Wang, Derek Huang, Poornima Padmanabhan, Gaddiel Ouaknin, and Emma Gonzalez. I am also very grateful to colleagues and friends outside the Zia group, such as Victoria Sorg and Nestor Hernandez, and members of the CBE and Diversity Programs in Engineering (DPE) community, for many fun and interesting conversations.

My thanks also go to my family and my parents, Jose Aponte Hernandez and Enid Rivera Rivera, for being present in my life.

I am very grateful to my wife and life partner, Andreea E. Mascan, for always being willing to listen to me ramble, and all of the happy memories we have made in Ithaca and in our travels abroad. My thanks also go to my daughter, Argelia E. Aponte Mascan, for making Andreea and I smile and giving us a different perspective on life.

TABLE OF CONTENTS

LIST OF FIGURES

CHAPTER 1

INTRODUCTION: PARTICLE MOTION IN 3D CONFINEMENT AS A MODEL FOR INTRACELLULAR TRANSPORT

This chapter provides an overview of previous models of particle motion in colloidal dispersions, as well as attempts to utilize such models to explain transport behavior in the intracellular environment. We begin with an overview of different approaches to model particle motion with hydrodynamic interactions, placing an emphasis on models developed to study particles in spherically confined domains. Then, we discuss studies utilizing dynamic simulations to model different features of the cell interior. Lacking in many of these models is accurate representation of hydrodynamic interactions in fully confined domains.

1.1 Particle motion in unbound and confined domains: a historical overview

Key to the development of theoretical and computational models of colloidal dispersions is accurate representation of the forces acting between the microstructural constituents of the suspension, which can include steric, entropic, and hydrodynamic forces, among others. A primary challenge in such models is the accurate and efficient representation of hydrodynamic interactions, whose long-range nature precludes simple pairwise approximations of many-body interactions in concentrated suspensions. Numerous approaches have been developed to describe microstructural evolution and its connection to material and flow properties in *unbound suspensions*, that is suspensions where

it may be assumed that particles are immersed in an infinite domain. These approaches range from pair Smoluchowsky theory for dilute suspensions, where assuming the suspension is dilute allows for the pairwise addition of hydrodynamic interactions, to computational approaches for more concentrated systems, where many-body hydrodynamic interactions play an important role. Many important insights into non-Newtonian rheological behaviors such as flow thinning[11, 15, 149, 91, 178] and flow-thickening[25, 15, 168, 91, 159], flow-induced diffusion[111, 26, 179, 69, 70], and normal stress differences[27, 50, 177, 35, 36] have been obtained from theoretical and computational models of unbound suspensions. However, the study of suspensions perturbed by microscopic confinement from a finite boundary still lags behind.

A confining boundary exerts a strong influence on hydrodynamic interactions between particles, and in turn on suspension dynamics and flow. Studies examining the effect of wall confinement on diffusion and rheology have revealed qualitative changes to particle dynamics and flow[19, 38, 130, 155, 109, 108, 14, 52, 156, 157, 158, 58, 176, 124, 158], setting a foundation for understanding the effects of confining boundaries. However, growing interest in the mechanical transport of fully confined, microscopic systems demands new models to account for the effects of fully enclosed domains, which can play a role in many biophysical systems. For example, eukaryotic cells can be viewed as crowded, watery compartments where particles undergo passive and active mechanical transport[164] while enclosed inside the cell membrane. Although the connection between mechanical transport and cell function is recognized, it is not well understood, leaving open questions such as what is the underlying origin of anomalous diffusion, and how does active motion stir the cell interior and alter diffusion [113, 53, 175, 164, 100, 153, 56, 96, 43, 107, 125, 39, 40, 95, 114, 65,

30, 66, 174, 129, 166].

Experimental studies of particle diffusion in 3D confined colloids provide information as to the effects of the enclosure, demonstrating anisotropic particle dynamics[33, 77] and suggesting that careful modeling and analysis can provide answers to questions in confined biophysical systems. The most straightforward approach to model a suspension of particles in a cavity filled with a Newtonian fluid is to solve the Navier-Stokes equations at all points in the cavity domain, subject to the appropriate boundary conditions. Numerous analytical and numerical solutions have been put forth for a variety of systems and boundary conditions, such as a single charged particle with both thin and thick Debye layers in an uncharged cavity[182, 140, 102, 74, 115, 87, 88], and a soft particle in a fluid filled cavity [105, 86], among others[101, 76, 75, 73, 163, 115, 110, 86, 103, 104, 105, 89, 72]. Underlying these single-particle problems is a pair-level hydrodynamic problem where there are two interacting surfaces: the particle and the cavity. While successful at the pair level, such methods become intractable or prohibitively expensive computationally when extended to three or more surfaces. A common theme in these approaches is that fluid motion is determined explicitly, and from it particle motion. An alternative approach would be to bypass the explicit calculation of fluid motion, accounting for the effect of the fluid via hydrodynamic functions that couple particle motion to applied forces. Approaches focusing on eigenfunction expansions to determine the hydrodynamic coupling between motion and applied forces for a single particle inside a fluid filled cavity have been developed[42, 131, 132, 85], but ultimately such analysis is also restricted to a single enclosed particle.

In unbound suspensions, a successful approach for modeling hydrodynamic

interactions between two or more hydrodynamically interacting particles has been through the application of a Green's function, as done in the Stokesian dynamics [22] technique. The Green's function is utilized in an integral representation of the velocity field propagated by a forced particle. Subsuequent Taylor expansion of the Green's function allows the velocity field to be expressed as a function of moments of the hydrodynamic surface traction over a particle surface. Faxén formulas can then be utilized to determine how the velocity disturbance of a forced particle impacts the motion of a second, entrained particle. A particle displacement equation determining how particle positions evolve over time as they are acted on by hydrodynamic, interparticle, and entropic forces can then be solved through computational methods. Techniques such as Stokesian dynamics [22] have been utilized to solve many problems in unbound suspensions[21, 139, 50, 146], and have been recently extended to suspensions confined by planar-walls[157, 158].

The first Green's function for spherical confinement was reported by Oseen[134], for a point particle in a fluid filled spherical cavity with no-flux and no-slip boundary conditions over its surface. This Green's function has been utilized to study the sedimentation of a non-colloidal particle inside a spherical cavity via numerical techniques[144], which again are difficult to generalize to many-body systems. Others have sought to express the Green's function in terms of the Green's function of an unbound suspension[119, 120]. This in hopes of making the Green's function more amenable to collocation methods which solve Ladyzhenskaya's[99] integral representation on a mesh. However, the approach is nearly intractable beyond the dilute limit due to the presence of line integrals in the resulting expression. Solutions via Fourier-space multipole expansions have also been developed[13]. However, these are accurate only in

the far-field, and the derived framework does not account for lubrication interactions. Felderhof and Sellier[49] applied a leading order approximation of the Faxén formula to Oseen's Green's function to obtain analytical expressions for the motion of a single particle inside a cavity, a result previously obtained numerically via a series expansion in bispherical coordinates[131, 132, 85]. However, this leading order approximation is not able to capture qualitative features of the torque-to-translational motion coupling, suggesting that the effects of finite size must be correctly accounted for in order to accurately model particle motion.

In this work, we put forth a theoretical model to predict the motion of an arbitrary number of particles in a fluid filled cavity that accounts for both many-body and lubrication hydrodynamic interactions, both between the particles themselves and the particles and the cavity. This allows accurate modeling of a 3D confinement suspension, which can be utilized as a model to study the effects of confinement on intracellular transport. Next, we discuss previous computational models developed to study different features of the intracellular environment.

1.2 Computational models of intracellular transport

Emergent interest in the development of predictive models for transport in and rheological properties of micro-confined colloidal suspensions is motivated in part by the degree to which they represent such behavior in confined biophysical suspensions. Eukaryotic cells are an important example for which mechanical transport has been shown to play a critical role in system function, where

e.g. reports of anomalous diffusion vary widely in measurement and explanation [30, 175, 53, 56, 40, 164, 30, 175]. These confined biophysical systems are typically crowded, watery suspensions of microscopic particles undergoing a variety of transport processes as they interact with one another and the confining wall. Thermal fluctuations are a primary source of particle motion in such systems, but the combined effects of crowding and 3D confinement on such Brownian motion have thus far not been extensively studied. The presence of a confining boundary introduces new length scales into a suspension, in contrast to unbound suspensions, where Brownian motion gives rises to three well-defined diffusive regimes set only by the particle length scale [11, 12, 142, 24]. Short-time self-diffusion of a particle occurs over length scales not even a fraction of particle size, without disturbing the positions of its neighbors. At intermediate times, its motion becomes correlated and subdiffusive as it exchanges places with its neighbors. At long times, it exchanges places with its neighbors many times, executing a random walk through the suspension as it undergoes long-time self-diffusion [24]. Introduction of a confining boundary introduces a new length scale over which such interactions take place. This in turn influences micro-structural configuration, particle dynamics, and particle transport [31, 111]. Accurate modeling of transport processes spanning these different temporal regimes in confined, crowded, hydrodynamically interacting particulate systems must address many-body interactions between the particles, interactions between particles and the confining boundary, and account for the time scales over which such processes take place.

Prior attempts to model such transport in spherically confined suspensions [162, 18] have focused on one or two of these features, but none has successfully modeled all three. While numerous methods of accounting for many-body hy-

drodynamic interactions in suspensions have been employed successfully in the study of mono-disperse and polydisperse suspensions in unconfined domains [22, 71, 97, 147], cylindrical confinement [17, 126, 127], and parallel wall confinement [16, 156, 157, 158], recent attempts to apply such models to study intracellular transport have neglected many-body hydrodynamic interactions entirely, modeling only pairwise interactions. This choice is typically motivated by steep computational expense and justified by the claim that such interactions can be included in a mean-field sense via an adjustable parameter or neglected entirely.

In a recent example, McGuffee and Elcock [122] modeled green fluorescent protein (GFP) motion in prokaryotic cells as a collection of spheres in an unbounded Newtonian solvent, restricting particle interactions to a pairwise electrostatic potential. While the model did recover the expected linear growth in time of mean-square displacement, the long-time self-diffusion coefficients were four or five times larger than those observed in experimental measurements. The authors interpreted the discrepancy as a result of attractive hydrophobic interactions neglected in their electrostatic potential. To counteract this effect, they added a Lennard-Jones potential with a potential-well depth as an adjustable parameter to tune the long-time diffusion coefficient obtained in simulation until it matched the experimental results. Such *ad hoc* modification slows diffusive motion, but limits the predictive value of the model and may mask the fundamental influence of hydrodynamic interactions. The simplification was justified based on a previous work that suggested a simple renormalization: that at biophysically relevant concentrations (volume fractions $10\% \leq \phi \leq 40\%$), hydrodynamic interactions reduce the long-time self-diffusivity measured in Brownian dynamics simulations of freely draining spheres by approximately 50% [154], a small reduction compared to the four to five fold reduction required by

McGuffee and Elcock [122]. The discrepancy may arise from two key aspects of the Sun and Weinstein simulation study that were not considered by McGuffee and Elcock: first, Sun and Weinstein neglected confinement entirely. We will show in this work that this simplification leads to qualitative errors in diffusive behavior. Second, the hydrodynamically interacting suspension in Sun and Weinstein was monodisperse, but polydisperse in the model of McGuffee and Elcock; relative particle mobility is strongly dependent on relative size [82] and the long-time self-diffusivity can exhibit qualitative changes when the size ratios are disparate [12, 68]. These two factors suggest that hydrodynamic interactions would exert a much stronger influence on the motion of GFP than originally hypothesized by the authors. While these studies advance the idea that crowding exerts an important influence on the dynamics of cell interior, the neglect of hydrodynamic interactions limits their applicability.

In a more recent attempt to study the effect of polydispersity on GFP diffusion in a prokaryotic cell, Ando and Skolnick (2010) [4] modeled many-body hydrodynamic interactions in a polydisperse suspension, neglecting confinement, utilizing Stokesian dynamics simulations. The authors calculated the long-time self-diffusivity, finding reasonable agreement with diffusion coefficients for GFP measured *in vivo*. Their incorporation of many-body hydrodynamic interactions resolved the five-fold error of [122], a finding that confirms the importance of hydrodynamic interactions in biophysical systems. It would be tempting to conclude that confinement exerts no influence, but it is important to recognize that the confining cavity of actual *E. Coli.* cells is 500 to 2000 times the size of the particles. That is, the *in vivo* behavior was essentially studied in the limit of an unbound suspension. Perhaps the most appropriate interpretation is that many-body hydrodynamic interactions matter and that confinement can some-

times be neglected, but only when the boundary is very far away — e.g. very small particles away from the cell wall.

More recent studies have attempted to model the effects of boundaries. As with unbound systems, most models simply neglect many-body hydrodynamic interactions, which can be appropriate in limited circumstances. For example, Weber et al. [171] simulated a passively diffusing, spherically confined polymer chain using a Rouse-like bead-spring model, where hydrodynamic interactions are neglected on the basis that they can be screened in concentrated polymer solutions [44]. This is an excellent approximation when particles exert a net force on the fluid over e.g. the chain length scale, owing to their fixed position constraint by the chain, permitting the use of the Rouse model. However, the effect of hydrodynamic interactions can become important in systems with low to moderate polymer concentration [44]. Indeed, the impact of hydrodynamic interactions on the behavior of confined polymer solutions remains an open question, important for understanding their dynamics in the dilute and semidilute regime, where their motion is not expected to follow Rouse dynamics over all length and time scales [1, 37]. While these studies set a foundation for understanding the role of confinement and particle interactions in biophysical transport, the neglect of many-body hydrodynamic interactions limits their applicability to biophysical systems of non-freely diffusing particles or long particle chains that obey Rouse dynamics.

In an effort to include the combined effects of hydrodynamics and the presence of an enclosure, other studies have opted to neglect Brownian motion and crowding. Shinar et al. [145] modeled pronuclear migration during fertilization of a eukaryotic cell via an immersed-boundary method, which permitted de-

tailed modeling of a spheroidal cavity. The pronucleus was modeled as a spherical particle and was immersed in a Newtonian fluid (cytoplasm). The authors showed that the presence of the enclosure significantly increases the hydrodynamic drag force on the nucleus, and that the dynamic behavior of microtubules produce complex cytoplasmic flows. The results highlight the importance of confinement on intracellular transport, and particle-motion induced flow. However, the interplay between Brownian motion and hydrodynamic forces is well known to lead to important deterministic forces and non-Newtonian effects that are relevant in such microtubule-driven flow. By neglecting Brownian motion in the model, these effects and their influence on e.g. osmotic pressure and effective cell "temperature" [100] are lost.

In a more recent approach to modeling crowding, many-body interactions and confinement, Chow and Skolnick [34] circumvented the detailed hydrodynamic modeling of the boundary by simply building a large spherical shell from small, individual particles. The size of the spherical "bricks" from which the cavity wall was constructed were the same size as particles placed inside the cavity. Unfortunately, such cavities are inherently leaky: as long as the "bricks" have finite size, it is impossible to avoid gaps through which solvent can flow. For example, the highest possible packing density for the spheres, hexagonal packing, is less than 91%, meaning that at a minimum 10% of the surface permits leaks. This would lead to an under-prediction of the hydrodynamic coupling between the particles and the wall. Beyond this inaccuracy, another disadvantage of approximating the boundary as a collection of spheres is the increased computational cost of having to model $N + N_b$ particles, where N is the number of enclosed particles of interest, and N_b is the number of particles that make up the boundary — the latter of which cannot be used to calculate dynamical

properties. This computational cost diverges as the cavity gets large because $N_b \sim (R/a_b)^2$, where a_b is the radius of the boundary particles. While the study did report that the enclosure slowed particle velocity, no diffusion coefficients were reported. The authors hypothesized that, if they could measure diffusion, it would be reduced by confinement, and claimed that the long-time behavior of the suspension yields no useful information, given that at long enough times, the mean-square displacement of particles will reach a plateau with a value related to cavity size [162]. In consequence, the simulations conducted were too short to identify short- or long-time behaviors. As will be shown in the present work, the mean-square displacement of concentrated spherically confined suspensions shows a rich set of behaviors at short and intermediate lag times such as anisotropy, position dependence and anomalous transport. Such behaviors motivate the need for a more careful consideration of diffusive temporal regimes in 3D confined suspensions.

The 'lag time' over which mean-square displacement is measured determines which relaxation and rate processes are sampled. Indeed, measurements of subdiffusive behavior may indicate so-called anomalous diffusion [167, 54, 28, 160] or may simply indicate that the measurement lag time sampled the correlated motion inherent in the transition from short- to long-time self diffusion. In an attempt to recover and explain anomalous diffusion in eukaryotic *HeLa* cancer cells, Weiss et al. [173] conducted Brownian dynamics simulations of a freely draining dense suspension of polydisperse spheres. Measurements of mean-square displacements revealed a sublinear temporal growth that weakened as crowding increased, from which the authors inferred that crowding produces subdiffusion of mobile colloids. However, the power-law exponent in simulations did not agree with that found in experiments, a discrepancy at-

tributed by the authors to their approximation of proteins as spheres. But the simulation particles were also mobile and the fluid force-free; thus, an equally likely cause for the measured subdiffusion was that the selected lag time sampled correlated motion — during the transition from the short-time to long-time regime. Although the study helped advance the idea that crowding is an important feature of the cell interior, the connection between the subdiffusive motion observed in simulations and experiments remains unclear. A more careful interrogation of diffusive regimes would shed light on this question, as would inclusion of hydrodynamic interactions and the presence of boundaries.

The work presented in this thesis aims to develop a simulation method that accurately accounted for both many-body and lubrication interactions between particles and the confining boundary in a spherically confined suspension. This model is then utilized to study the effects of confinement on short- and long-time transport properties of colloidal dispersions, which serve as a model system for micro-confined biophysical transport. The thesis is organized as follows. In chapter 2, we begin with a brief overview of the theory of Stokes flow and diffusion in colloidal dispersions. Chapter 3 then gives a brief overview of simulation techniques that will be utilized in later chapters to study transport and rheology in spherically confined suspensions. In chapter 4, we utilize a Green's-function approach to derive a new set of far-field hydrodynamic mobility functions for finite size particles confined inside a spherical cavity [6]. The Stokesian dynamics [22] framework is then utilized to develop a simulation method for spherically confined suspensions that accounts for both many-body and lubrication hydrodynamic interactions. In chapter 5 [8], we implement the theoretical framework from chapter 4 into dynamic simulations to study the short- and long-time transport properties of spherically confined suspensions.

Finally, we determine the concentrated pair mobility of particles in spherically confined suspensions to study the combined effects of confinement and crowding on hydrodynamic entrainment in chapter 6 [7].

CHAPTER 2

BACKGROUND: HYDRODYNAMIC INTERACTIONS IN COLLOIDAL SUSPENSIONS

In this chapter we give an overview of colloidal hydrodynamics and the methods utilized to model hydrodynamic interactions between particles in colloidal suspensions. We begin with a brief overview of the importance of hydrodynamic interactions, and different simulation techniques utilized to account for such interactions. This is followed by a discussion introducing the basics of Stokes flow, with which an arbitrary linear flow field can be constructed. We focus on the solution to simplified problems, such as a single particle in an unbound domain or a spherically confined particle concentric to the confining cavity. Finally, we discuss the method of reflections in the context of Stokesian dynamics simulations, where inversion of the far-field grand mobility matrix accounts for an infinite number of reflected far-field interactions between an arbitrary number of interacting particles.

2.1 Hydrodynamic interactions and their role in diffusion and rheology

Hydrodynamic interactions can strongly impact transport and rheology in colloidal dispersions and other complex fluids. Such interactions arise in systems containing a dispersed phase immersed in a solvent. Motion relative to the solvent or forces acting on any of the microscopic constituents of the dispersed phase propagate disturbances which impact the motion and forces over other elements of the dispersed phase. The traditional model system to study such

interactions in colloidal dispersions is that of no-slip, hard-sphere particles immersed in a Newtonian solvent. In this model system, particle motion relative to the fluid or forces acting on the particles will propagate a disturbance velocity field which will affect the motion and hydrodynamic drag force of other particles. The velocity disturbance in this model system is characterized by a slow $1/r$ decay, where r is the center-to-center separation between the particles. As a consequence, many-body interactions (i.e. interactions between three or more particles) are important. Due to the small size of colloidal particles, fluid inertia is negligible and fluid motion is governed by the Stokes equations. We begin with an overview of canonical problems in Stokes flow — translation, rotation and strain — from which an arbitrary linear flow field can be constructed due to the linearity of the Stokes equations. In unbound suspensions, exact solutions are available for the case of a single particle subjected to each of these flows. In addition to providing an overview of these well known cases in unbound domains, we will consider the case of a confined particle concentric with the spherical cavity, due to its relevance to the present work.

2.2 The Stokes equations

The Navier-Stokes equation governing the motion of an incompressible, Newtonian fluid can be derived from Cauchy's equation of motion. The required assumptions are that the fluid be of constant density, and that the deviatoric stress is given constitutively by Newtons law of viscosity. Conservation of momentum in the Navier-Stokes equations is then given by,

$$\frac{D\boldsymbol{u}}{Dt} = -\boldsymbol{\nabla} P + \eta \nabla^2 \boldsymbol{u}. \tag{2.1}$$

Here, $\boldsymbol{u}$ is the velocity field of the fluid, P is the fluid pressure, η the fluid viscosity, the operator D/Dt represents the material derivative, and the gradient operator $\boldsymbol{\nabla}$ is taken with respect to position variable $\boldsymbol{x}$. To recast equation 2.1 in dimensionless form, we scale the dimensional variables as,

$$\tilde{\boldsymbol{u}} = \frac{\boldsymbol{u}}{U}, \quad \tilde{t} = \frac{t}{L/U}, \quad \tilde{P} = \frac{P}{\eta U/L}, \quad \tilde{\boldsymbol{\nabla}} = \frac{\boldsymbol{\nabla}}{1/L}, \quad \tilde{\boldsymbol{x}} = \frac{\boldsymbol{x}}{1/L}, \tag{2.2}$$

where U is a characteristic velocity, L a characteristic length scale, L/U a characteristic time, and $\eta U/L$ the viscous scaling for the pressure. The scaled Navier-Stokes equations are then obtained as,

$$Re\frac{\tilde{D}\tilde{\boldsymbol{u}}}{\tilde{D}\tilde{t}} = -\tilde{\boldsymbol{\nabla}}\tilde{P} + \tilde{\nabla}^2\tilde{\boldsymbol{u}}, \tag{2.3}$$

where $Re = UL/\nu$ is the Reynolds number and ν the kinemactic viscosity. The Reynolds number is a dimensionless quantity representing the ratio of inertial to viscous forces acting on the fluid.

Conservation of mass is enforced by the continuity condition, written mathematically as

$$\boldsymbol{\nabla} \cdot \boldsymbol{u} = 0. \tag{2.4}$$

Both artificial and naturally occurring colloidal suspensions are comprised of microscopically small particles, ranging in size from tens of nanometers to tens of μ-meters, motivating the use of a scaling analysis of equation 2.3 to identify the important physics. Considering a spherical particle with a $1\,\mu m$ radius, immersed in water at 30^oC with a kinematic viscosity $\nu = 0.801 m^2/s$, yields a Reynolds number on the order of $\sim U\,10^{-12} s/m$. Such a small Reynolds number suggests that conservation of momentum on the particle length scale may

be modeled by taking the limit $Re \to 0$ in equation 2.3, which yields in dimensional form,

$$0 = -\boldsymbol{\nabla} P + \eta \nabla^2 \boldsymbol{u}. \tag{2.5}$$

Equations 2.5 and 2.4 form a set of linear, elliptical partial differential equations known as the Stokes equations, and in combination with the neccessary boundary conditions form a well posed problem. The Stokes equations describe fluid motion in the Low Reynolds number limit — where fluid inertia is negligible, and have been utilized extensively to describe the motion of microscopic bodies when they are immersed in Newtonian solvents. Examples inlcude the motion of colloidal particles[82], bacteria[116], and particles in the interior of cells[4].

Due to the linearity of Stokes equations, the fluid velocity field propagated by a particle subjected to an arbitrary linear flow field can be describe by superimposing three basic flows: translational flow, rotational flow, and straining flow. Next, we present basic solutions to these canonical problems, both in an unbound domain and in the simplified case of a spherically confined particle concentric with the confining cavity.

2.3 Canonical problems in Stokes flow

In this section we give an overview of the basic solutions to Stokes equations. In particular, we present the results that illustrate the basic building blocks of Stokes flow: rotational flow, translational flow, and straining flow. Because of the linearity of Stokes flow, results from these basic building blocks can be combined to represent an arbitrary linear flow field when fluid motion is governed

by Stokes equations. The basic solutions of Stokes equations are well known for a single particle in an unbound domain (e.g. see Guazzelli and Morris (2012)[60] for an overview). For a single particle concentric with a spherical cavity, several authors have studied rotational and translational motion[42, 106, 62, 63]. To the best of our knowledge, a straining flow inside a spherical cavity had not been studied in the literature, making the stresslet result presented here new.

2.3.1 Solid body rotation

Let us consider a hard, no-slip, spherical particle located at a position $\boldsymbol{x}_0$ in space and surrounded by a Newtonian solvent undergoing a solid body rotation. The particle is located at the center of rotation of the fluid, and thus no force is required to hold it fixed. We are interested in the hydrodynamic torque exerted by the fluid on the particle at its surface. To calculate the torque, we require the disturbance velocity and pressure fields. The disturbance velocity and pressure fields are defined as,

$$\boldsymbol{u}(\boldsymbol{x}) = \boldsymbol{u}'(\boldsymbol{x}) - \boldsymbol{u}^{\infty}, \tag{2.6}$$

$$P = P' - P^{\infty}, \tag{2.7}$$

where $\boldsymbol{u}^{\infty}$ and P^{∞} are the imposed velocity and pressure fields, and $\boldsymbol{u}'(\boldsymbol{x})$ and P' the velocity and pressure fields in the presence of the particle. The disturbance fields measure how the presence of the particle perturbs the fluid relative to the imposed flow. In the case of solid body rotation with a center of rotation at $\boldsymbol{x}_0$, the imposed velocity field is $\boldsymbol{u}^{\infty} = \boldsymbol{\omega}^{\infty} \wedge \boldsymbol{x}_0$, where $\boldsymbol{\omega}^{\infty}$ is the vorticity vector in the fluid and $\wedge$ represents the cross product operator. Because fluid perturbations arising due to the presence of the particle should decay as the distance to the

particle $\boldsymbol{x}$ increases, we infer the following boundary conditions far from the particle,

$$\boldsymbol{u}(\boldsymbol{x}) = 0, \qquad |\boldsymbol{x}| \to \infty, \tag{2.8}$$

$$P = 0, \qquad |\boldsymbol{x}| \to \infty. \tag{2.9}$$

The boundary condition over the surface of the particle is that of no-slip, thus the fluid velocity is equal to the particle velocity at the particle surface. As a consequence of Galilean invariance, we can a change the coordinate system to consider the equivalent problem of a rotating particle in an otherwise quiescent solvent. In this case, the boundary conditions over the particle surface are,

$$\boldsymbol{u}^{\infty} = -\boldsymbol{\omega}^{\infty} \wedge \boldsymbol{x}_0, \qquad r = |\boldsymbol{x} - \boldsymbol{x}_0| = a. \tag{2.10}$$

We proceed to solve the problem by using equations 2.8, 2.9, and 2.10 as boundary conditions.

To find a solution to the governing equations 2.5 and 2.4 subjected to the boundary conditions 2.8, 2.9, and 2.10, we will use the following strategy. First, we note that by taking the divergence of equation 2.5, we find that the pressure field satisfies Laplace's equations. This implies a solution for the pressure can be obtained in the form of spherical harmonics. Then, owing to the linearity of the governing equations, we can write the solution for the velocity as the sum of a homogeneous solution that satisfies Laplace's equations, and a particular solution related to the pressure field. In this form, the solution for the velocity field is given by,

$$\boldsymbol{u}(\boldsymbol{x}) = \boldsymbol{u}^{H}(\boldsymbol{x}) + \frac{P}{2\eta}\boldsymbol{x}, \tag{2.11}$$

where $\boldsymbol{u}^{H}$ and P both satisfy Laplace's equation. A general solution expressed as an infinite series of spherical harmonics can be found for $\boldsymbol{u}^{H}$ and P. Application

of the boundary conditions far from the particle demonstrate that any growing spherical harmonics need to be discarded. Due to the linearity of Stokes equations, the solution must be linear in the forcing, i.e. it must be linear in $\boldsymbol{\omega}^{\infty}$. By utilizing the requirement of linearity and parity symmetry — where the latter results in the requirement that a real tensor cannot be equal to a pseudo tensors — we can determine which spherical harmonics must be kept in the solution. Subsequent application of the boundary conditions and incompressibility yield the result,

$$\boldsymbol{u}(\boldsymbol{x}) = \boldsymbol{\omega}^{\infty} \wedge \boldsymbol{x} \left(\frac{a}{r}\right)^3, \tag{2.12}$$

$$P(\boldsymbol{x}) = 0, \tag{2.13}$$

where $r = |\boldsymbol{x} - \boldsymbol{x}_0|$.

The hydrodynamic torque acting on the particle in an unbound domain can then be determined by integrating the hydrodynamic surface traction over the particle surface yielding,

$$\boldsymbol{T}^h = 8\pi\eta a^3 \boldsymbol{\omega}^{\infty}. \tag{2.14}$$

Solutions of 2.5 in terms of an infinite series of spherical harmonics typically require a spherically symmetric geometry. For a particle confined inside a spherical cavity of radius R, the only spherically symmetric geometry is the limiting case of a particle that is concentric with the spherical cavity. To develop a solution for the disturbance velocity and pressure fields propagated by a confined particle concentric with the spherical cavity, we will follow the same procedure utilized to derive the corresponding result in an unbound domain. However, in contrast to the solution in an unbound domain, in the confined domain we

must keep the growing spherical harmonics, given that the velocity is finite at the cavity wall. We must also note that the velocity disturbance must now be defined relative to the velocity at the cavity wall. We will consider the problem where the particle rotates while the cavity remains fixed in space, meaning that at the cavity wall the fluid satisfies: $\boldsymbol{u} = 0$ at $|\boldsymbol{x}| = R$. In the confined domain, the velocity is given by,

$$\boldsymbol{v} = \boldsymbol{\omega}^c \wedge \boldsymbol{x}\left(C_1^r \frac{a^3}{r^3} + C_2^r\right). \tag{2.15}$$

The constants C_1^r and C_2^r are determined from the boundary conditions and the incompressibility condition as $C_1^r = (\lambda_c^3 - 1)^{-1}$ and $C_1^r = -\lambda_c^3(\lambda_c^3 - 1)^{-1}$, where $\lambda_c = a/R$ is the ratio of the particle size to the size of the cavity.

Integration of the hydrodynamic surface traction over the surface of the particle yields the hydrodynamic torque the particle surface as,

$$\boldsymbol{T}^h = -8\pi\eta a^3 C_1^r \boldsymbol{\omega}^\infty. \tag{2.16}$$

Note that in equation 2.15 and 2.16 , the velocity field and hydrodynamic torque in an unbound domain are recovered in the limit $\lambda_c \to 0$.

2.3.2 Translation

In this section, we consider a fixed particle immersed in a uniform velocity field $\boldsymbol{u} = \boldsymbol{U}^\infty$. In contrast to rigid body rotation of the fluid, the uniform stream does not cause the particle to rotate and thus no torque is required to hold it fixed. The uniform stream instead causes the particle to undergo translational motion, and thus a force is required to hold the sphere fixed in space. We are interested in the hydrodynamic drag force exerted by the fluid on the particle

surface. As with rigid body rotation, to determine the drag force we must determine the velocity disturbance propagated by the particle. To proceed with the method of solution we will again change the coordinate system to obtain an equivalent problem — a particle translating through the fluid with a constant velocity. The boundary condition at the particle surface is then,

$$\boldsymbol{u} = -\boldsymbol{U}^{\infty}, \qquad r = a. \tag{2.17}$$

We follow the same procedure outlined in the previous section to obtain the velocity and pressure fields propagated by a translating particle as,

$$\boldsymbol{u} = -\frac{3a}{4}\boldsymbol{U}^{\infty} \cdot \left(\frac{\boldsymbol{I}}{r} + \frac{\boldsymbol{xx}}{r^3}\right) - \frac{3a^3}{4}\boldsymbol{U}^{\infty} \cdot \left(\frac{\boldsymbol{I}}{r^3} - \frac{\boldsymbol{xx}}{r^5}\right), \tag{2.18}$$

$$P = -\frac{3\eta a}{2}\frac{\boldsymbol{U} \cdot \boldsymbol{x}}{r^3}. \tag{2.19}$$

Integrating the hydrodynamic surface traction over the surface of the particle yields the hydrodynamic drag force as,

$$\boldsymbol{F}^{H} = 6\pi\eta a \boldsymbol{U}^{\infty}. \tag{2.20}$$

Equation 2.20 is the well know Stokes drag law, determined by George Grabriel Stokes in 1851.

For a confined particle concentric with the spherical cavity, the boundary conditions far-from the particle must change. Instead of the flow decaying to zero infinitely far away from the particle, we consider the cavity to be motionless, and thus the flow decays to zero at the cavity wall $r = R$. By following

the same procedure as done in the case of a particle rotating at the center of the cavity, the instantaneous velocity and pressure disturbances propagated by a particle at the cavity center is obtained as,

$$\boldsymbol{u} = -\boldsymbol{U}^{\infty}\left[\frac{aC_1^t}{2}\left(\frac{\boldsymbol{I}}{r}+\frac{\boldsymbol{xx}}{r^3}\right)+C_2^t\boldsymbol{I}+\frac{C_3^t}{5a^2}\left(\boldsymbol{I}r^2-\frac{\boldsymbol{xx}}{2}\right)+a^3C_4^t\left(\frac{\boldsymbol{I}}{r^3}-\frac{3\boldsymbol{xx}}{r^5}\right)\right], \tag{2.21}$$

$$P = \eta(-\boldsymbol{U}^{\infty}\cdot\boldsymbol{x})\left[C_1^t\frac{a}{r^3}+\frac{C_3^t}{a^2}\right]. \tag{2.22}$$

The coefficients C_1^t, C_2^t, C_3^t, and C_4^t are determined from the boundary conditions to be equal to,

$$C_1^t = \frac{6\left(\lambda_c^4+\lambda_c^3+\lambda_c^2+\lambda_c+1\right)}{(\lambda_c-1)^3\left(4\lambda_c^2+7\lambda_c+4\right)} \tag{2.23}$$

$$C_2^t = \frac{-4\lambda_c^5-4\lambda_c^4-4\lambda_c^3-9\lambda_c^2-9\lambda_c}{(\lambda_c-1)^3\left(4\lambda_c^2+7\lambda_c+4\right)} \tag{2.24}$$

$$C_3^t = \frac{30\left(\lambda_c^4+\lambda_c^3\right)}{(\lambda_c-1)^3\left(4\lambda_c^2+7\lambda_c+4\right)} \tag{2.25}$$

$$C_4^t = \frac{\lambda_c^2+\lambda_c+1}{(\lambda_c-1)^3\left(4\lambda_c^2+7\lambda_c+4\right)} \tag{2.26}$$

By integrating the hydrodynamic surface traction over the particle surface, we obtain the drag force as,

$$\boldsymbol{F}^H = 4\pi\eta a C_1^t \boldsymbol{U}^{\infty}. \tag{2.27}$$

Note that the result in an unbound domain is recovered from equations 2.21, 2.22, and 2.27 in the limit $\lambda_c \to 0$.

2.3.3 Straining

In this section, we consider a particle subjected to a straining flow, which corresponds to a velocity field of the form $\boldsymbol{u} = \boldsymbol{E}^{\infty} \cdot \boldsymbol{x}$,where the second order tensor $\boldsymbol{E}^{\infty}$ is a constant rate of strain. As with rigid body motion or uniform flow, we can impose a straining flow far from the particle or consider the particle to undergo a straining motion that creates the same disturbance velocity and pressure fields. Note that the latter case might seem artificial, because we consider hard (i.e. non-deformable) particles, but it provides a convenient method of solution by considering the boundary conditions over the particle surface to be,

$$\boldsymbol{u} = -\boldsymbol{E}^{\infty} \cdot \boldsymbol{x}, \qquad r = a. \tag{2.28}$$

We interpret the resulting velocity and pressure disturbances propagated by the particle as the instantaneous disturbance propagated before the particle has had time to deform.

Solving the Stokes equations with the strain boundary conditions yields the disturbance velocity and pressure fields as,

$$\boldsymbol{u} = -\frac{5a^3}{2}\frac{\boldsymbol{x}(\boldsymbol{x} \cdot \boldsymbol{E}^{\infty} \cdot \boldsymbol{x})}{r^5} - \frac{a^5}{2}\left[\frac{\boldsymbol{x} \cdot \boldsymbol{E}^{\infty} + \boldsymbol{E}^{\infty} \cdot \boldsymbol{x}}{r^5} - \frac{5\boldsymbol{x}(\boldsymbol{x} \cdot \boldsymbol{E}^{\infty} \cdot \boldsymbol{x})}{r^7}\right], \tag{2.29}$$

$$P = -5\eta a^3 \frac{(\boldsymbol{x} \cdot \boldsymbol{E}^{\infty} \cdot \boldsymbol{x})}{r^5}. \tag{2.30}$$

The stresslet over the particle surface can then be calculated by integrating the symmetric first moment of the hydrodynamic surface traction, this yields,

$$\boldsymbol{S} = \frac{20\pi}{3}\eta a^3 \boldsymbol{E}^{\infty}. \tag{2.31}$$

To consider a straining flow inside a spherical cavity the boundary condition at the cavity wall must be $\boldsymbol{u} = \boldsymbol{E}^{\infty}\cdot\boldsymbol{x}|_{|x|=R}$, so as to produce a pure straining motion at the cavity surface. The flow instantaneously propagated by the cavity wall before it has time to deform can then be modeled has a straining flow inside a spherical cavity. To solve this problem we will follow the same strategy utilized for a particle in an unbound straining flow: we express the boundary condition as a straining motion at the particle surface with a motionless cavity wall via a change of coordinates. Solution of the Stokes equations with these boundary conditions yields the velocity and pressure disturbances inside the spherical cavity as,

$$\begin{aligned}\boldsymbol{u} = -\frac{1}{2}\left(C_1^s\frac{a^3}{r^5} + \frac{C_2^s}{a^2}\right)\boldsymbol{x}(\boldsymbol{x}\cdot\boldsymbol{E}^{\infty}\cdot\boldsymbol{x}) + \frac{5}{21}\frac{C_2^s}{2a^2}\left[r^2(\boldsymbol{x}\cdot\boldsymbol{E}^{\infty} + \boldsymbol{E}^{\infty}\cdot\boldsymbol{x}) - 5\boldsymbol{x}(\boldsymbol{x}\cdot\boldsymbol{E}^{\infty}\cdot\boldsymbol{x})\right] + \\ C_3^s a^5\left[\frac{\boldsymbol{x}\cdot\boldsymbol{E}^{\infty} + \boldsymbol{E}^{\infty}\cdot\boldsymbol{x}}{r^5} - \frac{5\boldsymbol{x}(\boldsymbol{x}\cdot\boldsymbol{E}^{\infty}\cdot\boldsymbol{x})}{r^7}\right] + C_4^s\boldsymbol{E}^{\infty}\cdot\boldsymbol{x}.\end{aligned} \tag{2.32}$$

$$P = \eta\left(C_1^s\frac{a^3}{r^5} + \frac{C_2^s}{a^2}\right)(\boldsymbol{x}\cdot\boldsymbol{E}^{\infty}\cdot\boldsymbol{x}) \tag{2.33}$$

The coefficients in equations 2.32 and 2.33 are determined from the boundary conditions as,

$$C_1^s = \frac{20\left(\lambda_c^6 + \lambda_c^5 + \lambda_c^4 + \lambda_c^3 + \lambda_c^2 + \lambda_c + 1\right)}{(\lambda_c - 1)^3\left(4\lambda_c^6 + 16\lambda_c^5 + 40\lambda_c^4 + 55\lambda_c^3 + 40\lambda_c^2 + 16\lambda_c + 4\right)}, \tag{2.34}$$

$$C_2^s = \frac{105\left(\lambda_c^6 + \lambda_c^5\right)}{(\lambda_c - 1)^3\left(4\lambda_c^6 + 16\lambda_c^5 + 40\lambda_c^4 + 55\lambda_c^3 + 40\lambda_c^2 + 16\lambda_c + 4\right)}, \tag{2.35}$$

$$C_3^s = \frac{2\left(\lambda_c^4 + \lambda_c^3 + \lambda_c^2 + \lambda_c + 1\right)}{(\lambda_c - 1)^3\left(4\lambda_c^6 + 16\lambda_c^5 + 40\lambda_c^4 + 55\lambda_c^3 + 40\lambda_c^2 + 16\lambda_c + 4\right)}, \tag{2.36}$$

$$C_4^s = -\frac{\lambda_c^3\left(4\lambda_c^6 + 4\lambda_c^5 + 4\lambda_c^4 + 4\lambda_c^3 + 4\lambda_c^2 + 25\lambda_c + 25\right)}{(b - 1)^3\left(4\lambda_c^6 + 16\lambda_c^5 + 40\lambda_c^4 + 55\lambda_c^3 + 40\lambda_c^2 + 16\lambda_c + 4\right)}. \tag{2.37}$$

Integration of the symmetric first moment of the hydrodynamic surface traction over the particle surface yields the stresslet as,

$$\boldsymbol{S} = \frac{4a^3\pi\eta}{3}\left(2 - \frac{3}{5}C_1^s - \frac{42}{105}C_2^s + 2C_4^s\right)\boldsymbol{E}^\infty \tag{2.38}$$

2.4 Beyond single particle results: Pairwise hydrodynamic interactions in hard-sphere suspensions

The study of particle motion in Low Reynolds number flows dates back to the work of George Gabriel Stokes, who in 1851 determined the drag force exerted over the surface of a particle moving at a known velocity through a Newtonian fluid in the Stokes flow regime. The resulting equation is the well known Stokes drag law. Later treatments aimed to calculate the drag force over the surface of a particle in the presence of a second particle, i.e. the hydrodynamic

interaction between a pair of particles in Stokes flow. Early methods to calculate hydrodynamic interactions between a pair of particles were developed by Jeffery and co-workers[79, 80, 151]. Jeffery and co-workers focused on particle motion giving rise to axisymmetric flows, which are amenable to solutions via the method of streamfunctions. The authors utilized an eigenfunction expansion of the streamfunction in bispherical coordinates to arrive at the hydrodynamic coupling in the form of an infinite series. The coefficients of the infinite series could be determined by solving a linear system of equations obtained from recursive relations, where the recursive relations were derived through applicatin of the boundary conditions and incompressilibty. Similar methods were later applied to study the coupling of a translating particle near a planar wall[31]. To study the motion of a particle rotating near a planar wall when the particle axis of rotation is parallel to the wall, Dean and O'Neill (1963) [45] developed a solution of Stokes equations in cylindrical coordinates by expressing the velocity and pressure fields in terms of a set of auxiliary functions. These auxiliary functions satisfied a set of partial differential equations which where amenable to a series solution in bispherical coordinates. Coefficients in the infinite series could then be determined by application of the neccessary boundary conditions and the incompressiblity condition. The method was later applied to study translational motion of a particle near a wall [130], and asymmetric motion between an unbound particle pair and a particle in a spherical cavity[169, 117, 131]. This early work focused on determination of the hydrodynamic force and torque on a pair of particles undergoing translational or rotational motion. Interest in determining the hydrodynamic stresslet did not begin until the work of Batchelor (1970) [10], which recognized the importance of the stresslet in the calculation of the particle-phase stress. Green and Batchelor (1972) [59] determined the hydro-

dynamic stresslet on a pair of particles of different radius subjected to a linear shear flow via the method of reflections, and provided numerical solutions for the hydrodynamic coupling between the stresslet and a linear shear flow. During the same year, Brenner and O'Neill (1972) [32] established the general framework for describing particle motion in terms of a 'grand resistance matrix'. They described the form of the resistance functions, and the corresponding solutions in bi-spherical coordinates, but did not provide numerical solutions.

Later work focused on establishing methods of solution that could be implemented in dilute theory of dynamic simulations. Notable work in this area included that of Jeffrey and Onishi (1984) [82], which focused on the force and toque couplings to translational and rotational velocities. They developed a well ordered set of analytical relations describing the hydrodynamic interactions between two different sized particles in both the resistance and mobility formulations. The first calculation of hydrodynamic resistance and mobility functions including couplings with the strain and the stresslet was carried out by Kim and Mifflin (1985) [94], who utilized boundary collocation techniques to numerically solve the Stokes equations. Solutions for particles of unequal radii for the hydrodynamic coupling functions involving the stresslet and strain field were later developed[84]. Although previous work had ignored the trace of the stresslet due to it not impacting particle motion, it was later demonstrated that the stresslet trace is related to the particle-phase osmotic pressure [23]. This motivated the development of the neccessary hydrodynamic coupling functions to determine the trace of the stresslet[83]. More recently the hydrodynamic coupling from axisymmetric motion of a particle inside a spherical cavity was determined[85]. Other recent work has focused on the motion of a pair of particles in non-linear flow fields and studying the hydrodynamic interactions be-

tween a pair of particles in quadratic flows [61, 141].

Pairwise hydrodynamic couplings have been utilized extensively for the modeling of dilute suspension via dilute Smoluchowsky theory, which has provided valuable insight into many problems in colloidal dispersions (cf. §1.1). However, predicting suspension behavior beyond the dilute limit requires the use of computational methods capable of accounting for many-body hydrodynamic interactions. The different methods to account for such interactions are discussed next.

2.5 Many-body interactions

Accounting for many-body hydrodynamic requires the consideration of three or more particles. Although analytical progress can be made [121, 13] to calculate such interactions, the complexity of the resulting expressions limits their use in many applications. This has motivated the development of computational techniques to study the effects of many-body hydrodynamic interactions.

At the finest level of detail, molecular dynamic (MD) simulations[3] are able to account for many-body hydrodynamic interactions through the explicit modeling of solvent molecule collisions. However, the large number of molecules needed to model fluid at the length scales relevant to colloidal particles make such simulations prohibitively expensive in most practical applications. To mitigate the high-computational cost of modeling solvent molecules explicitly, methods that are able to coarse grain the solvent molecules have been developed. Lattice Boltzmann techniques[123] model the effect of the solvent by con-

sidering particles moving through lattice. Utilizing collision operators particle collisions at lattice sites are resolve in such a way as to model fluid motion. The method is able to model fluids at finite Reynolds numbers as well as deformable particles. However, in the modeling of colloidal dispersions[97, 98], errors lead to a loss of Galilean invariance, which in turn results in poor prediction of sensitive rheological properties such as normal stress differences[2]. Another method that aims to coarse grain the solvent molecules is dissipative particle dynamics[71]. Here, effective solvent-solvent interactions are derived as to conserve mass and momentum in the fluid while reducing the number of explicit solvent molecules present in the simulations. The method is computationally efficient at modeling colloidal dispersions. However, because multiple solvent molecules are accounted for utilizing a single particle with an effective inter-particle potential, mapping the simulation data to properties of real systems and obtaining quantitatively accurate predictions remain areas of current research[20].

Another coarse-graining approach is to coarse-grain the solvent into a continuous medium, alowing it to be modeled utilizing Cauchy's equation of motion. For example, assuming the solvent to be Newtonian allows for the application of the Stokes equations. Several computational methods utilizing this coarse-graining approach have been applied to the modeling of colloidal suspensions. Direct numerical simulations[133] apply a variety of numerical methods to solve the fluid's governing equations with the necessary boundary conditions over particle surfaces. This approach can be utilized beyond the Stokes flow regime, for example to model Non-Newtonian solvents or systems with fluid inertia. However, modeling of concentrated suspensions via such 'brute force' approaches commonly results in a prohibitively high computational cost.

Other approaches that rely on obtaining explicit numerical solutions of the equations governing fluid motion are immersed boundary methods[137, 138]. Immersed boundary methods rely on solving the governing equations for fluid motion on a grid. The method is developed such that it models the boundary conditions over different surface without requiring the grid points to be located at such surfaces. As with direct numerical simulations, the method is able to model systems beyond the Stokes flow regime. However, modeling of concentrated suspension and lubrication interactions would require a large number of grid points, making the method computationally expensive. Other methods aim to not only coarse grain the solvent, but also the suspended medium. For example the multi-phase particle-in-cell method [5] couples the Navier-Stokes equations to a particle distribution function that models the evolution of the suspension microstructure. Although the method is able to model concentrated suspensions efficiently, it makes use of empirical relations and thus requires additional information on the system of interest.

The premier method to accurately model many-body and lubrication hydrodynamic interactions in colloidal suspensions of hard, spherical particles with a no-slip surface immersed in a Newtonian solvent is Stokesian dynamics[48, 22, 147]. The method circumvents the need to model fluid motion explicitly by modeling its effect on particle motion through the use of hydrodynamic couplings. It has been demonstrated to provide accurate measurements of both equilbrium and non-equilbrium properties in hard-sphere colloidal dispersions[22, 51, 146]. Because it provides a framework to accurately and efficiently simulate suspensions with many-body and lubrication hydrodynamic interactions, we will utilize this framework as a starting point to develop a new simulation method for spherically confined colloidal suspensions. An

brief overview of the Stokesian dynamics framework is given next.

2.6 Brief Overview of many-body low-*Re* hydrodynamics

In this section we present a brief review of the fundamentals of low-Reynolds number hydrodynamics for unbound suspensions, with a focus on the representation of many-body interactions. Although formulation of the problem begins with expressions for detailed fluid motion, solution of such expressions is bypassed utilizing well-known techniques that combine Taylor expansions and Faxén formulae. We consider a suspension of N particles of size a immersed in an incompressible Newtonian fluid of density ρ and viscosity η. Particle motion of characteristic speed U sets the fluid into motion; because the particles are small, the Reynolds number $Re = \rho UA/\eta << 1$. Thus the importance of inertial forces in the fluid compared to viscous forces is negligible, and the Navier-Stokes equations governing fluid motion become the Stokes equations.

In Stokes flow, fluid-surface interactions can be treated via the approach of Ladyzhenskaya [99] whereby the so-called integral representation gives the fluid disturbance velocity field $\boldsymbol{u}'(\boldsymbol{x}) = \boldsymbol{u}(\boldsymbol{x}) - \boldsymbol{u}^{\infty}(\boldsymbol{x})$, where $\boldsymbol{u}(\boldsymbol{x})$ is the velocity at any field point $\boldsymbol{x}$ in the suspension, including that due to forces exerted by particles on the fluid, where $\boldsymbol{u}^{\infty}(\boldsymbol{x})$ is any far-field imposed flow. The force density over the surface points $\boldsymbol{y}$ of a particle is given by the Cauchy relation, $\boldsymbol{f}(\boldsymbol{y}) = \boldsymbol{n}\cdot\boldsymbol{\sigma}$, where $\boldsymbol{n}$ is the unit surface normal pointing outward from the particle surface and $\boldsymbol{\sigma}$ is the stress exerted on the particle surface by the fluid. The fluid disturbance due to the force propagates from all $\boldsymbol{y}$ throughout the fluid, i.e. to all field

points $\boldsymbol{x}$, as set by the Green's function propagator $\boldsymbol{G}(\boldsymbol{x},\boldsymbol{y})$ corresponding to the physical domain. The fluid disturbance velocity $\boldsymbol{u}'(\boldsymbol{x})$ arising from forcing of a particle α is thus a sum over all points on its surface S_α:

$$\boldsymbol{u}'(\boldsymbol{x}) = -\Big[\int_{S_\alpha} \boldsymbol{f}(\boldsymbol{y})\cdot\boldsymbol{G}(\boldsymbol{x},\boldsymbol{y})dS_y + \int_{S_\infty} \boldsymbol{f}(\boldsymbol{y})\cdot\boldsymbol{G}(\boldsymbol{x},\boldsymbol{y})dS_y\Big], \tag{2.39}$$

where the second integral, over the surface at infinity, acts to conserve mass. In an unbound suspension of hard spheres, the Green's function $\boldsymbol{G}$ is the well-known Stokeslet [134]:

$$\boldsymbol{J}(\boldsymbol{x},\boldsymbol{y}) = \frac{1}{8\pi\eta a}\left(\frac{\boldsymbol{I}}{|\boldsymbol{x}-\boldsymbol{y}|} + \frac{(\boldsymbol{x}-\boldsymbol{y})(\boldsymbol{x}-\boldsymbol{y})}{|\boldsymbol{x}-\boldsymbol{y}|}\right), \tag{2.40}$$

which decays as $1/r$, where $r = |\boldsymbol{x}-\boldsymbol{y}|$. A simple scaling argument shows that the second integral in (2.39) decays with increasing distance from the surface of the forced particle and vanishes as the surface S_∞ grows infinitely far away [93], yielding

$$\boldsymbol{u}'(\boldsymbol{x}) = -\int_{S_\alpha} \boldsymbol{f}(\boldsymbol{y})\cdot\boldsymbol{G}(\boldsymbol{x},\boldsymbol{y})dS_y. \tag{2.41}$$

Direct solution by numerical methods is possible but leads to divergent contact forces, as discussed in §1.1. This difficulty is bypassed by moving the Green's function out of the surface integral via a Taylor expansion of $\boldsymbol{G}$ about the center of particle α. The resulting expansion, often referred to as a multipole expansion, comprises a series of moments of the hydrodynamic surface traction $\hat{\boldsymbol{r}}\cdot\boldsymbol{\sigma}$, where $\boldsymbol{\sigma}$ is the fluid stress and $\hat{\boldsymbol{r}} = (\boldsymbol{y}-\boldsymbol{y}_\alpha)/|\boldsymbol{y}-\boldsymbol{y}_\alpha|$ is the unit normal pointing outward from the surface of the particle and $\boldsymbol{y}_\alpha$ is the location of the center of particle α. Insertion of the Taylor expansion into (2.41) gives

$$\boldsymbol{u}'(\boldsymbol{x}) = -\left(1 + \frac{a_\alpha}{6}\boldsymbol{\nabla}_y^2\right)\boldsymbol{G}(\boldsymbol{x},\boldsymbol{y})\Big|_{\boldsymbol{y}=\boldsymbol{x}_\alpha}\cdot\boldsymbol{F}_\alpha^H +$$

$$- \frac{1}{2}\nabla_y \times \boldsymbol{G}(\boldsymbol{x},\boldsymbol{y})\Big|_{\boldsymbol{y}=\boldsymbol{x}_\alpha} \cdot \boldsymbol{L}_\alpha^H +$$

$$- \left(1 + \frac{a_\alpha}{10}\nabla_y^2\right)\boldsymbol{K}(\boldsymbol{x},\boldsymbol{y})\Big|_{\boldsymbol{y}=\boldsymbol{x}_\alpha} : \boldsymbol{S}_\alpha^H \; + \; ..., \tag{2.42}$$

where the hydrodynamic force $\boldsymbol{F}^H$, torque $\boldsymbol{L}^H$, and stresslet $\boldsymbol{S}^H$ are the zeroth moment and the antisymmetric and symmetric parts of the first moment of the hydrodynamic surface traction, respectively. In addition, irreducible second and third moments of the traction are included in $\boldsymbol{G}$ and $\boldsymbol{K}$, where the couplet $\boldsymbol{K}$ is given by

$$\boldsymbol{K}(\boldsymbol{x},\boldsymbol{y}) = (\nabla_y \boldsymbol{G}(\boldsymbol{x},\boldsymbol{y}) + (\nabla_y \boldsymbol{G}(\boldsymbol{x},\boldsymbol{y}))^T). \tag{2.43}$$

Physically, the motion of a particle α sets the fluid into motion with a velocity $\boldsymbol{u}'(\boldsymbol{x})$ relative to the imposed flow, which in turn entrains other particles β. The corresponding motion of particles β can be determined, to leading order, via Faxén formulae. The Faxén formulae for translational, rotational, and straining motion, $\boldsymbol{U}_\beta$, $\boldsymbol{\Omega}_\beta$, and $\boldsymbol{E}_\beta$ respectively of a particle β in any disturbance flow field $\boldsymbol{u}'(\boldsymbol{x})$ are

$$\boldsymbol{U}_\beta - \boldsymbol{u}^\infty(\boldsymbol{x}_\beta) = \frac{\boldsymbol{F}_\beta}{6\pi\eta a_\beta} + \left(1 + \frac{a_\beta^2}{6}\nabla_x^2\right)\boldsymbol{u}'(\boldsymbol{x})\Big|_{\boldsymbol{x}_\beta}, \tag{2.44}$$

$$\boldsymbol{\Omega}_\beta - \boldsymbol{\omega}^\infty(\boldsymbol{x}_\beta) = \frac{\boldsymbol{L}_\beta}{8\pi\eta a_\beta^3} + \frac{1}{2}\nabla_x^2 \times \boldsymbol{u}'(\boldsymbol{x})\Big|_{\boldsymbol{x}_\beta}, \tag{2.45}$$

$$- \boldsymbol{E}^\infty = \frac{\boldsymbol{S}_\beta}{\frac{20}{3}\pi\eta a_\beta^3} + \left(1 + \frac{a_\beta^2}{10}\nabla_x^2\right)\boldsymbol{E}'(\boldsymbol{x})\Big|_{\boldsymbol{x}_\beta}, \tag{2.46}$$

where $\boldsymbol{E}'(\boldsymbol{x})$ is the disturbance rate of strain,

$$\boldsymbol{E}'(\boldsymbol{x}) = \frac{1}{2}\left[\boldsymbol{\nabla}_x \boldsymbol{u}'(\boldsymbol{x}) + (\boldsymbol{\nabla}_x \boldsymbol{u}'(\boldsymbol{x}))^T\right]. \tag{2.47}$$

Because all N particles interact, the leading-order disturbance flow $\boldsymbol{u}'(\boldsymbol{x})$ is a sum given by

$$\begin{aligned}\boldsymbol{u}'(\boldsymbol{x}) = \sum_{\alpha=1}^{N}\Bigg(&-\left(1 + \frac{a_\alpha}{6}\boldsymbol{\nabla}_y^2\right)\boldsymbol{G}(\boldsymbol{x},\boldsymbol{y})\Big|_{\boldsymbol{y}=\boldsymbol{x}_\alpha} \cdot \boldsymbol{F}_\alpha^H \; + \\ &-\frac{1}{2}\boldsymbol{\nabla}_y \times \boldsymbol{G}(\boldsymbol{x},\boldsymbol{y})\Big|_{\boldsymbol{y}=\boldsymbol{x}_\alpha} \cdot \boldsymbol{L}_\alpha^H \; + \\ &-\left(1 + \frac{a_\alpha}{10}\boldsymbol{\nabla}_y^2\right)\boldsymbol{K}(\boldsymbol{x},\boldsymbol{y})\Big|_{\boldsymbol{y}=\boldsymbol{x}_\alpha} : \boldsymbol{S}_\alpha^H \; + \; ...\Bigg).\end{aligned} \tag{2.48}$$

Insertion of equation 2.48 into equations 2.44, 2.45 and 2.46 yields a set of linear relations between particle motion and hydrodynamic force, torque, stresslet, and higher-order moments:

$$\begin{pmatrix} \boldsymbol{U} - \boldsymbol{u}^\infty \\ \boldsymbol{\Omega} - \boldsymbol{\omega}^\infty \\ -\boldsymbol{E}^\infty \\ \vdots \end{pmatrix} = -\mathcal{M} \cdot \begin{pmatrix} \boldsymbol{F}^H \\ \boldsymbol{L}^H \\ \boldsymbol{S}^H \\ \vdots \end{pmatrix} \tag{2.49}$$

where the pair-wise couplings between motion and moments form the "grand

mobility matrix" $\mathcal{M}$,

$$\mathcal{M} = \begin{pmatrix} \boldsymbol{M}^{UF} & \boldsymbol{M}^{UL} & \boldsymbol{M}^{US} & \dots \\ \boldsymbol{M}^{\Omega F} & \boldsymbol{M}^{\Omega L} & \boldsymbol{M}^{\Omega S} & \dots \\ \boldsymbol{M}^{EF} & \boldsymbol{M}^{EL} & \boldsymbol{M}^{ES} & \dots \\ \vdots & \vdots & \vdots & \ddots \end{pmatrix}. \tag{2.50}$$

Each element of the grand mobility matrix comprises sub-matrices that couple the motion of each particle to the traction moments of all other particles. For example, for two particles α and β, the velocity-force coupling is

$$\boldsymbol{M}^{UF} = \begin{pmatrix} \boldsymbol{M}^{UF}_{\alpha\alpha} & \boldsymbol{M}^{UF}_{\alpha\beta} \\ \boldsymbol{M}^{UF}_{\beta\alpha} & \boldsymbol{M}^{UF}_{\beta\beta} \end{pmatrix}, \tag{2.51}$$

where each submatrix is itself a second-rank tensor coupling particles to one another. So-called self-mobility tensors ($\alpha\alpha$ and $\beta\beta$) characterize the motion of a particle in response to a hydrodynamic force on its own surface. In contrast, pair-mobility tensors ($\alpha\beta$ and $\beta\alpha$) characterize the entrainment of one particle by the motion of another. The grand mobility matrix depends only on geometry; for an unbound domain, it is set entirely by particle size, shape, and microstructural configuration. The minimum dissipation theorem demands a symmetric and positive-definite grand mobility matrix; this must be ensured in any model for hydrodynamically interacting colloidal particles based on this representation.

In many suspension mechanics problems, the forces acting on particles are known (e.g. gravity, electric fields, magnetic fields), and particle motion is sought. Equation 2.51 appears ready to solve this problem—but two issues remain. First, a practical problem: one must solve an infinite hierarchy of equations, relating motion to an infinitude of hydrodynamic moments. More funda-

mentally, the mobility matrix in equation 2.51 is a strictly pairwise formulation of the interaction between the particles and further, accounts only for the "first reflection" of hydrodynamic interactions—that is, the entrainment of particle β by particle α in turn creates a new disturbance flow that is not captured by summing the disturbance flow of individual particles via this integral formulation approach. Brady and co-workers [48] showed that inverting the mobility matrix, however, automatically couples all (infinitely many) reflections between all particles, similar in ethos to a geometric series expansion, thus accomplishing the task of transforming the pair-level problem into a full many-body hydrodynamic coupling. The inverse of the grand mobility matrix is the grand resistance matrix, $\mathcal{M}^{-1} = \mathcal{R}$:

$$\begin{pmatrix} \boldsymbol{R}^{UF} & \boldsymbol{R}^{UL} & \boldsymbol{R}^{US} & \dots \\ \boldsymbol{R}^{\Omega F} & \boldsymbol{R}^{\Omega L} & \boldsymbol{R}^{\Omega S} & \dots \\ \boldsymbol{R}^{EF} & \boldsymbol{R}^{EL} & \boldsymbol{R}^{ES} & \dots \\ \vdots & \vdots & \vdots & \end{pmatrix} = \begin{pmatrix} \boldsymbol{M}^{UF} & \boldsymbol{M}^{UL} & \boldsymbol{M}^{US} & \dots \\ \boldsymbol{M}^{\Omega F} & \boldsymbol{M}^{\Omega L} & \boldsymbol{M}^{\Omega S} & \dots \\ \boldsymbol{M}^{EF} & \boldsymbol{M}^{EL} & \boldsymbol{M}^{ES} & \dots \\ \vdots & \vdots & \vdots & \ddots \end{pmatrix}^{-1}, \tag{2.52}$$

giving the full many-body coupling between hydrodynamic traction moments and particle motion.

The practical problem of an infinite hierarchy of equations is solved in a correspondingly practical way: The mobility matrix is simply truncated to a finite number of moments. The physical consequence of such approximation is the omission of near-field interactions between particles, and thus it gives a far-field grand mobility tensor, denoted $\mathcal{M}_{ff}$. The task of accounting for near-field interactions is easily and rigorously carried at by simply re-introducing the omitted interactions by linear superposition of the analytical, exact pairwise resistance functions, a technique central to the Stokesian dynamics approach

pioneered by Brady and Bossis [22]. The resulting matrix forms a complete, many-body near- and far-field hydrodynamic coupling tensor

$$\mathcal{R} = (\mathcal{M}_{ff})^{-1} + \mathcal{R}_{nf}. \tag{2.53}$$

Here, $(\mathcal{M}_{ff})^{-1}$ is the inverse of the truncated far-field grand mobility matrix, capturing an infinite number of reflections between all particles. The near-field interactions are incorporated via a near-field two-body resistance tensor, $\mathcal{R}_{nf}$. The functions that form the unbound-suspension matrices are well-established and can be found in the literature [82, 93, 81]. Because the far-field coupling also counts the far-field pair interactions, the far-field pair couplings have been subtracted from $\mathcal{M}_{ff}$ to avoid double-counting. Recent computational studies of confinement effects have extended these ideas to account for confinement by single [155] or parallel [156, 157] walls, where the domain is still semi-infinite, i.e. only partially bound. In this study, we develop the theoretical model for 3D micro-confined hydrodynamically interacting particles enclosed inside a spherical no-slip boundary.

The linearity relation between particle motion and hydrodynamic force, torque, and stresslet are then expressed in terms of the grand resistance matrix $\mathcal{R}$ comprising the near-field resistance tensor and the inverse of the far-field grand mobility tensor, thus providing the complete hydrodynamic coupling:

$$\begin{pmatrix} \boldsymbol{F}^H \\ \boldsymbol{L}^H \\ \boldsymbol{S}^H \end{pmatrix} = -\left(\mathcal{R}_{nf} + (\mathcal{M}_{ff})^{-1}\right) \cdot \begin{pmatrix} \boldsymbol{U} - \boldsymbol{u}^\infty \\ \boldsymbol{\Omega} - \boldsymbol{\omega}^\infty \\ -\boldsymbol{E}^\infty \end{pmatrix}. \tag{2.54}$$

This expression can be decomposed line-by-line to obtain particle motion while retaining the reflections between all particles. For example, the first equation for the hydrodynamic force gives the velocity:

$$\boldsymbol{U} = -\left(\mathcal{R}^{FU}\right)^{-1} \cdot \left[\boldsymbol{F}^{H} + \mathcal{R}^{F\Omega} \cdot \boldsymbol{\Omega} - \mathcal{R}^{FE} \cdot \boldsymbol{E}^{\infty}\right] \tag{2.55}$$

$$\equiv -\mathcal{M}^{UF} \cdot \left[\boldsymbol{F}^{H} + \mathcal{R}^{F\Omega} \cdot \boldsymbol{\Omega} - \mathcal{R}^{FE} \cdot \boldsymbol{E}^{\infty}\right], \tag{2.56}$$

and the second line for the torque gives rotational motion, *viz.*

$$\boldsymbol{\Omega} = -\left(\mathcal{R}^{L\Omega}\right)^{-1} \cdot \left[\boldsymbol{L}^{H} + \mathcal{R}^{LU} \cdot \boldsymbol{U} - \mathcal{R}^{LE} \cdot \boldsymbol{E}^{\infty}\right] \tag{2.57}$$

$$\equiv -\mathcal{M}^{\Omega L} \cdot \left[\boldsymbol{L}^{H} + \mathcal{R}^{LU} \cdot \boldsymbol{U} - \mathcal{R}^{LE} \cdot \boldsymbol{E}^{\infty}\right]. \tag{2.58}$$

Thus, to compute the motion of particles in a hydrodynamically interacting suspension, one must compute the configuration-dependent couplings between particles $\mathcal{R}^{UF}$ and $\mathcal{R}^{\Omega L}$, along with the analogous couplings $\mathcal{R}^{UL}$, $\mathcal{R}^{\Omega F}$, $\mathcal{R}^{ES}$, $\mathcal{R}^{\Omega S}$, $\mathcal{R}^{EF}$. The total, many-body mobility $\mathcal{M}^{UF}$, $\mathcal{M}^{\Omega L}$, $\mathcal{M}^{UL}$, $\mathcal{M}^{\Omega F}$, $\mathcal{M}^{ES}$, $\mathcal{M}^{\Omega S}$, and $\mathcal{M}^{EF}$ couplings can be obtained upon blockwise inversion of the total, many-body resistance coupling as shown in equations 2.56 – 2.58. Henceforth this notation refers to the total, many-body couplings between all particles.

CHAPTER 3

THEORETICAL AND SIMULATION METHODS

In this chapter, we give a brief overview of computational techniques that will be utilized throughout this thesis. We begin with a discussion of the simulation techniques utilized to conduct dynamic simulations in 3.1. Section 3.2 discusses the stochastic techniques utilized to accurately and efficiently determine short-time transport properties. Finally, section 3.3 discusses the calculation of the concentrated pair mobility in spherically confined suspensions.

3.1 Dynamic simulation

We consider a suspension of N spherical colloidal particles of radius a immersed in a Newtonian solvent confined inside an impermeable, no-slip spherical boundary of radius R. The size of the particles relative to the enclosure is given by the particle-to-cavity size ratio $\lambda_c = a/R$. Figures 3.1(a)-(b) give snapshots from three simulations with different volume fractions and particle-to-cavity size ratio, illustrating the system of interest. In these micro-confined

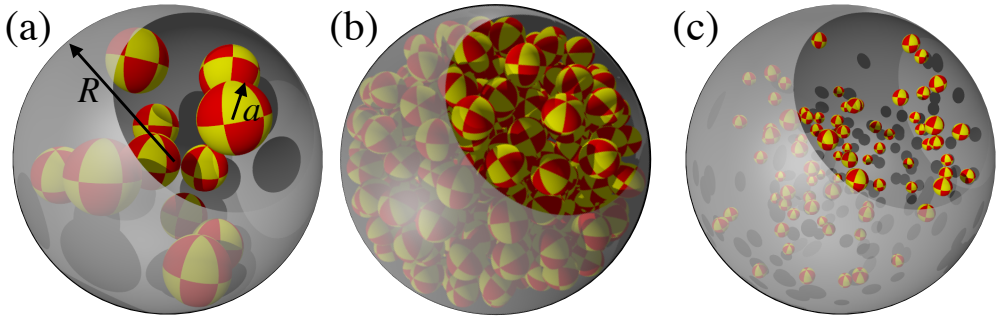

Figure 3.1: Simulation snapshots illustrating variation of particle-to-cavity size ratio λ_c and volume fraction ϕ. (a) $\lambda_c = 0.2$, $\phi = 0.1$. (b) $\lambda_c = 0.1$, $\phi = 0.3$. (c) $\lambda_c = 0.05$, $\phi = 0.05$.

suspensions, particle motion is governed by the N-body Langevin equation,

$$\boldsymbol{m} \cdot \frac{\mathrm{d}\boldsymbol{U}}{\mathrm{d}t} = \boldsymbol{F}^H + \boldsymbol{F}^B + \boldsymbol{F}^P + \boldsymbol{F}^{ext}, \tag{3.1}$$

where $\boldsymbol{m}$ is a generalized mass/moment of inertia tensor and $\boldsymbol{U}$ is a generalized velocity vector of the translational and rotational particle velocities relative to the fluid. The right-hand side of equation 3.1 represents the net force (and torque) acting on each particle. The total force and torque comprise four contributions: $\boldsymbol{F}^B$ is a Brownian (stochastic) force and torque satisfying Gaussian statistics and arising due to the numerous collisions of solvent molecules with the particle surface during time intervals much longer than the solvent time scale, and $\boldsymbol{F}^P$ gives the force and torque derivable from the inter-particle interaction potential. An externally applied force and torque, $\boldsymbol{F}^{ext}$, may also act on the particles. Finally, $\boldsymbol{F}^H$ is the hydrodynamic force and torque exerted by the fluid on the particle surface as a particle undergoes motion relative to the fluid. In Stokes flow, moments of the hydrodynamic surface traction are linearly coupled to particle motion via the inverse of the hydrodynamic resistance matrix. For the quiescent suspension considered here, this may be written using the generalized force and velocity matrices as

$$\boldsymbol{F}^H = -\boldsymbol{\mathcal{R}}_{FU} \cdot \boldsymbol{U}. \tag{3.2}$$

Here, $\boldsymbol{\mathcal{R}}_{FU}$ is a generalized resistance matrix of the hydrodynamic couplings between translational/rotational motion and forces/torques defined as

$$\boldsymbol{\mathcal{R}}_{FU} \equiv \begin{pmatrix} \boldsymbol{R}_{FU} & \boldsymbol{R}_{LU} \\ \boldsymbol{R}_{F\Omega} & \boldsymbol{R}_{L\Omega} \end{pmatrix}. \tag{3.3}$$

The hydrodynamic resistance depends only on geometry, which for spherically confined suspensions involves the configuration of the N particles in the spheri-

cal cavity and their sizes relative to the cavity radius. In the spherically confined domain, $\mathcal{R}_{FU}$ must account for hydrodynamic interactions between the particles themselves and between the particles and the cavity, and a method to account for such interactions is developed in chapter 4.

The displacement of particles over time is obtained by integrating equation 3.1 over a time long compared to the particle inertial relaxation time (the overdamped limit) but short compared to the time it takes for changes in structural configurations to take place. This yields a displacement equation that gives the change in particle positions $\boldsymbol{\Delta x}$ that takes place during a time interval Δt:

$$\boldsymbol{\Delta x}(\Delta t) = (\mathcal{R}_{FU}^{-1} \cdot \boldsymbol{F}^P + kT\boldsymbol{\nabla} \cdot \mathcal{R}_{FU}^{-1})\Delta t + \boldsymbol{X}(\Delta t) + O(\Delta t). \tag{3.4}$$

In equation 3.4, $\boldsymbol{\Delta x}$ is the particle displacement during a time interval Δt. The three terms on the righ-hand side correspond to displacements arising from interparticle forces, deterministic Brownian drift, and stochastic Brownian motion with zero mean, and variance proportional to a configuration-dependent drag:

$$\overline{\boldsymbol{X}} = 0, \qquad \overline{\boldsymbol{X}(t)\boldsymbol{X}(t)} = 2kT\mathcal{R}_{FU}^{-1}\Delta t. \tag{3.5}$$

In equation 3.5, the overbar denotes a noise average over times much longer than individual solvent collisions and over times long compared to particle momentum relaxation; k is Boltzmann's constant and T is the absolute temperature.

Hydrodynamic interactions that set the configuration-dependent resistance tensor $\mathcal{R}$ must capture both many-body and lubrication hydrodynamic interactions in spherically-confined colloidal suspensions. A method to account for such interactions is put forth in chapter 4[6]. The approach makes use of an ex-

pansion in moments of the hydrodynamic surface traction to develop a far-field grand mobility matrix that accounts for the presence of the spherical cavity. Because the expansion is truncated at the level of the stresslet, the method requires the inversion of an $11N \times 11N$ matrix to capture an infinitude of reflections, as done in the Stokesian dynamics framework [48]. Although traditional methods for matrix inversion incur a computational cost that scales as $O(N^3)$, we avoid such computationally expensive methods through the use of iterative solvers, which reduce the computational cost of calculating the required particle displacements to a more favorable $O(N^2)$ [9].

For modeling suspensions at equilibrium, further reduction in computational cost is achieved in chapter 5 by including the hydrodynamic force and torque in the calculations while neglecting the many-body stresslet, which reduces the $11N \times 11N$ matrix that must be inverted to $6N \times 6N$ (the pair-level stresslet is still included in the model). The accuracy of this simplification is restricted to equilibrium calculations, where the stresslet induced by reflected particle interactions produces disturbance flows that decay as $1/r^4$ (where r is the distance to a point in the fluid), as compared to the $1/r$ and $1/r^2$ disturbance flows that form leading-order disturbances from hydrodynamic force and torque. To demonstrate the validity of this approximation, results for the short-time self-diffusivity for force/torque only to force/torque/stresslet computations are compared in Appendix B.6. Similar truncation methods have been employed in the study of unbound suspensions, and have been shown to produce accurate results with reduced computational cost at equilibrium [48, 47].

3.2 Short-time transport properties

A stochastic sampling technique permits rapid and efficient calculation of the short-time self-diffusivity. Similar stochastic techniques have been used to calculate the short-time self-diffusivity in unbound suspensions [147] and suspensions confined inside a channel [157], and for calculating concentrated pair mobility tensors [180, 152] in unbound suspensions. The short-time self-diffusivity can be connected to the hydrodynamic mobility via the fluctuation-dissipation theorem, which dictates that the short-time self-diffusivity tensor must satisfy,

$$\boldsymbol{D}_0 = \langle \boldsymbol{M}_{UF,\alpha\alpha} \rangle, \tag{3.6}$$

where the angle brackets denote an ensemble average over many particle configurations, and the subscript $\alpha\alpha$ denotes the self-mobility of the particle. In equation 3.6, the mobility has been normalized by the mobility of an isolated particle $1/6\pi\eta a$, and the diffusivity by the Stokes-Einstein coefficient $D_0 = kT/(6\pi\eta a)$, where η is the viscosity of the solvent. The trace of equation 3.6 was previously measured for unbound suspensions via Accelerated Stokesian dynamics by [147], a measurement that assumes diffusion to be isotropic *a priori*. As will be shown, the ensemble-averaged mobility tensor in spherically confined suspensions is position dependent and anisotropic. Here, we demonstrate a method that captures both of these features.

To efficiently determine the short-time self-diffusivity, the stochastic techniques of [147] and [180] are followed, where particles are assigned stochastic forces with zero mean and identity covariance; particle velocities are then calculated for a given configuration. The full mobility tensor for one realization is then given by the outer product of the forces and velocities, and averaging

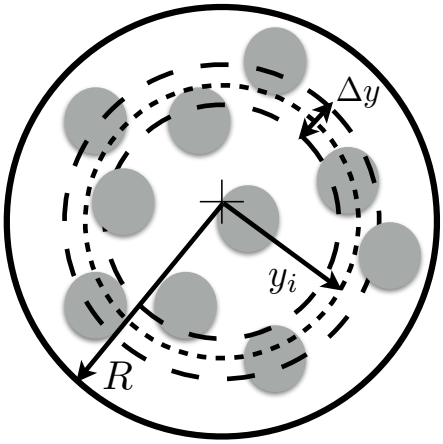

Figure 3.2: Illustration of model system. Particles of radius a are located at positions y_i inside the cavity of radius R. Dashed lines illustrate one bin, a spherical annulus of thickness Δy with nominal radius y_i.

over many configurations then yields the short-time self-diffusivity. To capture the anisotropy of the mobility tensor, the outer product is projected onto an orthogonal basis corresponding to diffusion along and perpendicular to the cavity radius. The orthogonal projection yields the radial and perpendicular components of the short-time self-diffusivity, $D_0^{\parallel}$ and $D_0^{\perp}$ respectively:

$$D_0^{\parallel} = \langle \boldsymbol{U}_\alpha \boldsymbol{F}_\alpha : \hat{\boldsymbol{y}}_\alpha \hat{\boldsymbol{y}}_\alpha \rangle, \tag{3.7}$$

$$D_0^{\perp} = \langle \boldsymbol{U}_\alpha \boldsymbol{F}_\alpha : \frac{1}{2}(\boldsymbol{I} - \hat{\boldsymbol{y}}_\alpha \hat{\boldsymbol{y}}_\alpha) \rangle, \tag{3.8}$$

where $\hat{\boldsymbol{y}}_\alpha$ is a unit vector pointing from the cavity center to the center of the particle. To capture the position dependence of the short-time self-diffusivity, radial bins are constructed as annular shells of radius $y_n = (n - 1/2)\Delta y$ from the center of the cavity. All particles a distance $y_n \pm \Delta y/2$ are assigned to the n^{th} bin. Averages are computed within each bin, thus averaging the statistics of particles within a bin and giving a radially dependent diffusion tensor. The total number of bins $n_{tot} = 100$ provides spatial resolution sufficient to observe structural and dynamical variation in the suspension. The statistics at the center of the cavity

are most challenging to capture, owing to small bin volume. An alternative is to define bins of fixed volume, but this would smear out the radial dependence of particle motion. To counteract the small-volume statistics, we opt to simply conduct a large enough number of simulations to minimize statistical noise near the center.

3.3 Concentrated pair mobility in spherically confined suspensions

A stochastic technique similar to the one utilized to determine short-time self diffusivity is utilized to determine the concentrated pair mobility in concentrated, spherically confined suspension. In contrast to short-time self diffusion in the spherically confined domain, the concentrated pair mobility not only depends on particle position, it also depends on inter-particle separation. Radial and perpendicular motion between two particles in the confined domain can also be coupled, requiring the consideration of five tensor components to fully specify the translational velocity to force coupling.

As with short-time self diffusion, a stochastic technique is implemented wherein particles are assigned stochastic forces with zero mean and identity covariance and particle velocities are subsequently calculated for given particle configurations. An outer product between the corresponding velocities and forces felt by the particles then yields the concentrated self and entrained mobilites. To capture self and entrained motion, we must project the mobility along the appropriate directions. We note that in spherical confinement, motion along the line of centers may be coupled to a force perpendicular to the line of centers

and vice-versa. The mobility tensor can thus be expressed as,

$$\boldsymbol{M}^{UF,\alpha\beta} = x^{A1}_{\alpha\beta}\hat{\boldsymbol{r}}\hat{\boldsymbol{r}} + x^{A2}_{\alpha\beta}\hat{\boldsymbol{r}}\hat{\boldsymbol{r}}^{\perp} + x^{A3}_{\alpha\beta}\hat{\boldsymbol{r}}^{\perp}\hat{\boldsymbol{r}} + x^{A4}_{\alpha\beta}\hat{\boldsymbol{r}}^{\perp}\hat{\boldsymbol{r}}^{\perp} + x^{A5}_{\alpha\beta}\boldsymbol{I}, \tag{3.9}$$

where β and α denote the forced and entrained particle, respectively. The scalar quantities $x^{A}_{\alpha\beta}$ represent the coupling between force and velocity in different directions, $\boldsymbol{I}$ is the isotropic unit tensor, and $\hat{\boldsymbol{r}}$ and $\hat{\boldsymbol{r}}^{\perp}$ are unit vectors pointing along and perpendicular to the line of center between the particles, respectively. Projection of equation 3.9 to the directions of interest demonstrates that each scalar component satisfies the equations,

$$\langle \boldsymbol{U}_{\alpha}\boldsymbol{F}_{\beta} : \hat{\boldsymbol{r}}\hat{\boldsymbol{r}} \rangle = x^{A1}_{\alpha\beta} + x^{A5}_{\alpha\beta}, \tag{3.10}$$

$$\langle \boldsymbol{U}_{\alpha}\boldsymbol{F}_{\beta} : \hat{\boldsymbol{r}}\hat{\boldsymbol{r}}^{\perp} \rangle = x^{A2}_{\alpha\beta}, \tag{3.11}$$

$$\langle \boldsymbol{U}_{\alpha}\boldsymbol{F}_{\beta} : \hat{\boldsymbol{r}}^{\perp}\hat{\boldsymbol{r}} \rangle = x^{A3}_{\alpha\beta}, \tag{3.12}$$

$$\langle \boldsymbol{U}_{\alpha}\boldsymbol{F}_{\beta} : \hat{\boldsymbol{r}}^{\perp}\hat{\boldsymbol{r}}^{\perp} \rangle = x^{A4}_{\alpha\beta} + x^{A5}_{\alpha\beta}, \tag{3.13}$$

$$\langle \boldsymbol{U}_{\alpha}\boldsymbol{F}_{\beta} : \boldsymbol{I} \rangle = x^{A1}_{\alpha\beta} + x^{A4}_{\alpha\beta} + 3x^{A5}_{\alpha\beta}. \tag{3.14}$$

Equations 3.10-3.14 can then be solved to obtain each scalar coupling for the concentrated pair mobility in the spherically confined domain. To capture the position dependence of the concentrated pair mobility, particles are binned according to their distance to the cavity center, as done with the short-time self diffusivity. These bins will be referred to as y-bins. Dependence with respect to particle center-to-center distance is accounted for by defining additional bins, but now with respect to inter-particle distance r, and will be denoted as r-bins. The r-bins are defined such that particles are placed in the n^{th} bin if they are separated a distance $r_n \pm \Delta r/2$. The parameter Δr is the size of the bin, which is set to $\Delta r = 0.1$, and provides enough resolution to observed structural variations

with respect to inter-particle distance. The concentrated pair mobility is calculated for particles located in the same y-bin, that is at equal distance to the cavity center, in order to distinguish effects of distance to the cavity wall from those of inter-particle separation. In chapter 6, particles located at 1/4, 1/2, 3/4, and 95/100 of their maximum radial position in the cavity $y_{max} = (R - a)/R$ are considered. This allows for the study of confinement induced changes to particle entrainment when particles are both near the cavity center and near the cavity wall.

CHAPTER 4

SIMULATION OF HYDRODYNAMICALLY INTERACTING PARTICLES CONFINED BY A SPHERICAL CAVITY

In this chapter, a Stokesian dynamics like framework is developed to model the behavior of concentrated, spherically confined colloidal suspensions while accounting for many-body and lubrication hydrodynamic interactions. The framework for many-body low-Reynolds number hydrodynamics is extended to spherically confined suspensions, and results in the development of a new set of hydrodynamic mobility functions that couple particle motion in the presence of the cavity wall. This is followed by a discussion of how the cavity wall impacts particle entrainment in the confined domain.

4.1 Spherical confinement: theoretical framework

In this section we present the framework with which to model the motion of hydrodynamically interacting particles confined inside a spherical boundary. Careful consideration is given to the development of the far-field grand mobility matrix to accurately represent the many-body hydrodynamic interactions of spherically confined particles, as well as the near-field and lubrication interactions. As in §2.6 we consider N hard, spherical particles of size a in a fluid of density ρ and viscosity η whose motion is governed by the Stokes equations, owing to a vanishingly small Reynolds number. The fluid and particles are confined to a finite domain: a hard, no-slip spherical cavity of radius R (figure 4.1). Any far-field flow $\boldsymbol{u}^{\infty}$ present can arise due only to external forces applied to the particles or to motion of the cavity. Ladyzhenskaya's integral representation

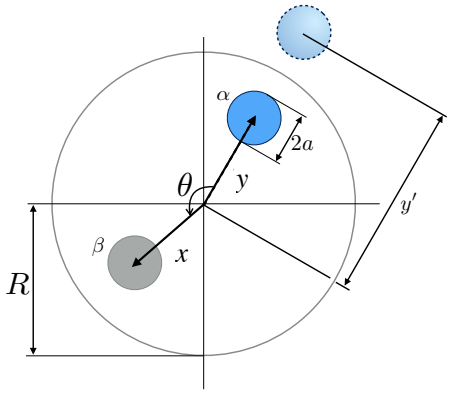

Figure 4.1: Model system with an image point external to the cavity.

gives the fluid disturbance arising from tractions on the particle surfaces S_α,

$$\boldsymbol{u}'(\boldsymbol{x}) = \; -\int_{S_a} \boldsymbol{f}(\boldsymbol{y}) \cdot \boldsymbol{G}(\boldsymbol{x},\boldsymbol{y}) dS_y - \int_{S_c} \boldsymbol{f}(\boldsymbol{y}) \cdot \boldsymbol{G}(\boldsymbol{x},\boldsymbol{y}) dS_y, \tag{4.1}$$

where now the integral at infinity has become an integral over the cavity surface S_c. The second integral does not vanish, in contrast to equation 2.39, a consequence of the finite domain size. Seeking a solution in this form requires the surface traction over the surface of the cavity. To avoid this tedious calculation, an image point is utilized to modify the Green's function so as to satisfy the no-slip and no-flux boundary conditions over the cavity surface. The image point creates a perturbation that exactly satisfies the no-slip and no-flux boundary conditions at the surface of the cavity:

$$\boldsymbol{G}(\boldsymbol{x},\boldsymbol{y}) = \boldsymbol{J}(\boldsymbol{x},\boldsymbol{y}) + \boldsymbol{J}^c(\boldsymbol{x},\boldsymbol{y}), \tag{4.2}$$

where $\boldsymbol{J}(\boldsymbol{x},\boldsymbol{y})$ is the unbound Stokeslet and $\boldsymbol{J}^c(\boldsymbol{x},\boldsymbol{y})$ is a tensor that enforces the no-slip and no-flux conditions that define the surface of the cavity. The tensor $\boldsymbol{J}^c(\boldsymbol{x},\boldsymbol{y})$, due to Oseen, is given by the expression [134]

$$\boldsymbol{J}^c(\boldsymbol{x},\boldsymbol{y}) = -\frac{1}{8\pi\eta R}\left(\frac{\boldsymbol{I}}{y \mid \boldsymbol{x}-\boldsymbol{y}' \mid} + \frac{(\boldsymbol{x}-\boldsymbol{y}')(\boldsymbol{x}-\boldsymbol{y}')}{y^3 \mid \boldsymbol{x}-\boldsymbol{y}' \mid^3} + \frac{y^2-1}{y}\left(\frac{\boldsymbol{y}\boldsymbol{y}}{y^4 \mid \boldsymbol{x}-\boldsymbol{y}' \mid}\right.\right.$$

$$- \frac{\boldsymbol{y}(\boldsymbol{x}-\boldsymbol{y}') + (\boldsymbol{x}-\boldsymbol{y}')\boldsymbol{y}}{y^4 \mid \boldsymbol{x}-\boldsymbol{y}' \mid^3} + \frac{2\boldsymbol{y}\boldsymbol{y}\boldsymbol{y}\cdot(\boldsymbol{x}-\boldsymbol{y}')}{y^6 \mid \boldsymbol{x}-\boldsymbol{y}' \mid^3}\Bigg) + (x^2-1)\boldsymbol{\nabla}_x\boldsymbol{\varphi}\Bigg) \tag{4.3}$$

where

$$\boldsymbol{\varphi} = \frac{y^2-1}{2y^3}\Bigg(\frac{3\boldsymbol{y}}{y} + \frac{\boldsymbol{x}-\boldsymbol{y}'}{\mid \boldsymbol{x}-\boldsymbol{y}' \mid^3} + 2\boldsymbol{y}\boldsymbol{y}'\cdot\boldsymbol{\nabla}_x\frac{1}{\mid \boldsymbol{x}-\boldsymbol{y}' \mid} + \frac{3x(x-(1-y \mid \boldsymbol{x}-\boldsymbol{y}' \mid)\frac{\boldsymbol{x}\cdot\boldsymbol{y}}{xy^2})}{\mid \boldsymbol{x}-\boldsymbol{y}' \mid}\frac{(\boldsymbol{x}-\boldsymbol{x}\cdot\boldsymbol{y}'\boldsymbol{y})}{((xy')^2-(\boldsymbol{x}\cdot\boldsymbol{y}')^2)}\Bigg). \tag{4.4}$$

Here, $\boldsymbol{y}' = \boldsymbol{y}/y^2$ is the position of the image point outside a spherical boundary, and all lengths have been made dimensionless on the radius R of the cavity. We note that the expression for $\boldsymbol{J}^c(\boldsymbol{x},\boldsymbol{y})$ differs from the corresponding expression in the study of an infinitesimal point of Felderhof and Sellier [49], owing to a typographical error in that publication. As written, equation 4.3 appears to diverge at the point $y = 0$, suggesting that even a weak disturbance at the center of the cavity produces infinitely strong flows. Fortunately, this is a mathematically removable singularity. Straightforward algebraic manipulation removes the singularity to show the Green's function is entire. Similarly, although at first glance some components of the mobility tensors (derived in Appendix A) appear to diverge for the values $\hat{\boldsymbol{x}}\cdot\hat{\boldsymbol{y}} = 1$, $\hat{\boldsymbol{x}}\cdot\hat{\boldsymbol{y}} = -1$, $\boldsymbol{x} = 0$ and $\boldsymbol{y} = 0$, the singularities can be removed upon taking the appropriate limits at those values.

As in §2.6, the disturbance flow $\boldsymbol{u}'(\boldsymbol{x})$ given by (4.1) accounts for the motion of all particles, where now equation 4.2 is utilized for the Green's function to give

$$\boldsymbol{u}'(\boldsymbol{x}) = -\sum_{\alpha=1}^{N}\int_{S_\alpha}\boldsymbol{f}(\boldsymbol{y})\cdot[\boldsymbol{J}(\boldsymbol{x},\boldsymbol{y}) + \boldsymbol{J}^c(\boldsymbol{x},\boldsymbol{y})]\,dS_y. \tag{4.5}$$

Now the integral over the cavity surface has been replaced by the no-slip and no-flux condition satisfied by the Green's function, i.e. $\boldsymbol{J}(\boldsymbol{x},\boldsymbol{y}) + \boldsymbol{J}^c(\boldsymbol{x},\boldsymbol{y}) = 0$ at

$y = R$. A Taylor expansion of $\boldsymbol{J}(\boldsymbol{x},\boldsymbol{y})$ and $\boldsymbol{J}^c(\boldsymbol{x},\boldsymbol{y})$ for a given particle α about its center $\boldsymbol{y}$ yields a sum of moments of the hydrodynamic surface tractions exerted on particle α. Upon integration these again become the hydrodynamic force, toque and stresslet, etc., projected through the Stokeslet, rotlet and couplet analogs:

$$\begin{aligned}\boldsymbol{u}'(\boldsymbol{x}) = & -\left(1+\tfrac{a_\alpha}{6}\boldsymbol{\nabla}_y^2\right)\left[\boldsymbol{J}(\boldsymbol{x},\boldsymbol{y})+\boldsymbol{J}^c(\boldsymbol{x},\boldsymbol{y})\right]\Big|_{\boldsymbol{y}=\boldsymbol{x}_\alpha}\cdot\boldsymbol{F}_\alpha^H + \\ & -\tfrac{1}{2}\boldsymbol{\nabla}_y\times\left[\boldsymbol{J}(\boldsymbol{x},\boldsymbol{y})+\boldsymbol{J}^c(\boldsymbol{x},\boldsymbol{y})\right]\Big|_{\boldsymbol{y}=\boldsymbol{x}_\alpha}\cdot\boldsymbol{L}_\alpha^H + \\ & -\left(1+\tfrac{a_\alpha}{10}\boldsymbol{\nabla}_y^2\right)\boldsymbol{K}^c(\boldsymbol{x},\boldsymbol{y})\Big|_{\boldsymbol{y}=\boldsymbol{x}_\alpha}:\boldsymbol{S}_\alpha^H + \ldots\end{aligned} \tag{4.6}$$

where an irreducible second and third moment are included in $\boldsymbol{J}+\boldsymbol{J}^c$ and $\boldsymbol{K}^c$, and the couplet $\boldsymbol{K}^c$ is given by

$$\begin{aligned}\boldsymbol{K}^c(\boldsymbol{x},\boldsymbol{y}) = & \boldsymbol{\nabla}_y(\boldsymbol{J}(\boldsymbol{x},\boldsymbol{y})+\boldsymbol{J}^c(\boldsymbol{x},\boldsymbol{y}))+ \\ & \left[\boldsymbol{\nabla}_y(\boldsymbol{J}(\boldsymbol{x},\boldsymbol{y})+\boldsymbol{J}^c(\boldsymbol{x},\boldsymbol{y}))\right]^T.\end{aligned} \tag{4.7}$$

As in §2.6, insertion of (4.6) into the Faxén formulae yields a set of linear relations between particle motion and hydrodynamic force, torque, stresslet, and higher-order moments, all coupled by a grand mobility tensor $\mathcal{M}$. The tensor is truncated as discussed in §2.6 to the level of the stresslet (taking care to retain the irreducible quadrupoles and octupole that capture finite particle size), to give a far-field mobility matrix for the spherical domain, $\mathcal{M}_{ff}$, which upon inversion, couples all particles to one another and to the cavity. Finally, to complete the theoretical framework, near-field and lubrication interactions are accounted for

in a pairwise fashion (cf §2.6), and the sum couples all near- and far-field many-body particle-particle and particle-cavity interactions, expressed compactly as

$$\mathcal{R} = (\mathcal{M}_{ff})^{-1} + \mathcal{R}_{nf}. \tag{4.8}$$

For convenience, the near-field particle-particle and particle-cavity interaction tensor $\mathcal{R}_{nf}$ is split into two contributions. Because near-field particle-particle interactions can be accounted for pairwise, they are given by the unbound resistance functions which we denote as $\mathcal{R}_{nf,unbound}$; the near-field particle-cavity interactions are given by the pairwise resistance tensor $\mathcal{R}_{nf,c}$. As discussed in §2.6, the former are well-established and can be found in the literature [82, 93, 81]. For the latter, the sub-matrices that correspond to particle-cavity interactions $\mathcal{R}^{FU}_{nf,c}$, $\mathcal{R}^{F\Omega,}_{nf,c}$, $\mathcal{R}^{LU,}_{nf,c}$ and $\mathcal{R}^{F\Omega,}_{nf,c}$, were determined by O'Neill and Majumdar [131] for couplings perpendicular to the line of center of the particle and the cavity, and by Jones [85] for motions along the line of centers. When combined as shown in equation 4.8, these couplings form a grand resistance matrix that accounts for all many-body particle-particle and particle-cavity hydrodynamic interactions over all separations and particle concentrations. This coupling depends only on the geometry of the suspension, which now comprises particle and cavity size and shape, as well as spatial arrangement of particles relative to one another and to the confining spherical boundary. With it, particle motion can be deduced from hydrodynamic force and torque without requiring knowledge of the hydrodynamic traction over the cavity. Any motion of the enclosure can be incorporated in a straightforward manner by introducing the corresponding far-field flow $\boldsymbol{u}^{\infty}(\boldsymbol{x})$. The functions that represent the components of the far-field grand mobility matrix are presented and evaluated next.

4.2 Results

We begin by presenting the components of the far-field grand mobility matrix developed in the present work. Its inverse is then combined with the near-field grand resistance tensor as described in §4.1. Block-wise inversion of the resulting many-body resistance tensor preserves all couplings and permits solution and examination of the velocity/force, velocity/torque, rotation/force, rotation/torque relationships. The translational motion of a single particle to which an external force is applied, and the entrainment of a second, passive particle in the flow of a forced particle, are then studied in §4.2.1 and §4.2.2 respectively. Higher-order couplings are then studied in §4.2.3. The effects of point-particle approximations is discussed in §4.2.4.

4.2.1 Single particle inside a spherical cavity: force-to-translation coupling

The simplest coupling of particle motion to hydrodynamic tractions is that between velocity $\boldsymbol{U}$ and hydrodynamic force $\boldsymbol{F}^H$. For an isolated sphere alone in a solvent, $\boldsymbol{U} = -\boldsymbol{M}^{UF} \cdot \boldsymbol{F}^H$, where $\boldsymbol{M}^{UF} = (1/6\pi\eta a)\boldsymbol{I}$. If the particle is then placed inside a solvent-filled cavity, one expects motion slower than its unbound Stokes velocity, owing to hydrodynamic coupling to the no-slip surface of the cavity, in some sense similar to coupling between an unbound pair. The correction to unbound mobility that accounts for the presence of the cavity was derived in the present study via the method described in §4.1. To reveal the strength of hydrodynamic coupling along and transverse to the line of centers $\hat{\boldsymbol{y}}$ between

a particle and the cavity, the tensor is projected onto the two corresponding orthogonal subspaces $\hat{\boldsymbol{y}}\hat{\boldsymbol{y}}$ and $\boldsymbol{I} - \hat{\boldsymbol{y}}\hat{\boldsymbol{y}}$, respectively. Projection onto the subspace $\hat{\boldsymbol{y}}\hat{\boldsymbol{y}}$, yields

$$6\pi\eta a M^{UF,\parallel}_{ff,\alpha\alpha} = 1 - \left(\frac{a}{R}\right)\left[\frac{9}{4(1-y^2)}\right] + \left(\frac{a}{R}\right)^3\left[-\frac{(3y^2+5)}{2\,(1-y^2)^3}\right] + \left(\frac{a}{R}\right)^5\left[-\frac{y^4+10y^2+5}{4\,(1-y^2)^5}\right]. \tag{4.9}$$

The term proportional to a/R corresponds to the motion of an infinitesimal point inside a spherical cavity and has been previously reported [49]. In this work, we account for the finite size of particles, which requires the terms of order $(a/R)^3$ and $(a/R)^5$ in equation 4.9 that arise from the irreducible components of the second and third moments of the hydrodynamic surface traction. While the computation is tedious, terms to this order are necessary to assure that the grand mobility matrix is positive definite. As expected, in the limit $a/R \to 0$, the unbound solution is recovered, giving the Stokes drag on a single hard particle. A similar projection in the perpendicular direction gives

$$\begin{aligned} 6\pi\eta a M^{UF,\perp}_{ff,\alpha\alpha} =& 1 - \left(\frac{a}{R}\right)\left[\frac{9\left(y^4-3y^2+4\right)}{16\,(1-y^2)}\right] + \left(\frac{a}{R}\right)^3\left[-\frac{3y^6-12y^4+21y^2-20}{8\,(1-y^2)^3}\right] \\ &+ \left(\frac{a}{R}\right)^5\left[-\frac{y^8-5y^6+11y^4+5y^2+20}{16\,(1-y^2)^5}\right]. \end{aligned} \tag{4.10}$$

Combined, (4.9) and (4.10) give the far-field velocity-force self-mobility of a sphere within a suspension of an arbitrary number of particles, confined by a hard spherical cavity. Analogous expressions for the remaining couplings (force, torque, velocity, rotation, straining, stresslet) derived in the present study are shown in Appendix A. As detailed in §4.1, all of the far-field couplings are then assembled into a far-field grand-mobility matrix, inverted, superimposed with the near-field grand resistance matrix, and solved block-wise. The resultant self-mobility couplings account for the infinite hierarchy of reflections be-

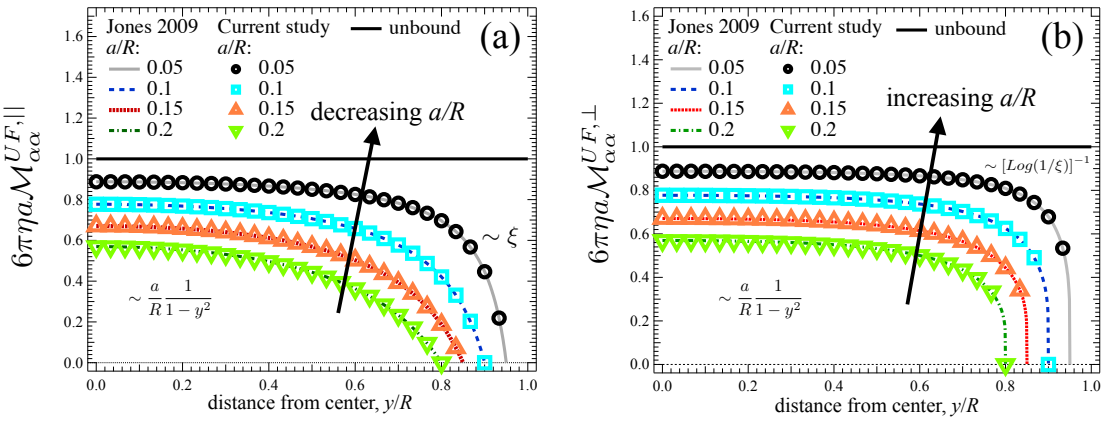

Figure 4.2: Confined self-mobility plotted as a function of position in the cavity, connecting a force acting (a) along and (b) transverse to the particle/cavity line-of-centers to the velocity of the particle in the same direction. The scaling for the decrease in the mobility is shown both when the particle is in the far-field $\sim (a/R)/(1-y^2)$, and in the lubrication region, where the decrease scales with the surface-to-surface separation $\xi = 1 - a/R - y_\alpha$ Open symbols: New mobility functions from the present study, obtained via block-wise inversion of equation 2.54 after insertion of equations A.1 (which includes equations 4.9, 4.10) to A.3, into (4.8). Solid lines: bispherical series solution [85].

tween a finite-size particle and an arbitrary number $N-1$ other particles and with the enclosing cavity. Its elements $\mathcal{M}^{UF}_{ff,\alpha\alpha}$, $\mathcal{M}^{\Omega L}_{ff,\alpha\alpha}$, $\mathcal{M}^{UL}_{ff,\alpha\alpha}$, $\mathcal{M}^{\Omega F}_{ff,\alpha\alpha}$, $\mathcal{M}^{ES}_{ff,\alpha\alpha}$, $\mathcal{M}^{\Omega S}_{ff,\alpha\alpha}$, and $\mathcal{M}^{US}_{ff,\alpha\alpha}$ give the corresponding self-motion of a particle subjected to hydrodynamic force, torque, and stresslet as it is hindered by interactions with other particles and with the enclosing cavity (all far-field self-mobilities UF, ΩL, UL, ES, ΩS, and US derived in the present study can be found in Appendix A.1).

We begin with the simplest case: a single particle suspended in pure solvent enclosed by the cavity ($N = 1$). We focus first on the coupling between translational velocity and force, for which the components along and transverse

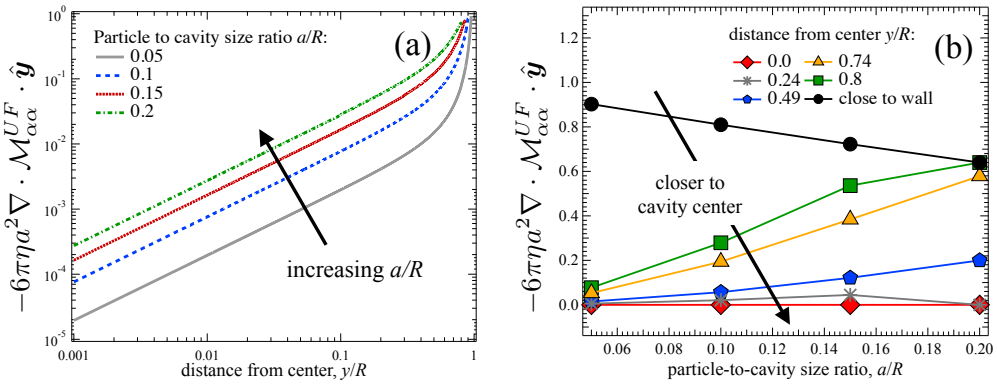

Figure 4.3: Drift velocity along the particle/cavity line-of-centers (a) as a function of position in the cavity, (b) as a function of particle-to-cavity size ratio, a/R.

to the line of centers, $\mathcal{M}_{\alpha\alpha}^{UF,\parallel}$ and $\mathcal{M}_{\alpha\alpha}^{UF,\perp}$, are plotted in figures 4.2(a) and **4.2(b)**, respectively, as a function of the position of the particle relative to the cavity center. The mobility is made dimensionless by the lone single-particle mobility, $1/6\pi\eta a$, and particle position is scaled on the cavity size, R. Two sets of curves are shown in each plot alongside the hydrodynamic mobility of a particle in an unbound domain (solid horizontal line). The open symbols give the results obtained via the present approach (valid for an arbitrary number of confined particles). The solid and dashed curves correspond to results obtained from the method of Jones (which cannot be generalized beyond a single confined particle) [2009]. Agreement between the prior theory and our new theory is excellent, for all particle-to-cavity size ratios a/R and particle positions y/R studied, validating the present framework by recovering previously published results for a single confined particle. However, unlike prior models, our framework can model the motion of an arbitrary number of particles.

Comparison of the curves to the isotropic, unbound mobility reveals that 3D confinement gives rise to anisotropic hindrance of partible mobility. The

confined-mobility curves all lie under the unbound mobility line, showing that hydrodynamic coupling between the two no-slip surfaces hinders particle motion. Further, in contrast to the position-independent mobility for a particle in an unbound domain, the mobility of a confined particle depends on its proximity to the cavity wall. Unsurprisingly, the mobility of a particle of finite size is greater near the center of a cavity than near the cavity surface, owing to the changing proximity of their no-slip surfaces. The mobility decreases monotonically from its maximum at the center as it approaches the cavity surface, vanishing entirely at particle-wall contact. Finally, comparison of figure 4.2(a) to panel 4.2(b) reveals that near the cavity wall, the mobility is anisotropic—with transverse motion decaying less rapidly than motion toward or away from the wall. This is consistent with near-contact mobility between a pair of spheres, where transverse lubrication interactions are weaker than longitudinal encounters.

While for all size ratios a/R the reduction in mobility becomes steeper as the particle approaches the wall, the rate of this decay depends qualitatively on particle-to-cavity size ratio. Because the size ratio affects the slope, it changes the divergence of the mobility $\boldsymbol{\nabla}\cdot\mathcal{M}$. The physical relevance of the divergence of the mobility is best understood in the context of colloidal particles where, owing to Brownian motion, a particle will migrate from regions of low to high mobility, moving as though driven by a deterministic force, the Brownian drift. The quantity $\boldsymbol{\nabla}\cdot\mathcal{M}$ sets the corresponding drift velocity, and gives the tendency of the particle to migrate toward the region of highest mobility. Because mobility is highest at the cavity center, projection of the drift velocity along the cavity radius gives the strength of the tendency of the particle to drift away from the wall and toward the center. The projection of $\boldsymbol{\nabla}\cdot\mathcal{M}$ onto a unit vector $-\hat{\boldsymbol{y}}$ pointing toward the center of the cavity is plotted in figure 4.3(a) as a function of the dis-

tance between the particle and the center of the cavity. Four curves are shown, each curve corresponding to a different particle-to-cavity size ratio. Near the wall (far right end of the horizontal axis) the drift velocity is large, indicating a strong tendency to migrate away from the wall. Near the center, the drift velocity is three orders of magnitude weaker, indicating the tendency of a lone particle to remain there. This position-dependent behavior, where the particle tends to drift away from the wall and remain near the center, is observed for all size ratios studied.

Alternatively, one can ask how the strength of the "push" away from the wall changes as a particle grows larger, by inspecting how the radial drift velocity changes with size ratio a/R, as shown in figure 4.3(b). The diamond symbols show behavior nearest the center of the cavity, the filled circles show behavior nearest the wall, with several other intervening positions shown as noted in the legend. The diamond symbols show that a particle at the center has zero drift velocity regardless of particle size, demonstrating that the preferred position of an isolated particle in a spherically confined domain is always at the center of the cavity. As the particle moves away from the center (star, pentagon, triangle, and square symbols), the drift velocity increases—for all particle sizes—tending to push a particle back toward the center. The strength of this push at a given position increases as the confined particle grows larger, as indicated by the positive slopes, owing to the growing distance of the particle to the region of highest mobility, i.e. the center of the cavity. However, this trend reverses very near the wall (filled circles): the strength of the push decreases as the particle grows larger, as evidenced by the negative slope. This behavior can be understood by recalling that the closest a particle can come to contacting the cavity wall is the position $y_{max} = 1 - a/R$, its "maximum position". A large particle at its maximum

position is thus closer to the region of highest mobility, i.e. the center of the cavity, than a small particle at its maximum position. Because a small particle can be farther from the center of the cavity than a large particle, its maximum drift velocity is higher.

4.2.2 Hydrodynamically interacting pair: force-to-translation coupling

In the previous section, we presented the expression derived in this study for the self-mobility $\mathcal{M}_{\alpha\alpha}^{UF}$ of a spherically confined particle in a suspension of arbitrary concentration, in response to a hydrodynamic force on its own surface, equations 4.9 and 4.10. The simplest case of a single confined particle was studied first, toward understanding the influence exerted on particle mobility by the cavity. Motion of such a particle entrains the fluid in the cavity and, in turn, any nearby particles will be entrained by this flow. This coupling was captured by the many-body entrainment mobility $\mathcal{M}_{\beta\alpha}$ as discussed in §4.1, to yield the full coupling and the motion of an arbitrary number of forced and entrained particles, as it is influenced by the cavity. Whether two, three, or many particles are enclosed in the cavity, forced or passive, their motion is given by precisely the same expressions and process. We illustrate this process here, utilizing the new many-body coupling derived in the present study and, from it, present novel results for the motion of a pair of spherically confined particles.

The entrained mobility, $\mathcal{M}_{\beta\alpha}^{UF}$, $\beta \neq \alpha$, is the hydrodynamic coupling that describes the entrainment of particle(s) β in the flow field produced by the motion of particle(s) α. Each particle interacts with the other and with the cavity via disturbance flows propagated by their motion. The initial disturbance propagated

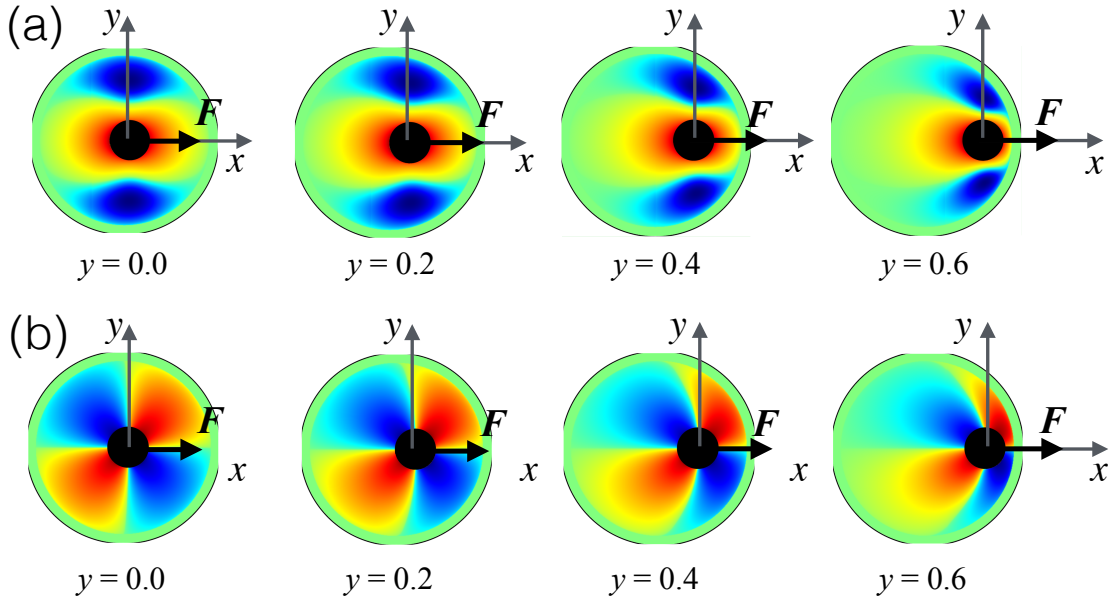

Figure 4.4: Hydrodynamic entrainment of a passive finite-size particle dragged by the disturbance flow of a forced particle. The distance y of the forced particle to the center of the cavity is given below each plot; the particle-to-cavity size ratio for all of the plots is $a/R = 0.1$. Brighter colored regions (red) represent entrainment in the positive direction and dark colored regions entrainment in the opposite direction. (a) Radial entrainment on a second particle due to a radial force on the forced particle; (b) perpendicular entrainment of a second particle due to a perpendicular force on another forced particle in the cavity.

by particle α is, as described in §2.6, given by the Stokeslet $\boldsymbol{J}$ plus a correction due to the hindrance of the cavity, $\boldsymbol{J}^c$, defined in equations 4.3 and 4.4. Thus, the strength of the entrainment of particle β is weaker than if the domain was unbound. Here, $\alpha, \beta \in [1, N]$, where N is arbitrary.

The grand mobility tensor for a confined system must ultimately recover the unbound behavior in the limit $a/R \to 0$. We leverage this fact to more clearly reveal the influence of the cavity, by artificially dividing the mobility into two expressions:

$$\boldsymbol{M}^{UF}_{\beta\alpha} = \left(\boldsymbol{M}^{UF}_{\beta\alpha}\right)^{unbound} + \boldsymbol{M}^{UF,c}_{\beta\alpha}, \tag{4.11}$$

where the motion due to unbound entrainment is $\left(\boldsymbol{M}_{\beta\alpha}^{UF}\right)^{unbound}$. Making lengths dimensionless by the radius of the cavity R gives

$$6\pi\eta a\left(\boldsymbol{M}_{\beta\alpha}^{UF}\right)^{unbound} : \hat{\boldsymbol{r}}\hat{\boldsymbol{r}} = \frac{a}{R}\left(\frac{3}{2}r^{-1} - r^{-3}\right). \tag{4.12}$$

The cavity contribution, $\boldsymbol{M}_{\beta\alpha}^{UF,c}$, as obtained in the present study via our method, can be projected radially to yield equation 4.13,

$$\begin{aligned}
6\pi\eta a M_{\beta\alpha}^{UF,\parallel,c} = \Bigg\{ & \left(\frac{a}{R}\right)\Big[-3((6-2y^2+4bxy(-5+y^2)+(1+b^2)x^4y^2(-1+3y^2)- \\
& 4bx^3y(-2+b^2+5y^2)+x^2(-4+9y^2+y^4+b^2(2+19y^2-3y^4)))/(8y^5\zeta^5)- \\
& 3(4b^3x^2y^2+b^2xy(3-5y^2+x^2(-5+3y^2))+xy(6-4y^2+3x^4y^2(-1+y^2)+ \\
& x^2(-4+9y^2-3y^4))+b(3(-1+y^2)-9x^4y^2(-1+y^2)+x^2(3-16y^2+ \\
& 9y^4)))/(8(-1+b^2)xy^4\zeta^3)+9b(-1+x^2)(-1+y^2)(-1+2bxy-x^2y^2)/(8(-1+ \\
& b^2)xy^3\zeta^2))\Big] + \left(\frac{a}{R}\right)^3\Big[3(4b^5x^4y^2(-1+2(-2+x^2)y^2+y^4)+b^4x^3y(2+(34- \\
& 7x^2)y^2+(-7-2x^2+x^4)y^4+3x^2y^6)+2b^3x^2y^2(-14+3y^2-3x^4y^2+x^2(7-2y^2 \\
& +y^4))-xy^3(2+x^8y^4+2x^2(-12+7y^2)+x^6y^2(5-2y^2+y^4)+x^4(14-6y^2+ \\
& 3y^4))-b^2xy(-14+5y^2+17x^6y^4+x^2(9-12y^2+14y^4)+x^4y^2(14-38y^2+ \\
& 21y^4))+b(-2+y^2+7x^8y^6+x^6y^4(33-14y^2+7y^4)+x^2(1-14y^2+15y^4)+ \\
& x^4y^2(11-50y^2+29y^4)))/(8(-1+b^2)xy^8\zeta^7)+(3b(-2+x^2+y^2)(-1+2bxy- \\
& x^2y^2)^3)/(8(-1+b^2)xy^7\zeta^6)\Big] + \left(\frac{a}{R}\right)^5\Big[(-10+81x^2y^2-48x^4y^4-32b^4x^4y^4+ \\
& x^6y^6-3b^2x^2y^2(21-46x^2y^2+x^4y^4)+4bxy(5-36x^2y^2+9x^4y^4)+b^3(72x^3y^3 \\
& -48x^5y^5))/(8y^9\zeta^9)+(24b^3x^4y^4+b^2(3xy-42x^3y^3-17x^5y^5)-xy(10-7x^2y^2 \\
& +4x^4y^4+x^6y^6)+b(1+21x^2y^2+11x^4y^4+7x^6y^6))/(8(-1+b^2)xy^8\zeta^7)+ \\
& (b(-1+2bxy-x^2y^2)^3)/(8(-1+b^2)xy^7\zeta^6)\Big]\Bigg\}\hat{\boldsymbol{y}}\hat{\boldsymbol{y}}
\end{aligned} \tag{4.13}$$

where $b = \hat{\boldsymbol{x}} \cdot \hat{\boldsymbol{y}}$ and the distance of the entrained particle to the image point of

the forced particle is $\zeta = y^{-1}\sqrt{1 - 2bxy + y^2}$. Higher-order moments of the hydrodynamic surface traction also give rise to cavity contributions corresponding to both self-mobility and pair-mobility, which describes many-body entrainment of particles by disturbance flows.

Equations 4.9 – 4.13 give only force-velocity couplings; the far-field grand mobility matrix must be populated with higher-order pair-level couplings to the level of the stresslet. Higher-order couplings for the confined self and entrained motion are provided in Appendix §A.2 up to the level of the stresslet. Following its construction, inversion of this far-field grand mobility matrix automatically captures an infinitude of reflected interactions between all particles and the cavity, giving an N-body far-field hydrodynamic coupling. *That is, coupling between an arbitrary number of particles to one another and the cavity is automatically captured by this Stokesian dynamics approach.*

To elucidate the effect of confinement on entrainment, we consider first the simplest case, $N = 2$ enclosed particles. A second particle β is inserted into the cavity, and we ask how it moves in response to a force exerted on particle α. In figure 4.4 a contour plot illustrating the complete analytical coupling—that is, including near-field and far-field interactions—is presented for the induced motion along and transverse to the line of external force, in panels (a) and (b) respectively. Here, the force $\boldsymbol{F}$ exerted on the source particle is directed along the radius of the cavity. Each contour plot shows the plane passing through the center of the spherical cavity; the forced particle is at the center of the filled black circle, which encloses a region excluding particle centers. In panel 4.4(a), the colorized regions represent the strength and direction of entrainment, ranging from dark red for strong entrainment in the same direction as the external force,

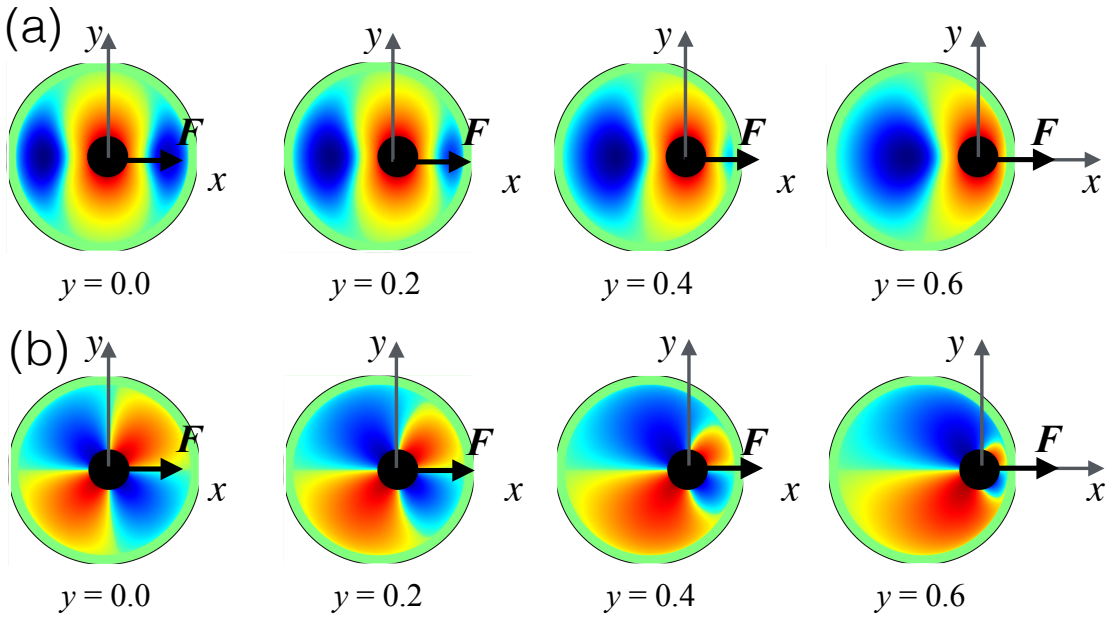

Figure 4.5: Contour plots of the hydrodynamic entrainment of a second particle inside the spherical cavity due to the disturbance flow propagated by another forced particle. The distance y of the forced particle to the center of the cavity is given below each plot; the particle-to-cavity size ratio for all of the plots is $a/R = 0.1$. Brighter colored regions (red) represent entrainment in the positive direction and dark colored regions entrainment in the opposite direction. (a) Perpendicular entrainment due to a radial force acting on a forced particle; (b) radial entrainment due to a perpendicular force on a forced particle.

to dark blue for strong entrainment in the direction anti-parallel to the external force. As can be seen in panel 4.4(a), the entrainment field is axisymmetric about the external force, regardless of the position of the forced particle. In the $y = 0$ contour plot, the forced particle is placed at the center of the cavity. As indicated by the dark red, orange and yellow regions ahead of and trailing the forced particle, a second particle placed in those regions will be pushed or pulled along by the motion of the forced particle. The regions flanking the line of forcing are initially dark red, close to the forced particle—but rapidly transition to dark blue. That is, a second particle closely flanking the forced particle will travel

along with it, but a short (transverse) distance away, an entrained particle will travel in the opposite direction. This trend continues when the forced particle is placed closer to the spherical cavity, i.e. for $y = 0.2$, $y = 0.4$, and $y = 0.6$ as shown in figure 4.4(a). Here it can be seen that entrainment is strongest in the region nearest the forced particle. As $y \to 0.9$, the region farthest from the forced particle (green region) is only weakly disturbed; particles in this region hardly move in response to the forced particle. The region closest to the cavity wall is green, regardless of the position of the forced particle, owing to the no-slip and no-flux condition of the cavity surface.

The entrained particle will also undergo motion transverse to the applied radial force, as illustrated in panel 4.4(b). As in panel 4.4(a), the strength of entrainment varies from dark red to dark blue, but here, dark red corresponds to strong entrainment in the positive y direction, and dark blue to strong entrainment in the negative y direction, as noted by the axes in each image. Thus, particles placed in the red region "ahead" of the forced particle (upper right-hand red region) will move orthogonal to the applied force and away from its line of action; those placed in the red region "trailing" the forced particle (lower left-hand red region) will move orthogonally toward the line of action of the force, i.e. in the positive y direction. Blue regions indicate entrainment mirrored across the x-axis.

The line of action of the applied force may also act transverse to the cavity radius (i.e. transverse to the line of centers between the cavity and the forced particle). The response of an entrained particle is shown in figure 4.5. The colorized regions in panel 4.5(a) again represent the strength and direction of entrainment, ranging from dark red for strong entrainment in the same direction

as the external force (positive direction along the y-axis), to dark blue for strong entrainment in the direction opposite the external force. The entrainment field in panel 4.5(a) is axisymmetric only when the forced particle is precisely at the center of the spherical cavity. As the particle moves away from the center, this symmetry is lost. The dark red, orange and yellow regions indicate that the motion of the forced particle will push or pull a second particle particle in the same direction. The region flanking the line of forcing is red close to the forced particle; however, it quickly transitions to dark blue. The size and location of the dark blue regions flanking the forced particle, i.e., regions where a second particle will be entrained in the opposite direction, vary with the position of the forced particle. For $y = 0.2$, blue regions also flank the line of action of the applied force, but the region of reverse entrainment to the right of the external force shrinks while that to the left grows. This trend continues as the forced particle moves nearer to the wall, as shown for $y = 0.4$ and $y = 0.6$. One can envision that, as the forced particle moves toward the wall, both parallel and transverse motion of an entrained particle vanish.

The entrained particle will also undergo motion transverse to the line of action of the force, as illustrated in 4.5(b). Again the strength of entrainment varies from dark red to dark blue; here, dark red corresponds to entrainment in the positive x direction and dark blue corresponds to entrainment in the negative x direction. In consequence, particles placed in the red region "ahead" of the forced particle (i.e. the upper right-hand red region) will move orthogonally to the applied force and away from its line of action; those placed in the red region "trailing" the forced particle (lower left-hand red region) will move orthogonally toward the line of action of the force, in the positive y direction. As in 4.4(b), blue regions indicate entrainment mirrored across the x-axis.

In summary, the hydrodynamic coupling between a pair of particles interacting inside a spherical cavity shows qualitative differences from that between an unbound pair. The coupling can be resolved into contributions of entrainment in response to radial and transverse components of an externally applied force. The most intuitively obvious difference is that apparent flow recirculation (conservation of mass) creates regions in which motion of a forced particle drives motion of a second particle in the opposite direction when the force on the forced particle acts along the line of the center of the particle and the cavity. In addition, regardless of the direction of the external force, entrainment is reduced owing to the presence of no-slip surface of the cavity. We emphasize that the model presented is not restricted to a confined pair; our framework is fully applicable to an arbitrary number of particles at arbitrary volume fractions and particle-to-cavity size ratio.

4.2.3 Higher-order couplings

In §4.2.1 and §4.2.2, it was shown that the presence of a confining spherical cavity influences the hydrodynamic coupling between interacting spheres. This influence alters couplings between particle velocity, rotation, and straining motion to moments of the hydrodynamic traction—force, torque, stresslet, and higher-order moments. This infinite hierarchy of couplings is summarized compactly in equation 2.50; expressions for the individual entries in the grand mobility matrix were given in that section and in Appendix A, and the coupling between particle translation and hydrodynamic force was studied. In the present section, we explore another coupling, that between particle translation and hydrodynamic torque. We recall that a hydrodynamic torque on the sur-

face of a single unbound particle produces no translation. However, proximity to a nearby surface can produce such coupling. For example, in the presence of a nearby wall, a particle subjected to a hydrodynamic torque about an axis parallel to the wall will translate along the wall. Similarly, for an unbound pair, a torque about an axis perpendicular to their line of centers will produce translation, but torque about their line of centers produces no translation. Let us examine the analogous couplings for particles confined inside a sphere.

Single particle inside a spherical cavity: torque to translational motion coupling

The element of the grand mobility matrix $\mathcal{M}$ that describes torque-to-translational *self*-mobility of a particle in a spherically confined suspension, $\mathcal{M}^{UL}_{\alpha\alpha}$, was derived in the present study utilizing the methods of §4.1, where the far-field contribution is given by equation A.2a (cf Appendix A). This expression gives the translational motion of a particle due to a hydrodynamic torque on its

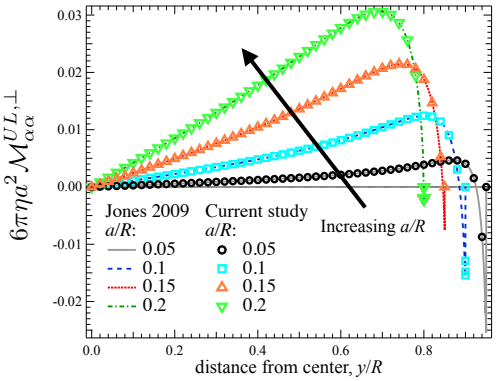

Figure 4.6: Torque to translation coupling for a single particle inside a spherical cavity.

surface, in the presence of an arbitrary number of other particles and the confining cavity. While it is a tensor, only the antisymmetric component $\boldsymbol{\epsilon} \cdot \hat{\boldsymbol{y}}$, where $\boldsymbol{\epsilon}$ is the Levi-Civita tensor, is non zero. This element, $\mathcal{M}_{\alpha\alpha}^{UL,\perp} = \mathcal{M}_{\alpha\alpha}^{UL} : -\frac{1}{2}\boldsymbol{\epsilon} \cdot \hat{\boldsymbol{y}}$ with the first index of $\mathcal{M}_{\alpha\alpha}^{UL,\perp}$ an inner product with the second index of $\boldsymbol{\epsilon}$ and vice versa, gives the translational motion of a particle α, along the cavity radius, due to a torque on its own surface, as influenced by other suspended particles β and the confining cavity.

To understand this coupling we study the simplest case of a single confined particle, $N = 1$, plotted in figure 4.6 as a function of the distance of the particle from the center of the cavity, for a range of particle-to-cavity size ratios a/R (open symbols). The solid curves give the corresponding self-mobilities obtained via the method of O'Neill and Majumdar [131], but which is limited to a single particle. Agreement between our N-body approach and the prior single-particle model is excellent.

Inspection of these plots reveals the effect of spherical confinement on the ability of a particle to translate in response to a torque. Due to the spherical symmetry of the configuration, when the particle is at the center, the torque-to-translation coupling is zero, so a particle will undergo no translational motion in response to torque. As the particle moves away from the center, it couples to the cavity, translating with a velocity $\boldsymbol{U}_\alpha = \mathcal{M}_{\alpha\alpha}^{UL} \cdot \boldsymbol{L}_\alpha$, in a direction perpendicular to both the torque and the line of centers between the particle and the cavity. With increasing proximity to the cavity surface, the particle translates faster, owing to stronger hydrodynamic coupling between the particle and the wall. This behavior is similar to the hydrodynamic coupling between a pair of unbound particles when one of the particles is acted on by a torque perpendicular to the

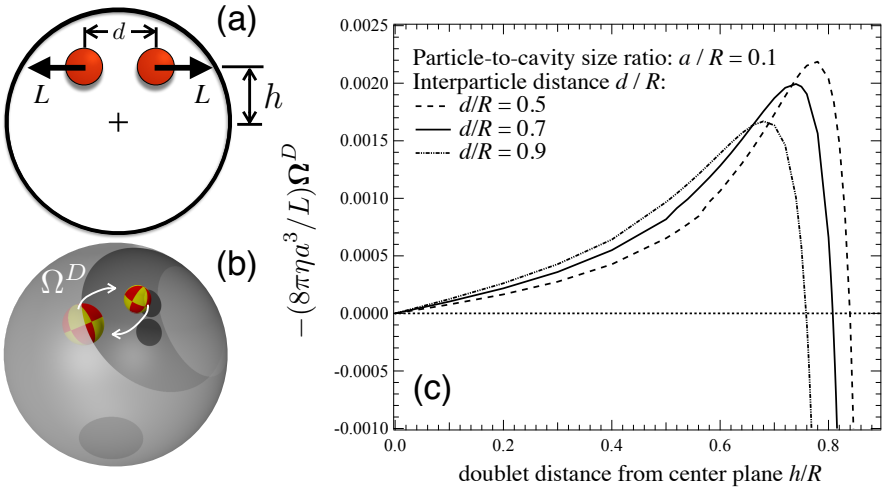

Figure 4.7: (a) Model system: two particles at a distance d from each other and at a height h from the center plane of the cavity are acted on by an external torque $\boldsymbol{L}$. (b) Simulation snapshot: Equal and opposite torques act on a pair of particles along their lines of centers, causing the particles to rotate as a doublet about an axis centered at the cavity. (c) The rate of rotation of the doublet as a function of the particles' height from the center plane of the cavity.

line of centers: outside the lubrication region, entrainment of the second particle will increase monotonically with increasing proximity. However, for a particle inside a spherical cavity, the translation of the particle reaches a maximum as it approaches the cavity surface. Beyond this point the translation of the particle reaches a "stall" condition near the wall, where translation ceases even with applied torque (points of intersection with the horizontal dashed line). Beyond this stall point, the direction of translation reverses and the particle translates in the opposite direction—undergoing a "rolling" motion over the surface of the cavity similar to the motion of a particle acted on by a torque near a planar wall. As the particle comes close to contact with the cavity surface its mobility must decrease again, eventually vanishing at the maximum position of the particle as a consequence of lubrication interactions between the no-slip surfaces. The

$N-$body far-field expressions (found in Appendix A.1) utilized here for $N = 1$ are just as easily utilized to describe the self-motion in the presence of many enclosed particles.

Hydrodynamically interacting pair inside the spherical cavity: doublet rotation

We again consider the effect of confinement on entrained translational motion, but now where such motion arises due to hydrodynamic torque, rather than hydrodynamic force. To study the motion, we implemented new hydrodynamic functions developed in the present study into Stokesian Dynamics: the mobility tensors coupling translation to force, $\boldsymbol{M}^{UF}_{\beta\alpha}$, translation to torque, $\boldsymbol{M}^{UL}_{\beta\alpha}$, and rotation to torque, $\boldsymbol{M}^{\Omega L}_{\beta\alpha}$ (cf equations A.1a - A.3a and A.7a - A.9a, in Appendix A.2). To illustrate the effect of the cavity on such motions, we again start with the simplest case of a pair of particles. They are placed in the cavity at a separation $d = 0.5R$, $d = 0.7R$, and $d = 0.9R$, with each particle equidistant from an axis passing through the center of the cavity, figure 4.7(a). When an external torque is applied to each particle along the line of centers of the particles, and pointing in an outward direction as shown, both particles translate. In addition, they rotate together as a doublet as indicated in figure 4.7(b). No force is required to maintain a fixed separation between the pair, a consequence of the symmetry of the grand mobility matrix.

Their rate of rotation varies with the distance of the doublet from the center plane of the cavity, h/R, as plotted in figure 4.7(c). Three curves are shown, each corresponding to a doublet of particles at different inter-particle distances. At the far left of the horizontal axis, where the pair is nearest the cavity center,

the particles do not revolve about the cavity center, regardless of their center-to-center separation. Away from the center plane of the cavity, the torque-to-translation coupling emerges, and they rotate as a doublet. Interestingly, the direction of doublet rotation depends on proximity to the cavity wall. As shown in figure 4.7(c), away from the wall, the doublet rotates in a clockwise sense (white arrows in figure 4.7(b)), revolving faster and faster around the cavity center for positions nearer the wall. However, a maximum is reached—and it depends on their separation. Beyond this point, their revolution about the cavity center slows down, until a "stall" condition is reached very near the wall where the rate of rotation becomes zero, as indicated by the horizontal dashed line in figure 4.7(c). Beyond this stall point, their revolution about the cavity center reverses, and the doublet commences to rotate in the counter clockwise direction—both particles undergo a "rolling" motion over the surface of the cavity. This motion is analogous to the "rolling" motion of a single particle inside the spherical cavity described in the previous section. This interesting result highlights how the presence of the cavity can reverse rotational motion. Notably, this behavior is captured in the far-field interactions by the finite size of the particle, which was neglected in prior models.

In summary, The presence of a confining cavity couples particle translation to torque. Depending on the position of the particles, such coupling leads to a surprising reversal of motion—behavior, it turns out, similar to that observed in some biophysical systems [116]. The presence of the cavity also leads to reversals of translational motion (as shown in the previous section). Accurate modeling of such behaviors requires a treatment of both far-field and near-field hydrodynamic interactions as done in this study. The $N-$body expressions far-field expressions (found in Appendix A) can be utilized to study such entrain-

ment in a suspension of arbitrary concentration.

4.2.4 The point-particle approximation and effects of finite size

In the present study, we have been careful to account for the finite particle size, but it is natural to ask what, if any, consequences would arise were we to simply model particles as infinitesimal points. In some problems, such simplifications can yield rapid insight into leading-order behavior, revealing the physics of primary interest. By way of example, the leading-order (point-particle) solution for a particle translating in (unbound) Stokes flow reveals the surprising strength of the hydrodynamic force coupling, $1/r$, compared to say, the gravitational or coulombic coupling, which both scale as $1/r^2$. However, the no-flux condition for hard particles can be respected only by accounting for finite size—a straightforward computation for spheres. When two particles interact in an unbound fluid, neglecting finite size gives a good leading-order estimate of the strength of force-velocity coupling, but under-predicts the strength of entrainment when the particles are separated by less than several particle diameters. The consequences grow more severe when the system becomes more geometrically complex. Perhaps the most familiar example resulted in the development of the Rotne-Prager tensor: early attempts to model the motion of polymer chains as interconnected point-particle beads led to loss of positive definiteness of the diffusion (mobility) tensor in some configurations [46, 181]. Rotne and Prager [143] addressed this situation by accounting for finite particle size in the force/translation coupling; the Rotne-Prager tensor has since been widely utilized to model hydrodynamic couplings between particles in an unbound suspension. However, its inclusion of pair-only coupling, and neglect of

higher-order traction moments, restricts its validity to widely-separated particles, e.g. dilute suspensions. In studies of concentrated suspensions, Durlofsky et al. [48] reported that neglect of finite size terms, even in a mobility matrix that includes force, torque, and stresslet couplings to account for many-body interactions, results in loss of positive-definiteness for an unbound suspension. Thus, especially for concentrated suspensions, inclusion of higher-order traction moments does not guarantee that the grand mobility matrix will remain positive definite, required to respect the energy dissipation theorem.

In the context of a spherically confined suspension, accounting for finite particle size becomes important at the level of just a single confined particle, and emerges first with the force-velocity coupling. This can be seen in the study of Felderhof and Sellier [49] who, in an attempt to approximate the force/velocity coupling via a point particle, projected Oseen's Green's function along and transverse to the cavity radius. They compared this result to the corresponding components of the invert of O'Neill and Majumdar's finite-size resistance tensor, and found good agreement for small particles in the latter study. However, closer interrogation of their results reveals two concerns: first, as particle size grows, the point-particle approximation severely under-predicts the hydrodynamic force. More troubling is the behavior obtained upon inversion of the point-particle coupling, shown by the dashed lines in figure 4.8(a), where the severe consequences of the approximation are clearly revealed: the force-velocity element of the resistance tensor diverges at arbitrary positions in the cavity. Because inversion is the key step that couples reflections and many-body interactions, the regime of validity of this approach is fixed-velocity motion of a single enclosed particle.

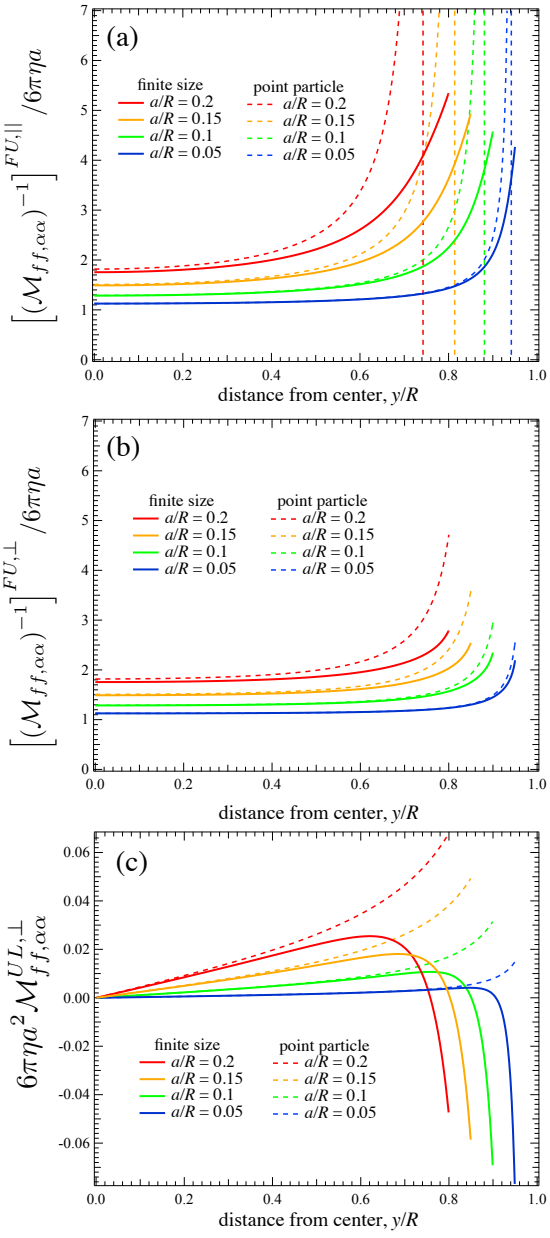

Figure 4.8: Self-mobility, as developed in the present study, of a particle modeled with finite size (solid curves) and as a point particle (dashed curves) Force/velocity coupling (a) along (equation 4.9) and (b) transverse (equation 4.10) to the cavity radius. (c) Torque/velocity coupling (equation A.2).

In the present study, we accounted for finite size (cf §4.1, equation 4.9), and these results are presented as solid curves in figure 4.8(a), showing monotonic increase of far-field resistance to a finite value, a physically reasonable result. We can utilize our result, equation 4.9, to identify the source of the divergent behavior in the point-particle approximation: a pole at $y = (1/2)(4 - 9(a/R))^{1/2}$ that can only be removed by inclusion of the finite-size terms of $O((a/R)^3)$ and $O((a/R)^5)$ in that expression. The transverse projection of the same coupling is shown in panel (b) of the figure, where the effect of finite size is quantitative.

The second consequence of neglecting finite size is failure to predict reversal of particle motion in the torque/translation coupling, originally predicted by O'Neill and Majumdar [131]. Felderhof and Sellier derived a Green's function for the torque-rotation coupling of an enclosed point particle by taking the curl of Oseen's confined Stokeslet, finding a continuous increase in particle velocity with approach to the wall, as shown by the dashed lines in figure 4.8(c). They compared their result with the corresponding result from O'Neill and Majumdar, finding significant qualitative disagreement: O'Neill and Majumdar predicted a sign reversal, whereby a particle will reverse its translational motion near the wall and begin to roll along the wall. The mobility functions derived in the present work (equation A.2) account for finite size and also find this reversal, as shown by the solid lines in panel (c) of the figure. The key advantage to our method is, of course, its built-in ability to model two, three, or many enclosed particles.

In summary, accounting for finite particle size is essential to the accurate modeling of particle motion in a spherically confined fluid. While approximating particles as points significantly simplifies formulation of the mathematical

model, it leads to qualitative errors so significant as to render the model unviable.

4.3 Conclusions

In this work, we have presented a framework to model particle motion in hydrodynamically interacting colloidal suspensions subjected to 3D confinement by a spherical cavity. This framework comprises analytical expressions for the far-field grand mobility tensor coupling particles hydrodynamically to one another and to the confining cavity which, when combined with near-field couplings, is valid for an arbitrary number of particles for a wide range of particle volume fractions, from dilute to near-maximum packing fraction. We presented couplings of translation, rotation, and straining motion to force, torque, and the stresslet, giving particular attention to the force/translation, torque/rotation, and torque translation behavior. We employed this new framework to study two fundamental aspects of particle movement: self-motion and entrained motion, with a view toward its ultimate employment for many-particle systems in dynamic simulation.

The self-motion was studied first, and utilized to illustrate the leading-order effects of confinement and to validate the model by recovering results reported in prior work [131, 85], namely the reduction of particle velocity by hydrodynamic coupling to the enclosing cavity. Beyond this result, we found that confinement gives rise to a drift velocity that tends to push a colloid away from the cavity wall toward the center. This "push" is strongest near the wall for smaller particles; once away from the wall however, larger particles experience

a stronger tendency to seek the cavity center. One implication of this finding is that particles in biophysical systems may segregate spatially according to size.

We have derived the first results for the motion of a pair of finite-size particles enclosed in a spherical cavity. We found that the entrainment velocity of a second, particle in the flow created by another forced particle is qualitatively changed by the presence of the cavity in two ways: first, the strength of the entrainment at a distance r from the forced particle depends on the proximity of both to the cavity. Second, a reversal in motion occurs for particles located some distance transverse to the line of external forcing, consistent with recirculation flows reported in a range of cellular systems [129, 55, 116, 29].

The study of higher-order couplings revealed several remarkable results. First, unlike a single unbound particle, a single confined particle will translate in response to a hydrodynamic torque on its surface. We find that such motion reverses in direction as a particle moves from the cavity center to the wall, resulting in a rolling motion of the particle along the cavity surface, similar to the behavior of a sphere near a planar wall. A confined pair of particles subjected to hydrodynamic torque will not only rotate individually but will also rotate as a doublet about the cavity axis. We explored the dependence of this coupling on proximity of the pair to the cavity wall, again finding a stall and reversal of motion as the pair approaches the surface.

Finally, the effect of finite size was explored, where we found that no regime of validity exists for approximating particles in spherical confinement as point particles. Such simplification results in errors ranging from spurious poles throughout the cavity domain to a failure to predict motion reversal near the cavity wall.

All functions derived give motion of particles in a suspension of N particles, where N is arbitrary. The framework presented herein provides a method by which to study a variety of crowded, 3D confined systems, ranging from eukaryotic cells to suspensions confined by micro-capsules, to study their transport and rheological properties in the presence of hydrodynamic interactions.

Acknowledgments

This work was supported in part by an NSF BRIGE grant #1342218 and by an NSF Graduate Research Fellowship #DGE-0707428. CA-R thanks Yu Su in the Zia Group for assistance with Stokesian dynamics simulations.

CHAPTER 5

EQUILIBRIUM STRUCTURE AND DIFFUSION IN CONCENTRATED SUSPENSIONS CONFINED BY A SPHERICAL CAVITY

In this chapter, we model spherically confined suspensions of volume fraction $0.05 \leq \phi \leq 0.40$ using the method of Aponte-Rivera and Zia developed in the last chapter, where the presence of the boundary is accounted for through the use of appropriate hydrodynamic mobility functions [6]. The method ensures that the correct boundary conditions are satisfied at the surface of the cavity, and also accounts for many-body and lubrication hydrodynamic interactions between the particles themselves and between the particles and the cavity. We determine both the short-time and long-time transport behavior of the confined suspension, for a range of particle-to-cavity size ratios and volume fractions from concentrated to dilute.

5.1 Results

While self-diffusion in an unbound suspension is independent of structure and position, any confinement leads to spatial variations in structure and to changes in the length scale over which ordered structure appears [148, 57, 128], which in turn influence particle motion and diffusion. We begin with structural results that reveal confinement-induced ordering. Followed by our measurements of the short-time self-diffusivity in the spherically confined domain, and the impacts of structural heterogeneity on this quantity. The long-time transport behavior is reported in §5.1.5 and §5.1.6.

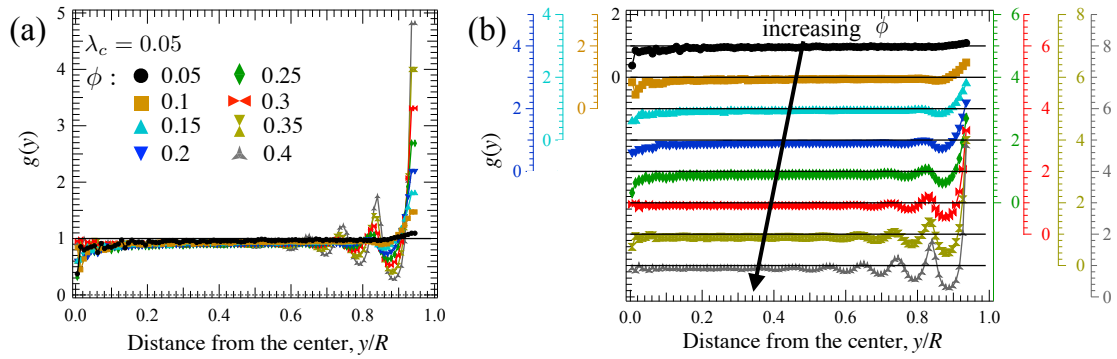

Figure 5.1: Cavity-centered radial distribution function g of particles inside a spherical cavity for volume fractions $0.05 \leq \phi \leq 0.40$, with particle-to-cavity relative size $\lambda_c = 0.05$. The cavity-centered radial distribution function is plotted as a function of normalized radial position y/R in plots with (a) a single axis and (b) multiple axes (one for each volume fraction).

5.1.1 Equilibrium structure in spherically confined suspensions

In any dispersion, individual particle dynamics are intrinsically connected to entropic and hydrodynamic interactions with the surrounding suspension. In a quiescent unbound dispersion, any particle can sample any position in the suspension, giving spatially homogeneous particle concentration over length scales longer than a particle size. One measure of such structure in unbound suspensions is the radial distribution function $g(r, \phi)$. in the dilute limit, $g(r, \phi \ll 1) \rightarrow 1$ for all r. At finite concentration, familiar nearest-neighbor peaks appear, strongest at contact and decaying to unity as $r \rightarrow \infty$. The Percus-Yevick closure provides a convenient approach for plotting this behavior [136]. However, the presence of an impenetrable boundary restricts accessible structural configurations; here, we investigate the extent to which such entropic restriction leads to spatial heterogeneities in particle concentration that ultimately affect relaxation length and time scales.

The spatial dependence can be quantified by defining a cavity-centered radial distribution function, giving a measure of the likelihood of finding a particle at a given position inside the cavity; it can be interpreted as a measure of the local density at that position. In the context of dynamic simulations, it describes the probability of finding the center of a particle in a thin annular shell, a "bin", within the cavity. This discretization is sketched in figure 3.2, and illustrates the cavity-centered radial distribution function

$$g(y_i) = \frac{V_T}{N}\left\langle \frac{N_i}{V_i} \right\rangle, \tag{5.1}$$

where N_i is the number of particles in bin i, $N = \phi/\lambda_c^3$ is the total number of confined particles, V_i is the volume of bin i, and the angle brackets denote an ensemble average over many configurations within a bin. As described in §3.2, the cavity was discretized into $i = 100$ annular-shell bins. The bin volume V_i changes with cavity size, λ_c, so that the discretization is the same for all λ_c. The cavity-centered radial distribution function $g(y_i)$ is defined over the total volume V_T accessible to particle centers. In consequence, the total volume is that contained by a sphere whose radius is equal to the maximum position of the particle inside the spherical cavity $y_{max} = (R - a)/R$. Normalizing the cavity-centered radial distribution function by N/V_T ensures that $g(y_i)$ approaches unity only when the local volume fraction is equal to the bulk volume fraction, i.e. $\phi = N\lambda_c^3$. Deviations from unity thus correspond to depletion and accumulation of particles, and permit analysis of the degree to which concentration or the cavity induces order. When confined in a cavity, one expects the particles to crowd each other near the center, and to be crowded by the wall far from the center. To understand how these local environments influence structure, we plot $g(y)$ as a function of radial position y in figure 5.1.

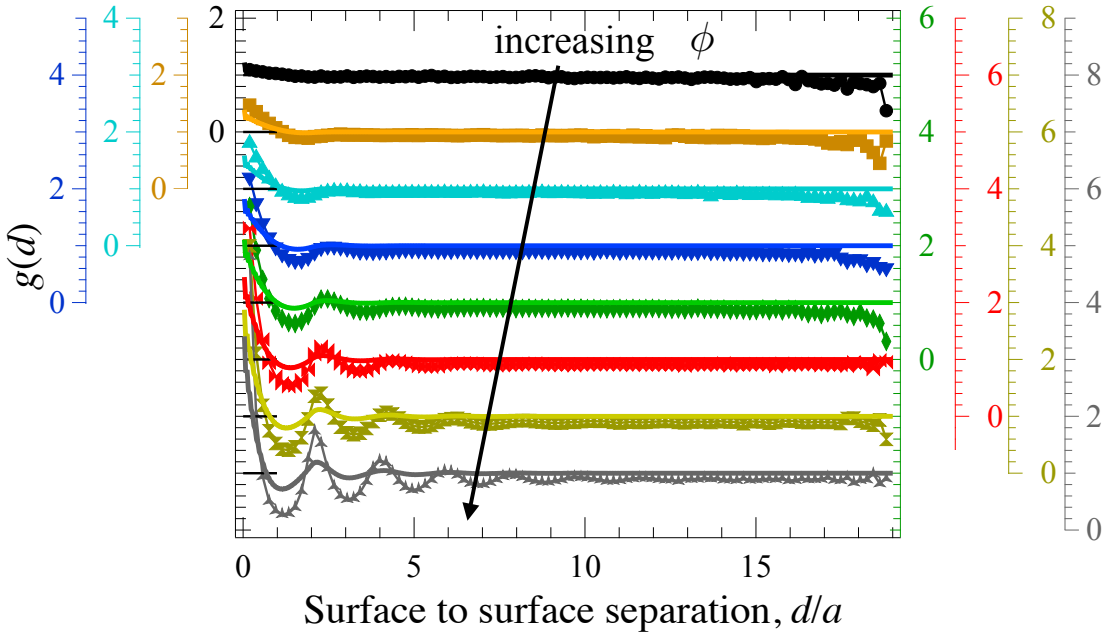

Figure 5.2: Cavity-centered radial distribution function of particles inside a spherical cavity (symbols) with particle-to-cavity relative size $\lambda_c = 0.05$ for $0.05 \leq \phi \leq 0.40$. Also shown: pair distribution function for unbound suspension (solid curves), for the same volume fractions. All are plotted as a function of separation between hard-sphere surfaces, i.e. particle-cavity and particle-particle surface separation for confined an unbound suspensions, respectively. The pair distribution function for unbound suspension is obtained from the Percus-Yevick closure relation [136].

In figure 5.1(a) the cavity-centered radial distribution function is plotted as a function of radial position for particles that are 1/20 the size of the cavity. Curves of different color represent various volume fractions, and the straight black line denotes a (normalized) uniform structure. Unsurprisingly, for tiny particles, the structure is nearly homogeneous away from the wall. But undulations appear near the wall and propagate inward as volume fraction increases. It seems surprising that structure appears at such low volume fraction; one might expect uniform distribution. Simulations in the present study (not shown in the plot) for a single particle in the cavity do indeed recover a uniform distri-

bution, but even a second additional particle produces structure. The appearance of structure at the wall can be independently recovered via other methods such as event-driven molecular dynamics simulations (see supplementary materials). To highlight the density undulations, the data are replotted with separate vertical axes for each volume fraction in figure 5.1(b). For the lowest volume fraction (black symbols), a weak peak is seen near the wall. As volume fraction increases, the peak near the wall narrows and grows taller, whilst depleting concentration near the center ($g(y) < 1$). The intermediate region of the cavity is structureless when $\phi \ll 1$, but as concentration grows, the peaks near the wall propagate inward, suggesting the emergence liquid-like structure, a non-continuum effect induced by confinement and concentration. Prior molecular dynamics studies of the configuration of spheres inside a sphere by [128] produce the same peaks and valleys as well; a comparison (shown in supplementary materials) for $a/R = 0.15$ and $\phi = 0.4$ shows excellent agreement. The peaks are reminiscent of nearest-neighbor peaks, where here we imagine that the 'surrounding' structure is now inside a test particle (the cavity). Confinement of these neighbors to a finite domain alters this structure — most obviously with the fact that no length scale exists where $g \to 1$, once volume fraction is sufficiently high, and that the onset of the liquid-like structure occurs at lower volume fractions than they do in the nearest-neighbor rings of unbound suspensions. To compare structural heterogeneity in spherically confined suspensions to the nearest-neighbor rings of unbound suspensions, we plot the cavity-centered radial distribution function in the confined domain (symbols) along side the pair distribution function of unbound suspensions (solid curves) in figure 5.2. Here, the pair distribution function for unbound suspensions has been obtained utilizing the Percus-Yevick closure relation [136]. To appropri-

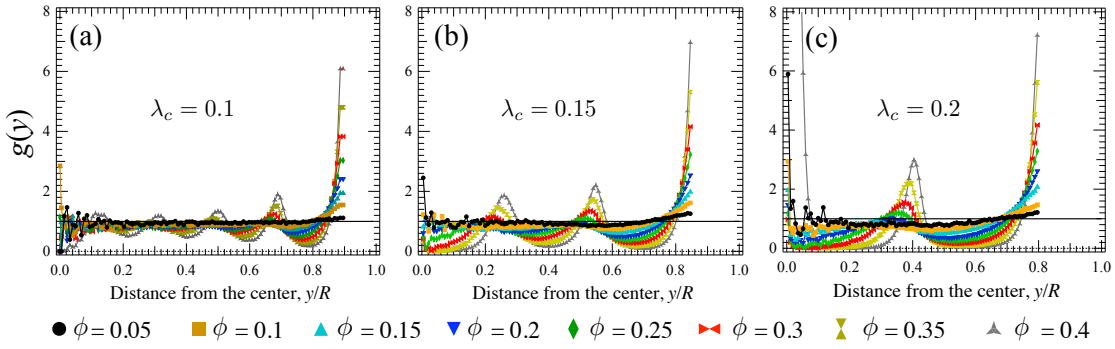

Figure 5.3: Emergence of confinement-induced liquid-like structure. Cavity-centered radial distribution function (density profile) $g(y)$ of particles inside a spherical cavity plotted as a function of normalized position y/R for: (a) $\lambda_c = 0.1$, (b) $\lambda_c = 0.15$, (c) $\lambda_c = 0.2$.

ately compare these two quantities, we plot them as a function of the separation distance between the appropriate hard-sphere surfaces normalized by the particle radius. As concentration increases, structural heterogeneity arises on length scales comparable to the particles size in both confined and unbound suspension, and propagates outward from the corresponding hard-sphere surface, i.e. the cavity surface in the confined domain and the test particle surface in the unbound domain. Two key differences arise: first, confinement induces stronger structural heterogeneity, with the amplitude of the structural undulations in the confined domain larger in magnitude for all volume fractions. Second, confinement propagates structural heterogeneity over longer length scales for all volume fractions. Thus, increasing the volume fraction in spherical confinement induces stronger and longer-ranged structural heterogeneity than that of unbound suspensions at matching volume fraction. We expect changes in cavity size to influence this behavior, and that this structural heterogeneity will influence short-time particle dynamics.

The effect of cavity size on this behavior is shown in figure 5.3, where the

the cavity-centered radial distribution function is plotted as a function of radial position for several additional values of λ_c. In figures 5.3(a), 5.3(b), 5.3(c) particles are 1/10, 1.5/10 and 1/5 of the cavity size, respectively, with colored symbols representing the same range of volume fraction studied for the large cavity of figure 5.1. The same qualitative trends appear — a peak near the cavity wall and density oscillations that increase in frequency and magnitude with increasing volume fraction. However, as the cavity shrinks, the undulations become more pronounced and occur at lower volume fractions, showing that confinement-induced ordering becomes more pronounced as entropic hindrance becomes more severe. The peaks of the undulation occur at multiples of the particle size $2a/R$, confirming the liquid-like layering induced by confinement and concentration persists to volume fractions as small as $\phi = 0.1$. For the largest particles, $\lambda_c = 0.2$, sharp peaks emerge close to the center of the cavity, $y/R \approx 0$, at an intermediate distance from the cavity center $y/R \approx 0.4$, and at the closest a particle can get to the wall, $y/R \approx (R-a)/R = 0.8$, while $\phi \approx 0$ elsewhere. Such a strongly layered structure suggests that a phase transition to crystal-like structure could occur; order parameters [150, 90] to quantify crystal formation in spherically confined domains [161] could be utilized to further interrogate this idea.

To more clearly illustrate the effects of particle-to-cavity relative size, the cavity-centered radial distribution function is evaluated at fixed volume fraction as the enclosure shrinks. In figure 5.4, the cavity-centered radial distribution function is plotted as a function of normalized position for two values of fixed volume fraction. In figure 5.4(a) the suspension is dilute and the cavity-centered radial distribution function for small particles ($\lambda_c = 0.05$) is nearly constant throughout the domain, save for a weak accumulation near the wall. As

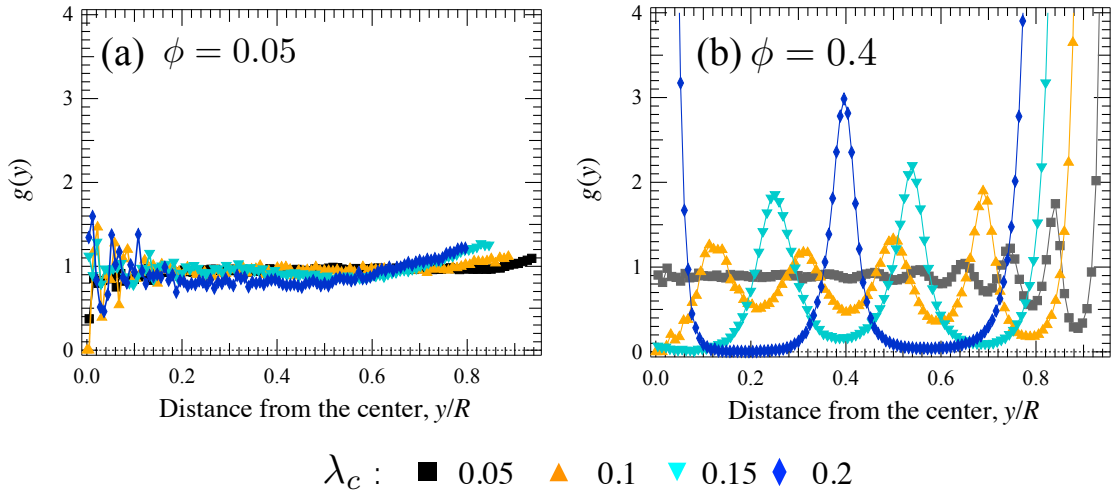

Figure 5.4: Cavity-centered radial distribution function (density profile) $g(y)$ of particles inside a spherical cavity plotted as a function of normalized position y/R for: (a) $\phi = 0.05$ and (b) $\phi = 0.4$. Particle-to-cavity size ratios as shown in legend.

the cavity shrinks ($\lambda_c = 0.1, 0.15, 0.2$), the effect of the boundary becomes more pronounced, until for $\lambda_c = 0.2$ accumulation near the wall is strong enough to deplete intermediate regions. Overall, dilute suspensions of small particles show little ordering near the center of the cavity, but larger particles order easily at the same volume fractions when small particles remain structureless in distribution. At just 40% volume fraction, even the smallest particles ($\lambda_c = 0.05$) form layers, but structural relaxation still permits the exchange of particles between layers, i.e. we expect liquid-like particle dynamics. Even the strongly layered larger particles, $\lambda_c = 0.1, 0.15$, can still exchange places, as evidenced by the finite probability of finding particles in the interstices between the layers.

In summary, we have found that the spherical boundary induces structure that propagates radially inward from the wall over a length scale set by volume fraction and particle-to-cavity relative size. In contrast to near-neighbor rings observed in the pair distribution function of concentrated, unbound suspen-

sions, the cavity-centered radial distribution function (or density profile) shows that confinement induces liquid-like structure that emerges at lower volume fractions, is of stronger magnitude, and propagates over longer length scales. For the smallest particles, the combined effects of concentration and confinement produce liquid-like structure, but only near the wall. Such layering can be pushed by the boundary inward throughout the domain as particles grow larger, but packing is still loose enough to permit the free exchange of particles between layers.

The underlying origin of this behavior is entropic exclusion from the space outside the impenetrable, finite-size sphere. Just as entropic interactions hinder equilibrium diffusivity in unbound suspensions [11, 24, 70], we expect the exclusion of volume to play a role in particle dynamics and confined diffusion. A secondary effect is also expected, whereby the structural ordering induced by entropic restrictions plays a role; we study both of these topics next.

5.1.2 Short-time self-diffusivity in spherically confined suspensions

The rate at which a particle diffusively probes the surrounding medium is slowed by hydrodynamic entrainment of other particles; at short times, such diffusive motion is so small that it does not distort the surrounding structure [11, 142], and thus is a purely hydrodynamic quantity. In an unbound suspension, this quantity depends only on the volume fraction of particles; the absolute positions of the particles do not matter. Only particle positions relative to one another influence transport, and particles can sample all relative separations

with equal probability.

Hydrodynamically, an enclosure provides another no-slip surface that hinders particle diffusion. As with the familiar example of an unbound pair, entrainment in the cavity depends on relative size, separation, and orientation of hydrodynamic forces to center-to-center orientation [6]. In the present case, hydrodynamic mobility also depends on particle distance from the cavity wall and particle-to-cavity relative size λ_c. Because hydrodynamic forces can act in any direction relative to the particle-to-cavity center-to-center axis, relative motion along the cavity radius differs from relative motion tangential to the cavity wall, given the same strength of forcing. The hydrodynamic mobility functions that describe such couplings in spherically confined suspensions were derived in our recent work [6] and result in a configuration-dependent mobility tensor. The short-time self-diffusivity, however, is an average over many configurations around a test particle, typically in a homogeneous domain. Since the spherical cavity produces structural heterogeneity in the suspension, one way to envision the average configuration around a test particle is to recognize that annular shells form homogeneous subdomains. These permit examination of variation of self-diffusion with radial position in the cavity. To examine this dependence, the n^{th} radial bin is defined at a location $y_n = \Delta y(n - 1/2)$, where n denotes the n^{th} bin, as discussed in §3.2. Averages within each bin give diffusion as a function of particle position, volume fraction, and size ratio. However, in contrast to isotropic structure that produces isotropic self-diffusion in unbound suspensions, spherical confinement permits isotropy only in the limiting case of a single particle located at its center [42]. We thus expect structural anisotropy to lead to anisotropic diffusion.

To examine the elements of the self-diffusion tensor, we recognize that within an annular bin, the suspension surrounding a test particle is, on average, isotropic in the solid angle. The short-time self-diffusivity is thus fully specified via projection through the orthogonal basis $\hat{\boldsymbol{y}}\hat{\boldsymbol{y}}$ and $\boldsymbol{I} - \hat{\boldsymbol{y}}\hat{\boldsymbol{y}}$, where $\hat{\boldsymbol{y}}$ is a unit vector along the center-to-center axis between the particle and cavity, and $\boldsymbol{I}$ is the isotropic unit tensor. Projection through the former gives diffusion along the cavity radius, while diffusion along the cavity is projected by the latter. Expressing the short-time self-diffusivity as a projection onto these two orthogonal subspaces obtains

$$\boldsymbol{D}_0 = \{[D_0^{\parallel}(y/R, \lambda_c, \phi)]\hat{\boldsymbol{y}}\hat{\boldsymbol{y}} + [D_0^{\perp}(y/R, \lambda_c, \phi)](\boldsymbol{I} - \hat{\boldsymbol{y}}\hat{\boldsymbol{y}})\}, \tag{5.2}$$

where $D_0^{\parallel}$ and $D_0^{\perp}$ are the diffusion coefficients for motion along and perpendicular to the cavity radius, respectively.

We utilized our recently developed confined mobility functions [6] implemented into a Stokesian dynamics simulation model to measure the diffusion coefficient $D_0^{\parallel}$ and $D_0^{\perp}$. The radial component, $D_0^{\parallel}$, is plotted in figure 5.5 as function of particle distance from the cavity center. Figures 5.5(a-d) give $D_0^{\parallel}$ for particles of size 1/5, 1.5/10, 1/10 and 1/20 the cavity size. Symbols correspond to simulations of spherically confined suspensions from the present study, accounting for many-body hydrodynamic interactions between all particles and the cavity; solid straight lines correspond to our simulation results for the short-time diffusion in *unbound* suspensions at matching volume fractions. Finally, the dashed lines correspond to the short-time self-diffusivity of a single particle inside the spherical cavity [85, 6]. This provides a means by which to assess the effects of crowding in confinement, similar in ethos to comparison of concentrated un-

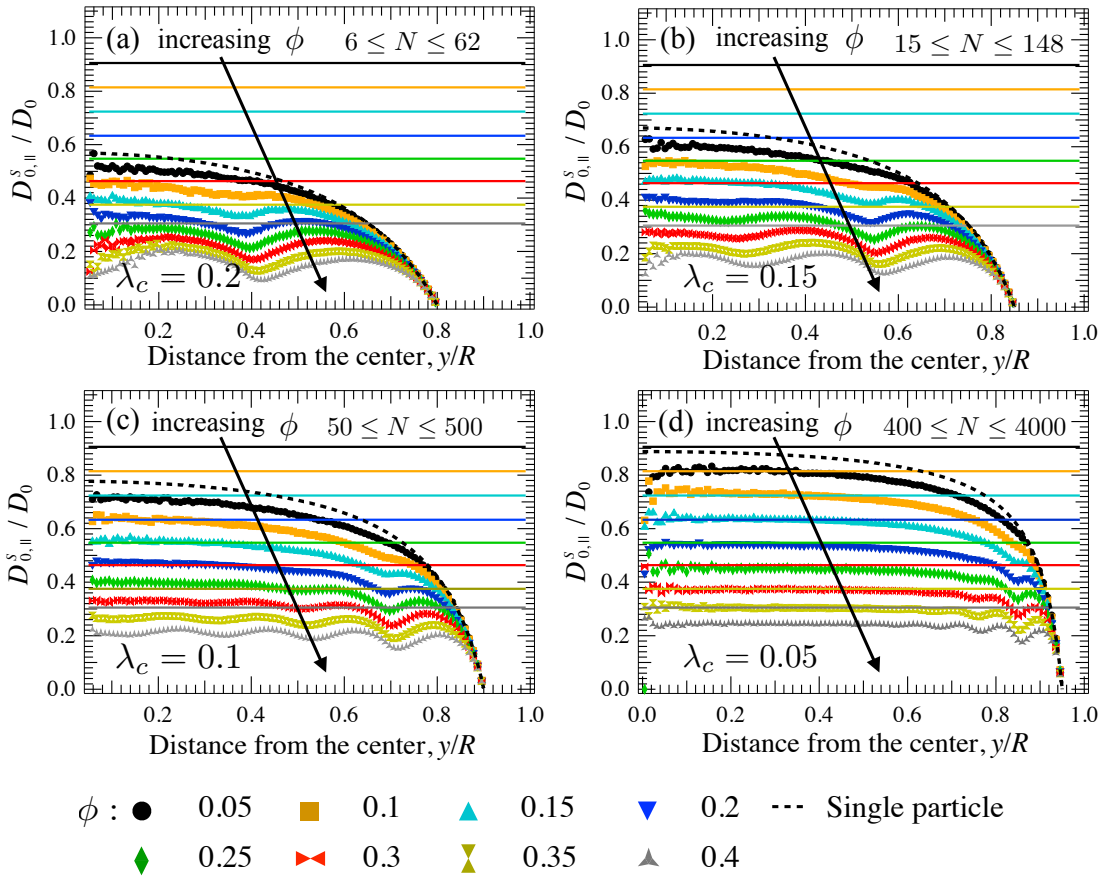

Figure 5.5: Radial component of the short-time self-diffusivity as a function of normalized distance from the center y/R for particle-to-cavity size ratios (a) $\lambda_c = 0.2$, (b) $\lambda_c = 0.15$, (c) $\lambda_c = 0.1$, and (d) $\lambda_c = 0.05$. In each plot, the symbols represent the diffusivity of particles in confined suspensions at varying volume fractions, and the straight solid lines represent the diffusivity in unbound suspension at matching volume fractions obtained here utilizing Accelerated Stokesian Dynamics simulations. The dashed line represents the diffusivity for a single particle inside the spherical cavity. Error bars are omitted for clarity, but can be found on plot in Appendix E. Number of particles per simulation varies with volume fraction as shown in plots.

bound suspension data to dilute pair theory.

As a particle diffuses in a suspension, the presence of the other particles' no-slip surfaces hinder its motion; spherical confinement introduces a distinct no-slip surface that provides additional viscous dissipation. Its effect can be seen in figure 5.5(a), where the data for confined diffusion falls everywhere below the corresponding volume-fraction data (straight lines). To isolate the contribution of particle-boundary interactions, we show the radial diffusivity of a single particle inside the cavity (dashed curve). A single enclosed particle diffuses fastest at the cavity center; its diffusivity decreases monotonically as it approaches the wall where lubrication forces drive its mobility to zero. The presence of additional particles introduces many-body couplings that change structure and diffusion. These effects emerge for volume fractions as small as $\phi = 0.05$, with undulations in the diffusivity that become more pronounced as concentration increases. The peaks and troughs appear at radial positions that correspond to regions of density accumulation or depletion shown in figure 5.3. When a pair of particles is separated just enough to fit a third particle (of size $2a/R$), mobility decreases owing to strong hydrodynamic coupling showing that structural heterogeneity produces dynamical heterogeneity.

However, volume fraction cannot be specified independently of particle-to-cavity size ratio; growth in cavity size at fixed volume fraction (plots 5.5(b), 5.5(c), and 5.5(d)) permits growth in self-diffusivity. As cavity size increases, position dependence of diffusivity becomes less pronounced(cf. figure 5.5(d)). Eventually in the limit $\lambda_c \to 0$ (unbound suspension) confinement effects will vanish. However, figure 5.5(d) shows that confinement effects are qualitatively important even when particles are only $1/20$ the cavity size illustrating confine-

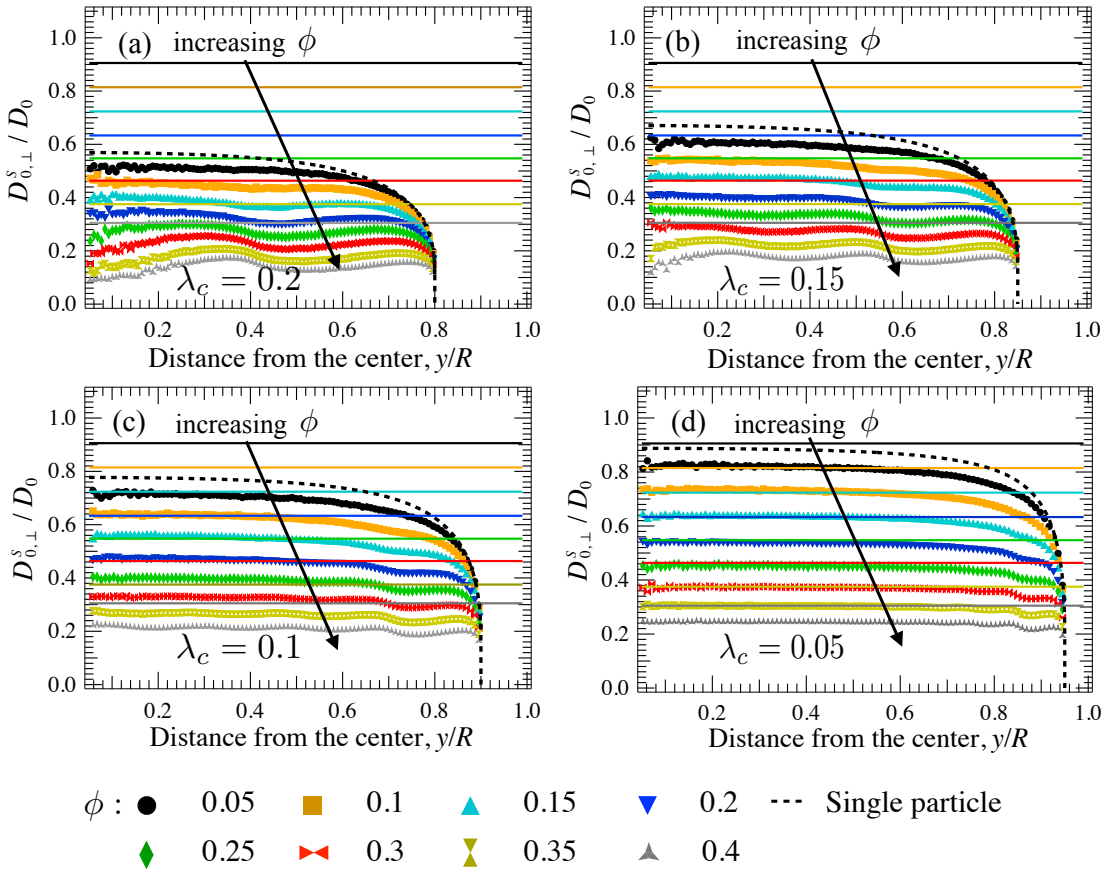

Figure 5.6: Perpendicular component of the short-time self-diffusivity as a function of normalized distance from the center y/R for particle-to-cavity size ratios (a) $\lambda_c = 0.2$, (b) $\lambda_c = 0.15$, (c) $\lambda_c = 0.1$, and (d) $\lambda_c = 0.05$. In each plot, the symbols represent the diffusivity of particles in confined suspensions of varying volume fractions, and the straight solid lines represent the diffusivity in an unbound suspension (obtained via Accelerated Stokesian dynamics) at matching volume fractions. The dashed line represents the diffusivity for a single particle inside the spherical cavity.

ment can strongly impact the diffusivity of particles with biophysically relevant particle-to-cavity size ratios [64].

Diffusivity transverse to the cavity radius is considered next. In figure 5.6, the perpendicular component of the short-time self-diffusivity is plotted as a

function of distance from the cavity center for several volume fractions. Figure 5.6 illustrates the interplay between cavity size and particle volume fraction, with $\lambda_c = 0.2, 0.15, 0.1$ and 0.05 in figure 5.6 (a)-(d), respectively. As before, a dashed curve in each plot gives the diffusivity of a single confined particle, and symbols and solid lines are simulation results from the present study for confined and unconfined domains, respectively. As with radial diffusion, the diffusivity of confined particles (λ_c = 0.2, 0.15, 0.1, 0.05) is hindered and position-dependent, with undulations arising from heterogeneous concentration. Overall, undulations of transverse self-diffusion are weaker than radial undulations, demonstrating that radial variations in volume fraction more strongly impact radial diffusion. Physically, when a particle in the confined suspension moves in the radial direction, the presence of other neighboring particles has a strong effect, owing to hindered entrainment. When a particle moves in the perpendicular direction, the presence of other neighboring particles has a weaker effect due to stronger entrainment. Thus, whether a particle is located in a region of accumulation or depletion will cause variations (or undulations) of larger magnitude in the radial diffusion coefficient. Unsurprisingly, perpendicular diffusion vanishes slower than radial diffusion for particles close to the wall, owing to logarithmically weaker hydrodynamic coupling associated with perpendicular motion (sliding flow), as compared to that resulting from radial motion (squeezing flow), an observation previously predicted for a single enclosed particle by [132].

Computing the ratio of radial to transverse diffusion removes the influence of the volume fraction on the anisotropy of the diffusion tensor, and should reveal the extent to which structure, e.g. layering, sets this anisotropy. The ratio $D_{\parallel}/D_{\perp}$, can be subtracted from unity to give a measure of the 'degree of

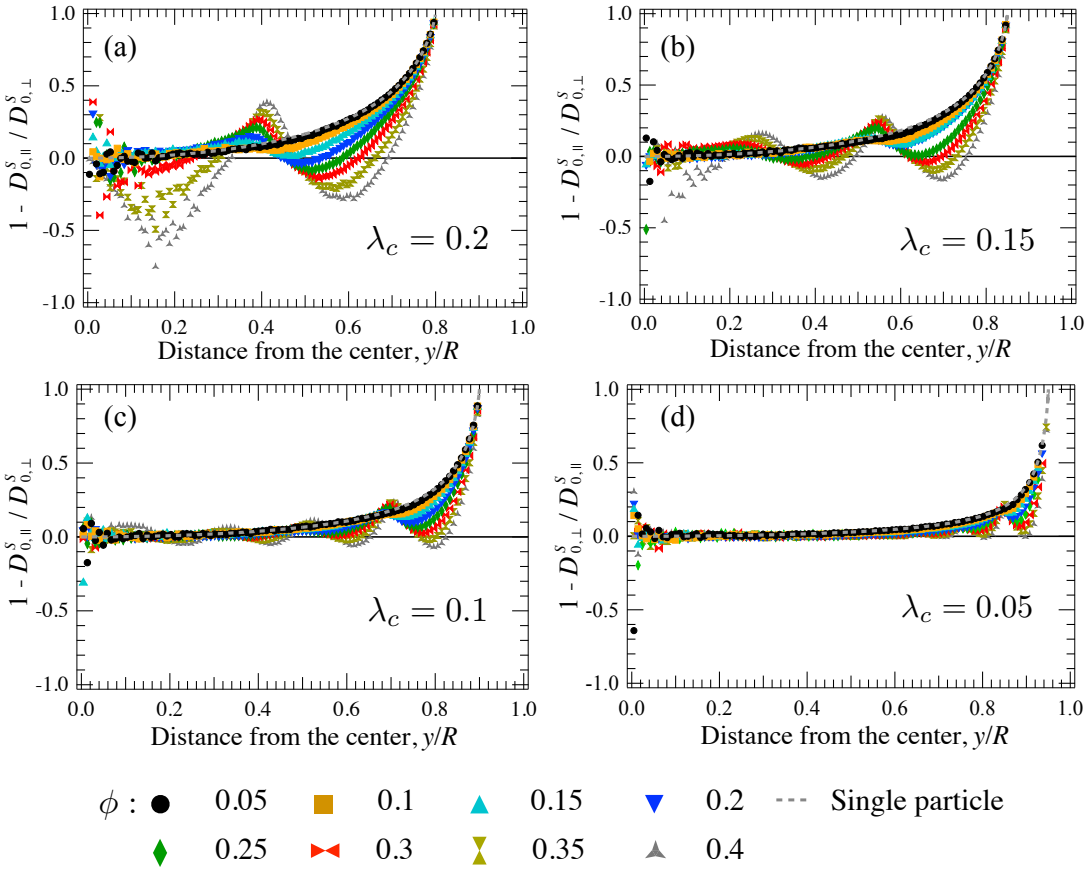

Figure 5.7: Anisotropy of diffusion plotted as a function of normalized particle position y/R for particle-to-cavity size ratios (a) λ_c = 0.2, (b) λ_c = 0.15, (c) λ_c = 0.1, and (d) λ_c = 0.05. In each plot, symbols represent the degree of anisotropy for spherically confined suspensions at varying volume fractions. The straight line represents a value of unity, the limit of isotropic diffusion.

anisotropy', where a value of zero corresponds to isotropic diffusion, negative values correspond to preferred radial diffusion, and positive values correspond to preferred transverse diffusion. This quantity is plotted in figure 5.7 as a function of radial position for particles that are 1/5, 1.5/10, 1/10, and 1/20 of the cavity size in figures 5.7(a)-(d), respectively. The dashed line corresponds to the degree of anisotropy of an isolated particle in the confined domain, and symbols to the degree of anisotropy in confined suspensions at various volume fractions. Isotropic diffusion is mapped onto the horizontal line through zero. Particles at

the center of the cavity (left end of axis), exhibit isotropic diffusion, regardless of particle-to-cavity size ratio. However, the higher standard error in measurements done in bins near the center of the cavity leads to non-zero values near the center. As the particle moves any distance away from the center, anisotropy emerges. Near particle-cavity contact $D_{\parallel}/D_{\perp} \approx 1$, owing to longitudinal lubrication interactions that are strong relative to transverse interactions.

Even though volume fraction dependence is automatically scaled out by the ratio, the undulations do not collapse together, confirming that heterogeneity in particle dynamics arises from structural heterogeneity. In contrast to the behavior of an isolated particle where radial diffusion is always slower than perpendicular diffusion, liquid-like structure at high volume fractions results in regions where radial diffusion is *faster* than perpendicular diffusion. In biophysical systems, such dynamic heterogeneity could serve to optimize the short-time diffusion of particles along the radial or perpendicular directions depending on their position. The dynamical heterogeneity also poses interesting questions for e.g. the formation of photonic crystals via decreasing cavity radius in spherically confined suspensions [165], where the time scale of shrinking the cavity radius may not allow the structure to relax into a fully crystallized state, or for interpretation of particle diffusive behavior in the interior of eukaryotic cells [43].

In summary, short-time self-diffusivity in spherically confined domain is position dependent, anisotropic and exhibits undulations that arise primarily due to boundary- and concentration-induced structure. Such features must be taken into consideration when measuring short-time diffusion coefficients in e.g. cells, as ignoring it will lead to artificially large or small diffusion coef-

ficients, depending on particle position and suspension structure. Finally, the ordered dynamical heterogeneity seen here suggests that confinement may promote self-organization of particles in biophysical systems based on their size and self-mobility.

5.1.3 Comparison to direct measurements: Numerical experiments

In the previous section, the short-time self-diffusivity was computed by calculating an ensemble-averaged mobility tensor utilizing a stochastic sampling technique to obtain the tensorial couplings between force and motion. However, particle-tracking experiments typically do not allow direct access to such couplings. Instead, experiments rely on measurement of particle positions, from which mean-square displacement may be calculated and utilized to determine diffusion coefficients. Here, we compare results from the previous section to the short-time self-diffusivity obtained via numerical particle-tracking 'experiments', in the present study. This provides an experimental protocol that accounts for confinement.

In a particle-tracking experiment, measurement of the *short*-time self-diffusivity requires measurement of the displacements of many particles over a short time interval (lag time)[135]. The mean absolute displacement at each moment in time is obtained by averaging over all particles; it is then subtracted from the absolute displacement of each particle to give its time-dependent displacement from mean motion. The square of this quantity is then averaged across all particles to give the mean-square displacement; if this quantity grows

linearly in time, its derivative gives the short-time self-diffusion coefficient. This procedure is utilized for unconfined suspensions, where the absolute starting position of any particle is irrelevant. However, as shown in §5.1.2, the short-time self-diffusivity in confinement varies qualitatively with position relative to the cavity center, an effect that is smeared out and lost by all-particle averaging.

To account for the effects of confinement, in §5.1.2 we established a radial binning technique that permits identification and tracking of particles according to their distance from the center of the cavity. An accurate measurement requires either a large number of particles in each bin to sample many representative configurations around test particles, or a finite number of particles per bin rearranged into many different configurations within the bin. The latter approach is easily taken by measuring a snapshot of particle positions, waiting until particles rearrange themselves, and carrying out the measurement again several more times. One way to do this is to trace particle displacements over time, where such data automatically identifies each particle's current bin; a judicious choice of lag time, Δt, is made, and a new 'snapshot' begun at each new initial time t_0.

The absolute displacement vector $\boldsymbol{\Delta y}_{ij}(\Delta t) = \boldsymbol{y}_{ij}(t_0 + \Delta t) - \boldsymbol{y}_{ij}(t_0)$ of a particle i located in bin j during the lag time interval Δt is measured, and each particle is binned according to its radial position at time t_0, $y_{ij} = \left|\boldsymbol{y}_{ij}(t_0)\right|$. The mean displacement within the j^{th} bin, $\langle \boldsymbol{y} \rangle_j(\Delta t)$, is then calculated. When the suspension is quiescent, the mean motion of the particles is vanishingly small. Displacements relative to the mean are then calculated and projected in directions along and perpendicular to the cavity radius by utilizing the orthogonal bases $\hat{\boldsymbol{y}}_{ij}(t_0)\hat{\boldsymbol{y}}_{ij}(t_0)$ and $[\boldsymbol{I} - \hat{\boldsymbol{y}}_{ij}(t_0)\hat{\boldsymbol{y}}_{ij}(t_0)]/2$, respectively. Along the radial direction, the displacement

relative to the mean is defined as

$$r_{ij,\parallel}(\Delta t, t_0) = [\Delta \boldsymbol{y}_{ij}(\Delta t) - \langle \boldsymbol{y} \rangle_j(\Delta t)] \cdot \hat{\boldsymbol{y}}_{ij}(t_0). \tag{5.3}$$

Similarly, we define displacements relative to the mean in the perpendicular direction as

$$r_{ij,\perp}(\Delta t, t_0) = \left| [\Delta \boldsymbol{y}_{ij}(\Delta t) - \langle \boldsymbol{y} \rangle_j(\Delta t)] \cdot [\boldsymbol{I} - \hat{\boldsymbol{y}}_{ij}(t_0)\hat{\boldsymbol{y}}_{ij}(t_0)]/2 \right|. \tag{5.4}$$

Anisotropy and radial dependence of the mean-square displacement are automatically captured by this method; the mean-square displacement in the radial direction varies with distance y from the center, i.e. it is the mean-square displacement in the j^{th} bin:

$$\langle r_\parallel^2 \rangle_j(\Delta t, \lambda_c) = \frac{1}{n_s N_j} \sum_{k=0}^{n_s} \sum_{i=1}^{N_j} [r_{ij,\parallel}(\Delta t, t_0 = k\Delta t)]^2. \tag{5.5}$$

In equation 5.5, the angle brackets represent an ensemble over many configurations within bin j, the indices denote the i^{th} particle in the j^{th} bin, N_j is the total number of particles in bin j, and n_s is the total number of snapshots (realizations) k of duration Δt. Similarly, the perpendicular mean-square displacement transverse to the radius is,

$$\langle r_\perp^2 \rangle_j(\Delta t, \lambda_c) = \frac{1}{n_s N_j} \sum_{k=0}^{n_s} \sum_{i=1}^{N_j} [r_{ij,\perp}(\Delta t, t_0 = k\Delta t)]^2. \tag{5.6}$$

The radial and perpendicular short-time self-diffusion coefficients, as they vary with position in the cavity, are directly obtained as

$$D_{0,j}^{\parallel}(\lambda_c, \phi) \;=\; \langle r_\parallel^2 \rangle_j(\Delta t, \lambda_c)/(2\Delta t), \tag{5.7}$$

and

$$D_{0,j}^{\perp}(\lambda_c, \phi) = \langle r_\perp^2 \rangle_j(\Delta t, \lambda_c)/(2\Delta t). \tag{5.8}$$

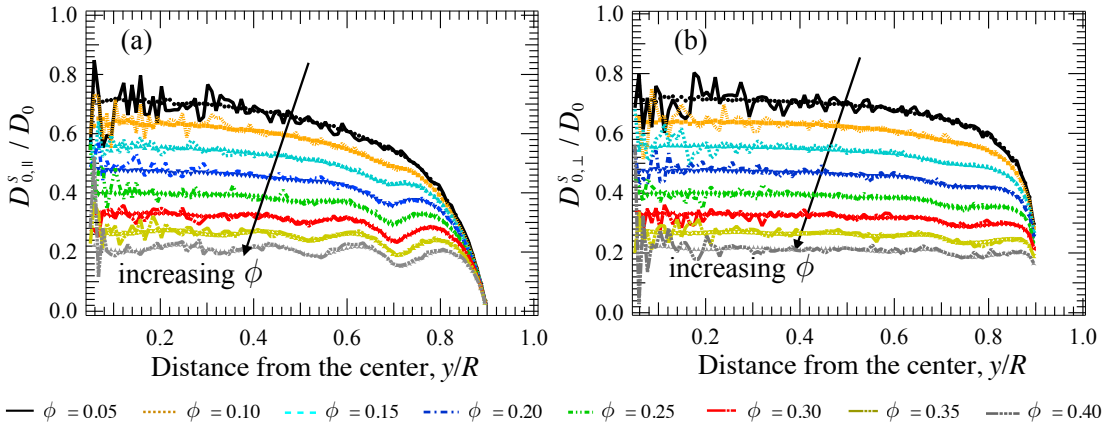

Figure 5.8: Short-time self-diffusivity in the (a) radial and (b) perpendicular directions obtained via 'numerical experiments' in the present study with lag time $\Delta t = 0.01$. Particles are 1/10 the cavity size and a range of volume fractions, $0.05 \leq \phi \leq 0.4$, are plotted as shown in the legend.

Short-time self-diffusion is plotted as a function of radial position by identifying the location of each bin as the distance of the bin center to the center of the cavity, given by $y_j = (j - 1/2)/(n_{tot}\lambda_c)$.

The short-time self-diffusivity measured via this method in our simulations is plotted as a function of particle radial position in figure 5.8 for a range of volume fractions ϕ and particles of size $a = R/10$. Two sets of data appear in each plot: solid curves correspond to the experimental measurement of mean-square displacement, and open symbols correspond to the mobility tensors utilized in §5.1.2. Each curve is nearly indistinguishable from its corresponding symbol series, indicating excellent agreement between numerical experiments and the stochastic sampling technique. This also shows that the lag time interval selected, $\Delta t = 0.01a^2/D_0$, accurately captures short-time self-diffusion for particles one-tenth the size of the enclosure. At lower volume fractions, there are fewer particles within the small volume at the center, which leads to a larger standard

error for measurements in that region. In a particle-tracking experiment, such error can be mitigated by increasing the number of snapshots (realizations). Another strategy to mitigate the reduced sampling near the center is to define bins of constant volume, such that bins near the cavity center have a larger radius and thus a higher probability of containing particles. However, bins of constant volume improve sampling near the center at the cost of spatial resolution in the measured diffusion coefficient.

It is natural to ask what errors would arise if the effects of the boundary, such as dependence on radial position and anisotropy, were neglected. A discussion of those errors is given next.

5.1.4 Relative error arising from common approximations

Here, we compare the short-time self-diffusivity that would be obtained in a particle tracking experiment if the tensor were assumed to be isotropic and position independent, an approximation often made when data are analyzed following the same protocols utilized for unbound suspension. We determine the relative error of this approximation, for diffusion along the cavity radius, by comparing the approximated numerical 'particle tracking experiments' to the results obtained in §5.1.2. As discussed in §5.1.3, in measurements of short-time diffusion in unconfined suspensions the starting position of any particle is irrelevant. In addition, motion is isotropic on average and so only the magnitude of particle displacements matters; direction does not matter. Absolute displacements are thus measured and averaged over all particles, to obtain the mean displacement within the cavity $\langle \boldsymbol{y} \rangle(\Delta t)$. The magnitude of the displacement rel-

ative to the mean is then,

$$r'_{ij}(\Delta t, t_0) = \left|\mathbf{\Delta y}_{ij}(\Delta t) - \langle \boldsymbol{y} \rangle(\Delta t)\right|, \tag{5.9}$$

Averaging the mean-square motion over all particles is equivalent to a spatially averaged mean; the spatially averaged mean-square displacement is then

$$\overline{\langle r^2 \rangle} = \frac{1}{n_s N} \sum_{k=0}^{n_s} \sum_{j=1}^{n_{tot}} \sum_{i=1}^{N_j} [r_{ij}(\Delta t, t_0 = k\Delta t)]^2, \tag{5.10}$$

where the overbar indicates a spatial average over the ensemble (bin) average indicated by the angle bracket.

This is a weighted average, where the weight is the probability of finding a particle in the *jth* bin and the average is taken along the cavity radius. As the cavity size increases, the probability of finding a particle in any bin far from the wall becomes uniform, indicating homogeneous suspension structure. Thus, the ensemble-averaged mean-square displacement of unbound suspensions is recovered in the limit $\lambda_c \rightarrow 0$. This approach smears out anisotropy and dependence on radial position, providing a means with which to determine the error arising from such approximation. Utilizing this approach, the diffusivity may then be approximated as

$$D_{MSD}(\lambda_c, \phi) = \overline{\langle r^2 \rangle}(\lambda_c, \phi)/6\Delta t, \tag{5.11}$$

where $\Delta t \ll a^2/D_0$ so that particle displacements are measured during the short-time self-diffusive regime. To quantify the error arising from this approximation, we define the relative error for diffusion along the cavity radius as

$$E_{\|}(y/R, \lambda_c, \phi) = 100 \, \frac{\left|D_0^{\|}(y/R, \lambda_c, \phi) - D_{MSD}(\lambda_c, \phi)\right|}{D_0^{\|}(y/R, \lambda_c, \phi)}. \tag{5.12}$$

In figures 5.9(a)-(c), the relative associated with approximating radial diffusion via this anisotropic, smeared averaging is plotted for particle-to-cavity relative sizes of 1/5, 1.5/10 and 1/10, respectively; different curves correspond to different volume fractions. Beginning with the relative error for dilute suspensions ($\phi = 0.05$) of particles that are 1/5 the cavity size, the plot shows that near the center, the relative error can be as high as 35%. Near the dilute limit, error decreases to a minimum and suddenly reverses toward a maximum as the wall is approached. This reversal occurs where the coarse prediction changes from an under-prediction to an over-prediction of the correct value. As volume fraction increases, several such reversals occur, evidence of the impact of neglecting structural heterogeneity. The spatial variation of error changes with volume fraction: the relative error in a concentrated suspension is higher than that of a dilute suspension at a position of $y/R \approx 0.3$, whereas the relative error in a concentrated suspension is smaller than that of a dilute suspension at a position of $y/R \approx 0.45$. This shows that pronounced error persists as concentration increases, i.e. that crowding and confinement do not give bulk behavior. With decreasing particle size, the relative error decreases for all positions away from the cavity wall. Large errors are still observed near the center for the smallest particles, with a particle-to-cavity relative size of 1/10. Close to the cavity wall, the relative error diverges regardless of particle-to-cavity relative size, showing that such approximations will lead to large errors when predicting the motion of particles near the cavity surface. Overall, assuming diffusion to be isotropic and independent of position leads to serious qualitative errors in the predicted radial diffusion which increase with increasing particle size. Large errors are obtained whether the particle is near the cavity center or close to the cavity wall. Similar behaviors are observed for the relative error along the direction

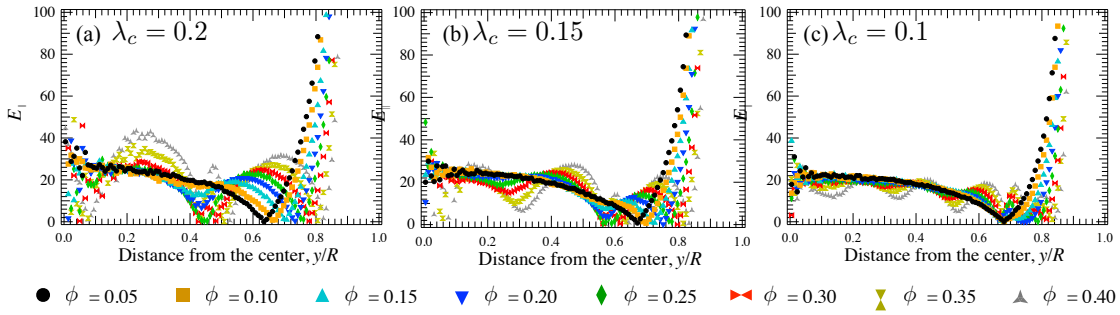

Figure 5.9: Relative error of the short-time self-diffusivity in the radial direction approximated by the early time behavior of the mean-square displacement. Plots (a), (b) and (c) correspond to the relative error in the radial direction for suspensions with a particle-to-cavity relative size of 1/5, 1.5/10 and 1/10, respectively.

perpendicular to the cavity radius and these are discussed in Appendix B.4.

Overall, assuming diffusion to be isotropic and independent of position leads to qualitative error in the predicted radial diffusion even for small particles at dilute concentrations; error only increases with increasing particle size. The relative errors observed for diffusion perpendicular (see Appendix B.4) to the cavity radius highlight the importance of accounting for the effect of confinement when measuring particle diffusivities in 3D confined suspensions, as such coarse approximations can fail to predict variations in mobility which could aid in self-organization.

5.1.5 Long-time behavior: mean-square displacement

A diffusing particle will distort suspension structure as it probes its surrounding medium, leading to correlated motion as it escapes a 'cage' of neighboring particles, during which its mean-square displacement grows sublinearly in time [142]. In an unbound domain, a particle executes a random walk

through the suspension after many such structural rearrangements, undergoing long-time self-diffusion. In a 3D-confined domain, a particle will also distort the surrounding structure as it exchanges places with its neighbors, but after many such exchanges, the particle is still confined to a finite domain. [162] showed that a single point-particle will exhibit a long-time plateau in mean-square displacement as this finite domain is explored. A question left open by previous studies is whether, between these two limits, a long-time diffusive regime exists. In this section, we continue our study of confined particle dynamics, but now study particle motion over longer times.

Over long times, a particle will wander from its starting point, sampling many different radial positions and, as a consequence, different radial bins within the cavity. This suggests that a spatially averaged mean-square displacement is appropriate for the study of long-time particle dynamics. Absolute displacements $\Delta \boldsymbol{y}_{ij}$ are thus measured and averaged over all particles to determine the mean displacement within the cavity $\langle \boldsymbol{y} \rangle(\Delta t)$. We note that, as before, the mean motion of the particles is vanishingly small in quiescent suspensions. Radial displacements relative to this mean are then calculated via

$$r'_{ij,\parallel}(\Delta t, t_0) = [\boldsymbol{\Delta y}_{ij}(\Delta t) - \langle \boldsymbol{y} \rangle(\Delta t)] \cdot \hat{\boldsymbol{y}}_{ij}(t_0), \tag{5.13}$$

where the prime indicates that displacements are relative to the mean displacement within the cavity. Similarly, the perpendicular displacement relative to the mean is given by

$$r'_{ij,\perp}(\Delta t, t_0) = \left| [\boldsymbol{\Delta y}_{ij}(\Delta t) - \langle \boldsymbol{y} \rangle(\Delta t)] \cdot [\boldsymbol{I} - \hat{\boldsymbol{y}}_{ij}(t_0)\hat{\boldsymbol{y}}_{ij}(t_0)]/2 \right|. \tag{5.14}$$

In contrast to equations 5.3 and 5.4, equations 5.13 and 5.14 give particle displacement relative to the spatially averaged mean motion, $\langle \boldsymbol{y} \rangle(\Delta t)$. The square

of these quantities are then ensemble-averaged to give the spatially averaged radial and perpendicular mean-square displacements:

$$\overline{\langle r_{\parallel}^2 \rangle}(\Delta t, \lambda_c) = \frac{1}{n_s N} \sum_{k=0}^{n_s} \sum_{j=1}^{n_{tot}} \sum_{i=1}^{N_j} [r_{ij,\parallel}(\Delta t, t_0 = k\Delta t)]^2, \tag{5.15}$$

and

$$\overline{\langle r_{\perp}^2 \rangle}(\Delta t, \lambda_c) = \frac{1}{n_s N} \sum_{k=0}^{n_s} \sum_{j=1}^{n_{tot}} \sum_{i=1}^{N_j} [r'_{ij,\perp}(\Delta t, t_0 = k\Delta t)]^2, \tag{5.16}$$

where the overbar on the left-hand side indicates a spatially averaged quantity with respect to the radial position, and the angle brackets represent an ensemble (realization) average. In the confined domain, equations 5.15 and 5.16 are weighted averages, where bins with more particles weight the average more than bins of smaller volume. The implication of such a technique is that the overall measurement gives a better idea of what is going on near the wall, but a less clear idea of dynamics elsewhere.

The radial and perpendicular spatially averaged mean-square displacements are plotted as a function of lag time for a particle-to-cavity size of 1.5/10 in figures 5.10(a) and 5.10(b), respectively. Several curves are shown, representing a range of volume fractions. In figure 5.10(a), the average radial mean-square displacement grows linearly in time at short times, as particles undergo short-time self-diffusion. At intermediate times, average radial mean-square displacement grows sublinearly for $0.05 \leq \phi \leq 0.15$, suggesting that particles undergo correlated motion as they exchange places with their neighbors. The power-law exponent of this subdiffusive motion decreases with increasing lag time, and eventually vanishes to a long-time plateau. The time required to reach the long-time limit corresponds to the time required for particles to sample the entire domain. When particles are dilute and large, 'caging' effects arise both from the cavity and other particles, as evidenced by the subdiffusive motion

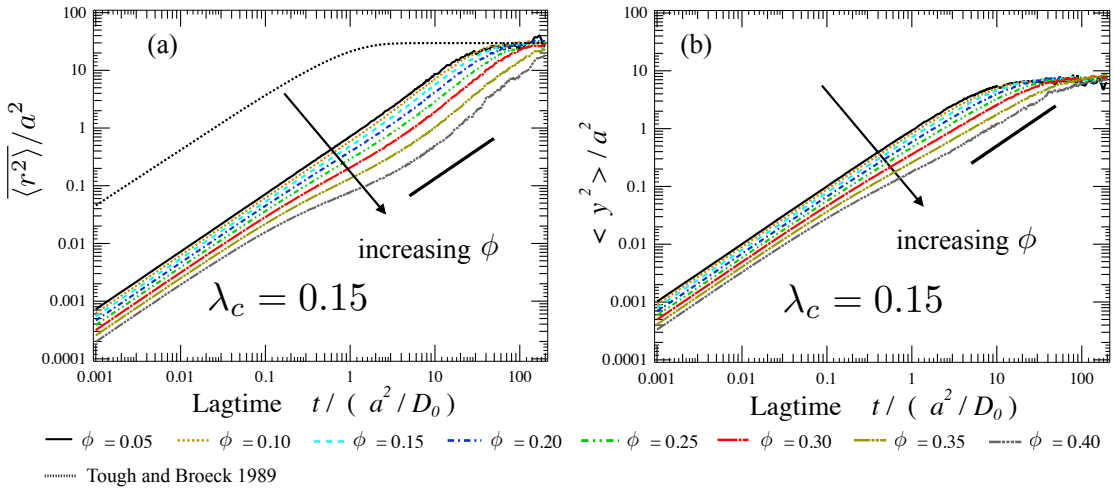

Figure 5.10: Average (a) radial and (b) perpendicular mean-square displacement plotted as a function of lag time for a suspension with particles that are 1.5/10 the size of the cavity, for several volume fractions, as shown in the legend. Solid, dashed, and dashed-dotted curves correspond to suspensions of different volume fractions from the present study as shown in the legend. The dotted curve in (a) corresponds to the result of [162] for a single point particle diffusing in one dimension.

prior to the long-time plateau. As concentration increases, $0.2 \leq \phi \leq 0.4$, an intermediate *superdiffusive* region emerges, separating the short-time diffusion and long-time plateau. Thus, the combined effects of crowding, hydrodynamic interactions and confinement can lead to anomalous transport. This region of superdiffusive motion occurs before the long-time plateau, but after the subdiffusive transition that occurs after short-time diffusion. This suggests that 'cage hopping' events play a role in setting the superdiffusive character of the average radial mean-square displacement.

The data from the present study can be compared to simplified theory, as shown by the dotted-line curve in figure 5.10(a), which corresponds to the model of [162] for point-particle diffusion along a line in a cavity. The data from the present study shown in the plot is projected along one direction as well,

providing a opportunity for qualitative comparison. Unsurprisingly, the point-particle theory and the concentrated, finite-size results reach the same long-time plateau since entropy (no flux) restricts long-time motion to the cavity boundary. However, the theory strongly over-predicts short-time diffusion owing to their neglect of particle size and hydrodynamic interactions. More seriously, it fails to predict the anomalous transport observed at higher volume fractions, confirming that crowding and hydrodynamic interactions play a critical role on this behavior.

The average perpendicular mean-square displacement is plotted in figure 5.10(b). For $0.05 \leq \phi \leq 0.15$, it is actually *subdiffusive*, with a power law exponent that vanishes to a long-time plateau. Consistent with the behavior observed in figures 5.10(a), 'caging' arises both from the cavity and other particles. As concentration increases, $0.2 \leq \phi \leq 0.4$, an intermediate subdiffusive region emerges during the lag times where the average radial mean-square displacement displays a superdiffusive behavior. As with the average radial mean-square displacement, this intermediate region occurs before the long-time plateau but after the short-time diffusion region, suggesting that 'cage hopping' events play a role in this behavior as well.

Overall, the combined effects of crowding, hydrodynamic interactions and confinement lead to anomalous transport that qualitatively depends on the direction of motion. Caging effects of both surrounding particles and the enclosing cavity produce anomalous transport – superdiffusion in the radial direction and subdiffusion in the transverse direction. In the next section we explore the idea that cage hopping dynamics underlie this behavior. In the next section, we provide further evidence that cage hopping events play a role in particle

dynamics at these time scales by analyzing the average excess kurtosis of the confined suspension.

5.1.6 Dynamics of cage hopping

The linear growth of mean-square displacement with time for diffusive motion produces a Gaussian distribution of particle displacements; deviation from Gaussian behavior can arise when behavior becomes sub- or super-diffusive. The excess kurtosis measures the deviation of the tails of a probability distribution from Gaussian behavior, focusing on regions of the distribution that are far from the mean. Here we define the average excess kurtosis of motion in a spherically confined domain, where positive values indicate a broader tail (increased probability of displacements far from the mean) and negative values indicate thinner tails (lower probability of displacements far from the mean), as compared to a Gaussian distribution. An increased likelihood of large displacements is associated with the structural rearrangements particles must undergo in order to jump between cages of neighboring particles [172]. The excess kurtosis thus provides a means by which to identify the time scale over which such 'cage hopping' events take place, as well as which direction plays a more important role in cage hopping.

We define the average excess kurtosis in the radial direction as

$$\alpha_{\parallel} = \frac{\sum_{j}^{n_{tot}} < r_{\parallel,j}^{4} >}{\sum_{j}^{n_{tot}} 3 < r_{\parallel,j}^{2} >^{2}} - 1, \tag{5.17}$$

where $r_{\parallel,j}^{4}$ represents the fourth moment of the probability distribution of particle displacements in the radial direction, and the angle brackets represent an

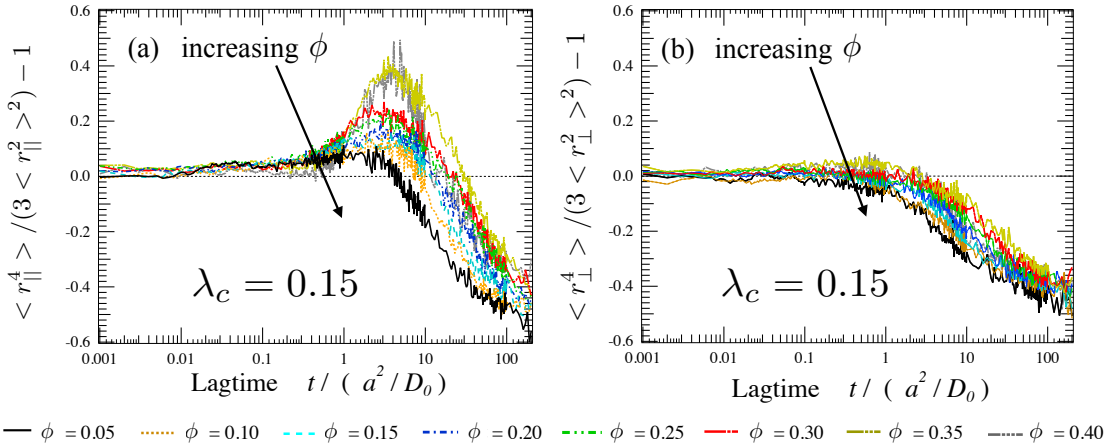

Figure 5.11: Average (a) radial and (b) perpendicular excess kurtosis as a function of lag time for a suspension with particles that are 1.5/10 the size of the cavity. Different curves represent different volume fractions, as shown in the legend.

average over particles within a bin j. Conducting the average within radial bins ensures that the average excess kurtosis will vanish at times small enough to observe short-time diffusion. Similarly, the average excess kurtosis in the perpendicular direction is

$$\alpha_\perp = \frac{\sum_j^{n_{tot}} < r_{\perp,j}^4 >}{\sum_j^{n_{tot}} 3 < r_{\perp,j}^2 >^2} - 1. \tag{5.18}$$

The average excess kurtosis in the radial direction is plotted as a function of lag time in figure 5.11 for a particle-to-cavity relative size of 1.5/10. Several curves are shown, representing the range of volume fractions $0.05 \leq \phi \leq 0.4$. In figure 5.11(a) the average radial excess kurtosis is vanishingly small at early times, that is, particle motion is primarily diffusive. With increasing lag time, the average radial excess kurtosis increases, suggesting that large displacements along the radial direction take place. A maximum is reached at intermediate times, after which the average radial excess kurtosis decreases towards a long-time plateau as particles sample the extent of the domain. The time required

for the average radial excess kurtosis to cross over from positive to negative increases with volume fraction. This suggests structural rearrangements become slower as crowding increases.

In figure 5.11(b) the average perpendicular excess kurtosis is plotted and again shown to be vanishingly small at early times where particle motion is diffusive. However, in contrast to the average radial excess kurtosis, for volume fractions $0.05 \leq \phi \leq 0.2$ the average perpendicular excess kurtosis does not increase to positive values; it remains vanishingly small and only becomes negative as particle dynamics approach the long-time plateau.

These results suggests that cage hopping events occur mainly along the radial direction for this range of volume fractions. In a biophysical system, such behaviors could allow particles to sample their environment more rapidly along the radial direction, an effect that would act to mitigate the hydrodynamic hindrance of the cavity surface. At higher volume fractions, $0.25 \leq \phi \leq 0.4$, the average perpendicular excess kurtosis becomes weakly positive, suggesting larger displacements are favored and cage hopping events occur along the perpendicular direction. However, the weakly positive values indicate that the role of perpendicular displacements is smaller than that of radial displacements, and that radial displacements are more important. Similar to the average radial excess kurtosis, the time required for the average perpendicular excess kurtosis to attain negative values increases with increasing volume fraction, suggesting slower dynamics as crowding increases.

Overall, the average excess kurtosis suggests that, unsurprisingly, the time scale required to escape cages of neighboring particles increases with volume fraction. It also suggests that cage effects from the confining boundary or neigh-

boring particles cause displacements along the radial direction to become larger, while having little effect on structural rearrangements along the perpendicular direction. These anisotropic long-time particle dynamics pose interesting questions for microconfined systems. For example, in the crowded environment of the cell interior, cage rearrangements occurring mainly along the radial direction could mitigate hydrodynamic hindrance from the surface of the cell membrane or a cellular micro-compartment, allowing particles to better explore their surroundings. Another example are the relaxation processes taking place during the formation of photonic balls [92, 165], where volume fraction is increased via a reduction of the radius of a spherical boundary.

5.2 Conclusions

We have studied the short- and long-time transport properties of concentrated, spherically confined colloidal suspensions for a range of particle-to-cavity relative sizes, finding that the hydrodynamic and entropic effects of confinement exert a qualitative impact on self-diffusion and micro-structure. At short times, diffusion in the 3D-confined domain is anisotropic and dependent on particle distance from the cavity center. As volume fraction increases, boundary- and concentration-induced spatial heterogeneity in particle concentration causes radial undulations in short-time diffusion. Confinement hinders short-time diffusion and such hindrance depends on particle-to-cavity relative size, volume fraction and radial position inside the spherical cavity. The ordered dynamical heterogeneity seen here could also promote particle self-organization based on self-mobility, which may have important implications in biophysical systems.

To account for confinement effects in particle tracking experiments, we propose a radial binning technique and decomposition of particle displacements into an orthogonal basis. The technique was tested by conducting 'numerical experiments', where particle displacements and positions are tracked throughout simulation an utilized to calculate short-time diffusion coefficients by computing mean-square displacement in directions along and perpendicular to the cavity radius. The method was found to accurately reproduce short-time diffusion coefficients obtained from the ensemble-averaged mobility, and illustrates the importance of selection of the lag time interval.

Long-time transport behavior was studied utilizing a spatially averaged mean-square displacement. No long-time self-diffusive regime exists in the confined domain; particle mean-square displacement instead reaches a plateau at long times. With increasing volume fraction, particles require a longer time to reach the long-time plateau, suggesting that long-time dynamics become slower as crowding increases. Caging effects were found to arise both from the cavity and other particles and, at moderate to high concentration, anomalous diffusion is observed, with superdiffusive and subdiffusive behaviors along the radial and perpendicular directions, respectively. The average excess kurtosis along the radial direction revealed that large displacements are favored in this direction as particles undergo cage hopping. In contrast, the average perpendicular excess kurtosis suggests small changes in the statistics of displacements along the perpendicular direction. The average excess kurtosis in both the radial and perpendicular directions was found to reach a long-time plateau as particles sample the domain extent. Overall, cage-hopping dynamics are primarily radial; perpendicular motion is less important for cage hopping events.

These confinement-induced effects answer some open questions and also pose interesting new ones relevant to confined biophysical transport. We have shown here that hydrodynamic coupling to the spherical boundary strongly hinders particle motion as particle-to-cavity relative size increases in concentrated suspensions. Our finding explains the observation of a 'finite size effect' observed in the experimental measurements of [77], wherein particle motion in a bidisperse concentrated suspension confined inside a high surface tension droplet was strongly hindered with decreasing particle-to-cavity relative size. This led the authors to hypothesize motion was perhaps slowed by the more pronounced curvature of smaller droplets. Results presented here suggest the motion of large particles is slowed primarily by stronger hydrodynamic coupling with the cavity wall. We also show that in concentrated suspensions of freely diffusing hydrodynamically interacting hard spheres, the presence of 3D confinement leads to mean-square displacement with an anomalous temporal growth. In addition, this long-time anomalous transport is anisotropic. This makes it clear that experimental measurements reporting anomalous transport in micro-confined biophysical systems [118, 173] require careful consideration of the particle-to-cavity relative size to address the role of the boundary. Now that we have shown that the role of particle-to-cavity size ratio is important, and quantified its effects, it opens new questions; for example, the particle-to-cavity relative size of some intracellular particles [170] changes during cellular processes such as cell division, which will qualitatively change particle transport due to confinement effects. How such changes in transport properties affect cellular processes remains an open question, but the idea that such sizes are tied to cell changes is an emergent area of study. Although many particle-tracking experiments have been conducted inside cells [153, 43, 78, 160] the particle-to-

cavity relative size of the tracked particle is seldom reported nor is the mean-square displacement projected through the most physically relevant orthogonal basis, which may mask important anisotropic behaviors that can explain difficulties in transport of e.g. DNA therapy vectors. Future modeling work in this area must also incorporate more detailed architecture, such as size polydispersity, spheroids and slender-bodies to model organelles and the cytoskeleton, deformable and slippery surface conditions, and active motion. Going forward it is clear that any such modeling must account for many-body hydrodynamic and lubrication interactions and a confining boundary.

Acknowledgements

This work was supported in part by the National Science Foundation Graduate Research Fellowship Grant No. DGE-0707428.

CHAPTER 6

HYDRODYNAMIC ENTRAINMENT IN SPHERICALLY CONFINED SUSPENSIONS

As seen in chapters 4 and 5, the combined effects of crowding and hydrodynamic interactions in a spherically confined domain exert a pronounced influence on the short- and long-time transport properties of particles in colloidal dispersions. Central to such behavior is how crowding and the presence of the boundary alter inter-particle hydrodynamic interactions — i.e. the effect of the boundary on self and entrained motion. In hard-sphere colloidal dispersions, self and entrained motion are given by the hydrodynamic mobility tensors. As discussed in chapter 2, determination of hydrodynamic mobilities tensors traditionally focused on solving the Stokes equations for a pair of no-slip surfaces. Extension of such calculations to include the effect of three or more particles renders the problem intractable when using traditional approaches (e.g. twin-multipole expansions, method of reflections, etc.). Although some methods have been developed to handle such many-body problems analytically[121], the complexity of the resulting equations limits their application.

Recent work has leveraged computational approaches to determine the hydrodynamic coupling between a pair of particles in suspensions near the presence of a confining boundary or at finite concentrations in an unbound domain while accounting for both many-body and lubrication hydrodynamic interactions. Of particular interest in such studies is whether confinement, crowding, or other features of the suspension result in the screening of hydrodynamic interactions. Here, screening of hydrodynamic interactions is defined as a faster decay of hydrodynamic interactions with inter-particle separation distance r,

as compared to the slow $1/r$ decay obtained for a pair of particles in an unbound domain. To study the effect of planar wall confinement on pair entrainment, Lele et al. (2011) [112] utilized experiments and Stokesian dynamic simulations to determine the hydrodynamic mobility between a single particle and a nearby hexagonal cluster of particles. They observed a faster decay of hydrodynamic entrainment as a function of inter-particle separation distance, suggesting confinement can weaken hydrodynamic interactions. More recently, Zia et al. [180, 152] utilized Accelerated Stokesian Dynamics[147] simulations to determine an effective concentrated pair mobility for particles immersed in a concentrated suspension. Their goal was to determine whether crowding, or increasing particle concentrations, led to a screening of hydrodynamic interactions. Of particular interested was whether crowding caused hydrodynamic interactions to be Brinkmann-screened, i.e. to exhibit a decay with inter-particle separation that scaled as $1/r^3$. The authors found that crowding led to an $O(1)$ suppression of particle entrainment, but did not result in hydrodynamic screening. That is, hydrodynamic entrainment was suppressed by crowding but found to decay as $1/r$ for widely separated particles for all the concentrations considered in the study. Although previous studies have focused separately on the effects of confinement and concentration on particle entrainment, their combined effects have not been studied. Here, we study the combined effects of crowding and confinement on particle entrainment by utilizing our simulation method for spherically confined colloidal suspensions.

In an unbound suspension, the interactions between a pair of spherical particles can be resolved by projecting the mobility into two orthogonal components. One component projects the forces and velocities onto a direction along the line of centers between the particles. The other, projects forces and velocities in a

direction perpendicular to the line of centers between the particles. However, as discussed in section 3.3, in a spherically confined domain two components are insufficient to fully specify the mobility matrix. As a pair of particles interact in the confined domain, reflected interactions from the cavity wall give rise to couplings between forces along (perpendicular to) the line of centers and motion perpendicular to (along) the line of centers. The consequence of such interactions is that five components are required to fully specify the hydrodynamic mobility (cf. equation 3.9). To compare hydrodynamic interactions in confined suspensions to those of unbound suspensions, we will define scalar quantities that couple a force along or perpendicular to the line of centers to the velocity in the same direction. For a force and velocity lying along the line of center between the particles we obtain,

$$x^a_{\alpha\beta} \equiv \hat{\boldsymbol{r}} \cdot \boldsymbol{M}^{UF,\alpha\beta} \cdot \hat{\boldsymbol{r}} = x^{A1}_{\alpha\beta} + x^{A5}_{\alpha\beta}. \tag{6.1}$$

In contrast, for a force and velocity lying perpendicular to the line of center between the particles we obtain,

$$y^a_{\alpha\beta} \equiv \hat{\boldsymbol{r}}^{\perp} \cdot \boldsymbol{M}^{UF,\alpha\beta} \cdot \hat{\boldsymbol{r}}^{\perp} = x^{A4}_{\alpha\beta} + x^{A5}_{\alpha\beta}. \tag{6.2}$$

In the limit $\lambda_c \to 0$, the components defined in equations 6.1 and 6.2 recover the two orthogonal components of the hydrodynamic mobility in unbound suspensions. These two components will thus be utilized to compare hydrodynamic interactions in confined suspensions to those of unbound suspensions. The terms of the concentrated pair mobility coupling a force along the line of center to motion perpendicular to it and vice-versa, i.e. components $x^{A3}_{\alpha\beta}$ and $x^{A4}_{\alpha\beta}$ in equation 3.9, have a small magnitude. As a consequence the value of each component in concentrated suspensions is of the same order as the simulation noise. Discussion of these components is thus left to appendix C.4.

In this chapter, we utilize our simulation method for spherically confined, hydrodynamically interacting particles (developed in chapter 4) to study the combined effects of confinement and crowding on the self and entrained motion of spherically confined particles. The stochastic technique discussed in section 3.3 is utilized to determine both the self and entrained concentrated pair mobility. This chapter is organized as follows. The self and entrained concentrated pair mobility along the line of centers between the particles is discussed in section 6.1. In section 6.2, we discuss the behavior of the perpendicular components of the concentrated pair mobility. We conclude the chapter with a discussion in section 6.3.

6.1 Entrainment along the line of centers

In colloidal dispersions with hydrodynamic interactions, a forced particle will propagate a velocity disturbance which entrains other suspension particles. The motion of the entrained particles will, in turn, propagate disturbances which alters the motion of all other particles. An infinite number of such reflected interactions propagate instantaneously throughout the fluid, the effect of which is captured by the hydrodynamic mobility. To study the combined effects of crowding and confinement on such interactions, we determine the concentrated pair mobility in spherically confined suspensions. We begin by projecting the concentrated pair mobility in the spherically confined domain along the particle line of centers utilizing equation 6.1. This component is then studied as a function of inter-particle separation distance, while maintaining both particles at the same distance to the cavity wall. Figure 6.1(a) illustrates the system of interest, where a pair of particles (labeled in red) increase their

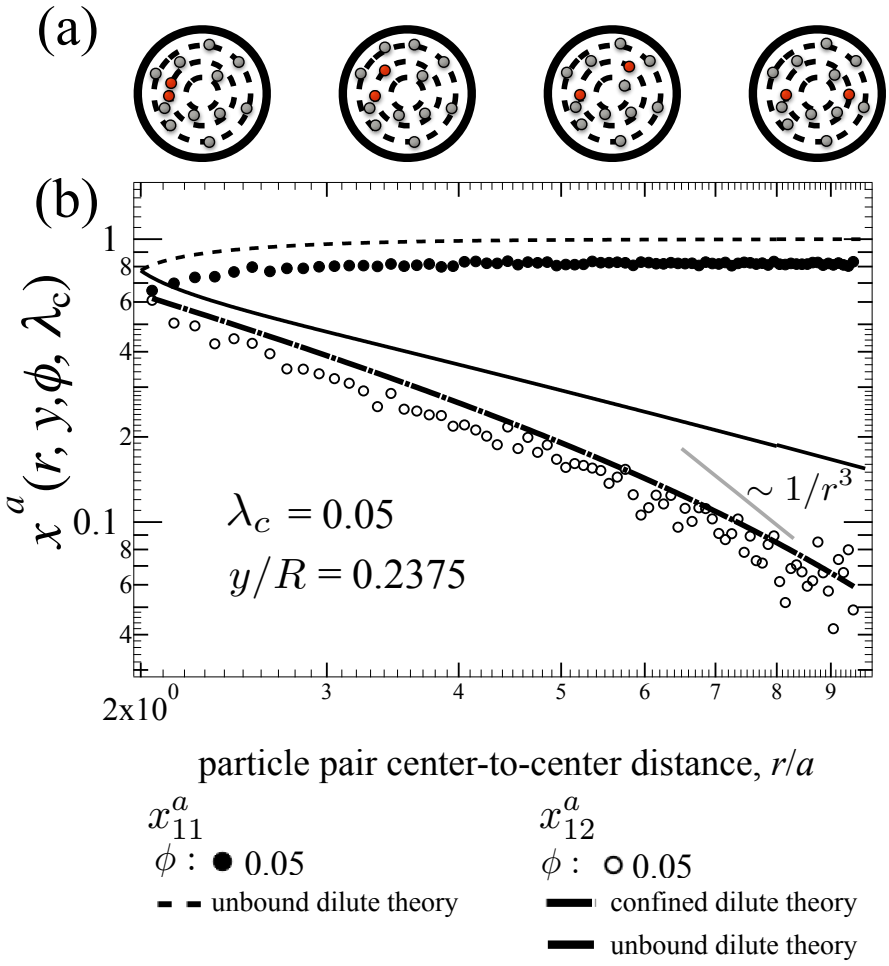

Figure 6.1: Self and entrained concentrated pair mobility along the line of centers for spherically confined particles in a dilute suspension as a function of particle separation distance for particles close to the cavity center. The dashed and solid lines correspond to the self and entrained pair mobility for a pair of unbound particles as determined by Jeffrey and Onishi (1984) [82].

separation distance from left to right, while maintaining the same distance to the cavity wall.

In figure 6.1(b) the concentrated mobility along the line of center between the particles is plotted as a function of inter-particle separation for particles that are 1/20 the cavity size. The interacting pair is located near the center, at a normalized distance of $y/R = 0.2375$. The solid and dashed lines represent the self

and entrainment mobility obtained from the dilute theory for a pair of particles in an unbound domain. The dashed-dotted line represents the leading order entrainment mobility obtained from the velocity field Green's function in spherical confinement, and the solid gray line represents a decay with inter-particle separation distance that scales as $1/r^3$. Filled and open symbols represent the concentrated mobility obtained from simulations of a spherically confined suspension at a volume fraction of $\phi = 0.05$. The presence of the confining boundary leads to hindrance of both self, and entrained motion, as evidenced by the lower magnitude of the concentrated pair mobility in the confined domain as compared to the mobility for particles in an unbound domain. Self motion in the confined domain displays a dependence on inter-particle separation that is qualitatively similar to that of unbound suspensions. However, confinement is clearly shown to result in a faster decay of particle entrainment with inter-particle separation, meaning that hydrodynamic interactions are weakened by confinement. Although hydrodynamic interactions are weakened by confinement, no Brinkmann-like screening of hydrodynamic interactinos is observed, given that the decay with inter-particle separation distance is slower than $1/r^3$ for all accessible particle separation distances in figure 6.1(b). Thus, we expect the effect of many-body hydrodynamic interactions to strongly impact particle motion of spherically confined particles immersed in a dilute suspension and located near the cavity center. Next, we consider the effects of crowding on the concentrated mobility of particles near the center of the cavity.

In figure 6.2, the concentrated pair mobility for particles in a spherically confined domain is plotted for suspensions at varying concentrations, as shown in the legend. The suspension contains particles that are 1/20 the cavity size, and the interacting pair is located near the cavity center, at a radial position of

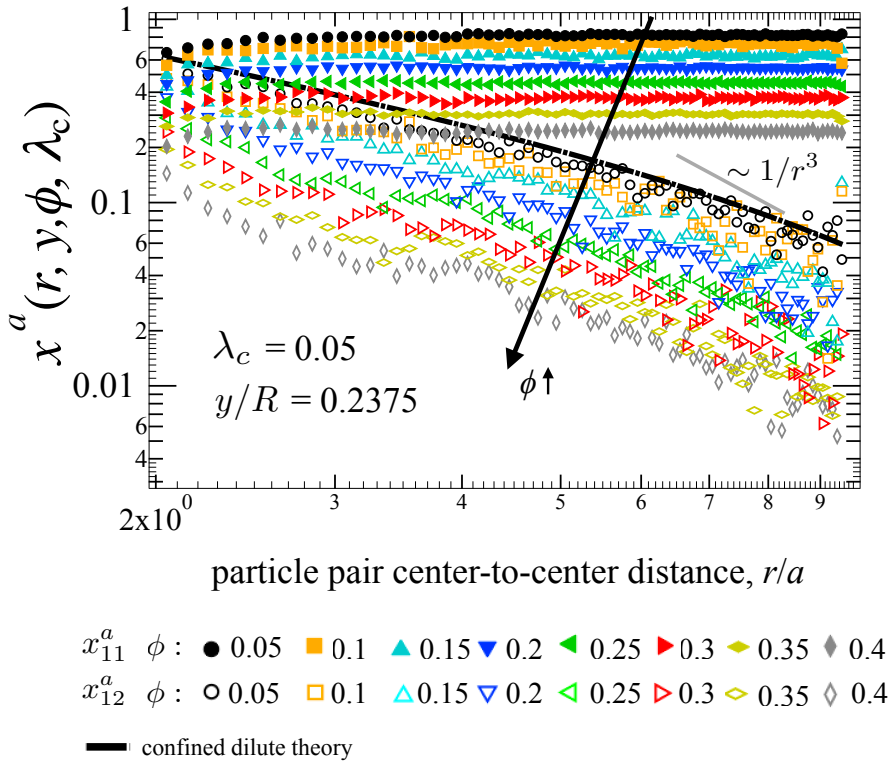

Figure 6.2: Self and entrained concentrated pair mobility along the line of centers for spherically confined particles in suspension of varying concentrations as a function of particle separation distance. The particles are close to the cavity center, and compared to the dilute theory in the confined domain and a scaling of $\sim 1/r^3$.

$y/R = 0.2375$. Filled and open symbols represent the self and entrained mobility of particles in the confined domain. As with figure 6.1, the dashed-dotted line is the leading order entrainment mobility obtained from the velocity Green's function in spherical confinement and the solid gray line represents a decay with inter-particle separation that scales as $1/r^3$. In the confined domain, increasing volume fractions leads only to an $O(1)$ suppression of self and entrained motion, and does not lead to any change in the decay of the hydrodynamic interactions with inter-particle separation distance. As concentration increases, weak undulations are observed in the pair and entrainment mobilites, a consequence of the local liquid like structure of the suspension.

Thus far we have considered particles near the cavity center, demonstrating that for particles 1/20 the cavity size confinement exerts a qualitative influence on particle mobility even for particles far from the cavity wall. We expect confinement to exert a stronger influence on an interacting pair that is closer to the wall, i.e. farther from the cavity center.

In figures 6.3(a), 6.3(b), and 6.3(c), the concentrated mobility for a pair of interacting particles located at $y/R = 0.475$, $y/R = 0.7125$, and $y/R = 0.9025$ are plotted as a function of particle separation distance. Solid and open symbols correspond to the self and entrained mobility, respectively. Various volume fractions are plotted as shown in legend. For particles at equal distance from the wall, their maximum inter-particle separation distance is $2y/a$. Meaning that an interacting pair of particles at a radial position closer to the wall can be found at larger inter-particle separation distances. At locations close to the cavity wall, stronger confinement induced behaviors are observed. The cavity wall further weakens particle entrainment, as evidenced by a faster decay of the concentrated entrainment mobility with inter-particle separation than the one observed in 6.2. For widely separated particles, the decay of hydrodynamic entrainment scales as $\sim 1/r^3$ or faster. This means that Brinkman-like screening of hydrodynamic entrainment can be observed in the confined domain for large interparticle distances. At large interparticle distances, the particles are much closer to the wall than they are to each other, and hydrodynamic interactions with the wall strongly hinder particle motion. Although interactions at large distances can exhibit Brinkmann-like screening, it does not occur throughout the domain, thus many-body hydrodynamic interactions remain important. The self mobility in figure 6.3 decreases for very large particle separations, this is a consequence of particle self motion recovering the short-time self diffusivity

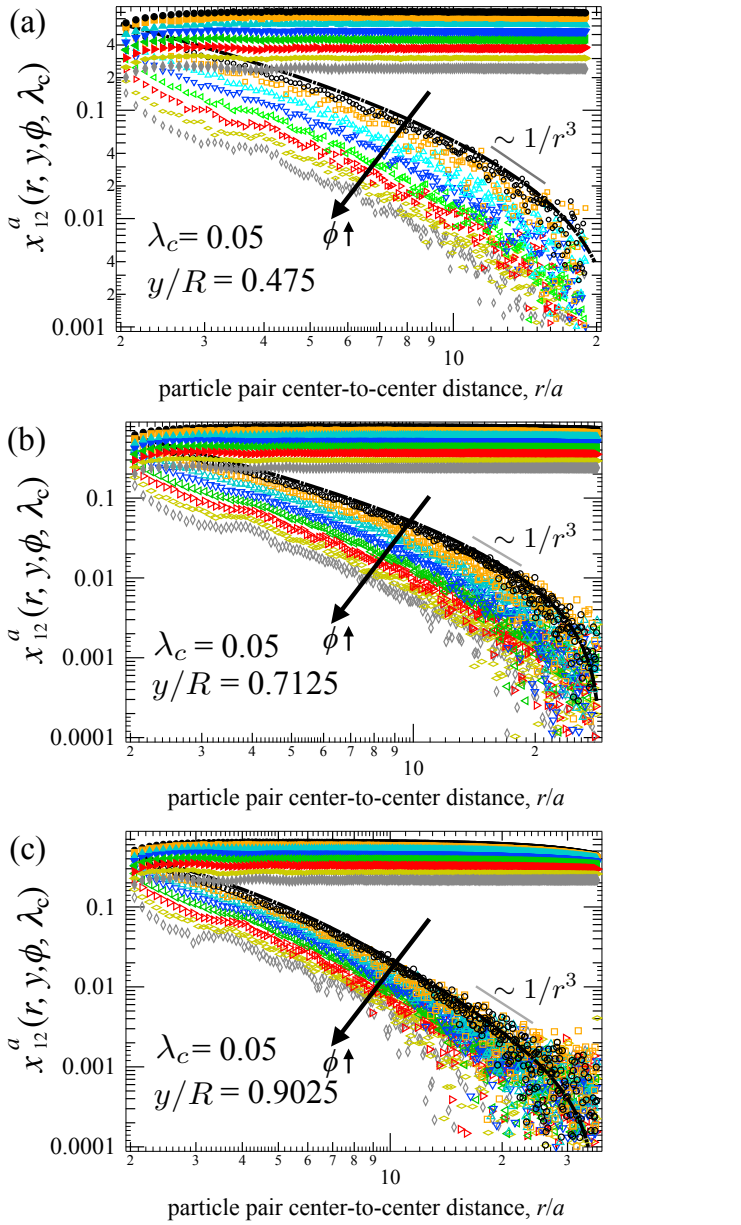

Figure 6.3: Self and entrained concentrated pair mobility along the line of centers for spherically confined particles in suspensions of varying volume fractions as a function of particle separation distance. Particles are at a radial position of (a)y/R = 0.475, (b) y/R = 0.7125, and y/R = 0.9025.

in the limit where the particles are far-apart and the direction along the particle line of centers aligns with the direction along the particle-cavity line of centers.

Overall, crowding leads to an $O(1)$ suppression of entrainment along the line of centers between the particles, whereas confinement leads to a faster decay of entrainment with particle separation distance. Brinkman-like screening is only observed for widely separated particles near the cavity wall, which suggests many-body hydrodynamic interactions are important to model particle motion. Increasing particle size leads to similar qualitative behaviors with more pronounced confinement induced effects, a discussion of such effects is found in C.1. Next, we determine the combined effects of crowding and confinement on the perpendicular concentrated pair mobility.

6.2 Entrainment perpendicular to the line of centers

In unbound suspensions, hydrodynamic interactions between an interacting pair of particles is characterized by a slow $1/r$ decay for interactions along and perpendicular to the line of centers between the particles. That is, the leading order hydrodynamic interaction along and perpendicular to the line of centers differ only by a scalar factor. Similar behavior arises in the pair interaction of particles in concentrated suspensions [180]. In this section, we study the combined effects of crowding and confinement on hydrodynamic entrainment perpendicular to the particle line of centers.

In figure 6.4(a) and 6.4(b) the concentrated pair mobility in the direction perpendicular to the particle line of centers, as given by equation 6.2, is plotted as a function of particle separation distance. In figure 6.4(a), the self (filled symbols)

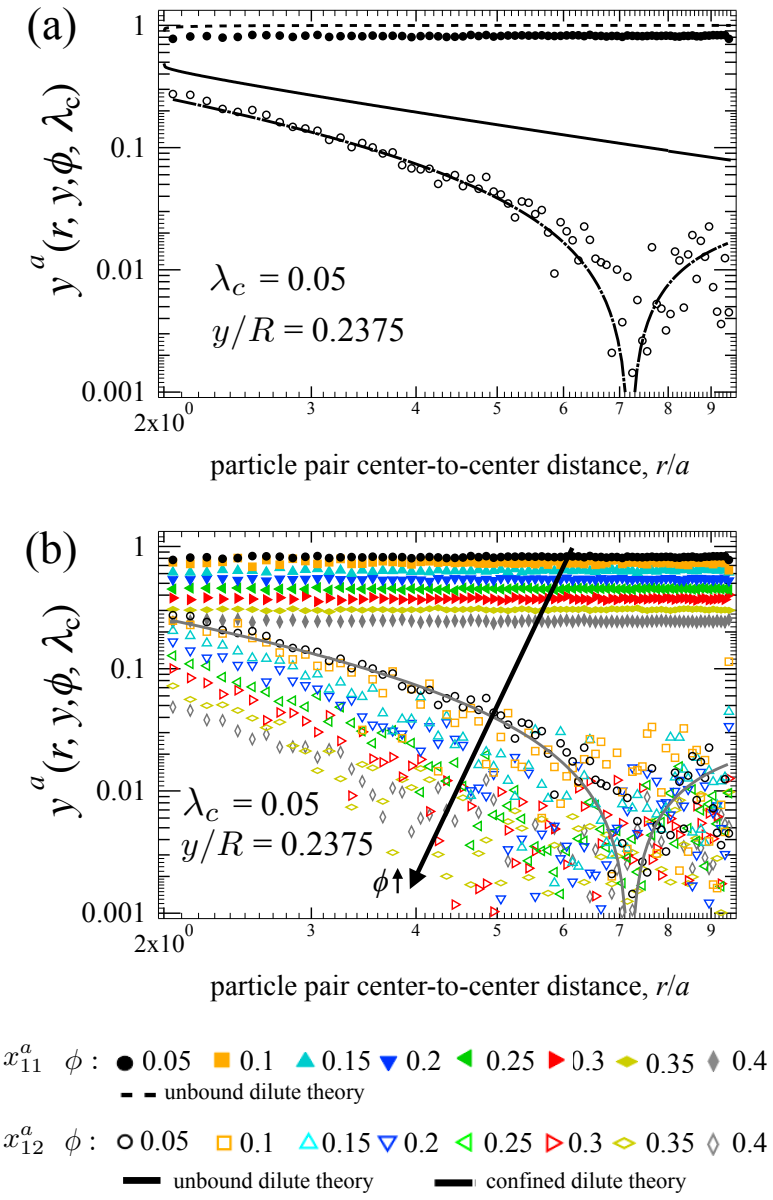

Figure 6.4: Self and entrained concentrated pair mobility perpendicular the line of centers for spherically confined particles in (a) dilute suspensions and (b) suspensions at varying volume fractions. Particles are close to the cavity center.

and entrained (open symbols) concentrated pair mobility in a dilute suspension inside the spherical cavity is compared with the self (dashed line) and entrained (solid line) mobility obtained from the dilute theory for a pair of particles in an unbound domain, and the leading order entrained mobility (dashed-dotted line) obtained from the velocity field Green's function in spherical confinement. The particles in the suspension are $1/20$ the cavity size and are located near the cavity center, at a radial position of $y/R = 0.2375$. As show in the figure, both self and entrained motion are hindered by the presence of the confining boundary. The decay of hydrodynamic interactions with particle separation distance along this direction is faster as compared to that of a pair of unbound particles (solid black line) and that of entrainment along their line of centers (cf. figure 6.1). For widely separated particles, the leading order entrainment mobility based on the spherically confined Green's function predicts a sign change of the mobility, shown in this log-log plot as a dip in the mobility at a separation distance of $r/a \sim 7$. However, due to the small magnitude of the mobility at locations close to $r/a \sim 7$, poor 'signal-to-noise' ratio does not allow us to conclude whether the concentrate pair mobility follows this trend. The small magnitude of the mobility, combined with poor sampling near the cavity center due to the small volume of bins near the center, leads to a poor 'singal-to-noise' ratio for widely separated particles near the cavity center. As will be shown in figure 6.2, where the interacting pair is far from the center and thus better sampling is obtained, the presence of the confining boundary does lead to a change in sign of the concentrated pair mobility along the perpendicular direction. This change in sign is in turn predicted by the spherically confined Green's function. This suggests that in figure 6.4(b), the sign change does occur in the concentrated pair mobilities, but is not discernible due to the numerical difficulties at this posi-

tion. As with the mobility along the line of centers, crowding does not cause a change in the decay of particle entrainment along the perpendicular direction with particle separation distance, it only leads to an $O(1)$ suppression of particle entrainment. Having demonstrated the effects of crowding and confinement on particles near the cavity center, we consider now such effects for particles closer to the cavity wall.

In figure 6.5(a), 6.5(b), and 6.5(c), the concentrated pair mobility perpendicular to the particle line of centers is plotted as a function of particle separation distance for particles at a radial position of $y/R = 0.475$, $y/R = 0.7125$, and $y/R = 0.9025$, respectively. As with figure 6.4, particles are 1/20 the cavity size, and various volume fractions are plotted as shown in the legend. The dashed-dotted line is the leading order entrained mobility as given by the Green's function in spherical confinement at the specified position. As with entrainment parallel to the particle line of centers, proximity to the wall leads to a faster decay of entrainment with particle separation distance as compared to the mobility of particles near the center. Perhaps more interesting is that the concentrated pair mobility perpendicular to the particle line of centers undergoes a sign change at a particle separation distance that is dependent on the radial position of the particles. For particles close together (far left of the horizonthal axis in figure 6.5) an entrained particle will move in the same direction as the forced particle because the disturbance flow propagated by the forced particle moves in the same direction. This behavior is qualitatively similar to that of particle in an unbound domain. However, inside the spherical cavity, there must be regions where the velocity field propagated by the forced particle travels in the opposite direction, i.e. regions of flow recirculation must be present in order to satisfy conservation of mass. Widely separated particles access such regions inside the spherical cav-

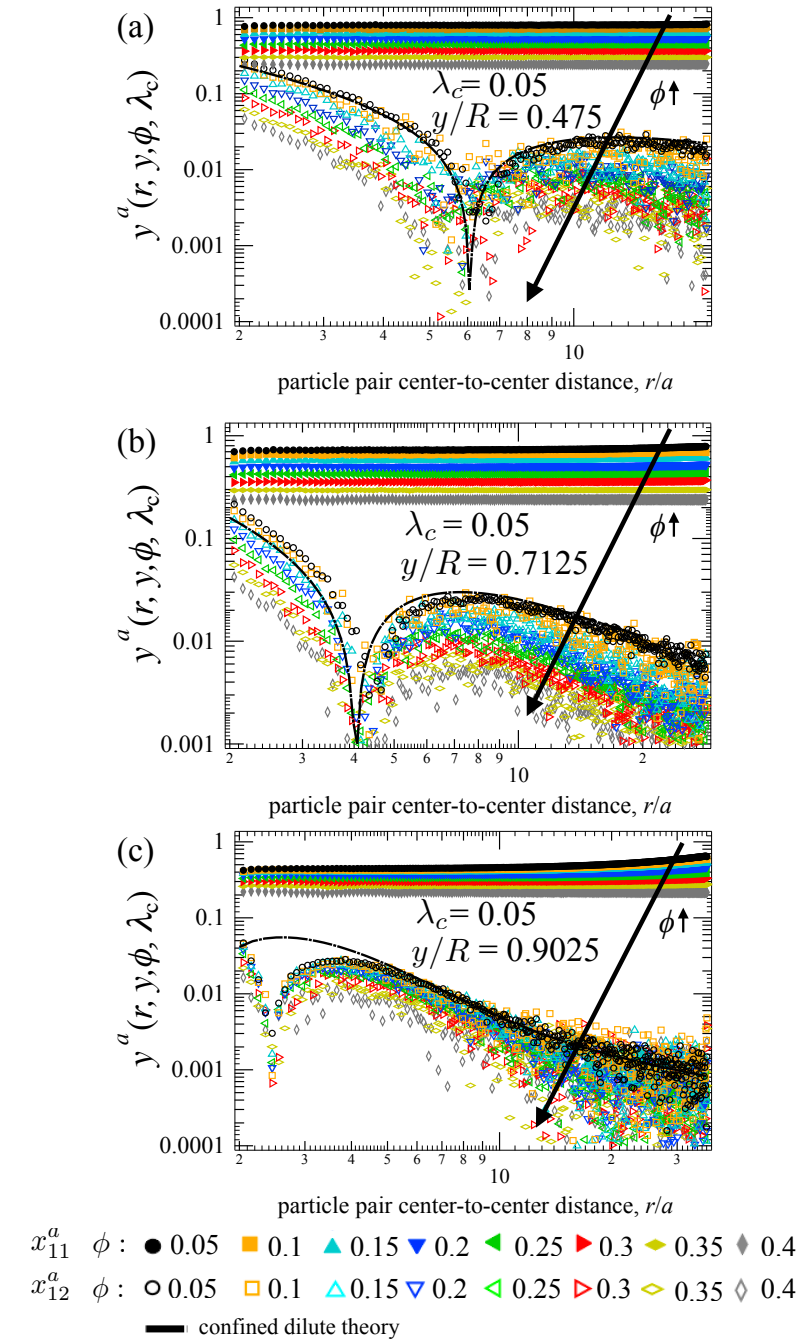

Figure 6.5: Self and entrained concentrated pair mobility perpendicular to the line of centers for spherically confined particles in suspensions of varying volume fractions as a function of particle separation distance. Particles are at a radial position of (a)y/R = 0.475, (b) y/R = 0.7125, and y/R = 0.9025.

ity, and can then move in a direction opposite that of the forced particle as they are entrained. The location of regions of flow recirculation varies with the radial position of the forced particle inside the spherical cavity (cf. figure 4.4), whicn in turn causes the particle separation at which the concentrated perpendicular mobility changes sign to change with proximity to the cavity wall. The separation distance at which the sign change occurs can be predicted by utilizing the leading order entrainment obtained from the Green's function in spherical confinement when the particle pair is not too close to the cavity wall, e.g. radial positions $y/R = 0.475$ and $y/R = 0.97125$ in figures 6.5(a) and 6.5(b), respectively. For particles very close to the wall, e.g. the radial position of $y/R = 0.9025$ in figure 6.5(c), the leading order entrainment obtained from the spherically confined Green's function predicts a negative mobility at wide separations, but not a sign change for particles that are close together. A failure to predict the behavior for particles that are both close together and close to the cavity wall is expected. This is because the Green's function approximation is most accurate in the limit where particle disturbances are felt by each other and by the cavity as point, i.e. at locations where particles are widely separated and near the center of the cavity.

Overall, as with entrainment along the particle line of centers, crowding leads to an $O(1)$ suppression of particle entrainment in the direction perpendicular to the particle line of centers. However, 3D confinement exerts a pronounced influence on particle entrainment in the perpendicular direction. Confinement leads to a faster decay of perpendicular hydrodynamic entrainment with particle separation distance. Confinement also leads to a reversal of particle entrainment as particles become widely separated, a consequence of regions of recirculating flow inside the spherical cavity.

6.3 Conclusions

We have studied the combined effects of crowding and confinement on the hydrodynamic entrainment of particles in spherically confined suspensions. It was shown that confinement induces a faster decay of hydrodynamic entrainment along the line of centers between the particles, and that the faster decay varies with the position of the interacting pair inside the spherical cavity. Crowding only leads to an $O(1)$ suppression of entrainment along this direction. Although entrainment along the line of centers in the confined domain has a decay faster than $1/r$, in general this weakening does not induce a Brinkmann-like screening of hydrodynamic interactions (i.e. the decay is slower than $1/r^3$). Only particles that are both widely separated and near the cavity wall exhibit a Brinkmann-like screening, with hydrodynamic entrainment decaying as $1/r^3$ or faster.

As with entrainment along the particle line of centers, crowding only leads to an $O(1)$ suppression of entrainment in the perpendicular direction. Confinement induces a sign change in the concentrated pair mobility along the perpendicular direction, and the particle separation distance at which the sign change occurs depends on the distance of the particle pair to the cavity center. This behavior is a consequence of regions of recirculating flow inside the spherical cavity, resulting in a reversal of particle motion.

Since crowding results only in an $O(1)$ suppression of entrainment, the decay of the entrainment mobility with particle separation distance is also well predicted by the leading order entrainment obtained from the velocity field Green's function in spherical confinement. This suggests that in a confined domain,

methods which aim to infer properties from particle correlations should account for the effect of confinement. For example, in two-point microrheology[41], the rheological properties of a material are inferred by tracking the motion of a pair of particles and utilizing it to determine particle correlations as a function of their separation distance and lag time interval. The dependence of the correlations on particle separation distance is assumed to follow the velocity field Green's function of a particle in an unbound domain. This permits the definition of a constant effective mean square displacement by scaling correlations on the unbound Green's function. The constant effective mean-square displacement is then utilized in the Generalized Stokes-Einstein relation to infer rheological properties of the material. This method has been utilized to infer rheological properties in the interior of cells[67], which are confined by a cell membrane. However, the results presented here suggest that in these microconfined systems, care must be taken when considering widely separated particles inside of a cell, as the dependence of particle correlations on particle separation distance will be given by the confined Green's function. This effect should be accounted for in such experiments.

APPENDIX A

CHAPTER 4 APPENDIX: CAVITY CONTRIBUTION TO THE GRAND MOBILITY MATRIX

In this appendix we list the contribution of the spherical cavity to all of the components of the grand mobility matrix required to carry out simulations of hydrodynamically interacting particles confined inside a spherical no-slip boundary. Note that the mobilities corresponding to the diagonal and upper blocks of the grand mobility matrix (UF, UL, US, ΩL, ΩS, ES) are listed since the remaining terms may be obtained by an appropriate transposition.

A.1 Self-Mobilities

The far-field self-mobilities of a particle inside a spherical cavity are listed for all the components of the grand mobility matrix. y is the magnitude of the position vector of the particle in a coordinate system whose origin lies at the center of the spherical cavity.

$$
\begin{aligned}
6\pi\eta a M^{UF,c}_{ij,\alpha\alpha} = &\left\{\left(\frac{a}{R}\right)\left[(9)/(4(-1+y^2))\right] + \left(\frac{a}{R}\right)^3\left[-(3y^2+5)/(2\left(-1+y^2\right)^3)\right] + \right. \\
&\left.\left(\frac{a}{R}\right)^5\left[(5+10y^2+y^4)/(4(-1+y^2)^5)\right]\right\}\hat{y}_i\hat{y}_j + \\
&\left\{\left(\frac{a}{R}\right)\left[(9(4-3y^2+y^4))/(16(-1+y^2))\right] + \right. \\
&\left(\frac{a}{R}\right)^3\left[(-20+21y^2-12y^4+3y^6)/(8(-1+y^2)^3)\right] + \\
&\left.\left(\frac{a}{R}\right)^5\left[(20+5y^2+11y^4-5y^6+y^8)/(16(-1+y^2)^5)\right]\right\}(\delta_{ij}-\hat{y}_i\hat{y}_j) \qquad \text{(A.1a)}
\end{aligned}
$$

$$6\pi\eta a^2 M^{UL,c}_{ij,\alpha\alpha} = \left\{ \left(\frac{a}{R}\right)^2 \left[(9y(-2+y^2))/(16(-1+y^2))\right] + \left(\frac{a}{R}\right)^4 \left[(3y(-10+5y^2-4y^4+y^6))/(16(-1+y^2)^4)\right] + \right\} \hat{y}_s \epsilon_{ijs} \qquad \text{(A.2a)}$$

$$6\pi\eta a^3 M^{\Omega L,c}_{ij,\alpha\alpha} = \left\{ \left(\frac{a}{R}\right)^3 \left[3/(4(-1+y^2)^3)\right] \right\} \hat{y}_i \hat{y}_j + \left\{ \left(\frac{a}{R}\right)^3 \left[3(4+12y^2-9y^4+3y^6)/(16(-1+y^2)^3)\right] \right\} (\delta_{ij} - \hat{y}_i \hat{y}_j) \qquad \text{(A.3a)}$$

$$\begin{aligned} 6\pi\eta a^2 M^{US,c}_{ijn,\alpha\alpha} = & \left\{ \left(\frac{a}{R}\right)^2 \left[-(27y)/(8(-1+y^2)^2)\right] + \right. \\ & \left(\frac{a}{R}\right)^4 \left[(9y(23+7y^2))/(20(-1+y^2)^4)\right] + \\ & \left. \left(\frac{a}{R}\right)^6 \left[-(9y(35+42y^2+3y^4))/(40(-1+y^2)^6)\right] \right\} \hat{y}_i (\delta_{jn} - \frac{1}{3}\hat{y}_j \hat{y}_n) + \\ & \left\{ \left(\frac{a}{R}\right)^2 \left[(9y(-3+y^2))/(16(-1+y^2)^2)\right] + \right. \\ & \left(\frac{a}{R}\right)^4 \left[-(3y(-138+59y^2-20y^4+3y^6))/(80(-1+y^2)^4)\right] + \\ & \left. \left(\frac{a}{R}\right)^6 \left[-(3y(105+42y^2+18y^4-6y^6+y^8))/(80(-1+y^2)^6)\right] \right\} (\delta_{ij}\hat{y}_n + \delta_{in}\hat{y}_j - 2\hat{y}_i\hat{y}_j\hat{y}_n) \end{aligned} \qquad \text{(A.4a)}$$

$$\begin{aligned} 6\pi\eta a^3 M^{\Omega S,c}_{ijn,\alpha\alpha} = & \left\{ \left(\frac{a}{R}\right)^3 \left[(9y^2(-3+y^2))/(16(-1+y^2)^3)\right] + \right. \\ & \left. \left(\frac{a}{R}\right)^5 \left[-(9y^2(-35+7y^2-5y^4+y^6))/(80(-1+y^2)^5)\right] \right\} (\delta_{ns}\hat{y}_m\hat{y}_j + \delta_{sj}\hat{y}_m\hat{y}_n)\epsilon_{ims} \end{aligned} \qquad \text{(A.5a)}$$

$$
\begin{aligned}
6\pi\eta a^3 M^{ES,c}_{mklr,\alpha\alpha} =& \left\{ \left(\frac{a}{R}\right)^3 \left[27(5+3y^2)/(16(-1+y^2)^3)\right] + \right. \\
& \left(\frac{a}{R}\right)^5 \left[-81(7+22y^2+3y^4)/(40(-1+y^2)^5)\right] + \\
& \left.\left(\frac{a}{R}\right)^7 \left[81(35+259y^2+177y^4+9y^6)/(400(-1+y^2)^7)\right]\right\} (\hat{y}_m\hat{y}_k - \frac{1}{3}\delta_{mk})(\hat{y}_l\hat{y}_r - \frac{1}{3}\delta_{li}) + \\
& \left\{ \left(\frac{a}{R}\right)^3 \left[(9(5+y^2))/(16(-1+y^2)^3)\right] + \left(\frac{a}{R}\right)^5 \left[-9(21+47y^2-5y^4+y^6)/(40(-1+y^2)^5)\right] + \right. \\
& \left.\left(\frac{a}{R}\right)^7 \left[9(105+609y^2+222y^4+30y^6-7y^8+y^{10})/(400(-1+y^2)^7)\right]\right\} (\delta_{ml}\hat{y}_k\hat{y}_r + \delta_{mr}\hat{y}_k\hat{y}_l + \\
& \delta_{kl}\hat{y}_m\hat{y}_r + \delta_{kr}\hat{y}_m\hat{y}_l + -4\hat{y}_m\hat{y}_l\hat{y}_k\hat{y}_r) + \left\{ \left(\frac{a}{R}\right)^3 \left[-(9(-10+10y^2-5y^4+y^6))/(32(-1+y^2)^3)\right] + \right. \\
& \left(\frac{a}{R}\right)^5 \left[-9(42-20y^2+15y^4-6y^6+y^8)/(80(-1+y^2)^5)\right] + \\
& \left.\left(\frac{a}{R}\right)^7 \left[9(210+210y^2+75y^4-21y^6+7y^8-y^{10})/(800(-1+y^2)^7)\right]\right\} (\delta_{ml}\delta_{kr} + \delta_{mr}\delta_{kl} - \\
& \delta_{ml}\hat{y}_k\hat{y}_r - \delta_{mr}\hat{y}_k\hat{y}_l - \delta_{kl}\hat{y}_m\hat{y}_r - \delta_{kr}\hat{y}_m\hat{y}_l + \hat{y}_m\hat{y}_k\hat{y}_r\hat{y}_l - \delta_{lr}\delta_{km} + \delta_{km}\hat{y}_l\hat{y}_r + \delta_{lr}\hat{y}_m\hat{y}_k)
\end{aligned}
\tag{A.6a}
$$

A.2 Entraiment Mobilities

The far-field entrainment mobilities for particles inside a spherical cavity are listed for all of the components of the grand mobility matrix. Here $\zeta = y^{-1}\sqrt{1-2bxy+y^2}$, where ζ is the distance of the entrained particle to the image point of the forced particle.

$$
6\pi\eta a M^{UF,c}_{ij,\beta\alpha} = M^{UF,c}_1 \hat{y}_i\hat{y}_j + M^{UF,c}_2 \hat{y}_i\hat{y}^{\perp}_j + M^{UF,c}_3 \hat{y}^{\perp}_i\hat{y}_j + M^{UF,c}_4 \hat{y}^{\perp}_i\hat{y}^{\perp}_j + M^{UF,c}_5 \delta_{ij} \tag{A.7a}
$$

$$
M^{UF,c}_1 = \left(\frac{a}{R}\right)\left[(3(-6+2y^2-4bxy(-5+y^2)-(1+b^2)x^4y^2(-1+3y^2)+4bx^3y(-2+b^2\right.
$$

$$+ 5y^2) - x^2(-4 + 9y^2 + y^4 + b^2(2 + 19y^2 - 3y^4))))/(8y^5\zeta^5)$$

$$- (3(4b^3x^2y^2 + b^2xy(3 - 5y^2 + x^2(-5 + 3y^2)) + xy(6 - 4y^2 + 3x^4y^2(-1 + y^2)$$

$$+ x^2(-4 + 9y^2 - 3y^4)) + b(3(-1 + y^2) - 9x^4y^2(-1 + y^2) + x^2(3 - 16y^2$$

$$+ 9y^4))))/(8(-1 + b^2)xy^4\zeta^3) + (9b(-1 + x^2)(-1 + y^2)(-1 + 2bxy$$

$$- x^2y^2))/(8(-1 + b^2)xy^3\zeta^2)\Big] +$$

$$\left(\frac{a}{R}\right)^3 \Big[(3(4b^5x^4y^2(-1 + 2(-2 + x^2)y^2 + y^4) + b^4x^3y(2 + (34 - 7x^2)y^2 + (-7 - 2x^2 +$$

$$x^4)y^4 + 3x^2y^6) + 2b^3x^2y^2(-14 + 3y^2 - 3x^4y^2 + x^2(7 - 2y^2$$

$$+ y^4)) - xy^3(2 + x^8y^4 + 2x^2(-12 + 7y^2) + x^6y^2(5 - 2y^2 + y^4) + x^4(14 - 6y^2$$

$$+ 3y^4)) - b^2xy(-14 + 5y^2 + 17x^6y^4 + x^2(9 - 12y^2 + 14y^4) + x^4y^2(14 - 38y^2 + 21y^4))$$

$$+ b(-2 + y^2 + 7x^8y^6 + x^6y^4(33 - 14y^2 + 7y^4) + x^2(1 - 14y^2 + 15y^4)$$

$$+ x^4y^2(11 - 50y^2 + 29y^4))))/(8(-1 + b^2)xy^8\zeta^7) + (3b(-2 + x^2$$

$$+ y^2)(-1 + 2bxy - x^2y^2)^3)/(8(-1 + b^2)xy^7\zeta^6)\Big] +$$

$$\left(\frac{a}{R}\right)^5 \Big[(-10 + 81x^2y^2 - 48x^4y^4 - 32b^4x^4y^4 + x^6y^6 - 3b^2x^2y^2(21 - 46x^2y^2$$

$$+ x^4y^4) + 4bxy(5 - 36x^2y^2 + 9x^4y^4) + b^3(72x^3y^3 - 48x^5y^5))/(8y^9\zeta^9) +$$

$$(24b^3x^4y^4 + b^2(3xy - 42x^3y^3 - 17x^5y^5) - xy(10 - 7x^2y^2$$

$$+ 4x^4y^4 + x^6y^6) + b(1 + 21x^2y^2 + 11x^4y^4 + 7x^6y^6))/(8(-1 + b^2)xy^8\zeta^7)$$

$$+ (b(-1 + 2bxy - x^2y^2)^3)/(8(-1 + b^2)xy^7\zeta^6)\Big] \qquad \text{(A.7b)}$$

$$M_2^{UF,c} = \left(\frac{a}{R}\right)\Big[- (9(-1 + x^2)(-1 + y^2))/(8(1 - b^2)^{1/2}xy) - (3(3(-1 + y^2) - 15bxy(-1$$

$$+ y^2) - 15b^2x^6y^4(-1 + y^2) + 3bx^7y^5(-1 + y^2) + x^2(3 - (5 + 28b^2)y^2$$

$$+ 30b^2y^4) + bx^5y^3(-7 + 12y^2 - 3y^4 + b^2(-23 + 21y^2)) + x^4y^2(4b^4 - 2y^2$$

$$+ b^2(26 - 43y^2 + 15y^4)) - bx^3y(13 - 28y^2 + 9y^4 + b^2(2 - 17y^2$$

$$+ 21y^4))))/(8(1 - b^2)^{1/2}xy^6\zeta^5)\Big] +$$

$$\left(\frac{a}{R}\right)^3 \Big[- (3(-2 + x^2 + y^2))/(8(1 - b^2)^{1/2}xy) + (3(-2 + y^2$$

$$+ 7b^2x^8y^6 - bx^9y^7 - 7bxy(-2 + y^2) - bx^7y^5(4 + 17b^2 - 2y^2 + y^4) + b^2x^6y^4(11 + 24b^2$$

$$- 14y^2 + 7y^4) + x^2(1 + (14 - 56b^2)y^2 + (-9 + 30b^2)y^4) + bx^5y^3(14 + 8y^2 - 2y^4$$

$$+ b^2(-49 + 34y^2 - 19y^4)) + x^4y^2(-9 - 4y^2 + b^2(26 - 18y^2 + 7y^4) + 4b^4(1$$
$$- 12y^2 + 7y^4)) - bx^3y(5 + 16y^2 - 14y^4 + b^2(2 - 86y^2$$
$$+ 49y^4)))))/(8(1 - b^2)^{1/2}xy^8\zeta^7)\Big]+$$
$$\left(\frac{a}{R}\right)^5\Big[- (1)/(8(1 - b^2)^{1/2}xy) + (1 - 48x^2y^2 + 81x^4y^4 - 96b^5x^5y^5 - 10x^6y^6+$$
$$8b^4x^4y^4(27 + 2x^2y^2) - 3b^3x^3y^3(63 - 26x^2y^2 + 11x^4y^4)$$
$$+ 3b^2x^2y^2(28 - 57x^2y^2 + 26x^4y^4 + 3x^6y^6) - bxy(9 - 105x^2y^2 + 108x^4y^4$$
$$+ 3x^6y^6 + x^8y^8))/(8(1 - b^2)^{1/2}xy^{10}\zeta^9)\Big] \qquad \text{(A.7c)}$$

$$M_3^{UF,c} = \left(\frac{a}{R}\right)\Big[(3(1 - b^2)^{1/2}x(4b^2x^2y + bx(-2 + (-7 + x^2)y^2 - 3(-1 + x^2)y^4)$$
$$+ y(5 - 3y^2 + x^2(-3 + 5y^2))))/(8y^5\zeta^5)\Big]+$$
$$\left(\frac{a}{R}\right)^3\Big[- (3x(4b^4x^2y(-1 + 2(-2 + x^2)y^2 + y^4) - bx(2 + (26 - 7x^2)y^2 + (-7 - 2x^2$$
$$+ x^4)y^4 + 3x^2y^6) + b^3x(2 + (26 - 7x^2)y^2 + (-7 - 2x^2 + x^4)y^4 + 3x^2y^6)$$
$$+ b^2y(-14 + 5y^2 - 13x^4y^2 + x^2(9 + 22y^2 - 9y^4)) + y(14 - 5y^2 + 5x^4y^2$$
$$+ x^2(-5 - 6y^2 + 5y^4))))/(8(1 - b^2)^{1/2}y^7\zeta^7)\Big]+$$
$$\left(\frac{a}{R}\right)^5\Big[(x(32b^5x^3y^3 + 24b^4x^2y^2(-3 + 2x^2y^2) + b^2(-35$$
$$+ 162x^2y^2 - 63x^4y^4) - 3bxy(21 - 38x^2y^2 + x^4y^4) + b^3xy(63 - 146x^2y^2 + 3x^4y^4) + 5(7$$
$$- 18x^2y^2 + 3x^4y^4)))/(8(1 - b^2)^{1/2}y^8\zeta^9)\Big] \qquad \text{(A.7d)}$$

$$M_4^{UF,c} = \left(\frac{a}{R}\right)\Big[- (9b(-1 + x^2)(-1 + y^2))/(4(-1 + b^2)xy) - (3(4b^5x^4y^2 + b^4x^3y(-2$$
$$+ (21 - 23x^2)y^2 + 21(-1 + x^2)y^4) + x^3y(-2 + (6 - 8x^2)y^2 - 3(2 - 3x^2 + x^4)y^4$$
$$+ 3x^2(-1 + x^2)y^6) + b^3x^2y^2(45(-1 + y^2) - 15x^4y^2(-1 + y^2) + x^2(37$$
$$- 60y^2 + 15y^4)) + b(6(-1 + y^2) - 15x^6y^4(-1 + y^2) + 3x^2(2 - 7y^2 + 5y^4) + x^4y^2(19$$
$$- 30y^2 + 15y^4)) + b^2xy(-30(-1 + y^2) + 3x^6y^4(-1 + y^2) + x^2(-26 + 63y^2$$
$$- 33y^4) + x^4(-29y^2 + 36y^4 - 3y^6))))/(8(-1 + b^2)xy^6\zeta^5)\Big]+$$
$$\left(\frac{a}{R}\right)^3\Big[(3(4b^5x^4y^2(1 + 6(-2 + x^2)y^2 + 7y^4) - b^4x^3y(2 + (-94 + 49x^2)y^2$$
$$+ (49 - 34x^2 + 17x^4)y^4 + 19x^2y^6) - x^3y(2 + 2(-12 + 7x^2)y^2 + (14 - 6x^2$$

$$+ 3x^4)y^4 + x^2(5 - 2x^2 + x^4)y^6 + x^4y^8) + b^3x^2y^2(7x^6y^4 + 35(-2 + y^2)$$
$$+ x^4y^2(22 - 14y^2 + 7y^4) + x^2(27 - 44y^2 + 14y^4)) - b^2xy(x^8y^6 + 14(-2 + y^2) + x^6y^4(22$$
$$- 2y^2 + y^4) + x^2(10 - 22y^2 + 7y^4) + x^4y^2(7 - 44y^2 + 18y^4)) + b(7x^8y^6 + 2(-2$$
$$+ y^2) + x^2(2 - 14y^2 + 7y^4) + x^6y^4(24 - 14y^2 + 7y^4) + x^4y^2(11 - 48y^2$$
$$+ 28y^4)))))/(8(-1 + b^2)xy^8\zeta^7) + (3b(-2 + x^2 + y^2)(-1 + 2bxy$$
$$- x^2y^2)^3)/(4(-1 + b^2)xy^7\zeta^6)\Big]+$$
$$\left(\frac{a}{R}\right)^5\Big[(b)/(4xy - 4b^2xy) + (-96b^6x^5y^5 + 8b^5x^4y^4(27$$
$$+ 2x^2y^2) - 3b^4x^3y^3(63 - 18x^2y^2 + 11x^4y^4) - x^3y^3(84 - 51x^2y^2 + 6x^4y^4$$
$$+ x^6y^6) + b^3x^2y^2(63 - 117x^2y^2 + 157x^4y^4 + 9x^6y^6) - b^2xy(18 - 105x^2y^2$$
$$+ 261x^4y^4 + 33x^6y^6 + x^8y^8) + b(2 + 9x^2y^2 + 153x^4y^4 - 5x^6y^6$$
$$+ 9x^8y^8))/(8(-1 + b^2)xy^{10}\zeta^9)\Big] \qquad \text{(A.7e)}$$

$$M_5^{UF,c} = \left(\frac{a}{R}\right)\Big[(3(4b^3x^2y^2 + b^2xy(3 - 5y^2 + x^2(-5 + 3y^2)) + xy(6 - 4y^2 + 3x^4y^2(-1 + y^2)+$$
$$x^2(-4 + 9y^2 - 3y^4)) + b(3(-1 + y^2) - 9x^4y^2(-1 + y^2) + x^2(3 - 16y^2$$
$$+ 9y^4)))))/(8(-1 + b^2)xy^4\zeta^3) - (9b(-1 + x^2)(-1 + y^2)(-1 + 2bxy$$
$$- x^2y^2))/(8(-1 + b^2)xy^3\zeta^2)\Big]+$$
$$\left(\frac{a}{R}\right)^3\Big[(3b(-2 + x^2 + y^2))/(8(-1 + b^2)xy) + (8b^3x^2y^2 + xy(3x^6y^4 + 4(-5 + 3y^2)$$
$$+ 3x^4y^2(3 - 2y^2 + y^4) + x^2(12 - 14y^2 + 9y^4)) + b^2xy(-10 + 3y^2 + 21x^4y^2$$
$$+ x^2(3 - 46y^2 + 21y^4)) - b(15x^6y^4 + 3(-2 + y^2) + 15x^4y^2(2 - 2y^2 + y^4)$$
$$+ x^2(3 - 52y^2 + 30y^4)))/(8(-1 + b^2)xy^6\zeta^5)\Big]+$$
$$\left(\frac{a}{R}\right)^5\Big[(-24b^3x^4y^4 + b^2xy(-3 + 42x^2y^2 + 17x^4y^4) + xy(10 - 7x^2y^2 + 4x^4y^4$$
$$+ x^6y^6) - b(1 + 21x^2y^2 + 11x^4y^4 + 7x^6y^6))/(8(-1 + b^2)xy^8\zeta^7)$$
$$- (b(-1 + 2bxy - x^2y^2)^3)/(8(-1 + b^2)xy^7\zeta^6)\Big] \qquad \text{(A.7f)}$$

$$6\pi\eta a^2 M_{is,\beta\alpha}^{UL,c} = M_1^{UL,c}\hat{y}_i(\hat{y}_n \cdot \epsilon_{nsj} \cdot \hat{y}_j^{\perp}) + M_2^{UL,c}\hat{y}_i^{\perp}(\hat{y}_n \cdot \epsilon_{nsj} \cdot \hat{y}_j^{\perp})+$$

$$M_3^{UL,c}\epsilon_{isj}\cdot\hat{y}_j + M_4^{UL,c}\epsilon_{isj}\cdot\hat{y}_j^{\perp} \tag{A.8a}$$

$$\begin{aligned}M_1^{UL,c} = &\left(\frac{a}{R}\right)^2\Big[(9(-1+x^2))/(8(1-b^2)^{1/2}x) + (9(-1+x^2)(-1+x^2y^2\\ &+ 8b^3x^3y^3 - b^2x^2y^2(11+5x^2y^2) + bxy(5+2x^2y^2\\ &+ x^4y^4)))/(8(1-b^2)^{1/2}xy^5\zeta^5)\Big]+\\ &\left(\frac{a}{R}\right)^4\Big[(3(-1+14x^2y^2-5x^4y^4-32b^4x^4y^4+8b^3x^3y^3(7+2x^2y^2)\\ &+ b^2(-35x^2y^2+2x^4y^4-7x^6y^6) + bxy(7-21x^2y^2+5x^4y^4\\ &+ x^6y^6)))/(8(1-b^2)^{1/2}xy^7\zeta^7) + (3(1-2bxy+x^2y^2)^3)/(8(1-b^2)^{1/2}xy^6\zeta^6)\Big]\end{aligned} \tag{A.8b}$$

$$\begin{aligned}M_2^{UL,c} = &\left(\frac{a}{R}\right)^2\Big[(9b(-1+x^2))/(4(-1+b^2)x) + (9(-1+x^2)(8b^4x^3y^3 - 5b^3x^2y^2(3\\ &+ x^2y^2) + x^3y^3(3+x^2y^2) + b^2xy(10+9x^2y^2+x^4y^4) - b(2+5x^2y^2\\ &+ 5x^4y^4)))/(8(-1+b^2)xy^5\zeta^5)\Big]+\\ &\left(\frac{a}{R}\right)^4\Big[(3(-32b^5x^4y^4 + 8b^4x^3y^3(7+2x^2y^2) + x^3y^3(21+2x^2y^2\\ &+ x^4y^4) - b^3x^2y^2(35+6x^2y^2+7x^4y^4) + b^2xy(14-7x^2y^2+24x^4y^4\\ &+ x^6y^6) - b(2+7x^2y^2+32x^4y^4+7x^6y^6)))/(8(-1+b^2)xy^7\zeta^7)\\ &- (3b(-1+2bxy-x^2y^2)^3)/(4(-1+b^2)xy^6\zeta^6)\Big]\end{aligned} \tag{A.8c}$$

$$\begin{aligned}M_3^{UL,c} = &\left(\frac{a}{R}\right)^2\Big[-(3(2b^3x^2+b^2(4xy-6x^3y)+b(-3+9x^4y^2+x^2(1-9y^2))+xy(5-3x^4y^2\\ &+ 3x^2(-1+y^2))))/(8(-1+b^2)xy^3\zeta^3) - (9b(-1+x^2)(-1\\ &+ 2bxy - x^2y^2))/(8(-1+b^2)xy^2\zeta^2)\Big]+\\ &\left(\frac{a}{R}\right)^4\Big[(3b)/(8(-1+b^2)x) + (3(8b^2x^3y^3 + xy(5+2x^2y^2+x^4y^4) - b(1+10x^2y^2\\ &+ 5x^4y^4)))/(8(-1+b^2)xy^5\zeta^5)\Big]\end{aligned} \tag{A.8d}$$

$$M_4^{UL,c} = \left(\frac{a}{R}\right)^2\Big[-(3(1-b^2)^{1/2}x)/(4y^3\zeta^3)\Big] + \left(\frac{a}{R}\right)^4\Big[0\Big] \tag{A.8e}$$

$$6\pi\eta a^3 M^{\Omega L,c}_{ij,\beta\alpha} = M^{\Omega L,c}_1 \hat{y}_i\hat{y}_j + M^{\Omega L,c}_2 \hat{y}_i\hat{y}^{\perp}_j + M^{\Omega L,c}_3 \hat{y}^{\perp}_i\hat{y}_j + M^{\Omega L,c}_4 \hat{y}^{\perp}_i\hat{y}^{\perp}_j + M^{\Omega L,c}_5 \delta_{ij} \tag{A.9a}$$

$$M^{\Omega L,c}_1 = \left(\frac{a}{R}\right)^3 \Big[(9)/(8(-1+b^2)) - (9(1-2x^2y^2+b^4x^2y^2+b^2x^2y^2(11 + 5x^2y^2) - 2b^3(xy+4x^3y^3) - bxy(3+2x^2y^2+x^4y^4)))/(8(-1+b^2)y^5\zeta^5)\Big] \tag{A.9b}$$

$$M^{\Omega L,c}_2 = \left(\frac{a}{R}\right)^3 \Big[(9b)/(8(1-b^2)^{1/2}) - (9(b+7bx^2y^2+3b^3x^2y^2+5bx^4y^4-b^2xy(4 + 7x^2y^2) - xy(1+3x^2y^2+x^4y^4)))/(8(1-b^2)^{1/2}y^5\zeta^5)\Big] \tag{A.9c}$$

$$M^{\Omega L,c}_3 = \left(\frac{a}{R}\right)^2 \Big[-(9(1-b^2)^{1/2}x(-1+bxy))/(8y^4\zeta^5)\Big] \tag{A.9d}$$

$$M^{\Omega L,c}_4 = \left(\frac{a}{R}\right)^2 \Big[(9(1+b^2))/(8(-1+b^2)) - (9(1-2x^2y^2+3b^4x^2y^2-5b^3(xy + 3x^3y^3) - bxy(5+5x^2y^2+2x^4y^4) + b^2(1+19x^2y^2+10x^4y^4)))/(8(-1 + b^2)y^5\zeta^5)\Big] \tag{A.9e}$$

$$M^{\Omega L,c}_5 = \left(\frac{a}{R}\right)^3 \Big[(9)/(8-8b^2) - (3(-5+7x^2y^2+2b^3(xy+12x^3y^3) + b^2(2-37x^2y^2-15x^4y^4) + bxy(13+6x^2y^2+3x^4y^4)))/(8(-1+b^2)y^5\zeta^5)\Big] \tag{A.9f}$$

$$6\pi\eta a^3 \boldsymbol{M}^{US,c}_{\beta\alpha} = M^{US,c}_1 \hat{y}_i(\hat{y}_n\hat{y}_j - \frac{1}{3}\delta_{nj}) + M^{US,c}_2 \hat{y}^{\perp}_i(\hat{y}_n\hat{y}_j - \frac{1}{3}\delta_{ij}) + M^{US,c}_3 \hat{y}_i(\hat{y}^{\perp}_n\hat{y}^{\perp}_j - \frac{1}{3}\delta_{ij}) + M^{US,c}_4 \hat{y}^{\perp}_i(\hat{y}^{\perp}_n\hat{y}^{\perp}_j - \frac{1}{3}\delta_{ij}) + M^{US,c}_5(\hat{y}_i\hat{y}_n\hat{y}^{\perp}_j + \hat{y}_i\hat{y}^{\perp}_n\hat{y}_j) + M^{US,c}_6(\hat{y}^{\perp}_i\hat{y}_n\hat{y}^{\perp}_j + \hat{y}_i\hat{y}^{\perp}_n\hat{y}_j) + M^{US,c}_7(\delta_{in}\hat{y}^{\perp}_j + \delta_{ij}\hat{y}^{\perp}_n - \frac{2}{3}\delta_{jn}\hat{y}^{\perp}_i) + M^{US,c}_8(\delta_{in}\hat{y}_j + \delta_{ij}\hat{y}_n - \frac{2}{3}\delta_{jn}\hat{y}^{\perp}_i) + \tag{A.10a}$$

$$M^{US,c}_1 = \left(\frac{a}{R}\right)^2 \Big[(9(4b^6x^5y^3+b^5x^4y^2(-2+(-25+11x^2)y^2-13(-1+x^2)y^4) + b^4x^3y^3(70-36y^2+19x^4y^2(-1+y^2)+x^2(-68+73y^2-19y^4)) + x^3y^5(2 + x^6y^2(-3+y^2) - 4x^2(-1+y^2) - x^4(8-5y^2+y^4)) + b(-7x^8y^6(-3+y^2)$$

$$+ 2(-2 + y^2) + 2x^2(2 - 8y^2 + 3y^4) + 2x^4y^2(7 - 15y^2 + 5y^4) + x^6y^4(30 - 21y^2$$
$$+ 7y^4)) + b^3x^2y^2(-70 + 36y^2 - 7x^6y^4(-1 + y^2) + x^4y^2(99 - 64y^2 + 7y^4) + x^2(72$$
$$- 127y^2 + 47y^4)) + b^2xy(-14(-2 + y^2) + x^8y^6(-1 + y^2) - x^6y^4(57 - 22y^2$$
$$+ y^4) - 4x^2(7 - 21y^2 + 9y^4) + x^4(-76y^2 + 77y^4 - 19y^6))))/(8(-1$$
$$+ b^2)xy^9\zeta^7) - (9b(-1 + x^2)(-2 + y^2)(-1 + 2bxy - x^2y^2)^3)/(4(-1 + b^2)xy^8\zeta^6)\Big] +$$
$$\left(\frac{a}{R}\right)^4 \Big[(3b(-16 + 6x^2 + 5y^2))/(20(-1 + b^2)xy^2) + (3(4b^6x^5y^3(-15 + 18(-8$$
$$+ 3x^2)y^2 + 65y^4) + b^5x^4y^2(30 + (1496 - 351x^2)y^2 + (-585$$
$$+ 776x^2 - 291x^4)y^4 - 435x^2y^6) + x^3y^5(-70 + 9x^8y^4 + x^2(-624 + 290y^2) + x^6y^2(63 - 24y^2$$
$$+ 5y^4) + x^4(264 - 88y^2 + 15y^4)) + b^2xy(-288 + 90y^2 + 3x^{10}y^8$$
$$+ x^8y^6(288 - 8y^2 + 5y^4) - 3x^4y^2(-168 + 360y^2 + 5y^4) + 2x^2(54 - 552y^2$$
$$+ 185y^4) + x^6y^4(645 - 848y^2 + 210y^4)) - b(-32 + 10y^2 + 81x^{10}y^8 + 4x^2(3 - 36y^2$$
$$+ 5y^4) + 3x^8y^6(187 - 72y^2 + 15y^4) + 6x^4y^2(9 - 152y^2 + 30y^4) + x^6y^4(432$$
$$- 1096y^2 + 365y^4)) - b^3x^2y^2(27x^8y^6 + 4(-252 + 85y^2) + 3x^6y^4(52 - 24y^2$$
$$+ 15y^4) + x^4y^2(729 - 816y^2 + 40y^4) + x^2(408 - 1624y^2 + 495y^4)) + b^4x^3y^3(81x^6y^4$$
$$+ 36(-44 + 15y^2) + 9x^4y^2(43 - 24y^2 + 15y^4) + x^2(564 - 1752y^2$$
$$+ 725y^4))))/(40(-1 + b^2)xy^{11}\zeta^9)\Big] +$$
$$\left(\frac{a}{R}\right)^6 \Big[(3(-288b^7x^6y^6 + 8b^6x^5y^5(99 + 34x^2y^2) + b^5x^4y^4(-891 - 454x^2y^2$$
$$+ 161x^4y^4) + 3x^5y^5(286 - 127x^2y^2 + 8x^4y^4 + x^6y^6) + 3b^4x^3y^3(126$$
$$+ 77x^2y^2 - 104x^4y^4 + 21x^6y^6) - b^3x^2y^2(198 - 363x^2y^2 + 39x^4y^4$$
$$+ 915x^6y^6 + 11x^8y^8) + b^2xy(44 + 282x^2y^2 - 33x^4y^4 + 1741x^6y^6$$
$$+ 133x^8y^8 + x^{10}y^{10}) - b(4 + 22x^2y^2 + 792x^4y^4 + 1067x^6y^6 - 94x^8y^8$$
$$+ 33x^{10}y^{10}))))/(40(-1 + b^2)xy^{13}\zeta^{11}) - (3b(-1 + 2bxy$$
$$- x^2y^2)^5)/(10(-1 + b^2)xy^{12}\zeta^{10})\Big] \qquad \text{(A.10b)}$$

$$M_2^{US,c} = \left(\frac{a}{R}\right)^2 \Big[(9b^2(-1 + x^2)(-1 + y^2))/(4(1 - b^2)^{3/2}xy^2)$$
$$+ (3(1 - b^2)^{1/2}x(5 - 9y^2 + 3bx^5y^3(-1 + y^2) + bx(y + 15y^3) + bx^3y(3 + 12b^2 + 4y^2$$

$$
\begin{aligned}
&- 3y^4) + x^4y^2(12 - 10y^2 + 3b^2(-5 + 3y^2)) - x^2(3 + 5y^2 - 6y^4 + b^2(6 + 7y^2 \\
&+ 9y^4)))))/(8y^7\zeta^7) + (3(x^2y^2(-5 + 3y^2 + x^2(3 - 5y^2)) + 4b^5x^3y^3(7 - 6y^2 + 6x^2(-1 \\
&+ y^2)) + b^3xy(-30(-1 + y^2) + 3x^6y^4(-1 + y^2) + x^2(-30 \\
&+ 49y^2 - 27y^4) - 3x^4y^2(9 - 10y^2 + y^4)) + bx^3y^3(13 - 9y^2 + 3x^4y^2(-1 + y^2) - 3x^2(3 - 4y^2 \\
&+ y^4)) + b^4x^2y^2(-50 + 48y^2 - 15x^4y^2(-1 + y^2) + x^2(48 - 65y^2 + 15y^4)) \\
&+ b^2(6(-1 + y^2) - 15x^6y^4(-1 + y^2) + x^2(6 - 11y^2 + 9y^4) + x^4y^2(9 - 20y^2 \\
&+ 15y^4)))))/(8(1 - b^2)^{3/2}xy^7\zeta^5)\Big] + \\
&\left(\frac{a}{R}\right)^4\Big[(3b^2(-8 + 3x^2 + 5y^2))/(20(1 - b^2)^{3/2}xy^2) + (3(4b^7x^5y^3(-15 + 18(-8 + \\
&3x^2)y^2 + 65y^4) + b^6x^4y^2(30 + (1336 - 351x^2)y^2 + (-585 \\
&+ 776x^2 - 291x^4)y^4 - 435x^2y^6) + 5x^2y^4(10 + 15x^6y^2 + x^2(88 - 45y^2) \\
&+ 3x^4(-9 - 8y^2 + 5y^4)) - b^4x^2y^2(-504 + 265y^2 + 27x^8y^6 + 2x^4y^2(189 \\
&+ 80y^2) + 9x^6y^4(-10 - 8y^2 + 5y^4) + 3x^2(83 - 96y^2 + 210y^4)) + bx^3y^3(141x^4y^2 + 3x^8y^6 \\
&+ 8(-48 + 5y^2) + x^6y^6(-8 + 5y^2) + x^2(84 - 696y^2 + 335y^4)) + b^5x^3y^3(-1224 \\
&+ 565y^2 + 81x^6y^4 + 3x^4y^2(92 - 72y^2 + 45y^4) + x^2(519 - 1056y^2 + 760y^4)) \\
&+ b^3xy(3x^{10}y^8 + 18(-8 + 5y^2) + x^8y^6(135 - 8y^2 + 5y^4) + 3x^6y^4(41 - 120y^2 \\
&+ 75y^4) + x^2(54 + 264y^2 + 235y^4) + x^4(-39y^2 + 312y^4 - 95y^6)) \\
&+ b^2(16 - 10y^2 - 27x^{10}y^8 + x^2(-6 + 72y^2 - 145y^4) - 9x^8y^6(42 - 8y^2 + 5y^4) + 3x^4(y^2 - 16y^4 \\
&+ 60y^6) + x^6(108y^4 + 848y^6 - 480y^8)))))/(40(1 - b^2)^{3/2}xy^{11}\zeta^9)\Big] + \\
&\left(\frac{a}{R}\right)^6\Big[(3b^2)/(20(1 - b^2)^{3/2}xy^2) - (3(1 - b^2)^{1/2}x(-35 \\
&+ 550x^2y^2 - 615x^4y^4 + 32b^4x^4y^4 + 60x^6y^6 - 8b^3x^3y^3(11 + 26x^2y^2) \\
&+ b^2(99x^2y^2 + 558x^4y^4 - 201x^6y^6) - bxy(119 + 627x^2y^2 - 603x^4y^4 \\
&+ 9x^6y^6)))/(40y^{11}\zeta^{11}) + (3(128b^7x^5y^5 + 32b^6x^4y^4(-9 + x^2y^2) - 5x^2y^2(7 \\
&- 18x^2y^2 + 3x^4y^4) + 4b^5x^3y^3(63 - 58x^2y^2 + 9x^4y^4) + bx^3y^3(147 \\
&- 165x^2y^2 + 9x^4y^4 + x^6y^6) - b^4x^2y^2(98 - 351x^2y^2 + 268x^4y^4 + 9x^6y^6) \\
&+ b^2(-2 + 61x^2y^2 - 405x^4y^4 + 83x^6y^6 - 9x^8y^8) + b^3xy(18 - 231x^2y^2
\end{aligned}
$$

$$+ 521x^4y^4 + 27x^6y^6 + x^8y^8))))/(40(1 - b^2)^{3/2}xy^{11}\zeta^9)\Big] \tag{A.10c}$$

$$M_3^{US,c} = \left(\frac{a}{R}\right)^2 \Big[- (9(4b^6x^5y^3 + b^5x^4y^2(-2 + (31 - 37x^2)y^2 + 35(-1 + x^2)y^4) + x^3y^3(-8+$$
$$10y^2 - 2x^6y^4(-1 + y^2) + x^4y^2(7 - 9y^2 + 2y^4) + x^2(10 - 15y^2 + 7y^4))$$
$$+ b^4x^3y^3(-78 + 80y^2 - 35x^4y^2(-1 + y^2) + x^2(72 - 113y^2 + 35y^4))$$
$$+ 2b^3x^2y^2(-35(-1 + y^2) + 7x^6y^4(-1 + y^2) + x^2(-33 + 74y^2 - 35y^4)$$
$$+ x^4(-33y^2 + 42y^4 - 7y^6)) + b(4 - 4y^2 + 14x^8y^6(-1 + y^2) - 2x^2(2 - 9y^2 + 7y^4)$$
$$+ x^4(-16y^2 + 45y^4 - 35y^6) + x^6(-37y^4 + 49y^6 - 14y^8)) + 2b^2xy(14(-1 + y^2) + x^6y^4(21$$
$$- 22y^2 + y^4) + 3x^4y^2(9 - 16y^2 + 7y^4) + x^2(14 - 41y^2 + 25y^4) + x^8(y^6$$
$$- y^8))))/(8(-1 + b^2)xy^9\zeta^7) - (9b(-1 + x^2)(-1 + y^2)(-1 + 2bxy$$
$$- x^2y^2)^3)/(2(-1 + b^2)xy^8\zeta^6)\Big] +$$
$$\left(\frac{a}{R}\right)^4 \Big[(3b(-8 + 3x^2 + 5y^2))/(10(-1 + b^2)xy^2) + (3(20b^6x^5y^3(3 + 6(-8 + 3x^2)y^2 +$$
$$35y^4) - 5b^5x^4y^2(6 + 3(-152 + 63x^2)y^2 + (315 - 152x^2 + 57x^4)y^4$$
$$+ 105x^2y^6) + x^3y^3(-480 + 350y^2 + 6x^8y^6 + x^6y^4(27 - 16y^2 + 10y^4)$$
$$+ 3x^4y^2(7 - 24y^2 + 15y^4) + x^2(210 + 24y^2 + 35y^4)) - b(54x^{10}y^8 + 4(-8$$
$$+ 5y^2) + 6x^2(2 - 24y^2 + 15y^4) + 3x^8y^6(53 - 48y^2 + 30y^4) + 3x^4y^2(28 - 424y^2$$
$$+ 315y^4) + x^6y^4(567 - 424y^2 + 315y^4)) + 2b^2xy(3x^{10}y^8 + 18(-8 + 5y^2)$$
$$+ x^2(54 - 24y^2 - 35y^4) + x^8y^6(108 - 8y^2 + 5y^4) + 12x^6y^4(29 - 24y^2 + 15y^4) + 9x^4(y^2$$
$$- 112y^4 + 70y^6)) + b^4x^3y^3(189x^6y^4 + 40(-54 + 35y^2) + 15x^2(48 - 72y^2$$
$$+ 35y^4) + x^4(435y^2 - 504y^4 + 315y^6)) - 2b^3x^2y^2(27x^8y^6 + 63(-8 + 5y^2)$$
$$- 3x^2(-53 + 80y^2) + 3x^6y^4(94 - 24y^2 + 15y^4) + x^4(-752y^4$$
$$+ 420y^6))))/(40(-1 + b^2)xy^{11}\zeta^9)\Big] +$$
$$\left(\frac{a}{R}\right)^6 \Big[- (3(480b^7x^6y^6 + 40b^6x^5y^5(-33 + 2x^2y^2) + b^5x^4y^4(1485 - 790x^2y^2 +$$
$$281x^4y^4) - b^4x^3y^3(882 - 1485x^2y^2 + 1504x^4y^4$$
$$+ 99x^6y^6) - x^3y^3(420 - 693x^2y^2 + 156x^4y^4 + 11x^6y^6 + 2x^8y^8) + 2b^3x^2y^2(99$$
$$- 561x^2y^2 + 1456x^4y^4 + 115x^6y^6 + 11x^8y^8) - 2b^2xy(22 - 321x^2y^2$$

$$+ 1353x^4y^4 - 130x^6y^6 + 55x^8y^8 + x^{10}y^{10}) + b(4 + 22x^2y^2 + 957x^4y^4 - 754x^6y^6$$
$$+ 149x^8y^8 + 22x^{10}y^{10})))/(40(-1 + b^2)xy^{13}\zeta^{11}) - (3b(-1$$
$$+ 2bxy - x^2y^2)^5)/(10(-1 + b^2)xy^{12}\zeta^{10})\Big] \qquad \text{(A.10d)}$$

$$M_4^{US,c} = \left(\frac{a}{R}\right)^2 \Big[- (9(2 - 2y^2 + 4b^7x^5y^3 + 2x^6y^4 + x^4y^2(-5 + 7y^2) + x^2(-2 + 9y^2 - 7y^4)$$
$$+ b^6x^4y^2(-2 + (35 - 37x^2)y^2 + 35(-1 + x^2)y^4) + b^4x^2y^2(-105(-1 + y^2)$$
$$+ 14x^6y^4(-1 + y^2) + x^2(-99 + 245y^2 - 140y^4) - 2x^4y^2(67 - 77y^2 + 7y^4))$$
$$+ bxy(14(-1 + y^2) - 6x^8y^6(-1 + y^2) + 3x^6y^4(7 - 9y^2 + 2y^4) + 7x^2(2 - 7y^2$$
$$+ 5y^4) + x^4y^2(31 - 56y^2 + 21y^4)) - 2b^3xy(-21(-1 + y^2) + x^8y^6(-1$$
$$+ y^2) - x^6y^4(56 - 57y^2 + y^4) - 7x^2(3 - 13y^2 + 10y^4) - 2x^4y^2(38 - 63y^2$$
$$+ 28y^4)) + b^5x^3y^3(105(-1 + y^2) - 35x^4y^2(-1 + y^2) + x^2(93 - 140y^2 + 35y^4))$$
$$+ b^2(6 - 6y^2 + 42x^8y^6(-1 + y^2) + x^2(-6 + 62y^2 - 56y^4) - 3x^6y^4(37 - 49y^2 + 14y^4)$$
$$+ x^4(-62y^2 + 161y^4 - 105y^6)))))/(8(1 - b^2)^{3/2}xy^9\zeta^7) - (9(1 + 3b^2)(-1$$
$$+ x^2)(-1 + y^2)(-1 + 2bxy - x^2y^2)^3)/(4(1 - b^2)^{3/2}xy^8\zeta^6)\Big] +$$
$$\left(\frac{a}{R}\right)^4 \Big[(3(1 + 3b^2)(-8 + 3x^2 + 5y^2))/(20(1 - b^2)^{3/2}xy^2)$$
$$+ (3(16 - 10y^2 - 30x^8y^6 + x^6y^4(189 + 80y^2) + x^2(-6 + 72y^2 - 45y^4)$$
$$+ 20b^7x^5y^3(3 + 6(-8 + 3x^2)y^2 + 35y^4) + x^4y^2(3 - 424y^2 + 315y^4) - 5b^6x^4y^2(6 + (-488$$
$$+ 189x^2)y^2 + (315 - 152x^2 + 57x^4)y^4 + 105x^2y^6) + 3b^5x^3y^3(63x^6y^4 + 105(-8$$
$$+ 5y^2) + 3x^4y^2(90 - 56y^2 + 35y^4) + 5x^2(51 - 144y^2 + 70y^4)) + 2b^3xy(3x^{10}y^8$$
$$+ 27(-8 + 5y^2) + x^8y^6(297 - 8y^2 + 5y^4) + 9x^6y^4(102 - 88y^2 + 55y^4) + 3x^2(27$$
$$- 392y^2 + 245y^4) + 3x^4y^2(177 - 816y^2 + 560y^4)) - 3b^4x^2y^2(18x^8y^6 + 63(-8$$
$$+ 5y^2) + 6x^6y^4(68 - 8y^2 + 5y^4) + x^2(159 - 920y^2 + 525y^4) + x^4y^2(315$$
$$- 1088y^2 + 630y^4)) - 3b^2(54x^{10}y^8 + 2(-8 + 5y^2) + 6x^2(1 - 40y^2 + 25y^4)$$
$$+ 3x^8y^6(53 - 48y^2 + 30y^4) + x^6y^4(441 - 424y^2 + 315y^4) + x^4y^2(120 - 1096y^2$$
$$+ 735y^4)) + bxy(18x^{10}y^8 + 18(-8 + 5y^2) + 3x^8y^6(27 - 16y^2 + 10y^4) + 9x^6y^4(2$$
$$- 24y^2 + 15y^4) + 9x^2(6 - 56y^2 + 35y^4)$$

$$+ x^4(129y^2 - 48y^4 - 70y^6)))))/(40(1 - b^2)^{3/2}xy^{11}\zeta^9)\Big] +$$

$$\left(\frac{a}{R}\right)^6\Big[- (3(2 + 11x^2y^2 - 594x^4y^4 + 607x^6y^6 + 480b^8x^6y^6 - 50x^8y^8$$

$$+ 40b^7x^5y^5(-33 + 2x^2y^2) + b^6x^4y^4(1485 - 430x^2y^2$$

$$+ 281x^4y^4) - 3b^5x^3y^3(231 - 165x^2y^2 + 773x^4y^4 + 33x^6y^6) + b^4x^2y^2(297 - 528x^2y^2$$

$$+ 4647x^4y^4 + 642x^6y^6 + 22x^8y^8) - 2b^3xy(33 + 264x^2y^2 + 1749x^4y^4 - 21x^6y^6$$

$$+ 154x^8y^8 + x^{10}y^{10}) - bxy(22 + 99x^2y^2 - 627x^4y^4 + 443x^6y^6$$

$$+ 33x^8y^8 + 6x^{10}y^{10}) + 3b^2(2 + 44x^2y^2 + 759x^4y^4 - 536x^6y^6$$

$$+ 149x^8y^8 + 22x^{10}y^{10})))/(40(1 - b^2)^{3/2}xy^{13}\zeta^{11}) - (3(1$$

$$+ 3b^2)(-1 + 2bxy - x^2y^2)^5)/(20(1 - b^2)^{3/2}xy^{12}\zeta^{10})\Big] \qquad \text{(A.10e)}$$

$$M_5^{US,c} = \left(\frac{a}{R}\right)^2\Big[(9(-1 + x^2)(-2 + (1 + b^2)y^2))/(8(1 - b^2)^{3/2}xy^2) + (9(-2 + (1$$

$$+ b^2)y^2 - 7b^2x^8y^6(-3 + b^2 + 2y^2) + bx^9y^7(-3 + b^2 + 2y^2) - 7bxy(-2 + (1$$

$$+ b^2)y^2) - 2bx^3y(7 + (-19 - 25b^2 + 2b^4)y^2 + (9 + 17b^2 + 9b^4)y^4) + x^2(2 - 4(2$$

$$+ 9b^2)y^2 + (5 + 18b^2 + 19b^4)y^4) + 2bx^7y^5(-5 + 9b^4 + 5y^2 - y^4 + b^2(-25$$

$$+ 17y^2)) + bx^5y^3(-27 + 4b^6 + 36y^2 + 8b^4y^2 - 7y^4 + b^2(-47 + 68y^2 - 35y^4)) - x^6y^4(y^2$$

$$+ b^6(13 + 5y^2) + b^4(-26 + 19y^2) + b^2(-57 + 59y^2 - 14y^4)) + x^4y^2(7$$

$$- 7y^2 - y^4 + b^6(-2 + 3y^2 + 5y^4) + b^4(4 - 27y^2 + 24y^4) + b^2(33 - 81y^2$$

$$+ 42y^4)))))/(8(1 - b^2)^{3/2}xy^9\zeta^7)\Big] + \left(\frac{a}{R}\right)^4\Big[(3(-16 + 6x^2 + 5(1 + b^2)y^2))/(40(1 - b^2)^{3/2}xy^2) -$$

$$(3(-16 + 5(1 + b^2)y^2 - 27b^2(-3 + b^2)x^{10}y^8 + 3b(-3 + b^2)x^{11}y^9 - 9bxy(-16 + 5(1$$

$$+ b^2)y^2) + 3x^2(2 - 24(1 + 7b^2)y^2 + 5(4 + 7b^2 + 13b^4)y^4) - bx^3y(54 + 24(-9$$

$$- 59b^2 + 12b^4)y^2 + 5(29 + 89b^2 + 50b^4)y^4) + bx^9y^7(-45 + 90b^4 + 24y^2 - 10y^4$$

$$- b^2(261 + 8y^2)) + 3b^2x^8y^6(68 - 79b^4 - 72y^2 + 30y^4 + b^2(179 + 24y^2))$$

$$+ 3bx^7y^5(79 + 24b^6 + 40y^2 - 15y^4 + b^4(94 - 80y^2) + b^2(-449 + 232y^2 - 105y^4))$$

$$+ x^4y^2(27 + 424y^2 - 270y^4 + 3b^4(20 - 288y^2 + 75y^4) + b^6(-30 + 392y^2$$

$$+ 225y^4) + 3b^2(53 - 656y^2 + 360y^4)) + x^6y^4(-189 - 80y^2 + 25y^4 + b^6(-297 + 632y^2$$

$$- 125y^4) + 4b^2(162 - 96y^2 + 35y^4) + 2b^4(297 - 756y^2 + 400y^4)) - bx^5y^3(21$$

$$+ 312y^2 - 265y^4 - 6b^4(8 - 72y^2 + 25y^4) + 4b^6(-15 + 48y^2 + 25y^4) + 3b^2(197$$
$$- 984y^2 + 525y^4)))))/(40(1 - b^2)^{3/2}xy^{11}\zeta^9)\Big] + \left(\frac{a}{R}\right)^6\Big[(3(-2 - 11x^2y^2 + 594x^4y^4 - 607x^6y^6 + 96b^8x^6y^6$$
$$+ 50x^8y^8 - 8b^7x^5y^5(33 + 58x^2y^2) - 18b^5x^3y^3(14 + 11x^2y^2 - 80x^4y^4$$
$$+ 3x^6y^6) + b^4x^4y^4(-264 - 2961x^2y^2 + 54x^4y^4 + 11x^6y^6) + b^6(297x^4y^4 + 802x^6y^6$$
$$- 35x^8y^8) + b^3x^3y^3(735 + 2112x^2y^2 - 894x^4y^4 + 152x^6y^6 - x^8y^8)$$
$$- 3b^2x^2y^2(33 + 429x^2y^2 - 582x^4y^4 + 133x^6y^6 + 11x^8y^8) + bxy(22 - 153x^2y^2$$
$$- 726x^4y^4 + 578x^6y^6 + 12x^8y^8$$
$$+ 3x^{10}y^{10})))/(40(1 - b^2)^{3/2}xy^{13}\zeta^{11}) + (3(1 - 2bxy + x^2y^2)^5)/(20(1 - b^2)^{3/2}xy^{12}\zeta^{10})\Big] \quad \text{(A.10f)}$$

$$M_6^{US,c} = \left(\frac{a}{R}\right)^2\Big[- (9(4b^6x^5y^3 + b^5x^4y^2(-2 + (7 - 13x^2)y^2 - 5(-1 + x^2)y^4)$$
$$+ b^4x^3y^3(-31 - 5y^2 + 18x^4y^2 + x^2(25 - 11y^2)) + x^3y^3(4 - 5y^2 + x^6y^4 - x^4y^2(-4$$
$$+ y^2) + x^2(-2 + 3y^2)) + b^3x^2y^2(35 - 7x^6y^4 + x^4y^2(-44 + 17y^2) + x^2(-31$$
$$+ 56y^2 - 10y^4)) + b(2 - 7x^8y^6 + x^6y^4(-13 + 2y^2) + x^2(-2 + 7y^2)$$
$$+ x^4y^2(-9 + 7y^2 + 5y^4)) + b^2xy(-14 + x^8y^6 - x^6y^4(-20 + y^2) + x^4(43y^2$$
$$- 34y^4) + x^2(14 - 43y^2 + 10y^4))))/(8(-1 + b^2)xy^9\zeta^7) + (9b(-1$$
$$+ x^2)(-1 + 2bxy - x^2y^2)^3)/(4(-1 + b^2)xy^8\zeta^6)\Big] +$$
$$\left(\frac{a}{R}\right)^4\Big[(3b(-8 + 3x^2))/(20(-1 + b^2)xy^2) + (3(4b^6x^5y^3(15 + 6(-8$$
$$+ 3x^2)y^2 - 25y^4) + b^5x^4y^2(-30 + (552 - 297x^2)y^2 + (225 + 632x^2 - 237x^4)y^4$$
$$- 125x^2y^6) + b^4x^3y^3(-648 - 175y^2 + 90x^6y^4 + x^4(597y^2 - 240y^4) + 3x^2(51$$
$$- 504y^2 + 125y^4)) + x^3y^3(192 - 175y^2 + 3x^8y^6 - 6x^4y^2(-29 + 4y^2) + x^2(-42$$
$$- 384y^2 + 175y^4) + x^6(9y^4 - 8y^6)) + b^3x^2y^2(504 - 27x^8y^6 - 3x^2(43$$
$$- 472y^2 + 150y^4) + x^4y^2(-351 + 248y^2 + 250y^4) + x^6(-93y^4 + 72y^6)) + b(16$$
$$- 27x^{10}y^8 + 6x^8y^6(-29 + 12y^2) + x^2(-6 + 72y^2) + 3x^4y^2(-19 + 16y^2 + 75y^4)$$
$$+ x^6(-108y^4 + 464y^6 - 125y^8)) + b^2xy(-144 + 3x^{10}y^8 - 3x^6y^4(29$$
$$+ 104y^2) - 9x^4y^2(-37 - 8y^2 + 50y^4) + x^2(54 - 888y^2 + 350y^4) + x^8(117y^6$$

$$
\begin{aligned}
&- 8y^8))))/(40(-1+b^2)xy^{11}\zeta^9)\Big]+\\
&\left(\frac{a}{R}\right)^6\Big[(3(-96b^7x^6y^6+8b^6x^5y^5(33+58x^2y^2)+b^5x^4y^4(-297-1162x^2y^2\\
&+35x^4y^4)+b^4x^3y^3(63+1188x^2y^2-625x^4y^4+54x^6y^6)+x^3y^3(-168\\
&+792x^2y^2-291x^4y^4+10x^6y^6+x^8y^8)-b^3x^2y^2(99\\
&+330x^2y^2-1226x^4y^4+466x^6y^6+11x^8y^8)+b^2xy(22+435x^2y^2-1320x^4y^4\\
&+1112x^6y^6+46x^8y^8+x^{10}y^{10})-b(2+11x^2y^2+33x^4y^4+892x^6y^6\\
&-101x^8y^8+11x^{10}y^{10})))/(40(-1+b^2)xy^{13}\zeta^{11})-(3b(-1\\
&+2bxy-x^2y^2)^5)/(20(-1+b^2)xy^{12}\zeta^{10})\Big] \qquad \text{(A.10g)}
\end{aligned}
$$

$$
\begin{aligned}
M_7^{US,c}=&\left(\frac{a}{R}\right)^2\Big[-(9(1+b^2)(-1+x^2)(-1+y^2))/(8(1-b^2)^{3/2}xy^2)+(9(-1+x^2)(-1\\
&+y^2)(1+5b^4x^2y^2-5b^3(xy+3x^3y^3)-bxy(5+5x^2y^2+2x^4y^4)+b^2(1\\
&+15x^2y^2+10x^4y^4)))/(8(1-b^2)^{3/2}xy^7\zeta^5)\Big]+\\
&\left(\frac{a}{R}\right)^4\Big[(3(-8+5y^2+32b^5x^3y^3-x^4y^2(27+16y^2)+x^2(3\\
&+56y^2-45y^4)-bxy(6x^8y^6+x^2(21-32y^2)+7(-8+5y^2)+7x^4y^4(-8+5y^2)+x^6y^4(21\\
&-16y^2+10y^4))+b^4x^2y^2(-56+25y^2+105x^4y^2+x^2(15-296y^2+175y^4))\\
&+b^2(-8+5y^2+42x^8y^6+7x^6y^4(15-16y^2+10y^4)+x^4y^2(138-248y^2\\
&+175y^4)+x^2(3-336y^2+230y^4))-b^3xy(105x^6y^4+7(-8+5y^2)+35x^4y^2(6-8y^2\\
&+5y^4)+x^2(21-496y^2+350y^4))))/(40(1-b^2)^{3/2}xy^9\zeta^7)+(3(1\\
&+b^2)(-8+3x^2+5y^2)(-1+2bxy-x^2y^2)^3)/(40(1-b^2)^{3/2}xy^8\zeta^6)\Big]+\\
&\left(\frac{a}{R}\right)^6\Big[-(3(1+b^2))/(40(1-b^2)^{3/2}xy^2)-(3(-1+48x^2y^2-81x^4y^4\\
&+120b^5x^5y^5+10x^6y^6+b^4(21x^2y^2-270x^4y^4-95x^6y^6)+3b^3xy(3\\
&+63x^2y^2+25x^4y^4+21x^6y^6)+bxy(9-21x^2y^2+57x^4y^4+9x^6y^6+2x^8y^8)\\
&-b^2(1+141x^2y^2-99x^4y^4+83x^6y^6\\
&+18x^8y^8)))/(40(1-b^2)^{3/2}xy^{11}\zeta^9)\Big] \qquad \text{(A.10h)}
\end{aligned}
$$

$$
M_8^{US,c}=\left(\frac{a}{R}\right)^2\Big[(9b(-1+x^2))/(8(-1+b^2)xy^2)+(9(-1+x^2)(b^3x^2y^2(-5+y^2)+xy^3(1
$$

$$+ 2x^2 + x^4y^2) + b^2xy(5 + (-1 + 8x^2)y^2) - b(1 + 5x^4y^4 + x^2y^2(5$$
$$+ y^2)))))/(8(-1 + b^2)xy^7\zeta^5)\Big]$$
$$+ \left(\frac{a}{R}\right)^4 \Big[(3(32b^4x^3y^3 + xy^3(15 - 3x^8y^4 + x^2(96 - 35y^2) + 6x^4(-7 + 4y^2)$$
$$+ x^6y^2(-15 + 8y^2)) + b^3x^2y^2(-56 + 5y^2 + 21x^4y^2 + x^2(15 - 104y^2$$
$$- 25y^4)) + b^2xy(56 - 15y^2 - 48x^6y^4 + 9x^4y^2(-7 + 16y^2) + x^2(-21 + 152y^2$$
$$+ 35y^4)) + b(-8 + 21x^8y^6 + x^2(3 - 112y^2 - 5y^4) + x^4y^2(48 - 176y^2 + 25y^4)$$
$$+ x^6(84y^4 - 56y^6)))))/(40(-1 + b^2)xy^9\zeta^7) + (3b(-8 + 3x^2)(-1 + 2bxy$$
$$- x^2y^2)^3)/(40(-1 + b^2)xy^8\zeta^6)\Big]+$$
$$\left(\frac{a}{R}\right)^6 \Big[- (3b)/(40(-1 + b^2)xy^2) - (3(24b^4x^5y^5$$
$$+ b^3(21x^2y^2 - 54x^4y^4 - 79x^6y^6) + x^3y^3(84 - 51x^2y^2 + 6x^4y^4 + x^6y^6) + 3b^2xy(3$$
$$+ 51x^4y^4 + 10x^6y^6) - b(1 + 57x^2y^2 + 72x^4y^4 + 5x^6y^6 + 9x^8y^8)))/(40(-1 + b^2)xy^{11}\zeta^9)\Big] \quad \text{(A.10i)}$$

$$6\pi\eta a^3 M^{OS,c}_{sjn,\beta\alpha} = \Big[M_1^{OS,c}\hat{y}_m^{\perp}\hat{y}_i(\hat{y}_n\hat{y}_j - \frac{1}{3}\delta_{nj}) + M_2^{OS,c}(\hat{y}_m^{\perp}\hat{y}_i\hat{y}_n^{\perp}\hat{y}_j + \hat{y}_m^{\perp}\hat{y}_i\hat{y}_n\hat{y}_j^{\perp}) +$$
$$M_3^{OS,c}\hat{y}_m^{\perp}\hat{y}_i(\hat{y}_n^{\perp}\hat{y}_j^{\perp} - \frac{1}{3}\delta_{nj}) + M_4^{OS,c}(\delta_{in}\hat{y}_m\hat{y}_j + \delta_{ij}\hat{y}_m\hat{y}_n) +$$
$$M_5^{OS,c}(\delta_{in}\hat{y}_m^{\perp}\hat{y}_j + \delta_{ij}\hat{y}_m^{\perp}\hat{y}_n - \frac{2}{3}\delta_{jn}\hat{y}_m^{\perp}\hat{y}i) +$$
$$M_6^{OS,c}(\delta_{in}\hat{y}_m\hat{y}_j^{\perp} + \delta_{ij}\hat{y}_m\hat{y}_n^{\perp} - \frac{2}{3}\delta_{jn}\hat{y}_i^{\perp}\hat{y}_m) +$$
$$M_7^{OS,c}(\delta_{in}\hat{y}_m^{\perp}\hat{y}_j^{\perp} + \delta_{ij}\hat{y}_m^{\perp}\hat{y}_n^{\perp})\Big]\epsilon_{smi} \quad \text{(A.11a)}$$

$$M_1^{OS,c} = \left(\frac{a}{R}\right)^3 \Big[(9(4b^6x^3y^3(-5 + y^2) + b^5x^2y^2(35 + (-7 + 25x^2)y^2$$
$$+ 11x^2y^4) - b^2xy(-28 + (14 - 85x^2)y^2 + (43x^2 - 44x^4)y^4 + x^4(18 + x^2)y^6$$
$$+ x^6y^8) + b(-4 + (2 - 14x^2)y^2 - 45x^4y^4 + (11x^4 - 21x^6)y^6 + 7x^6y^8)$$
$$+ x^3y^5(6 + x^2(13 - 5y^2) - x^4y^2(-3 + y^2)) - b^4xy(14 + x^4y^4(15 + 19y^2) + x^2y^2(-5 + 37y^2))$$
$$+ b^3(2 + 7x^2y^2(-9 + 7y^2) + x^4(-50y^4 + 48y^6) + 7x^6(y^6$$
$$+ y^8)))))/(8(1 - b^2)^{3/2}y^9\zeta^7) + (9b(-2 + b^2 + y^2)(-1 + 2bxy - x^2y^2)^3)/(4(1 - b^2)^{3/2}y^8\zeta^6)\Big]+$$

$$\left(\frac{a}{R}\right)^5\Big[(9b(-2+b^2))/(20(1-b^2)^{3/2}y^2)-(9(40b^6x^5y^5+x^5y^5(143$$
$$+6x^2y^2+3x^4y^4)+b^5(63x^2y^2-90x^4y^4-5x^6y^6)-3b^4xy(6+21x^2y^2$$
$$+13x^6y^6)+b^3(2-117x^2y^2+117x^4y^4-11x^6y^6+9x^8y^8)-b(4+18x^2y^2$$
$$+279x^4y^4+152x^6y^6+27x^8y^8)+b^2(36xy+231x^3y^3+69x^5y^5$$
$$+105x^7y^7-x^9y^9)))/(40(1-b^2)^{3/2}y^{11}\zeta^9)\Big] \qquad \text{(A.11b)}$$

$$M_2^{OS,c}=\left(\frac{a}{R}\right)^3\Big[-(9(2+(-1+7x^2)y^2-x^2(7+5x^2)y^4+4x^4y^6+4b^5x^3y^3(-5+3y^2)$$
$$+b^4x^2y^2(35+(-21+65x^2)y^2-31x^2y^4)+b^3xy(-14+(7-100x^2)y^2$$
$$+(46x^2-70x^4)y^4+35x^4y^6)+bxy(-14+(7-20x^2)y^2-2x^2(-6+7x^2)y^4$$
$$+(7x^4-4x^6)y^6+2x^6y^8)-b^2(-2+(1-42x^2)y^2+(14x^2-80x^4)y^4+(43x^4$$
$$-28x^6)y^6+14x^6y^8)))/(8(-1+b^2)y^9\zeta^7)+(9(1+b^2)(-2+y^2)(-1$$
$$+2bxy-x^2y^2)^3)/(8(-1+b^2)y^8\zeta^6)\Big]+$$
$$\left(\frac{a}{R}\right)^5\Big[-(9(1+b^2))/(20(-1+b^2)y^2)-(9(-2-9x^2y^2+108x^4y^4$$
$$+120b^5x^5y^5-25x^6y^6-b^4x^2y^2(63+270x^2y^2+235x^4y^4)+6b^3xy(3$$
$$+63x^2y^2+65x^4y^4+21x^6y^6)+2bxy(9-21x^2y^2-3x^4y^4+9x^6y^6+2x^8y^8)$$
$$-2b^2(1+36x^2y^2+171x^4y^4+38x^6y^6+18x^8y^8)))/(40(-1+b^2)y^{11}\zeta^9)\Big] \qquad \text{(A.11c)}$$

$$M_3^{OS,c}=\left(\frac{a}{R}\right)^3\Big[(9(-1+y^2)(20b^6x^3y^3+x^3y^3(15+7x^2y^2+2x^4y^4)-35b^5(x^2y^2+3x^4$$
$$y^4)+b^4xy(14+185x^2y^2+105x^4y^4)-b(6+21x^2y^2+35x^4y^4+14x^6y^6)-$$
$$2b^3(1+56x^2y^2+70x^4y^4+21x^6y^6)+b^2(42xy+60x^3y^3+56x^5y^5+6x^7y$$
$$^7)))/(8(1-b^2)^{3/2}y^9\zeta^7)-(9b(3+b^2)(-1+y^2)(-1+2bxy-x^2y^2)^3)/(4(1-b^2)^{3/2}y^8\zeta^6)\Big]+$$
$$\left(\frac{a}{R}\right)^5\Big[-(9b(3+b^2))/(20(1-b^2)^{3/2}y^2)-(9(280b^6x^5y^5$$
$$+x^3y^3(105-28x^2y^2+9x^4y^4+2x^6y^6)-63b^5(x^2y^2+10x^4y^4+5x^6y^6)$$
$$+3b^4xy(6+231x^2y^2+140x^4y^4+63x^6y^6)+6b^2xy(9-21x^2y^2+56x^4y^4$$
$$+15x^6y^6+x^8y^8)-3b(2+9x^2y^2+42x^4y^4+21x^6y^6+6x^8y^8)-2b^3(1+99x^2y^2$$
$$+126x^4y^4+147x^6y^6+27x^8y^8)))/(40(1-b^2)^{3/2}y^{11}\zeta^9)\Big] \qquad \text{(A.11d)}$$

$$M_4^{OS,c} = \left(\frac{a}{R}\right)^3 \Big[(9b^2)/(8(-1+b^2)y^2) + (9(-x^2y^4 + b^4x^2y^2(-4+y^2) + bxy^3(2+3x^2 + x^4y^2) + b^3xy(5+(-2+7x^2)y^2) - b^2(1+6x^2y^2+5x^4y^4)))/(8(-1+b^2)y^7\zeta^5)\Big] + \left(\frac{a}{R}\right)^5 \Big[(9b(8b^3x^4y^4 - x^3y^3(21+2x^2y^2+x^4y^4) - b^2xy(7+14x^2y^2 + 19x^4y^4) + b(1+21x^2y^2+27x^4y^4+7x^6y^6)))/(40(-1+b^2)y^9\zeta^7) + (9b^2(-1+2bxy-x^2y^2)^3)/(40(-1+b^2)y^8\zeta^6)\Big] \quad \text{(A.11e)}$$

$$M_5^{OS,c} = \left(\frac{a}{R}\right)^3 \Big[-(9b)/(8(1-b^2)^{1/2}y^2) - (9(b^3x^2y^2(-4+y^2) + xy^3(1+3x^2 + x^4y^2) + b^2xy(5+(-1+7x^2)y^2) - b(1+5x^4y^4 + x^2y^2(6 + y^2))))/(8(1-b^2)^{1/2}y^7\zeta^5)\Big] + \left(\frac{a}{R}\right)^5 \Big[(9(-8b^3x^4y^4 + x^3y^3(21+2x^2y^2+x^4y^4) + b^2xy(7+14x^2y^2 + 19x^4y^4) - b(1+21x^2y^2+27x^4y^4 + 7x^6y^6)))/(40(1-b^2)^{1/2}y^9\zeta^7) - (9b(-1+2bxy-x^2y^2)^3)/(40(1-b^2)^{1/2}y^8\zeta^6)\Big] \quad \text{(A.11f)}$$

$$M_6^{OS,c} = \left(\frac{a}{R}\right)^3 \Big[-(9b(1+b^2)(-1+y^2))/(8(1-b^2)^{3/2}y^2) + (9(-xy^3 + b^5x^2y^2(-4 + 5y^2) + b(-1+(1+x^2)y^2) + b^4xy(5+3(-2+5x^2)y^2 - 15x^2y^4) + b^2xy(5+(-3 + 5x^2)y^2 + x^2(-5+2x^2)y^4 - 2x^4y^6) + b^3(-1+(1-17x^2)y^2 - 5x^2(-3 + 2x^2)y^4 + 10x^4y^6)))/(8(1-b^2)^{3/2}y^7\zeta^5)\Big] + \left(\frac{a}{R}\right)^5 \Big[(9b(1-14x^2y^2+5x^4y^4+40b^4x^4y^4 - 7b^3(xy+10x^3y^3+5x^5y^5) - bxy(7+ 7x^4y^4 + 2x^6y^6) + b^2(1+56x^2y^2+25x^4y^4 + 14x^6y^6)))/(40(1-b^2)^{3/2}y^9\zeta^7) + (9b(1+b^2)(-1 + 2bxy - x^2y^2)^3)/(40(1-b^2)^{3/2}y^8\zeta^6)\Big] \quad \text{(A.11g)}$$

$$M_7^{OS,c} = \left(\frac{a}{R}\right)^3 \Big[(9(1+b^2)(-1+y^2))/(8(-1+b^2)y^2) + (9(1-(1+x^2)y^2 + b^4x^2y^2(4-5y^2) + 5b^3xy(-1+y^2)(1+3x^2y^2) + bxy(-1+y^2)(5+5x^2y^2+2x^4y^4) - b^2(-1+(1-17x^2)y^2 - 5x^2(-3+2x^2)y^4 + 10x^4y^6)))/(8(-1+b^2)y^7\zeta^5)\Big] +$$

$$\left(\frac{a}{R}\right)^5\Big[(9(-1+14x^2y^2-5x^4y^4-40b^4x^4y^4+7b^3(xy+10x^3y^3+5x^5y^5)+bxy(7+$$
$$7x^4y^4+2x^6y^6)-b^2(1+56x^2y^2+25x^4y^4+14x^6y^6)))/(40(-1$$
$$+b^2)y^9\zeta^7)-(9(1+b^2)(-1+2bxy-x^2y^2)^3)/(40(-1+b^2)y^8\zeta^6)\Big] \qquad \text{(A.11h)}$$

$$\begin{aligned}6\pi\eta a^3 M^{ES,c}_{minj,\beta\alpha} =& M^{ES,c}_1(\hat{y}_m\hat{y}_i-\frac{1}{3}\delta_{mi})(\hat{y}_n\hat{y}_j-\frac{1}{3}\delta_{nj})+M^{ES,c}_2(\hat{y}_n\hat{y}_j-\frac{1}{3}\delta_{nj})(\hat{y}^\perp_m\hat{y}_i+\hat{y}_m\hat{y}^\perp_i)+\\ & M^{ES,c}_3(\hat{y}_m\hat{y}_i-\frac{1}{3}\delta_{mi})(\hat{y}^\perp_n\hat{y}_j+\hat{y}_n\hat{y}^\perp_j)+M^{ES,c}_4(\hat{y}^\perp_m\hat{y}_i\hat{y}^\perp_n\hat{y}_j+\hat{y}^\perp_m\hat{y}_i\hat{y}_n\hat{y}^\perp_j+\\ & \hat{y}_m\hat{y}^\perp_i\hat{y}^\perp_n\hat{y}_j+\hat{y}_m\hat{y}^\perp_i\hat{y}_n\hat{y}^\perp_j)+M^{ES,c}_5(\hat{y}^\perp_m\hat{y}^\perp_i-\frac{1}{3}\delta_{mi})(\hat{y}_n\hat{y}_j-\frac{1}{3}\delta_{nj})+\\ & M^{ES,c}_6(\hat{y}_m\hat{y}_i-\frac{1}{3}\delta_{mi})(\hat{y}^\perp_n\hat{y}^\perp_j-\frac{1}{3}\delta_{nj})+M^{ES,c}_7(\hat{y}^\perp_m\hat{y}^\perp_i-\frac{1}{3}\delta_{mi})(\hat{y}^\perp_n\hat{y}_j+\hat{y}_n\hat{y}^\perp_j)+\\ & M^{ES,c}_8(\hat{y}^\perp_n\hat{y}^\perp_j-\frac{1}{3}\delta_{nj})(\hat{y}^\perp_m\hat{y}_i+\hat{y}_m\hat{y}^\perp_i)+M^{ES,c}_9(\hat{y}^\perp_m\hat{y}^\perp_i-\frac{1}{3}\delta_{mi})(\hat{y}^\perp_n\hat{y}^\perp_j-\frac{1}{3}\delta_{nj})+\\ & M^{ES,c}_{10}(\delta_{mn}\hat{y}_i\hat{y}_j+\delta_{mj}\hat{y}_i\hat{y}_n+\delta_{in}\hat{y}_m\hat{y}_j+\delta_{ij}\hat{y}_m\hat{y}_n-\frac{4}{3}\delta_{nj}\hat{y}_i\hat{y}_m-\frac{4}{3}\delta_{im}\hat{y}_n\hat{y}_j\\ & +\frac{4}{9}\delta_{im}\delta_{nj})+M^{ES,c}_{11}(\delta_{mn}\hat{y}^\perp_i\hat{y}_j+\delta_{mj}\hat{y}^\perp_i\hat{y}_n+\delta_{in}\hat{y}^\perp_m\hat{y}_j+\delta_{ij}\hat{y}^\perp_m\hat{y}_n\\ & -\frac{2}{3}\delta_{nj}(\hat{y}_i\hat{y}^\perp_m+\hat{y}^\perp_i\hat{y}_m)-\frac{2}{3}\delta_{mi}(\hat{y}_n\hat{y}^\perp_j+\hat{y}^\perp_n\hat{y}_j))+M^{ES,c}_{12}(\delta_{mn}\hat{y}_i\hat{y}^\perp_j+\delta_{mj}\hat{y}_i\hat{y}^\perp_n+\\ & \delta_{in}\hat{y}_m\hat{y}^\perp_j+\delta_{ij}\hat{y}_m\hat{y}^\perp_n-\frac{2}{3}\delta_{nj}(\hat{y}_i\hat{y}^\perp_m+\hat{y}^\perp_i\hat{y}_m)-\frac{2}{3}\delta_{mi}(\hat{y}_n\hat{y}^\perp_j+\hat{y}^\perp_n\hat{y}_j))+\\ & M^{ES,c}_{13}(\delta_{mn}\hat{y}^\perp_i\hat{y}^\perp_j+\delta_{mj}\hat{y}^\perp_i\hat{y}^\perp_n+\delta_{in}\hat{y}^\perp_m\hat{y}^\perp_j+\delta_{ij}\hat{y}^\perp_m\hat{y}^\perp_n-\frac{4}{3}\delta_{nj}\hat{y}^\perp_i\hat{y}^\perp_m-\frac{4}{3}\delta_{im}\hat{y}^\perp_n\hat{y}^\perp_j\\ & +\frac{4}{9}\delta_{im}\delta_{nj})+M^{ES,c}_{14}(\delta_{mn}\delta_{ij}+\delta_{mj}\delta_{ni}-\frac{2}{3}\delta_{nj}\delta_{im}) \qquad \text{(A.12a)}\end{aligned}$$

$$\begin{aligned}M^{ES,c}_1 =& \left(\frac{a}{R}\right)^3\Big[(9(2b^4x^2(-2+y^2)-2(-1+x^2)(-2+y^2)+b^2(1+y^2-3x^2(-1\\ & +y^2))))/(4(-1+b^2)^2x^2y^2)+(9(8-4y^2+4b^9x^7y^5(-18+13y^2)-2x^2(4-20y^2\\ & +9y^4)+x^6y^4(-63+49y^2+10y^4)+b^8x^6y^4(312+(-143+97x^2)y^2-3(5\\ & +29x^2)y^4)+x^4(-36y^2+81y^4-39y^6)+b^7x^5y^3(-418+(209\\ & -507x^2)y^2+(33+164x^2-27x^4)y^4+3x^2(13+9x^2)y^6)-b^6x^4y^2(-252-6(-35\\ & +66x^2)y^2+(78+163x^2-455x^4)y^4+(17x^2+50x^4-9x^6)y^6+9(x^4+x^6)y^8)\\ & -b^4x^2(-8+(67+153x^2)y^2+(63-339x^2+720x^4)y^4+4x^2(81-159x^2\\ & +106x^4)y^6+(142x^4-211x^6-99x^8)y^8+27x^6(-1+x^2)y^{10})+b^5x^3y(-72+(141\end{aligned}$$

$$+ 59x^2)y^2 + (107 - 23x^2 + 54x^4)y^4 - 18x^2(-8 + 5x^2 + 20x^4)y^6 - x^4(108 - 107x^2$$
$$+ x^4)y^8 + (x^6 + x^8)y^{10}) + bxy(36(-2 + y^2) - 2x^{10}y^8(-9 + 5y^2) + x^8y^6(81$$
$$- 57y^2 + 8y^4) + 8x^2(9 - 36y^2 + 16y^4) + x^6y^4(273 - 254y^2 + 33y^4)$$
$$+ x^4y^2(252 - 403y^2 + 147y^4)) + b^3xy(18(1 + y^2) + x^{10}y^8(-11 + 3y^2)$$
$$+ x^8y^6(522 - 299y^2 - 3y^4) + 4x^6y^4(252 - 211y^2 + 63y^4) + x^2(54 - 411y^2$$
$$+ 269y^4) + x^4y^2(611 - 1043y^2 + 432y^4)) + b^2(-2(1 + y^2) + 18x^{10}y^8(-9 + 5y^2) - 4x^8y^6(158$$
$$- 121y^2 + 18y^4) - 3x^2(2 - 83y^2 + 45y^4) - 3x^4y^2(93 - 254y^2 + 105y^4)$$
$$+ x^6(-681y^4 + 881y^6 - 340y^8))))/(8(-1 + b^2)^2x^2y^{11}\zeta^9)\Big]$$
$$+ \left(\frac{a}{R}\right)^5 \Big[- (9(288b^{10}x^8y^6 - 4(-4 + y^2) + x^8y^6(567 + 140y^2 - 50y^4) + x^2(-8$$
$$+ 88y^2 - 22y^4) - 8b^9x^7y^5(99 + (65 + 34x^2)y^2 - 15y^4) + x^6y^4(-99 - 994y^2$$
$$+ 481y^4) + x^4(-44y^2 + 198y^4 - 117y^6) + b^8x^6y^4(1136 + (890 + 481x^2)y^2$$
$$+ (-327 + 926x^2 - 161x^4)y^4 - 393x^2y^6) - b^7x^5y^3(910 + (150 + 979x^2)y^2$$
$$+ (-363 - 556x^2 + 496x^4)y^4 + x^2(-490 + 54x^2 + 63x^4)y^6 - 27x^4y^8)$$
$$+ b^6x^4y^2(396 + (-660 + 524x^2)y^2 + (-274 - 3218x^2 + 2135x^4)y^4 + x^2(-95 - 3728x^2$$
$$+ 2198x^4)y^6 + x^4(1228 + 22x^2 + 11x^4)y^8 - 11x^6y^{10}) + b^5x^3y(-88 + (462$$
$$+ 269x^2)y^2 + (245 + 1698x^2 - 55x^4)y^4 + (407x^2 + 3312x^4 - 2386x^6)y^6$$
$$+ (-1492x^4 + 562x^6 - 523x^8)y^8 - x^6(89 + 2x^2 + x^4)y^{10} + x^8y^{12}) + b^4x^2(8$$
$$- 11(18 + 23x^2)y^2 + (-99 + 1782x^2 - 2047x^4)y^4 + (-1021x^2 + 3696x^4 - 3064x^6)y^6$$
$$+ (-658x^4 + 4554x^6 - 2461x^8)y^8 + x^6(-1855 - 154x^2 + 121x^4)y^{10}$$
$$+ 33x^8y^{12}) - b^2(198x^{12}y^{10} + 2(2 + y^2) + x^8y^6(3179 - 88y^2 - 80y^4)$$
$$+ 2x^{10}y^8(283 - 132y^2 + 44y^4) + x^2(6 - 770y^2 + 209y^4) + x^4y^2(429 - 2640y^2$$
$$+ 568y^4) + x^6y^4(1494 - 5170y^2 + 2173y^4)) + b^3xy(-11x^{12}y^{10}$$
$$+ 22(2 + y^2) + x^{10}y^8(817 + 14y^2 - 3y^4) + x^8y^6(5830 - 1006y^2 + 339y^4) + x^2(66 - 1650y^2$$
$$+ 533y^4) + x^4y^2(1235 - 6642y^2 + 1793y^4) + x^6y^4(4367 - 8456y^2 + 3476y^4))$$
$$+ bxy(18x^{12}y^{10} + 44(-4 + y^2) + x^{10}y^8(99 - 24y^2 + 8y^4) + 4x^2(22$$

$$
\begin{aligned}
&- 198y^2 + 53y^4) + x^8y^6(-696 - 162y^2 + 53y^4) + x^4y^2(396 - 450y^2 + 209y^4) \\
&+ x^6(231y^4 + 1148y^6 - 614y^8)))))/(40(-1 + b^2)^2x^2y^{13}\zeta^{11}) \\
&- (9(-1 + 2bxy - x^2y^2)^5(4b^4x^2 - 2(-4 + 2x^2 + y^2) - b^2(2 + 3x^2 \\
&+ y^2)))/(20(-1 + b^2)^2x^2y^{12}\zeta^{10})\Big] + \left(\frac{a}{R}\right)^7 \Big[- (9(-4 + b^2)(-1 + 2bxy - x^2y^2)^7)/(100(-1 + b^2)^2x^2y^{16}\zeta^{14}) \\
&+ (9(8 + 52x^2y^2 + 143x^4y^4 - 7748x^6y^6 + 5663x^8y^8 \\
&+ 2080b^{10}x^8y^8 - 350x^{10}y^{10} - 8b^9x^7y^7(710 + 467x^2y^2) \\
&+ b^8x^6y^6(5785 + 1642x^2y^2 - 1883x^4y^4) + b^7x^5y^5(-2145 + 11431x^2y^2 + 19909x^4y^4 \\
&- 139x^6y^6) + b^6x^4y^4(-1122 - 16627x^2y^2 - 30455x^4y^4 + 5055x^6y^6 \\
&+ 13x^8y^8) + b^4x^2y^2(-143 + 3102x^2y^2 + 12441x^4y^4 + 55901x^6y^6 - 4954x^8y^8 \\
&- 91x^{10}y^{10}) + b^5x^3y^3(429 + 9438x^2y^2 + 8109x^4y^4 - 33577x^6y^6 \\
&+ 674x^8y^8 - x^{10}y^{10}) + b^3xy(26 - 1573x^2y^2 - 18876x^4y^4 \\
&- 37229x^6y^6 + 19511x^8y^8 - 970x^{10}y^{10} + 7x^{12}y^{12}) - bxy(104 + 572x^2y^2 - 3861x^4y^4 \\
&- 13073x^6y^6 + 6397x^8y^8 + 33x^{10}y^{10} + 12x^{12}y^{12}) + b^2(-2 + 559x^2y^2 \\
&+ 2167x^4y^4 + 16445x^6y^6 - 27109x^8y^8 + 3848x^{10}y^{10} \\
&+ 156x^{12}y^{12})))/(200(-1 + b^2)^2x^2y^{15}\zeta^{13})\Big] \qquad \text{(A.12b)}
\end{aligned}
$$

$$
\begin{aligned}
M_2^{ES,c} = &\left(\frac{a}{R}\right)^3 \Big[(9b(4 - 2y^2 + x^2(-2 + y^2 + b^2(-3 + 2y^2))))/(4(1 - b^2)^{3/2}x^2y^2) \\
&+ (9(4b^8x^7y^5(-18 + 13y^2) + b^7x^6y^4(252 + (-135 + 97x^2)y^2 - 3(5 \\
&+ 29x^2)y^4) + b^6x^5y^3(-318 + (246 - 422x^2)y^2 + (-26 + 241x^2 - 27x^4)y^4 \\
&+ 3x^2(13 + 9x^2)y^6) + b^5x^4y^2(189 + 9(-47 + 64x^2)y^2 + 3(52 - 180x^2 \\
&+ 125x^4)y^4 + x^2(62 - 178x^2 + 9x^4)y^6 - 9(x^4 + x^6)y^8) + b^3x^2(6 + (-256 + 153x^2)y^2 + 9(14 \\
&- 83x^2 + 47x^4)y^4 + 6x^2(53 - 120x^2 + 68x^4)y^6 + x^4(299 - 322x^2 + 81x^4)y^8 \\
&- 9x^6(-4 + 5x^2)y^{10}) + b^4x^3y(-54 + (456 - 393x^2)y^2 + (-214 \\
&+ 893x^2 - 606x^4)y^4 - 3x^2(100 - 174x^2 + 99x^4)y^6 - x^4(138 - 170x^2 \\
&+ x^4)y^8 + (x^6 + x^8)y^{10}) - x^3y^5(4 + x^2(22 - 26y^2) + x^6y^4(-3 + y^2) + x^4(-35 + 19y^2 \\
&+ 6y^4)) + b^2xy(-4x^8y^6(-3 + y^2)^2 - 36(-2 + y^2) + x^{10}y^8(-9 + 5y^2) - 2x^2(18 - 135y^2
\end{aligned}
$$

$$+ 59y^4) + x^4(-129y^2 + 395y^4 - 204y^6) + x^6(-195y^4 + 248y^6 - 39y^8))$$

$$+ b(4(-2 + y^2) + 6x^4y^2(3 - 9y^2 + 5y^4) + 2x^2(2 - 19y^2 + 9y^4) + x^8y^6(-40 + 11y^2$$

$$+ 9y^4) + x^6(9y^4 - 33y^6 - 10y^8))))/(8(1 - b^2)^{3/2}x^2y^{11}\zeta^9)\Big] + \left(\frac{a}{R}\right)^5 \Big[(9b((2 + 3b^2)x^2 + 2(-4$$

$$+ y^2)))/(20(1 - b^2)^{3/2}x^2y^2) - (9(288b^9x^8y^6 - 8b^8x^7y^5(99 + (65 + 34x^2)y^2 - 15y^4) +$$

$$b^7x^6y^4(996 + (650 + 681x^2)y^2 + (-91 + 926x^2 - 161x^4)y^4 - 393x^2y^6) - b^6x^5y^3(714 + 8(-90$$

$$+ 143x^2)y^2 + (286 - 366x^2 + 451x^4)y^4 + x^2(-271 + 54x^2 + 63x^4)y^6$$

$$- 27x^4y^8) + b^5x^4y^2(297 + 165(-12 + 7x^2)y^2 + (548 - 4248x^2 + 2115x^4)y^4 + 2x^2(301$$

$$- 1581x^2 + 921x^4)y^6 + x^4(1193 + 22x^2 + 11x^4)y^8 - 11x^6y^{10}) - b^4x^3y(66$$

$$+ 3(-616 + 239x^2)y^2 + (490 - 5328x^2 + 2343x^4)y^4 + x^2(946 - 6228x^2$$

$$+ 3477x^4)y^6 + (2362x^4 - 478x^6 + 424x^8)y^8 + x^6(143 + 2x^2 + x^4)y^{10} - x^8y^{12})$$

$$+ b^3x^2(6 + 33(-24 + 7x^2)y^2 + 6(33 - 572x^2 + 217x^4)y^4 + x^2(752 - 4542x^2$$

$$+ 2277x^4)y^6 - 7x^4(-263 - 54x^2 + 33x^4)y^8 + x^6(-415 - 132x^2 + 99x^4)y^{10}$$

$$+ 44x^8y^{12}) - x^3y^5(28 + x^2(624 - 330y^2) + x^8y^6(-6 + y^2) + x^6y^2(245$$

$$- 18y^2 + y^4) + x^4(-385 - 648y^2 + 272y^4)) - b^2xy(9x^{12}y^{10} + 44(-4 + y^2) + x^{10}y^8(63$$

$$- 12y^2 + 4y^4) + 2x^2(22 - 396y^2 + 71y^4) + x^8y^6(-1145 - 438y^2 + 103y^4)$$

$$+ x^4y^2(219 - 1968y^2 + 946y^4) + x^6(726y^4 + 1442y^6 - 923y^8)) + b(4(-4 + y^2)$$

$$+ 2x^4y^2(11 + 66y^2 + 10y^4) + x^{10}y^8(200 - 66y^2 + 11y^4) + x^2(4 - 88y^2$$

$$+ 22y^4) + x^8y^6(-741 - 782y^2 + 275y^4) + x^6(-153y^4$$

$$+ 748y^6 - 504y^8))))/(40(1 - b^2)^{3/2}x^2y^{13}\zeta^{11})\Big] +$$

$$\left(\frac{a}{R}\right)^7 \Big[- (9b(-1 + 2bxy - x^2y^2)^7)/(25(1 - b^2)^{3/2}x^2y^{16}\zeta^{14})$$

$$+ (9(2080b^9x^8y^8 - 8b^8x^7y^7(650 + 467x^2y^2) + b^7x^6y^6(4225$$

$$+ 3482x^2y^2 - 1883x^4y^4) + b^6x^7y^7(7281 + 17178x^2y^2 - 139x^4y^4)$$

$$+ 3x^5y^5(-1144 + 2764x^2y^2 - 699x^4y^4 + 14x^6y^6 + x^8y^8)$$

$$+ b^5x^4y^4(-1518 - 14742x^2y^2 - 32673x^4y^4 + 4312x^6y^6 + 13x^8y^8) + b^4x^3y^3(1716$$

$$+ 8580x^2y^2 + 26490x^4y^4 - 19525x^6y^6 + 580x^8y^8 - x^{10}y^{10}) - b^3x^2y^2(572$$

$$+ 5544x^2y^2 + 7215x^4y^4 - 29420x^6y^6 + 5835x^8y^8 + 78x^{10}y^{10}) + b(-8 - 52x^2y^2$$
$$+ 1342x^4y^4 + 4004x^6y^6 - 12605x^8y^8 + 1118x^{10}y^{10} - 39x^{12}y^{12})$$
$$+ b^2xy(104 + 572x^2y^2 + 5148x^4y^4 - 23135x^6y^6 + 13900x^8y^8$$
$$+ 141x^{10}y^{10} + 6x^{12}y^{12})))/(200(1 - b^2)^{3/2}x^2y^{15}\zeta^{13})\Big] \qquad \text{(A.12c)}$$

$$M_3^{ES,c} = \left(\frac{a}{R}\right)^3 \Big[(9b(5 - 4y^2 + x^2(-7 + (5 + b^2)y^2)))/(4(1 - b^2)^{3/2}x^2y^2)$$
$$+ (9(4b^8x^7y^5(6 + 5y^2) + b^7x^6y^4(-24 - (63 + 79x^2)y^2 + 5(-7 + 5x^2)y^4)$$
$$+ b^6x^5y^3(6 + (213 - 151x^2)y^2 + (-55 + 197x^2 + 30x^4)y^4) + b^4x^3y^3(543 - 415y^2$$
$$+ x^8y^6 + 23x^6y^4(-12 + 11y^2) + x^2(-747 + 1358y^2 - 690y^4) - 3x^4y^2(383$$
$$- 376y^2 + 42y^4)) + b(-10 + 8y^2 + 18x^{10}y^8(3 - 2y^2) + 21x^4y^2(3 - 7y^2$$
$$+ 3y^4) + x^8y^6(199 - 182y^2 + 36y^4) + x^2(14 - 55y^2 + 36y^4) + x^6y^4(129 - 228y^2$$
$$+ 136y^4)) + b^3x^2y^2(-317 + 252y^2 - 9x^8y^6(-9 + 8y^2) + 4x^6y^4(138 - 115y^2$$
$$+ 9y^4) + 3x^2(147 - 355y^2 + 210y^4) + x^4y^2(1041 - 1224y^2 + 281y^4))$$
$$+ b^5x^4y^4(-480 + 315y^2 - 9x^6y^4 + x^4(504y^2 - 481y^4) + x^2(618 - 837y^2 + 290y^4)) + b^2xy(90$$
$$- 72y^2 + x^{10}y^8(-9 + 8y^2) + x^2(-126 + 405y^2 - 262y^4) + x^8y^6(-231$$
$$+ 165y^2 - 4y^4) - 2x^6y^4(216 - 233y^2 + 72y^4) + x^4(-435y^2 + 656y^4 - 219y^6))$$
$$+ x^3y^5(5 + x^2(41 - 44y^2) + x^4(-56 + 61y^2 - 18y^4) + x^6(-27y^2 + 24y^4 - 4y^6)$$
$$+ x^8(-6y^4 + 4y^6))))/(8(1 - b^2)^{3/2}x^2y^{11}\zeta^9)\Big] +$$
$$\left(\frac{a}{R}\right)^5 \Big[(9(96b^9x^8y^6 - 8b^8x^7y^5(33 + (-25 + 58x^2)y^2 + 35y^4) + b^7x^6y^4(192$$
$$+ (470 + 207x^2)y^2 + (235 + 626x^2 - 35x^4)y^4 - 175x^2y^6) + b^6x^5y^3(-42$$
$$+ (-2370 + 1727x^2)y^2 + (605 - 3714x^2 + 2525x^4)y^4 - 3x^2(-645 + 28x^2$$
$$+ 18x^4)y^6) + x^3y^5(-35 + 6x^{10}y^6 + 7x^2(-156 + 77y^2) + x^4(616 + 114y^2$$
$$- 38y^4) + x^8y^4(33 - 12y^2 + 4y^4) + x^6y^2(13 - 66y^2 + 22y^4)) + b^5x^4y^4(3300$$
$$- 1175y^2 + 11x^8y^6 + x^6y^4(-639 + 22y^2) + x^2(-2574 + 6612y^2 - 3695y^4)$$
$$- 2x^4y^2(2793 + 99y^2 + 31y^4)) - b(-20 + 8y^2 + 66x^{12}y^{10} + 2x^2(7 - 55y^2$$
$$+ 22y^4) + x^{10}y^8(247 - 132y^2 + 44y^4) + 2x^8y^6(825 - 197y^2 + 74y^4) + x^4y^2(77 - 660y^2$$

$$+ 119y^4) + x^6y^4(342 - 2932y^2 + 1377y^4)) - b^3x^2y^2(99x^{10}y^8 + 198(-5$$
$$+ 2y^2) + x^8y^6(1389 - 66y^2 + 44y^4) + x^6y^4(-465 - 2478y^2 + 935y^4) + x^2(693$$
$$- 2640y^2 + 1346y^4) + x^4(1896y^2 + 774y^4 - 1141y^6)) + b^2xy(9x^{12}y^{10}$$
$$+ 44(-5 + 2y^2) + 2x^{10}y^8(171 - 3y^2 + 2y^4) + x^8y^6(2033 - 612y^2 + 220y^4)$$
$$+ 2x^2(77 - 495y^2 + 233y^4) + x^6y^4(-33 - 4202y^2 + 1715y^4) + x^4(651y^2 - 186y^4$$
$$- 473y^6)) + b^4x^3y^3(-2310 + 889y^2 - x^{10}y^8 + x^6y^4(513 - 338y^2$$
$$+ 198y^4) + x^2(1701 - 5592y^2 + 3025y^4) + x^4(4422y^2 + 1002y^4 - 692y^6)$$
$$+ x^8(449y^6 - 2y^8)))))/(40(1 - b^2)^{3/2}x^2y^{13}\zeta^{11}) - (9b(-10 + 7x^2$$
$$+ 4y^2)(-1 + 2bxy - x^2y^2)^5)/(20(1 - b^2)^{3/2}x^2y^{12}\zeta^{10})\Big] +$$
$$\left(\frac{a}{R}\right)^7 \Big[- (9b(-1 + 2bxy - x^2y^2)^7)/(20(1 - b^2)^{3/2}x^2y^{16}\zeta^{14})$$
$$+ (9(800b^9x^8y^8 + 8b^8x^7y^7(-70 + 557x^2y^2) + b^7x^6y^6(-3055$$
$$- 18062x^2y^2 + 893x^4y^4) + b^6x^5y^5(6435 + 28044x^2y^2 - 13389x^4y^4$$
$$+ 94x^6y^6) + 3x^5y^5(2002 - 2287x^2y^2 + 342x^4y^4 + 13x^6y^6 + 2x^8y^8)$$
$$- b^5x^4y^4(5610 + 21528x^2y^2 - 35445x^4y^4 + 3430x^6y^6 + 13x^8y^8) + b^3x^2y^2(-715$$
$$+ 495x^2y^2 + 22191x^4y^4 - 41354x^6y^6 + 606x^8y^8 - 39x^{10}y^{10})$$
$$+ b^4x^3y^3(2145 + 8151x^2y^2 - 39819x^4y^4 + 21586x^6y^6 + 176x^8y^8 + x^{10}y^{10})$$
$$+ b^2xy(130 + 715x^2y^2 - 7722x^4y^4 + 36356x^6y^6 - 6529x^8y^8$$
$$+ 471x^{10}y^{10} + 3x^{12}y^{12}) - b(10 + 65x^2y^2 + 2035x^4y^4 + 14768x^6y^6 - 10301x^8y^8$$
$$+ 929x^{10}y^{10} + 78x^{12}y^{12})))/(200(1 - b^2)^{3/2}x^2y^{15}\zeta^{13})\Big] \qquad \text{(A.12d)}$$

$$M_4^{ES,c} = \left(\frac{a}{R}\right)^3 \Big[- (9((-2 + x^2)(-2 + y^2) + b^4x^2(2 + y^2) + b^2(5 - 7y^2 + x^2(-9$$
$$+ 7y^2))))/(8(-1 + b^2)^2x^2y^2) - (3(x^8y^6(-27 + y^2) + 12(-2 + y^2)$$
$$+ 24b^9x^7y^5(6 + 5y^2) - 3x^6y^4(-76 + 73y^2 + 9y^4) + x^2(12 - 119y^2 + 57y^4) + 3x^4y^2(19$$
$$- 105y^2 + 76y^4) + 6b^8x^6y^4(-84 - (39 + 79x^2)y^2 + 5(-7 + 5x^2)y^4)$$
$$+ 4b^7x^5y^3(159 + (139 + 141x^2)y^2 + 3(-13 + 37x^2 + 15x^4)y^4) - 6b^6x^4y^2(63 + (227$$
$$- 200x^2)y^2 + (-263 + 452x^2 - 184x^4)y^4 + x^2(-241 + 321x^2 + 9x^4)y^6)$$

$$+ 2b^5x^3y(54 + (831 - 1248x^2)y^2 + (-1113 + 2537x^2 - 2193x^4)y^4 - 3x^2(668 - 773x^2$$
$$+ 70x^4)y^6 + 3x^4(-79 + 143x^2 + x^4)y^8) + b^4x^2(-12 + 2(-478 + 825x^2)y^2 + 3(442$$
$$- 1591x^2 + 1607x^4)y^4 + 3x^2(1355 - 1895x^2 + 758x^4)y^6 + x^4(1806 - 1727x^2$$
$$+ 135x^4)y^8 - 27x^6(-5 + 9x^2)y^{10}) + b^2(-81x^{10}y^8(-5 + 3y^2) + 6(-5$$
$$+ 7y^2) + 3x^4y^2(205 - 766y^2 + 311y^4) + x^8y^6(1659 - 1520y^2 + 351y^4) + 3x^6y^4(353$$
$$- 830y^2 + 507y^4) + x^2(54 - 923y^2 + 561y^4)) + b^3xy(54(5 - 7y^2)$$
$$+ 3x^{10}y^8(-5 + 9y^2) - 3x^8y^6(503 - 320y^2 + 5y^4) - 3x^6y^4(793 - 876y^2 + 431y^4) - 3x^2(162$$
$$- 839y^2 + 637y^4) + x^4(-2271y^2 + 4438y^4 - 1911y^6)) + 3bxy(-36(-2 + y^2)$$
$$+ 3x^{10}y^8(-5 + 3y^2) + x^2(-36 + 281y^2 - 133y^4) + x^8y^6(-65 + 60y^2 - 13y^4)$$
$$+ x^4(-135y^2 + 424y^4 - 243y^6) + x^6(-249y^4 + 306y^6 - 59y^8))))/(16(-1$$
$$+ b^2)^2x^2y^{11}\zeta^9)\Big] + \left(\frac{a}{R}\right)^5 \Big[(9(-192b^{10}x^8y^6 + 45x^{10}y^8 + 4(-4 + y^2) + x^2(4 - 102y^2 + 27y^4)$$
$$+ 16b^9x^7y^5(33 + (-25 + 58x^2)y^2 + 35y^4) + x^8y^6(-801 - 194y^2 + 45y^4)$$
$$+ x^4y^2(27 - 770y^2 + 437y^4) + 2b^8x^6y^4(-332 + (122 - 647x^2)y^2 + (-351$$
$$- 626x^2 + 35x^4)y^4 + 175x^2y^6) + 4b^7x^5y^3(119 + (344 - 66x^2)y^2 + (-143$$
$$+ 1238x^2 - 840x^4)y^4 + 3x^2(-291 + 14x^2 + 9x^4)y^6) + x^6(437y^4$$
$$+ 1642y^6 - 801y^8) - 2b^6x^4y^2(99 + (1320 - 955x^2)y^2 + (-883 + 4262x^2 - 3516x^4)y^4 + x^2(-3438$$
$$- 1524x^2 + 233x^4)y^6 + x^4(257 + 22x^2 + 11x^4)y^8) + 2b^5x^3y(22 + (1208$$
$$- 982x^2)y^2 + (-829 + 4378x^2 - 3465x^4)y^4 + 3x^2(-1089 - 818x^2 + 345x^4)y^6$$
$$+ (1083x^4 - 94x^6 - 131x^8)y^8 + x^6(-123 + 2x^2 + x^4)y^{10}) + b^4x^2(-4 + 2(-502$$
$$+ 437x^2)y^2 + (698 - 6842x^2 + 4285x^4)y^4 + (3901x^2 + 402x^4 - 1437x^6)y^6 + x^4(-1821$$
$$- 7022x^2 + 3011x^4)y^8 + x^6(2927 + 66x^2 + 55x^4)y^{10}$$
$$+ 55x^8y^{12}) - bxy(15x^{12}y^{10} + 44(-4 + y^2) + 2x^6y^4(627 + 808y^2 - 444y^4) + x^{10}y^8(90$$
$$- 38y^2 + 13y^4) + 2x^8y^6(-420 - 118y^2 + 35y^4) + x^2(44 - 898y^2 + 239y^4)$$
$$+ x^4y^2(253 - 2268y^2 + 1210y^4)) - b^3xy(5x^{12}y^{10} + 22(-10 + 7y^2) + x^4(1229y^2$$
$$- 4232y^4) + x^{10}y^8(746 + 6y^2 + 5y^4) + 2x^8y^6(3209 - 882y^2 + 337y^4)$$

$$+ x^2(198 - 2626y^2 + 1073y^4) + 2x^6y^4(198 - 6926y^2 + 3031y^4)) + b^2(-20$$
$$+ 14y^2 + 165x^{12}y^{10} + 2x^8y^6(2504 - 260y^2 + 81y^4) + x^{10}y^8(310 - 418y^2$$
$$+ 143y^4) + x^2(18 - 874y^2 + 265y^4) + 4x^6y^4(-7 - 2599y^2 + 1191y^4)$$
$$+ x^4(287y^2 - 1628y^4 - 164y^6))))/(80(-1 + b^2)^2x^2y^{13}\zeta^{11})$$
$$- (9(-1 + 2bxy - x^2y^2)^5(2b^4x^2 + b^2(10 - 9x^2 - 7y^2) - 2(-4 + x^2$$
$$+ y^2)))/(40(-1 + b^2)^2x^2y^{12}\zeta^{10})\Big] +$$
$$\left(\frac{a}{R}\right)^7 \Big[- (9(4 + 5b^2))/(200(-1 + b^2)^2x^2y^2) + (9(-8 - 87x^2y^2 - 2598x^4y^4$$
$$+ 15678x^6y^6 - 9038x^8y^8 + 1600b^{10}x^8y^8 + 485x^{10}y^{10}$$
$$+ 16b^9x^7y^7(-218 + 557x^2y^2) + 2b^8x^6y^6(793 - 15774x^2y^2 + 893x^4y^4)$$
$$+ 4b^7x^5y^5(572 + 11655x^2y^2 - 8506x^4y^4 + 47x^6y^6) - 2b^6x^4y^4(1108$$
$$+ 19123x^2y^2 - 41949x^4y^4 + 3289x^6y^6 + 13x^8y^8) + 2b^5x^3y^3(1216 + 8177x^2y^2$$
$$- 42886x^4y^4 + 28762x^6y^6 - 166x^8y^8 + x^{10}y^{10}) + b^4x^2y^2(-750$$
$$- 11751x^2y^2 + 47086x^4y^4 - 116904x^6y^6 + 4136x^8y^8 + 39x^{10}y^{10}) + bxy(104$$
$$+ 859x^2y^2 + 4199x^4y^4 - 27878x^6y^6 + 9062x^8y^8 + 83x^{10}y^{10} + 19x^{12}y^{12})$$
$$- b^2(10 + 567x^2y^2 - 3695x^4y^4 + 56992x^6y^6 - 48826x^8y^8$$
$$+ 4977x^{10}y^{10} + 247x^{12}y^{12}) + b^3(130xy + 1857x^3y^3 + 325x^5y^5$$
$$+ 101406x^7y^7 - 28604x^9y^9 + 1465x^{11}y^{11} - 3x^{13}y^{13}))\zeta)/(400(-1 + b^2)^2x^2y(-1$$
$$+ 2bxy - x^2y^2)^7)\Big] \qquad \text{(A.12e)}$$

$$M_5^{ES,c} = \left(\frac{a}{R}\right)^3 \Big[- (9b^2(-3 + (1 + 2b^2)x^2)(-1 + y^2))/(4(-1 + b^2)^2x^2y^2)$$
$$+ (3(12b^9x^7y^5(18 - 13y^2) + 3b^8x^6y^4(-192 + (127 - 97x^2)y^2 + 3(5$$
$$+ 29x^2)y^4) + b^7x^5y^3(654 + (-677 + 699x^2)y^2 + 3(53 - 234x^2 + 27x^4)y^4 - 9x^2(13$$
$$+ 9x^2)y^6) + 3b^6x^4y^2(-126 + (347 - 293x^2)y^2 + (-239 + 529x^2 - 146x^4)y^4$$
$$+ (-104x^2 + 167x^4 - 9x^6)y^6 + 9(x^4 + x^6)y^8) + b^4x^2(-12 + (574 - 240x^2)y^2 - 3(188$$

$$
\begin{aligned}
&- 569x^2 + 265x^4)y^4 - 3x^2(445 - 577x^2 + 334x^4)y^6 + (-1254x^4 + 1045x^6 \\
&- 135x^8)y^8 + 135x^6(-1 + x^2)y^{10}) + b^5x^3y(108 + 60(-17 + 10x^2)y^2 + 2(462 \\
&- 1126x^2 + 507x^4)y^4 + 3x^2(428 - 509x^2 + 175x^4)y^6 + 3x^4(175 - 174x^2 + x^4)y^8 \\
&- 3(x^6 + x^8)y^{10}) + 3bx^3y^3(11 - 7y^2 + x^2(-15 + 16y^2 - 33y^4) + 2x^6y^4(2 \\
&- 3y^2 + y^4) + x^4y^2(-51 + 19y^2 + 16y^4)) + b^3xy(162(-1 + y^2) \\
&- 15x^{10}y^8(-1 + y^2) + 15x^8y^6(2 - 3y^2 + y^4) + 12x^6y^4(41 - 49y^2 + 16y^4) + x^2(54 - 687y^2 \\
&+ 609y^4) + x^4y^2(303 - 899y^2 + 924y^4)) + x^2y^2(-5 + 3y^2 + x^2(3 - 45y^2 \\
&+ 66y^4) + x^4(66y^2 - 42y^6) + x^6(-42y^4 + 40y^6)) - b^2(18(-1 + y^2) + x^8y^6(-261 + 173y^2 \\
&+ 54y^4) + x^2(6 - 97y^2 + 87y^4) + 3x^4y^2(11 - 71y^2 + 94y^4) \\
&+ x^6(84y^4 - 81y^6 - 51y^8))))/(8(-1 + b^2)^2x^2y^{11}\zeta^9)\Big] + \\
&\left(\frac{a}{R}\right)^5 \Big[(9(288b^{10}x^8y^6 - 8b^9x^7y^5(99 + (65 + 34x^2)y^2 - 15y^4) \\
&+ b^8x^6y^4(856 + (666 + 465x^2)y^2 + (17 + 926x^2 - 161x^4)y^4 - 393x^2y^6) \\
&+ b^7x^5y^3(-518 + (574 - 165x^2)y^2 + (-583 + 312x^2 + 58x^4)y^4 + (124x^2 - 54x^4 \\
&- 63x^6)y^6 + 27x^4y^8) + b^6x^4y^2(198 + (-1650 + 199x^2)y^2 + (919 - 3738x^2 \\
&+ 613x^4)y^4 + x^2(913 - 3274x^2 + 1523x^4)y^6 + x^4(1427 + 22x^2 \\
&+ 11x^4)y^8 - 11x^6y^{10}) - b^5x^3y(44 + 20(-64 + 11x^2)y^2 + 2(326 - 2168x^2 + 759x^4)y^4 + 3x^2(440 \\
&- 1974x^2 + 977x^4)y^6 + x^4(2973 - 352x^2 + 214x^4)y^8 + x^6(176 + 2x^2 \\
&+ x^4)y^{10} - x^8y^{12}) + b^4x^2(4 + 116(-5 + x^2)y^2 + (292 - 2002x^2 + 941x^4)y^4 + x^2(749 \\
&- 3726x^2 + 2613x^4)y^6 + (2661x^4 + 1538x^6 - 785x^8)y^8 + x^6(-557 - 110x^2 \\
&+ 55x^4)y^{10} + 55x^8y^{12}) + bx^3y^3(-106 + 41y^2 - 2x^8y^6(-6 - 2y^2 + y^4) \\
&+ x^6y^4(-529 - 20y^2 + 10y^4) + x^2(97 - 60y^2 + 286y^4) + x^4(396y^2 \\
&+ 1422y^4 - 583y^6)) - x^2y^2(-14 + 5y^2 + 70x^8y^6 + 2x^6y^4(-190 - 72y^2 + 35y^4) + x^2(5 - 242y^2 \\
&+ 185y^4) + x^4(185y^2 + 888y^4 - 380y^6)) - b^3xy(5x^{12}y^{10} + 66(-2 + y^2) \\
&+ 5x^{10}y^8(13 - 2y^2 + y^4) + x^8y^6(-1694 - 382y^2 + 191y^4) + x^2(22 - 806y^2 \\
&+ 379y^4) + x^4y^2(349 - 694y^2 + 1155y^4) + x^6(693y^4 + 3176y^6 - 1332y^8))
\end{aligned}
$$

$$+ b^2(6(-2+y^2) + x^{10}y^8(483 - 44y^2 + 22y^4) + x^2(2 - 94y^2 + 43y^4) + x^4y^2(21$$
$$- 550y^2 + 497y^4) + x^8y^6(-1587 - 1314y^2 + 583y^4) + x^6(169y^4$$
$$+ 2142y^6 - 1199y^8)))))/(40(-1+b^2)^2x^2y^{13}\zeta^{11}) + (9b^2(-6 + x^2 + 2b^2x^2$$
$$+ 3y^2)(-1 + 2bxy - x^2y^2)^5)/(20(-1+b^2)^2x^2y^{12}\zeta^{10})\Big] +$$
$$\left(\frac{a}{R}\right)^7 \Big[(27b^2(-1 + 2bxy - x^2y^2)^7)/(100(-1$$
$$+ b^2)^2x^2y^{16}\zeta^{14}) - (9(2080b^{10}x^8y^8 - 8b^9x^7y^7(654 + 467x^2y^2)$$
$$+ b^8x^6y^6(4329 + 3626x^2y^2 - 1883x^4y^4) + b^7x^5y^5(-143 + 6659x^2y^2 + 18039x^4y^4$$
$$- 139x^6y^6) + 5x^2y^2(7 + 194x^2y^2 - 1469x^4y^4 + 1044x^6y^6 - 72x^8y^8)$$
$$+ b^6x^4y^4(-2305 - 13572x^2y^2 - 34696x^4y^4 + 5600x^6y^6 + 13x^8y^8) + b^5x^3y^3(1000$$
$$+ 10244x^2y^2 + 28019x^4y^4 - 26611x^6y^6 + 549x^8y^8 - x^{10}y^{10})$$
$$+ bx^3y^3(-287 + 949x^2y^2 + 12771x^4y^4 - 6031x^6y^6 + 76x^8y^8 + 2x^{10}y^{10})$$
$$- b^4x^2y^2(394 + 855x^2y^2 + 11206x^4y^4 - 42544x^6y^6 + 8056x^8y^8 + 65x^{10}y^{10})$$
$$+ b^3xy(78 + 1003x^2y^2 - 3328x^4y^4 - 31921x^6y^6 + 22629x^8y^8$$
$$- 18x^{10}y^{10} + 5x^{12}y^{12}) - b^2(6 + 109x^2y^2 + 2100x^4y^4$$
$$- 17498x^6y^6 + 26496x^8y^8 - 2983x^{10}y^{10} + 26x^{12}y^{12})))/(200(-1+b^2)^2x^2y^{15}\zeta^{13})\Big] \quad \text{(A.12f)}$$

$$M_6^{ES,c} = \left(\frac{a}{R}\right)^3 \Big[(9(3 + (-3 - 4b^2 + 4b^4)x^2)(-1+y^2))/(4(-1+b^2)^2x^2y^2) + (3(-18(-1$$
$$+ y^2) + 162bxy(-1+y^2) - 27b^2(-15 + 7b^2 + 2b^4)x^{10}y^8(-1+y^2)$$
$$+ 3b(-15 + 7b^2 + 2b^4)x^{11}y^9(-1+y^2) + 3bx^9y^7(67 - 78y^2 + 11y^4$$
$$+ 63b^6(-1+y^2) + b^2(442 - 435y^2 - 7y^4) + 2b^4(-115 + 114y^2 + y^4)) + x^2(-18 + 94y^2 - 78y^4$$
$$+ b^2(-24 + 601y^2 - 573y^4) + b^4(24 - 29y^2 + 3y^4)) - 3bx^3y(-54 + 232y^2 - 182y^4$$
$$+ b^2(-72 + 409y^2 - 329y^4) + b^4(72 - 83y^2 + 7y^4)) + 3bx^7y^5(90 - 155y^2$$
$$+ 49y^4 + 20b^8(-6 + 7y^2) + b^4(-193 + 409y^2 - 212y^4) + b^6(-277 + 174y^2$$
$$+ 63y^4) + 4b^2(314 - 385y^2 + 79y^4)) + x^8y^6(3 - 5y^2 + b^8(285 - 315y^2)$$
$$+ b^2(-1395 + 1726y^2 - 297y^4) - 6b^6(-230 + 206y^2 + 9y^4) + b^4(-1785 + 1504y^2 + 189y^4))$$

$$
\begin{aligned}
&- 3x^6y^4(-16 + 9y^2 - y^4 + 5b^8(-72 + 61y^2 + 21y^4) - 4b^6(34 - 77y^2 + 76y^4) + b^2(751 \\
&- 1116y^2 + 349y^4) + b^4(517 - 766y^2 + 355y^4)) - 3x^4y^2(-2(-13 + 9y^2 + 8y^4) \\
&+ b^6(-252 + 226y^2 + 44y^4) + b^4(215 - 344y^2 + 85y^4) + b^2(227 - 836y^2 \\
&+ 643y^4)) + bx^5y^3(b^4(573 + 286y^2 - 1227y^4) + 6(96 - 145y^2 + 33y^4) + b^6(-1290 + 997y^2 \\
&+ 429y^4) + b^2(1653 - 4193y^2 + 2868y^4)))))/(8(-1 + b^2)^2x^2y^{11}\zeta^9)\Big]+ \\
&\left(\frac{a}{R}\right)^5\Big[(9(6 + (-3 - 4b^2 + 4b^4)x^2 - 3y^2))/(20(-1 + b^2)^2x^2y^2) - (9(11b^2(-15 \\
&+ 7b^2 + 2b^4)x^{12}y^{10} + b(15 - 7b^2 - 2b^4)x^{13}y^{11} - 6(-2 + y^2) \\
&+ 66bxy(-2 + y^2) + bx^{11}y^9(84 - 99b^6 - 22y^2 + 11y^4 + b^2(701 + 14y^2 - 7y^4) \\
&+ 2b^4(-178 - 2y^2 + y^4)) + x^2(-6 + 52y^2 - 28y^4 + b^2(-8 + 622y^2 - 307y^4) + b^4(8 \\
&- 14y^2 + 5y^4)) + x^{10}y^8(-5 + 281b^8 + b^2(-774 + 242y^2 - 121y^4) + b^6(766 \\
&+ 44y^2 - 22y^4) + b^4(-1258 - 154y^2 + 77y^4)) + x^8y^6(-131 + 480b^{10} + 6y^2 - 5y^4 \\
&+ b^2(354 + 1200y^2 - 526y^4) + b^8(-897 + 322y^2 - 231y^4) + 2b^6(2764 - 508y^2 \\
&+ 359y^4) - 2b^4(4053 - 734y^2 + 473y^4)) + bx^9y^7(367 + 80b^8 - 124y^2 + 62y^4 \\
&+ b^4(2661 + 668y^2 - 334y^4) + b^6(-2686 - 198y^2 + 99y^4) + b^2(1558 - 1006y^2 \\
&+ 503y^4)) + x^6y^4(482 + 390y^2 - 131y^4 + b^4(346 + 13752y^2 - 7674y^4) \\
&+ b^8(1520 + 3174y^2 - 1937y^4) + 2b^2(-1520 - 858y^2 + 493y^4) + 8b^6(-161 - 1257y^2 \\
&+ 748y^4)) + bx^3y(66 - 488y^2 + 256y^4 + b^4(-88 + 106y^2 - 41y^4) + b^2(88 - 1598y^2 \\
&+ 775y^4)) + bx^7y^5(-1122 - 786y^2 + 265y^4 + b^6(1683 + 4416y^2 - 2488y^4) + 40b^8(-33 \\
&- 35y^2 + 21y^4) + b^2(7755 - 1168y^2 + 840y^4) + 3b^4(-1408 - 1674y^2 + 841y^4)) \\
&- x^4y^2(28 + 836y^2 - 482y^4 + b^4(347 + 572y^2 - 538y^4) + 4b^6(-99 - 165y^2 \\
&+ 106y^4) + b^2(351 - 4708y^2 + 2576y^4)) + bx^5y^3(326 + 2040y^2 - 1276y^4 \\
&+ b^4(697 + 7148y^2 - 4422y^4) + b^6(-994 - 2554y^2 + 1573y^4) + b^2(961 - 12178y^2 \\
&+ 6897y^4)))))/(40(-1 + b^2)^2x^2y^{13}\zeta^{11})\Big]+ \\
&\left(\frac{a}{R}\right)^7\Big[(27(-1 + 2bxy - x^2y^2)^7)/(100(-1 + b^2)^2x^2y^{16}\zeta^{14}) + (9(6 \\
&+ 4x^2y^2 - 4204x^4y^4 + 7969x^6y^6 - 1704x^8y^8
\end{aligned}
$$

$$+ 5600b^{10}x^8y^8 - 15x^{10}y^{10} + 8b^9x^7y^7(-2106 + 371x^2y^2) + b^8x^6y^6(20631$$
$$- 29210x^2y^2 + 779x^4y^4) - b^7x^5y^5(12727 - 67279x^2y^2 + 11241x^4y^4$$
$$+ 143x^6y^6) + 2b^6x^4y^4(1697 - 34827x^2y^2 + 28352x^4y^4 - 1171x^6y^6 + 13x^8y^8)$$
$$+ b^5x^3y^3(287 + 37375x^2y^2 - 104483x^4y^4 + 15115x^6y^6 + 492x^8y^8$$
$$- 2x^{10}y^{10}) + b^3x^3y^3(-1861 - 45578x^2y^2 + 61651x^4y^4 - 12669x^6y^6$$
$$- 750x^8y^8 + 7x^{10}y^{10}) - b^4x^2y^2(35 + 8847x^2y^2 - 93106x^4y^4 + 44734x^6y^6$$
$$- 2761x^8y^8 + 91x^{10}y^{10}) + b^2x^2y^2(499 + 13947x^2y^2 - 41756x^4y^4 + 21066x^6y^6$$
$$+ 533x^8y^8 + 143x^{10}y^{10}) - bxy(78 + 142x^2y^2 - 13208x^4y^4$$
$$+ 17895x^6y^6 - 1537x^8y^8 + 67x^{10}y^{10} + 11x^{12}y^{12})))/(200(-1$$
$$+ b^2)^2x^2y^{15}\zeta^{13})\Big] \qquad \text{(A.12g)}$$

$$M_7^{ES,c} = \left(\frac{a}{R}\right)^3 \Big[- (9b(-2 + (1 + b^2)x^2))/(2(1 - b^2)^{3/2}x^2y^2) - (9(4b^8x^7y^5(6 + 5y^2)$$
$$+ b^7x^6y^4(-144 - (15 + 79x^2)y^2 + 5(-7 + 5x^2)y^4) + b^6x^5y^3(206 + 5(-17$$
$$+ 79x^2)y^2 + (35 - 61x^2 + 30x^4)y^4) + x^5y^3(4 + (22 - 26x^2)y^2 + (-35 + 19x^2$$
$$+ 6x^4)y^4 + x^4(-3 + x^2)y^6) - 3b^5x^4y^2(42 + 3(-35 + 57x^2)y^2 + x^2(-57$$
$$+ 89x^2)y^4 + x^2(-35 + 28x^2 + 3x^4)y^6) - b^3x^2(4 + 36(-7 + 4x^2)y^2$$
$$+ 18x^2(-35 + 17x^2)y^4 + (-459x^4 + 321x^6)y^6 + 3x^4(35 - 43x^2 + 18x^4)y^8) + b^4x^3y(36$$
$$+ 12(-35 + 29x^2)y^2 + 12x^2(-47 + 31x^2)y^4 + 3x^2(-35 - 9x^2 + 66x^4)y^6 + (x^6$$
$$+ x^8)y^8) + b(8 - 9x^{10}y^8 + x^8y^6(-5 + 2y^2) + 9x^4y^2(-2 + 7y^2) + 4x^2(-1$$
$$+ 9y^2) + x^6y^4(-45 + 57y^2 + 35y^4)) + b^2xy(-72 + 6x^{10}y^8 - 6x^8y^6(-9 + y^2)$$
$$- 36x^2(-1 + 7y^2) + 3x^4y^2(38 - 127y^2 + 35y^4)$$
$$+ x^6(243y^4 - 239y^6)))))/(8(1 - b^2)^{3/2}x^2y^{11}\zeta^9)\Big] +$$
$$\left(\frac{a}{R}\right)^5 \Big[(9b(-4 + (1 + b^2)x^2))/(10(1 - b^2)^{3/2}x^2y^2) - (9(96b^9x^8y^6 - 8b^8x^7y^5(33+$$
$$(-25 + 58x^2)y^2 + 35y^4) + b^7x^6y^4(472 + (-970$$
$$+ 1311x^2)y^2 + (595 + 626x^2 - 35x^4)y^4 - 175x^2y^6) - b^6x^5y^3(434 + 3(-670$$
$$+ 693x^2)y^2 + (385 + 654x^2 - 179x^4)y^4 + x^2(-1085 + 84x^2 + 54x^4)y^6) - x^5y^3(28 + (624$$

$$
\begin{aligned}
&- 330x^2)y^2 + (-385 - 648x^2 + 272x^4)y^4 + x^2(245 - 18x^2 + x^4)y^6 + x^6(-6 \\
&+ x^2)y^8) + b^5x^4y^2(198 + 3(-770 + 529x^2)y^2 + 6x^2(-208 + 57x^2)y^4 + 3x^2(-595 \\
&- 824x^2 + 398x^4)y^6 + x^4(525 + 22x^2 + 11x^4)y^8) - b^4x^3y(44 + 24(-77 \\
&+ 31x^2)y^2 + 12x^2(-229 + 22x^2)y^4 + 3x^2(-385 - 2036x^2 + 978x^4)y^6 + x^4(1575 \\
&- 538x^2 + 289x^4)y^8 + x^8(2 + x^2)y^{10}) + b^3x^2(4 + 44(-18 + 5x^2)y^2 + 6x^2(-462 \\
&+ 71x^2)y^4 + 3x^4(-1894 + 797x^2)y^6 - 3x^4(-595 + 34x^2 + 13x^4)y^8 + 3x^6(-175 \\
&- 44x^2 + 22x^4)y^{10}) + b^2xy(176 - 6x^{12}y^{10} + 12x^{10}y^8(-8 + y^2) \\
&+ 44x^2(-1 + 18y^2) + x^8y^6(851 + 408y^2) - 3x^4y^2(38 - 1086y^2 + 385y^4) \\
&+ x^6y^4(-1419 - 1022y^2 + 1015y^4)) + b(-16 + 11x^{12}y^{10} + x^2(4 - 88y^2) - 22x^4y^2(-1 \\
&+ 9y^2) + x^8y^6(-444 - 692y^2 + 175y^4) + x^6(155y^4 + 508y^6 - 595y^8) \\
&+ x^{10}(200y^8 - 66y^{10}))))/(40(1 - b^2)^{3/2}x^2y^{13}\zeta^{11})\Big] + \\
&\left(\frac{a}{R}\right)^7 \Big[(9b)/(25(1 - b^2)^{3/2}x^2y^2) - (9(800b^9x^8y^8 + 8b^8x^7y^7(-430 \\
&+ 557x^2y^2) + b^7x^6y^6(6305 - 12302x^2y^2 + 893x^4y^4) + b^6x^5y^5(-6435 \\
&+ 13464x^2y^2 - 16323x^4y^4 + 94x^6y^6) + b^5x^4y^4(3003 - 6903x^2y^2 \\
&+ 39828x^4y^4 - 2107x^6y^6 - 13x^8y^8) - 3x^5y^5(-1144 + 2764x^2y^2 - 699x^4y^4 \\
&+ 14x^6y^6 + x^8y^8) + b^4x^3y^3(-1716 + 4290x^2y^2 - 42060x^4y^4 + 15655x^6y^6 \\
&- 490x^8y^8 + x^{10}y^{10}) + b^3x^2y^2(572 + 2574x^2y^2 + 18915x^4y^4 \\
&- 28790x^6y^6 + 4395x^8y^8 + 78x^{10}y^{10}) - b^2xy(104 + 572x^2y^2 + 11583x^4y^4 \\
&- 26600x^6y^6 + 11605x^8y^8 + 186x^{10}y^{10} + 6x^{12}y^{12}) + b(8 \\
&+ 52x^2y^2 + 143x^4y^4 - 4589x^6y^6 + 10760x^8y^8 - 893x^{10}y^{10} \\
&+ 39x^{12}y^{12})))/(200(1 - b^2)^{3/2}x^2y^{15}\zeta^{13})\Big] \qquad \text{(A.12h)}
\end{aligned}
$$

$$
\begin{aligned}
M_8^{ES,c} = &\left(\frac{a}{R}\right)^3 \Big[(9b(-8 + (7 + 5b^2)x^2)(-1 + y^2))/(4(1 - b^2)^{3/2}x^2y^2) \\
&+ (9(20b^8x^7y^5(-6 + 7y^2) - 5b^7x^6y^4(-84 + (69 - 19x^2)y^2 + 21(1 + x^2)y^4) \\
&+ b^6x^5y^3(-530 + (610 - 730x^2)y^2 + (-70 + 617x^2 - 63x^4)y^4 + 63(x^2 \\
&+ x^4)y^6) - 3b^5x^4y^2(-105 - 105(-3 + 4x^2)y^2 + (-210 + 579x^2 - 346x^4)y^4 - 3x^2(63 - 110x^2
\end{aligned}
$$

$$+ 2x^4)y^6 + 6(x^4 + x^6)y^8) + x^5y^3(5 + (41 - 44x^2)y^2 + (-56 + 61x^2 - 18x^4)y^4$$
$$+ (-27x^2 + 24x^4 - 4x^6)y^6 + (-6x^4 + 4x^6)y^8) + b^3x^2(10 + (-514 + 486x^2)y^2$$
$$+ 18(28 - 97x^2 + 70x^4)y^4 + 9x^2(140 - 227x^2 + 83x^4)y^6 + 3x^4(231 - 295x^2$$
$$+ 54x^4)y^8 - 54x^6(-2 + 3x^2)y^{10}) + b^4x^3y(-90 - 15(-62 + 69x^2)y^2 - 3(280$$
$$- 811x^2 + 584x^4)y^4 - 3x^2(476 - 717x^2 + 192x^4)y^6 + (-369x^4 + 574x^6 - 2x^8)y^8$$
$$+ 2(x^6 + x^8)y^{10}) + b(16(-1 + y^2) - 36x^{10}y^8(-1 + y^2) + 2x^8y^6(68 - 90y^2$$
$$+ 27y^4) + 2x^2(7 - 43y^2 + 36y^4) + 3x^6y^4(28 - 81y^2 + 63y^4) + 63x^4(y^2 - 3y^4$$
$$+ 2y^6)) + b^2xy(-144(-1 + y^2) + 18x^{10}y^8(-1 + y^2) - 3x^8y^6(69 - 73y^2$$
$$+ 4y^4) - 126x^2(1 - 5y^2 + 4y^4) - 6x^4y^2(76 - 158y^2 + 77y^4) + x^6(-378y^4$$
$$+ 631y^6 - 243y^8)))))/(8(1 - b^2)^{3/2}x^2y^{11}\zeta^9)\Big] +$$
$$\left(\frac{a}{R}\right)^5 \Big[(9b((7 + 5b^2)x^2 + 8(-2 + y^2)))/(20(1 - b^2)^{3/2}x^2y^2) - (9(480b^9x^8y^6 +$$
$$40b^8x^7y^5(-33 + (-35 + 2x^2)y^2 + 21y^4) + b^7x^6y^4(1660$$
$$+ 125(14 + 3x^2)y^2 + (-1085 + 322x^2 + 281x^4)y^4 - 231x^2y^6) - b^6x^5y^3(1190$$
$$+ 40(-42 + 55x^2)y^2 + (770 - 5502x^2 + 4139x^4)y^4 + x^2(3101 + 198x^2 + 99x^4)y^6$$
$$- 99x^4y^8) + b^5x^4y^2(495 + 15(-308 + 207x^2)y^2 + 6(385 - 2261x^2$$
$$+ 1527x^4)y^4 + 3x^2(2471 - 718x^2 + 676x^4)y^6 + 11x^4(117 + 4x^2 + 2x^4)y^8 - 22x^6y^{10})$$
$$- x^5y^3(-35 + 7(-156 + 77x^2)y^2 + (616 + 114x^2 - 38x^4)y^4 + x^2(13 - 66x^2$$
$$+ 22x^4)y^6 + x^4(33 - 12x^2 + 4x^4)y^8 + 6x^6y^{10}) - b^4x^3y(110 + 3(-1232$$
$$+ 669x^2)y^2 + 3(616 - 4172x^2 + 2629x^4)y^4 + 6x^2(1078 - 431x^2 + 392x^4)y^6 + x^4(1083$$
$$- 1166x^2 + 902x^4)y^8 + x^6(583 + 4x^2 + 2x^4)y^{10} - 2x^8y^{12}) + b^3x^2(10$$
$$+ 44(-36 + 17x^2)y^2 + 6(132 - 924x^2 + 533x^4)y^4 - 3x^2(-924 + 98x^2 + 39x^4)y^6$$
$$+ 3x^4(-161 - 998x^2 + 501x^4)y^8 + 33x^6(39 - 8x^2 + 6x^4)y^{10}$$
$$+ 132x^8y^{12}) + b(44x^{12}y^{10} + 16(-2 + y^2) + 11x^4y^2(7 - 36y^2 + 18y^4) + 2x^{10}y^8(74 - 66y^2$$
$$+ 33y^4) + 2x^2(7 - 88y^2 + 44y^4) + x^8y^6(1188 - 454y^2 + 297y^4) + x^6y^4(-43$$
$$- 2674y^2 + 1547y^4)) - b^2xy(18x^{12}y^{10} + 176(-2 + y^2) + 42x^4y^2(19 + 12y^2$$

$$
\begin{aligned}
&- 11y^4) + 3x^{10}y^8(99 - 8y^2 + 4y^4) + 22x^2(7 - 72y^2 + 36y^4) + x^8y^6(1547 \\
&- 726y^2 + 363y^4) + x^6y^4(-858 - 3986y^2 \\
&+ 1923y^4)))))/(40(1 - b^2)^{3/2}x^2y^{13}\zeta^{11})\Big] + \\
&\left(\frac{a}{R}\right)^7 \Big[(18b)/(25(1 - b^2)^{3/2}x^2y^2) + (9(5600b^9x^8y^8 + 56b^8x^7y^7(-250 \\
&+ 53x^2y^2) + b^6x^7y^7(59157 - 8214x^2y^2 - 143x^4y^4) \\
&+ b^7x^6y^6(11375 - 27146x^2y^2 + 779x^4y^4) + 3x^5y^5(2002 - 2287x^2y^2 + 342x^4y^4 \\
&+ 13x^6y^6 + 2x^8y^8) + b^5x^4y^4(-6006 - 58149x^2y^2 + 32394x^4y^4 - 3481x^6y^6 \\
&+ 26x^8y^8) + b^4x^3y^3(3432 + 30030x^2y^2 - 48855x^4y^4 + 19990x^6y^6 \\
&+ 845x^8y^8 - 2x^{10}y^{10}) - b^3x^2y^2(1144 + 5148x^2y^2 - 34125x^4y^4 + 40070x^6y^6 \\
&+ 1095x^8y^8 + 156x^{10}y^{10}) + b^2xy(208 + 1144x^2y^2 - 15444x^4y^4 \\
&+ 38015x^6y^6 - 4330x^8y^8 + 507x^{10}y^{10} + 12x^{12}y^{12}) - b(16 + 104x^2y^2 \\
&+ 286x^4y^4 + 14807x^6y^6 - 8630x^8y^8 + 779x^{10}y^{10} \\
&+ 78x^{12}y^{12})))/(200(1 - b^2)^{3/2}x^2y^{15}\zeta^{13})\Big] \qquad \text{(A.12i)}
\end{aligned}
$$

$$
\begin{aligned}
M_9^{ES,c} = &\left(\frac{a}{R}\right)^3 \Big[- (9(-2 + x^2 + 3b^4x^2 + 2b^2(-5 + 4x^2))(-1 + y^2))/(2(-1 \\
&+ b^2)^2x^2y^2) - (9(-10x^8y^6 + 8(-1 + y^2) + 20b^9x^7y^5(-6 + 7y^2) + 9x^4y^2(2 - 9y^2 \\
&+ 7y^4) + 4x^2(1 - 10y^2 + 9y^4) - 5b^8x^6y^4(-96 + (77 - 19x^2)y^2 + 21(1 \\
&+ x^2)y^4) + x^6(39y^4 - 49y^6) + b^7x^5y^3(-630 - 15(-63 + 73x^2)y^2 - 7(45 - 136x^2 + 9x^4)y^4 \\
&+ 63(x^2 + x^4)y^6) + b^6x^4y^2(378 + 3(-651 + 725x^2)y^2 + (1575 - 3122x^2 \\
&+ 1573x^4)y^4 + 3x^2(329 - 505x^2 + 6x^4)y^6 - 18(x^4 + x^6)y^8) - 3b^4x^2(-4 \\
&+ (424 - 354x^2)y^2 - 3(140 - 503x^2 + 313x^4)y^4 + (-1155x^2 + 1694x^4 - 589x^6)y^6 \\
&+ (-735x^4 + 669x^6 - 84x^8)y^8 + 12x^6(-5 + 7x^2)y^{10}) + b^5x^3y(-108 \\
&- 6(-368 + 343x^2)y^2 - 3(700 - 1757x^2 + 1059x^4)y^4 + (-3213x^2 + 3918x^4 - 891x^6)y^6 \\
&+ (-621x^4 + 889x^6 - 2x^8)y^8 + 2(x^6 + x^8)y^{10}) + b^2(40(-1 + y^2) \\
&- 162x^{10}y^8(-1 + y^2) + 135x^4y^2(2 - 9y^2 + 7y^4) + 16x^2(2 - 29y^2 + 27y^4) + x^8y^6(607 \\
&- 837y^2 + 270y^4) + x^6y^4(537 - 1442y^2 + 945y^4)) + b^3xy(-360(-1 + y^2)
\end{aligned}
$$

$$+ 28x^{10}y^8(-1+y^2) + x^8y^6(-693+713y^2-20y^4) - 48x^2(6-41y^2+35y^4) - 21x^4y^2(58$$
$$- 163y^2+105y^4) + x^6(-1473y^4+2428y^6-1035y^8)) + bxy(-72(-1+y^2)$$
$$+ 18x^{10}y^8(-1+y^2) - 63x^4y^2(2-7y^2+5y^4) - 36x^2(1-8y^2+7y^4) - 3x^8y^6(27$$
$$- 37y^2+10y^4) + x^6(-183y^4+338y^6-135y^8)))))/(8(-1+b^2)^2x^2y^{11}\zeta^9)\Big] +$$
$$\left(\frac{a}{R}\right)^5\Big[(9(480b^{10}x^8y^6+50x^{10}y^8+8(-2+y^2) - x^8y^6(481+140y^2)$$
$$+ 11x^4y^2(2-18y^2+9y^4) + 40b^9x^7y^5(-33+(-35+2x^2)y^2+21y^4) + x^2(4$$
$$- 88y^2+44y^4) + b^8x^6y^4(1800+35(2+37x^2)y^2+(-105+322x^2$$
$$+ 281x^4)y^4 - 231x^2y^6) + x^6(117y^4+994y^6-567y^8) - b^7x^5y^3(1386+165(-42$$
$$+ 31x^2)y^2 + (3465-8372x^2+5864x^4)y^4 + 3x^2(1582+66x^2+33x^4)y^6$$
$$- 99x^4y^8) + b^6x^4y^2(594+3(-3850+2143x^2)y^2+(5775-22456x^2$$
$$+ 13582x^4)y^4 + x^2(11508-3862x^2+3133x^4)y^6 + 11x^4(201+4x^2+2x^4)y^8 - 22x^6y^{10})$$
$$- b^5x^3y(132+330(-28+13x^2)y^2+33(140-742x^2+373x^4)y^4+3x^2(4081$$
$$- 3536x^2+1754x^4)y^6 + x^4(4464-1958x^2+1397x^4)y^8 + x^6(979+4x^2$$
$$+ 2x^4)y^{10} - 2x^8y^{12}) + b^4x^2(12+330(-12+5x^2)y^2+15(132-1078x^2$$
$$+ 445x^4)y^4 + 15x^2(539-896x^2+234x^4)y^6 + 15x^4(420-650x^2+251x^4)y^8 + 11x^6(405$$
$$- 40x^2+28x^4)y^{10} + 220x^8y^{12}) + b^2(198x^{12}y^{10}+40(-2+y^2)+8x^2(4$$
$$- 154y^2+77y^4) + 11x^4y^2(34-342y^2+171y^4) + 5x^8y^6(758-482y^2$$
$$+ 297y^4) + x^{10}y^8(691-660y^2+330y^4) + 7x^6y^4(117-1360y^2$$
$$+ 720y^4)) - b^3xy(28x^{12}y^{10}+440(-2+y^2)+5x^{10}y^8(209-8y^2+4y^4)+88x^2(4-66y^2$$
$$+ 33y^4) + 33x^4y^2(62-350y^2+175y^4) + 5x^8y^6(988-638y^2+319y^4)$$
$$+ 5x^6y^4(561-2836y^2+1530y^4)) - bxy(18x^{12}y^{10}+88(-2+y^2)+99x^4y^2(2-14y^2$$
$$+ 7y^4) + 44x^2(1-18y^2+9y^4) + 3x^{10}y^8(33-20y^2+10y^4) + x^8y^6(-146$$
$$- 330y^2+165y^4) + x^6(627y^4+80y^6-180y^8)))))/(40(-1$$
$$+ b^2)^2x^2y^{13}\zeta^{11}) + (9(-1+2bxy-x^2y^2)^5(-4+x^2+3b^4x^2+2y^2$$
$$+ 2b^2(4x^2+5(-2+y^2))))/(10(-1+b^2)^2x^2y^{12}\zeta^{10})\Big] +$$

$$\left(\frac{a}{R}\right)^7 \Big[(9(1+5b^2)(-1+2bxy-x^2y^2)^7)/(25(-1$$
$$+b^2)^2x^2y^{16}\zeta^{14}) - (9(-8-52x^2y^2-143x^4y^4+7748x^6y^6-5663x^8y^8$$
$$+5600b^{10}x^8y^8+350x^{10}y^{10}+56b^9x^7y^7(-190+53x^2y^2)+b^8x^6y^6(455$$
$$-31066x^2y^2+779x^4y^4)+b^7x^5y^5(15015+69587x^2y^2-8011x^4y^4$$
$$-143x^6y^6)+b^6x^4y^4(-15015-70889x^2y^2+25793x^4y^4-5547x^6y^6+26x^8y^8)$$
$$+b^5x^3y^3(8580+33033x^2y^2-28233x^4y^4+39973x^6y^6$$
$$+1417x^8y^8-2x^{10}y^{10})-b^4x^2y^2(2860+15873x^2y^2-17745x^4y^4+79115x^6y^6$$
$$+5765x^8y^8+260x^{10}y^{10})+b^3xy(520+4576x^2y^2+12441x^4y^4+61865x^6y^6$$
$$-4865x^8y^8+2275x^{10}y^{10}+20x^{12}y^{12})+bxy(104+572x^2y^2$$
$$+1287x^4y^4-10211x^6y^6+4255x^8y^8+195x^{10}y^{10}+30x^{12}y^{12})-b^2(40$$
$$+832x^2y^2+3289x^4y^4+37427x^6y^6-22675x^8y^8+3545x^{10}y^{10}$$
$$+390x^{12}y^{12})))/(200(-1+b^2)^2x^2y^{15}\zeta^{13})\Big] \qquad \text{(A.12j)}$$

$$M_{10}^{ES,c} = \left(\frac{a}{R}\right)^3 \Big[-(3(12b^7x^5y^3(-6+y^2)-6(-2+y^2)+x^6y^4(-3+5y^2)+x^2(-12$$
$$+53y^2-33y^4)+x^4y^2(-45+46y^2+3y^4)+2b^6x^4y^2(48+(4$$
$$+69x^2)y^2+(-39+36x^2)y^4)-2b^5x^3y(21+(46-12x^2)y^2+(-114+115x^2+78x^4)y^4$$
$$+27x^2(-1+x^2)y^6)+b^4x^2(6-2(-55+87x^2)y^2-3(74-143x^2+93x^4)y^4+x^2(-261$$
$$+260x^2+63x^4)y^6+21x^4(-1+x^2)y^8)+bxy(42(-2+y^2)-3x^8y^6(-9+5y^2)$$
$$+3x^6y^4(32-25y^2+5y^4)+x^4y^2(195-227y^2+54y^4)+x^2(84-239y^2$$
$$+123y^4))+b^3xy(-42+84y^2-3x^8y^6(3+y^2)+3x^6y^4(146-89y^2+y^4)$$
$$+x^4y^2(483-563y^2+270y^4)+x^2(84-425y^2+279y^4))+b^2(6-12y^2+21x^8y^6(-9$$
$$+5y^2)+x^2(-12+233y^2-123y^4)-3x^4y^2(85-175y^2+98y^4)+x^6(-486y^4$$
$$+419y^6-105y^8))))/(16(-1+b^2)^2x^2y^9\zeta^7)-(9(-1+2bxy$$
$$-x^2y^2)^3(b^4x^2+(-1+x^2)(-2+y^2)+b^2(1-2y^2+2x^2(-1+y^2))))/(8(-1+b^2)^2x^2y^8\zeta^6)\Big]+$$
$$\left(\frac{a}{R}\right)^5 \Big[-(9(4-2x^2+b^4x^2-y^2-2b^2(-1+x^2+y^2)))/(40(-1$$
$$+b^2)^2x^2y^2)-(9(-5x^8y^6+2(-4+y^2)+8b^7x^5y^3(5+2(2+x^2)y^2-13y^4)+x^6y^4(-126$$

$$
\begin{aligned}
&- 34y^2 + 5y^4) + x^2(4 - 50y^2 + 29y^4) + x^4(23y^2 + 204y^4 - 108y^6) \\
&- 2b^6x^4y^2(24 + 9(6 + 7x^2)y^2 + (-117 - 94x^2 + 93x^4)y^4 - 7x^2y^6) + 2b^5x^3y(9 + (72 \\
&+ 11x^2)y^2 + 2(-59 - 13x^2 + 64x^4)y^4 + x^2(-7 - 30x^2 + 48x^4)y^6 - 15x^4y^8) \\
&+ b^4x^2(-2 + 4(-35 + 23x^2)y^2 + (146 - 462x^2 + 315x^4)y^4 + x^2(117 - 872x^2 \\
&+ 430x^4)y^6 + (376x^4 + 18x^6 - 27x^8)y^8 + 9x^6y^{10}) + b^2(81x^{10}y^8 \\
&+ 4(-1 + y^2) + x^2(4 - 242y^2 + 41y^4) + x^8y^6(265 - 126y^2 + 45y^4) + x^6y^4(693 - 290y^2 \\
&+ 109y^4) + x^4y^2(149 - 1146y^2 + 513y^4)) - bxy(9x^{10}y^8 + 18(-4 + y^2) + x^8y^6(39 \\
&- 14y^2 + 5y^4) + 3x^6y^4(-33 - 22y^2 + 7y^4) + x^2(36 - 186y^2 + 89y^4) + x^4(87y^2 \\
&+ 114y^4 - 93y^6)) + b^3xy(3x^{10}y^8 - 36(-1 + y^2) + x^2(-36 \\
&+ 678y^2 - 179y^4) - x^8y^6(273 + 2y^2 + y^4) + x^4(-479y^2 + 1646y^4 - 731y^6) \\
&+ x^6(-1127y^4 + 426y^6 - 165y^8)))))/(80(-1 + b^2)^2x^2y^{11}\zeta^9)\Big] + \\
&\left(\frac{a}{R}\right)^7\Big[- (9(4 + 57x^2y^2 - 1243x^4y^4 + 1139x^6y^6 + 64b^8x^6y^6 - 85x^8y^8 \\
&+ 16b^7x^5y^5(-11 + 54x^2y^2) + 2b^6x^4y^4(99 - 906x^2y^2 + 55x^4y^4) \\
&+ 2b^5x^3y^3(28 + 539x^2y^2 - 1610x^4y^4 + 27x^6y^6) + b^4x^2y^2(134 - 187x^2y^2 \\
&+ 6881x^4y^4 + 223x^6y^6 - 11x^8y^8) + b^3xy(-22 - 1135x^2y^2 - 5324x^4y^4 \\
&+ 1406x^6y^6 - 350x^8y^8 + x^{10}y^{10}) - bxy(44 - 89x^2y^2 - 1650x^4y^4 + 1030x^6y^6 \\
&+ 34x^8y^8 + 7x^{10}y^{10}) + b^2(2 + 139x^2y^2 + 3212x^4y^4 - 3500x^6y^6 \\
&+ 742x^8y^8 + 77x^{10}y^{10})))/(400(-1 + b^2)^2x^2y^{13}\zeta^{11}) - (9(2 \\
&+ b^2)(-1 + 2bxy - x^2y^2)^5)/(200(-1 + b^2)^2x^2y^{12}\zeta^{10})\Big] \qquad \text{(A.12k)}
\end{aligned}
$$

$$
\begin{aligned}
M_{11}^{ES,c} = &\left(\frac{a}{R}\right)^3\Big[(9b(-2 + (1 + b^2)x^2))/(8(1 - b^2)^{3/2}x^2y^2) - (9(2b^6x^5y^3(-6 + y^2) \\
&+ b^5x^4y^2(16 + (-10 + 31x^2)y^2 + (-5 + 4x^2)y^4) + b^4x^3y(-7 + (32 - 41x^2)y^2 \\
&+ (5 + 8x^2 - 35x^4)y^4) + b^3x^2(1 + (-35 + 24x^2)y^2 + x^2(-50 + 43x^2)y^4 \\
&+ x^2(10 - 15x^2 + 14x^4)y^6) + x^3y^3(-3 + 5y^2 + x^4y^4 + x^2(5 - 2y^2)) - b(2 \\
&+ x^6y^4(4 + 3y^2) + x^2(-1 + 7y^2) + x^4y^2(-2 + 10y^2 + 5y^4)) + b^2xy(14 - 2x^8y^6 \\
&+ x^6y^4(-7 + y^2) + x^2(-7 + 41y^2 - 10y^4) + x^4(-22y^2
\end{aligned}
$$

$$+ 34y^4))))/(8(1-b^2)^{3/2}x^2y^9\zeta^7)\Big]+$$
$$\left(\frac{a}{R}\right)^5\Big[-(9b(-4+(1+b^2)x^2))/(40(1-b^2)^{3/2}x^2y^2)-(9(4b^6x^5y^3(5+2(-6$$
$$+5x^2)y^2-5y^4)+b^5x^4y^2(-24-3(-46+45x^2)y^2+(45$$
$$+158x^2-125x^4)y^4-25x^2y^6)+b^4x^3y(9+6(-27+19x^2)y^2+(-35-378x^2$$
$$+270x^4)y^4+(75x^2-60x^4+63x^6)y^6)-b^3x^2(1+3(-42+17x^2)y^2+3x^2(-118$$
$$+57x^2)y^4+x^2(90-62x^2+23x^4)y^6+2x^4(-25-9x^2+9x^4)y^8)-x^3y^3(-48+35y^2$$
$$+2x^6y^6+x^4y^2(-35+6y^2)+x^2(35+96y^2-35y^4))+b(4+2x^8y^6(-10+9y^2)$$
$$+x^2(-1+18y^2)+3x^4(y^2+4y^4+15y^6)+x^6(54y^4+116y^6-25y^8))$$
$$+b^2xy(-36+2x^{10}y^8-3x^6y^4(31+26y^2)+x^2(9-222y^2+70y^4)+x^4(69y^2+18y^4$$
$$-90y^6)+x^8(9y^6-2y^8))))/(40(1-b^2)^{3/2}x^2y^{11}\zeta^9)\Big]+$$
$$\left(\frac{a}{R}\right)^7\Big[(9(96b^7x^6y^6-8b^6x^5y^5(33+58x^2y^2)-b^4x^3y^3(63$$
$$+1188x^2y^2-625x^4y^4+54x^6y^6)+b^5(297x^4y^4+1162x^6y^6-35x^8y^8)$$
$$-x^3y^3(-168+792x^2y^2-291x^4y^4+10x^6y^6+x^8y^8)+b^3x^2y^2(99+330x^2y^2$$
$$-1226x^4y^4+466x^6y^6+11x^8y^8)-b^2xy(22+435x^2y^2-1320x^4y^4$$
$$+1112x^6y^6+46x^8y^8+x^{10}y^{10})+b(2+11x^2y^2+33x^4y^4+892x^6y^6$$
$$-101x^8y^8+11x^{10}y^{10})))/(200(1-b^2)^{3/2}x^2y^{13}\zeta^{11})$$
$$+(9b(-1+2bxy-x^2y^2)^5)/(100(1-b^2)^{3/2}x^2y^{12}\zeta^{10})\Big] \qquad \text{(A.12l)}$$

$$M_{12}^{ES,c}=\left(\frac{a}{R}\right)^3\Big[-(9b(-4+(5+b^2)x^2)(-1+y^2))/(8(1-b^2)^{3/2}x^2y^2)-(9(2b^6x^5y^3(-6+5y^2)+b^5x^4y^2(16+$$
$$(-48+71x^2)y^2+(35-70x^2)y^4)+b^4x^3y(-7+(86-126x^2)y^2-2(40-82x^2+35x^4)y^4+$$
$$35x^2(-1+2x^2)y^6)+b^3x^2(1+(-71+94x^2)y^2+(70-170x^2+103x^4)y^4+7x^2(10-17x^2$$
$$+4x^4)y^6+(14x^4-28x^6)y^8)+b(4(-1+y^2)-14x^8y^6(-1+y^2)+x^6y^4(36-49y^2+14y^4)+x^2(5$$
$$-19y^2+14y^4)+x^4y^2(16-48y^2+35y^4))+x^3y^3(9-10y^2$$
$$+2x^6y^4(-1+y^2)+x^2(-10+16y^2-7y^4)+x^4(-7y^2+9y^4-2y^6))+b^2xy(-28(-1+y^2)$$
$$+4x^8y^6(-1+y^2)+x^2(-35+87y^2-50y^4)-2x^4y^2(31-52y^2+21y^4)$$
$$+x^6(-49y^4+51y^6-2y^8))))/(8(1-b^2)^{3/2}x^2y^9\zeta^7)\Big]+$$

$$\left(\frac{a}{R}\right)^5\Big[-(9b((5+b^2)x^2+4(-2+y^2)))/(40(1-b^2)^{3/2}x^2y^2)-(9(20b^6x^5y^3(1+2(-6+$$
$$5x^2)y^2+7y^4)-b^5x^4y^2(24+15(-38+33x^2)y^2+5(63$$
$$-38x^2+41x^4)y^4+105x^2y^6)+b^4x^3y(9+(-540+429x^2)y^2+10(28-27x^2$$
$$+30x^4)y^4+21x^2(5-6x^2+6x^4)y^6+63x^4y^8)-b^3x^2(1+3(-84+59x^2)y^2+3(42$$
$$-40x^2+27x^4)y^4+x^4(-376+241x^2)y^6+12x^4(14-3x^2+3x^4)y^8$$
$$+18x^6y^{10})+x^3y^3(-120+70y^2+2x^8y^6+x^6y^4(9-4y^2+2y^4)+x^2(70+6y^2$$
$$+7y^4)+x^4y^2(7-18y^2+9y^4))-b(18x^{10}y^8+4(-2+y^2)+2x^8y^6(29-18y^2$$
$$+9y^4)+x^2(5-36y^2+18y^4)+3x^4y^2(5-106y^2+63y^4)+x^6y^4(180-106y^2$$
$$+63y^4))+b^2xy(4x^{10}y^8+36(-2+y^2)+x^2(45-12y^2-14y^4)$$
$$+x^8y^6(81-4y^2+2y^4)+3x^6y^4(83-48y^2+24y^4)+3x^4y^2(-5-168y^2$$
$$+84y^4))))/(40(1-b^2)^{3/2}x^2y^{11}\zeta^9)\Big]+$$
$$\left(\frac{a}{R}\right)^7\Big[(9(480b^7x^6y^6+40b^6x^5y^5(-33+2x^2y^2)+b^5x^4y^4(1485-790x^2y^2$$
$$+281x^4y^4)-b^4x^3y^3(882-1485x^2y^2+1504x^4y^4$$
$$+99x^6y^6)-x^3y^3(420-693x^2y^2+156x^4y^4+11x^6y^6+2x^8y^8)+2b^3x^2y^2(99$$
$$-561x^2y^2+1456x^4y^4+115x^6y^6+11x^8y^8)-2b^2xy(22-321x^2y^2+1353x^4y^4$$
$$-130x^6y^6+55x^8y^8+x^{10}y^{10})+b(4+22x^2y^2+957x^4y^4-754x^6y^6$$
$$+149x^8y^8+22x^{10}y^{10})))/(200(1-b^2)^{3/2}x^2y^{13}\zeta^{11})$$
$$+(9b(-1+2bxy-x^2y^2)^5)/(50(1-b^2)^{3/2}x^2y^{12}\zeta^{10})\Big] \qquad \text{(A.12m)}$$

$$M_{13}^{ES,c}=\left(\frac{a}{R}\right)^3\Big[(9(-2+x^2+b^4x^2+7b^2(-1+x^2))(-1+y^2))/(8(-1+b^2)^2x^2y^2)$$
$$+(3(12(-1+y^2)+12b^7x^5y^3(-6+5y^2)-x^6y^4(3+5y^2)+x^4y^2(33-46y^2$$
$$+3y^4)+x^2(6-53y^2+45y^4)+2b^6x^4y^2(48+(-178+237x^2)y^2-3(-43$$
$$+78x^2)y^4)+2b^5x^3y(-21+(400-477x^2)y^2+(-375+631x^2-237x^4)y^4$$
$$+3x^2(-44+79x^2)y^6)+b^4x^2(6+(-746+786x^2)y^2+3(246-583x^2$$
$$+313x^4)y^4+x^2(957-1064x^2+189x^4)y^6-21x^4(-5+9x^2)y^8)+b^2(42(-1+y^2)$$
$$-189x^8y^6(-1+y^2)+3x^4y^2(73-291y^2+224y^4)+x^6y^4(480-731y^2+273y^4)+x^2(42$$

$$
\begin{aligned}
&- 389y^2 + 351y^4)) + b^3xy(-294(-1 + y^2) + 27x^8y^6(-1 + y^2) + x^2(-294 \\
&+ 1193y^2 - 915y^4) - 3x^6y^4(188 - 193y^2 + 5y^4) + x^4(-711y^2 + 1391y^4 - 732y^6)) \\
&+ bxy(-84(-1 + y^2) + 27x^8y^6(-1 + y^2) + x^2(-42 + 275y^2 - 225y^4) - 3x^6y^4(32 \\
&- 45y^2 + 13y^4) + x^4(-153y^2 + 311y^4 - 138y^6)))))/(16(-1 + b^2)^2x^2y^9\zeta^7)\Big] + \\
&\left(\frac{a}{R}\right)^5 \Big[(9(-4 + x^2 + b^4x^2 + 2y^2 + 7b^2(-2 + x^2 + y^2)))/(40(-1 + b^2)^2x^2y^2) \\
&+ (9(8 - 4y^2 - 5x^8y^6 + x^2(-2 + 50y^2 - 23y^4) + x^6y^4(108 + 34y^2 + 5y^4) \\
&+ 8b^7x^5y^3(5 + (-76 + 58x^2)y^2 + 43y^4) + x^4y^2(-29 - 204y^2 + 126y^4) \\
&- 2b^6x^4y^2(24 + (-762 + 567x^2)y^2 + (387 - 254x^2 + 237x^4)y^4 + 137x^2y^6) + 2b^5x^3y(9 \\
&+ (-774 + 512x^2)y^2 + (383 - 622x^2 + 382x^4)y^4 + x^2(247 - 156x^2 + 141x^4)y^6 \\
&+ 78x^4y^8) - b^4x^2(2 + (-896 + 500x^2)y^2 + (446 - 1410x^2 + 459x^4)y^4 + x^2(657 \\
&- 1748x^2 + 758x^4)y^6 + x^4(812 - 90x^2 + 81x^4)y^8 + 45x^6y^{10}) \\
&+ bxy(9x^{10}y^8 + 36(-2 + y^2) + 13x^8y^6(3 - 2y^2 + y^4) - 3x^4y^2(-53 + 22y^2 \\
&+ 5y^4) + 3x^6y^4(-3 - 38y^2 + 19y^4) + x^2(18 - 330y^2 + 157y^4)) + b^3xy(9x^{10}y^8 \\
&+ 126(-2 + y^2) + x^8y^6(327 - 10y^2 + 5y^4) + 17x^4y^2(17 - 154y^2 + 85y^4) + x^6y^4(1049 \\
&- 870y^2 + 435y^4) + x^2(126 - 1146y^2 + 589y^4)) - b^2(81x^{10}y^8 + 14(-2 + y^2) \\
&+ x^8y^6(275 - 234y^2 + 117y^4) + x^2(14 - 350y^2 + 179y^4) + x^6y^4(783 - 734y^2 \\
&+ 431y^4) + x^4y^2(71 - 1806y^2 + 963y^4)))))/(80(-1 + b^2)^2x^2y^{11}\zeta^9)\Big] + \\
&\left(\frac{a}{R}\right)^7 \Big[(9(2 + 7b^2))/(200(-1 + b^2)^2x^2y^2) - (9(4 + 57x^2y^2 - 1243x^4y^4 \\
&+ 1139x^6y^6 + 1216b^8x^6y^6 - 85x^8y^8 + 16b^7x^5y^5(-209 + 6x^2y^2) \\
&+ 2b^6x^4y^4(1881 - 534x^2y^2 + 301x^4y^4) - 2b^5x^3y^3(917 - 836x^2y^2 \\
&+ 2489x^4y^4 + 126x^6y^6) + b^4x^2y^2(728 - 1771x^2y^2 + 10253x^4y^4 \\
&+ 1615x^6y^6 + 55x^8y^8) - b^3xy(154 + 721x^2y^2 + 8096x^4y^4 + 298x^6y^6 + 662x^8y^8 + 5x^{10}y^{10}) \\
&- bxy(44 + 415x^2y^2 - 1452x^4y^4 + 760x^6y^6 + 76x^8y^8 + 13x^{10}y^{10}) \\
&+ b^2(14 + 205x^2y^2 + 5192x^4y^4 - 3224x^6y^6 + 838x^8y^8 \\
&+ 143x^{10}y^{10})))/(400(-1 + b^2)^2x^2y^{13}\zeta^{11})\Big] \qquad \text{(A.12n)}
\end{aligned}
$$

$$M_{14}^{ES,c} = \left(\frac{a}{R}\right)^3 \Big[-(9(1+2b^2)(-1+x^2)(-1+y^2))/(8(-1+b^2)^2x^2y^2) + (3(6-6y^2$$
$$+ x^4y^2(-3+5y^2) + x^2(-6+11y^2-3y^4) - 4b^5x^3y^3(7-6y^2+6x^2(-1+y^2))$$
$$+ b^4x^2y^2(80-78y^2+15x^4y^2(-1+y^2) + x^2(-78+95y^2-15y^4))$$
$$+ bxy(30(-1+y^2) - 15x^6y^4(-1+y^2) + 3x^4y^2(13-18y^2+5y^4) + x^2(30-73y^2$$
$$+ 39y^4)) + b^3xy(60(-1+y^2) - 3x^6y^4(-1+y^2) + 3x^4y^2(39-40y^2+y^4) + x^2(60$$
$$- 169y^2+117y^4)) + b^2(-12(-1+y^2) + 75x^6y^4(-1+y^2) + x^2(-12+107y^2$$
$$- 99y^4) + x^4(-99y^2+170y^4-75y^6))))/(16(-1+b^2)^2x^2y^7\zeta^5)\Big] +$$
$$\left(\frac{a}{R}\right)^5 \Big[(9(-5x^6y^4+2(-2+y^2)+32b^6x^4y^4(-2+x^2+y^2) + x^2(2$$
$$+ 14y^2-13y^4) - x^4y^2(13+2y^2+5y^4) - 8b^5x^3y^3(-17+7y^2+2x^4y^2$$
$$+ x^2(7-4y^2+2y^4)) - bxy(5x^8y^6 + 14(-2+y^2) + x^6y^4(16-10y^2+5y^4) + x^4y^2(21-32y^2$$
$$+ 16y^4) + x^2(14-66y^2+21y^4)) + b^4x^2y^2(-112+50y^2+7x^6y^4 + x^4y^2(71$$
$$- 14y^2+7y^4) + x^2(50-154y^2+71y^4)) + b^2(35x^8y^6 + 4(-2+y^2) + 7x^6y^4(16$$
$$- 10y^2+5y^4) + x^2(4-154y^2+89y^4) + x^4y^2(89-200y^2+112y^4))$$
$$- b^3xy(x^8y^6 + 28(-2+y^2) + x^6y^4(94-2y^2+y^4) + x^4y^2(133-188y^2+94y^4) + x^2(28$$
$$- 218y^2+133y^4))))/(80(-1+b^2)^2x^2y^9\zeta^7) + (9(1+2b^2)(-2+x^2$$
$$+ y^2)(-1+2bxy-x^2y^2)^3)/(40(-1+b^2)^2x^2y^8\zeta^6)\Big] +$$
$$\left(\frac{a}{R}\right)^7 \Big[(9(1+2b^2)(-1+2bxy-x^2y^2)^5)/(200(-1+b^2)^2x^2y^{12}\zeta^{10}) - (9$$
$$(-2+61x^2y^2-72x^4y^4+128b^7x^5y^5+5x^6y^6+32b^6x^4y^4(-9+x^2y^2) + 4$$
$$b^5x^3y^3(63+2x^2y^2+9x^4y^4) - b^4x^2y^2(56+189x^2y^2+458x^4y^4+9x^6$$
$$y^6) + b^3xy(36+147x^2y^2+671x^4y^4+153x^6y^6+x^8y^8) + bxy(18+105x^2y^2$$
$$- 51x^4y^4+27x^6y^6+5x^8y^8) - b^2(4+221x^2y^2+207x^4y^4+83x^6y^6$$
$$+ 45x^8y^8)))/(400(-1+b^2)^2x^2y^{11}\zeta^9)\Big] \qquad \text{(A.12o)}$$

APPENDIX B

APPENDICES RELATED TO CHAPTER 5

B.1 Size ratio dependence of long time particle dynamics

Here we extend the data presented in §5.1.5 figure 5.10 to illustrate the effects of increasing particle-to-cavity relative size on the average radial and perpendicular mean-square displacement.

The average radial and perpendicular mean-square displacements are plotted as a function of particle radial position in figure B.1(a) and (b), respectively, for particles with a size 1/5 that of the cavity. Several curves represent several volume fractions, and are qualitatively similar to those of figure 5.10. For radial mean-square displacement, particle motion is diffusive at short times, leading to an average radial mean-square displacement that grows linearly in time. In contrast, at times long enough for particles to sample the domain extents, the average radial mean-square displacement reaches a plateau. In figure B.1(a), superdiffusive motion is observed for $0.15 \leq \phi \leq 0.4$, showing that a smaller confining cavity causes superdiffusion at smaller volume fractions.

The average perpendicular mean-square displacement is plotted as a function of particle radial position in figure B.1(b) for particles with a size 1/5 that of the cavity. As before, several curves represent different volume fractions. The average perpendicular mean-square displacement for these larger particles is qualitatively similar to that of figure 5.10(b); at short-times motion is diffusive, then the average perpendicular mean-square displacement reaches a plateau at times long enough for particles to sample the domain extent. Between the short-

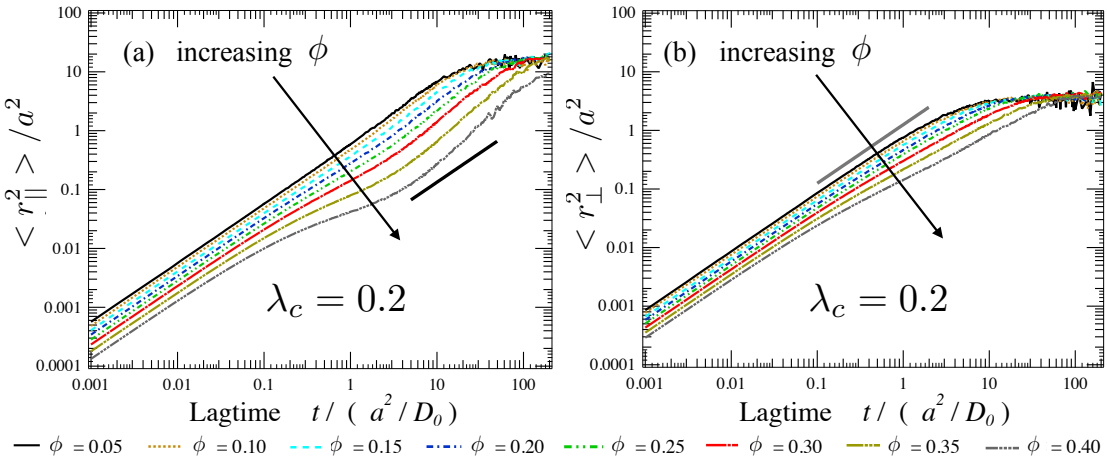

Figure B.1: The (a) radial and (b) perpendicular spatially averaged mean-square displacement as a function of lag time. Plots (a) and (b) correspond to suspensions with a particle-to-cavity relative size of 1/5. Different curves correspond to different volume fractions.

and long-time regimes, the average perpendicular mean-square displacement becomes subdiffusive as concentration increases — in contrast to the superdiffusive motion along the radial direction.

Overall, larger particles show similar qualitative behaviors to the smaller particles discussed in §5.1.5, where the long-time dynamics of particles that are 1/10 the cavity size where discussed, in both the radial and perpendicular directions. As expected, cavity-induced effects are more pronounced for larger particles.

B.2 Isotropic approximation at long times

In experiments, the long-time self-diffusivity is often reported as an isotropic tensor, owing to the practice of determining mean-square motion by averaging

the square of the magnitude of particle displacements; however, this masks the anisotropy induced by confinement. To highlight the qualitative and quantitative impacts of that approximation, we define here an average isotropic mean-square displacement in terms of the average radial and perpendicular mean-square displacements:

$$\overline{\langle r^2 \rangle} = \overline{\langle r_{\parallel}^2 \rangle} + 2\overline{\langle r_{\perp}^2 \rangle}. \tag{B.1}$$

That is, we smear out the details of anisotropy capture by orthogonal projection.

This isotropic average mean-square displacement is plotted as a function of position in figure B.2(a), and (b) for particles with sizes 1/5 and 1.5/10 that of the cavity, respectively. As before, different curves represent different volume fractions. As with the anisotropic mean-square displacements, the isotropic mean-square displacement grows diffusively at short times; a long-time plateau is reached for times long enough for particles to sample the domain extents. Between the short- and long-time limits, an intermediate subdiffusive region emerges as volume fraction increases. The subdiffusive behavior in this isotropic measurement is a consequence of the higher contribution of the perpendicular component relative to the radial component. *The superdiffusive behavior is lost entirely.* Because motion is less hindered in the perpendicular direction, the magnitude of mean-square motion is larger, and thus contributes more to the isotropic mean-square displacement. This highlights the importance of capturing anisotropy in confined suspensions: without it, key behavior, superdiffusion, is lost entirely.

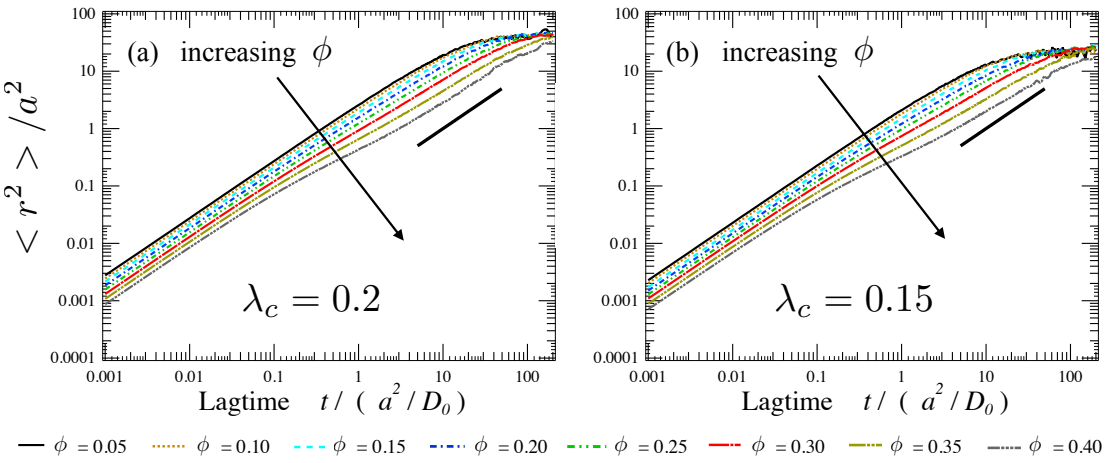

Figure B.2: Isotropic mean-square displacement $< r^2 >$ vs. lag time. Plots (a), and (b) correspond to suspensions with a particle-to-cavity relative size of 1/5, and 1.5/10, respectively, for several volume fractions.

B.3 Size-ratio dependence of cage hopping dynamics

Here we discuss the effects of increasing particle-to-cavity relative size on the average excess kurtosis. We utilize the same quantities defined in §5.1.6 to determine the dynamics of cage hopping for large particles. This extends the discussion of the cage hopping dynamics at long times in §5.1.6 that were plotted in figure 5.11.

The average radial and perpendicular excess kurtosis are plotted as a function of lag time for suspensions with particles 1/5 the size of the cavity in figure B.3(a) and (b), respectively. Several curves are plotted, corresponding to different volume fractions. For the larger particles, the average radial excess kurtosis is vanishingly small at short times, revealing particle motion is primarily diffusive. For volume fractions $0.05 \leq \phi \leq 0.30$, the average radial excess kurtosis becomes to positive at intermediate times, indicating large displacements are favored at intermediate times. Kurtosis reaches a maximum and then reverses

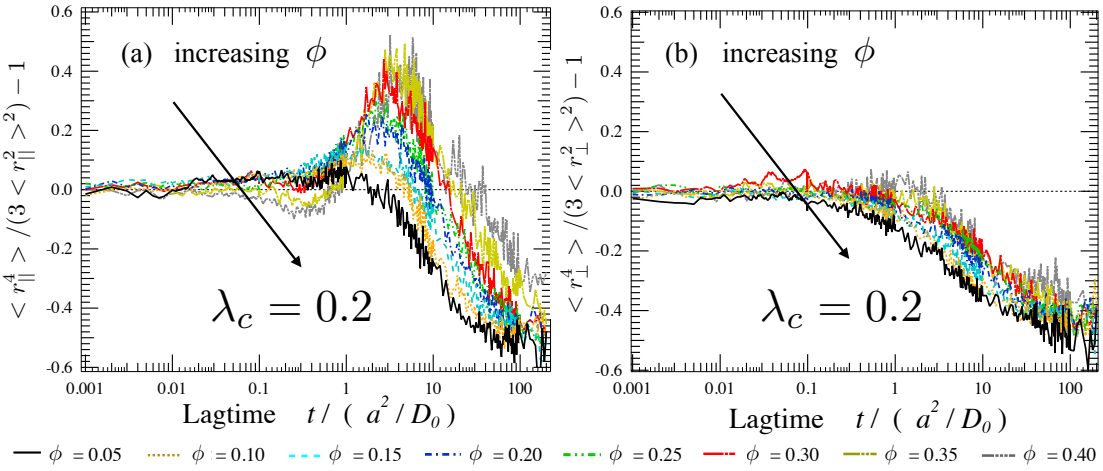

Figure B.3: Average radial excess kurtosis plotted as a function of lag time. Plots (a) and (b) correspond to suspensions with a particle-to-cavity relative size of 1/5, for several volume fractions.

to become negative, before it reaches a long time plateau as particles sample the domain extents. In contrast, for volume fractions $0.35 \leq \phi \leq 0.40$, the average radial excess kurtosis is weakly negative before obtaining positive values, suggesting that the combined effects of confinement and crowding are severe enough to restrict large displacements before particles undergo cage hopping. Another interesting feature of the average radial excess kurtosis of these concentrated suspensions is that its magnitude seems to saturate for $\phi = 0.35$ and $\phi = 0.45$, suggesting that as volume fraction increases the tendency of particles to sample large displacements reaches a maximum. With increasing lag time, the average radial excess kurtosis increases to a maximum before starting to decreases toward its long time plateau.

The average perpendicular excess kurtosis is plotted as a function of lag time for suspensions with particles 1/5 the size of the cavity in figure B.3(b). For the largest particles, the average perpendicular excess kurtosis is vanishingly small at short times, indicating motion is primarily diffusive. As lag time in-

creases, the average perpendicular excess kurtosis decreases to negative values and eventually reaches its long-time plateau. However, weakly positive values are observed for volume fractions $0.3 \leq \phi \leq 0.40$, indicating large displacement are only weakly favored at these time scales. As discussed in §5.1.6, the positive values for the average radial excess kurtosis indicate that cage hopping events occur primarily along that direction.

Overall, the average excess kurtosis for larger particles exhibits similar qualitative behaviors to that of the smaller particles discussed in §5.1.6, in both the radial and perpendicular directions. The only difference occurs for the largest particles, where the average radial excess kurtosis for suspensions with volume fractions $\phi = 0.35$, and $\phi = 0.40$ is weakly negative at intermediate times, before becoming positive. This shows that the combined effects of crowding and confinement can be severe enough to restrict large displacements before particles undergo cage hopping.

B.4 Relative error arising from common approximations

An isotropic diffusivity was computed in §5.1.4 (equation 5.12), smearing out all spatial dependence of particle dynamics. The loss of information associated with that calculation was illustrated for the radial, spatially-dependent diffusion tensor in that section. Here we give the corresponding calculation for the error associated with using that approximation in place of the perpendicular diffusivity. The relative error for diffusion perpendicular to the cavity radius is then given by

$$E_{\perp}(y/R, \lambda_c, \phi) \;=\; 100\,\frac{\left|D_0^{\perp}(y/R, \lambda_c, \phi) - D_{MSD}(\lambda_c, \phi)\right|}{D_0^{\perp}(y/R, \lambda_c, \phi)}. \tag{B.2}$$

This error is plotted in figures B.4(a)-(c) for particle-to-cavity relative sizes 1/5, 1.5/10 and 1/10, respectively; different curves correspond to different volume fractions. As was found for the radial direction, near the center, the relative error may again be as high as 35% and, near the dilute limit, error decreases to a minimum and suddenly reverses to maximum as the wall is approached, revealing that the coarse approximation transitions from under-predicting to over-predicting perpendicular diffusion. Close to particle-to-cavity contact (far right of the plot), the relative error diverges because the coarse approach cannot account for vanishing mobility at the wall, and thus would vastly over-predict the speed of particle motion there — possibly permitting particle 'escape'. As volume fraction increases the relative error oscillates but does not undergo additional reversals, reflecting the fact that the effect of structural heterogeneity on perpendicular diffusion is weaker than its effect on radial diffusion. With decreasing particle-to-cavity relative size, the relative error decreases; however, error is still quite significant near the center for the smallest particles.

Overall, the assumptions of isotropy and position independence lead to significant error in the predicted perpendicular diffusion even for relatively small particles at dilute concentrations. As with the relative error obtained for radial diffusion, error only increases with increasing particle size.

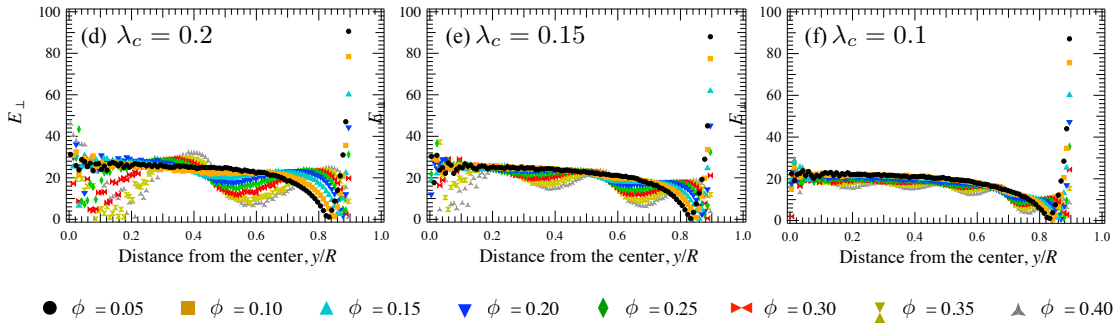

Figure B.4: Relative error of the short-time self-diffusivity in the perpendicular direction approximated by the early time behavior of the mean-square displacement. Plots (a), (b) and (c) correspond to the relative error in the perpendicular direction for suspensions with a particle-to-cavity relative size of 1/5, 1.5/10 and 1/10, respectively.

B.5 Statistical sampling and standard error

Here we discuss statistical error associated with spatial averaging of particle positions and displacements and how these impact results presented for the radial distribution function, short-time self diffusion, and anisotropy of diffusion. Division of the cavity into spherical shells of fixed thickness (cf. §3.2) permitted a discretized means by which to compute the probability of finding a particle a given radial distance from the cavity center. Fixed shell thickness gives a clear location of the inner radius of each shell, but also produces shells of progressively smaller volume as the center of the cavity is approached. Statistical sampling is thus best in the large shells far from the center, and noisiest near the center.

This behavior is illustrated in figure B.5, where the radial short-time self diffusivity is plotted as a function of radial position and the error bars correspond to the standard error of the reported value. The standard error is largest for radial positions near the cavity center, where bin volume is smallest. The error be-

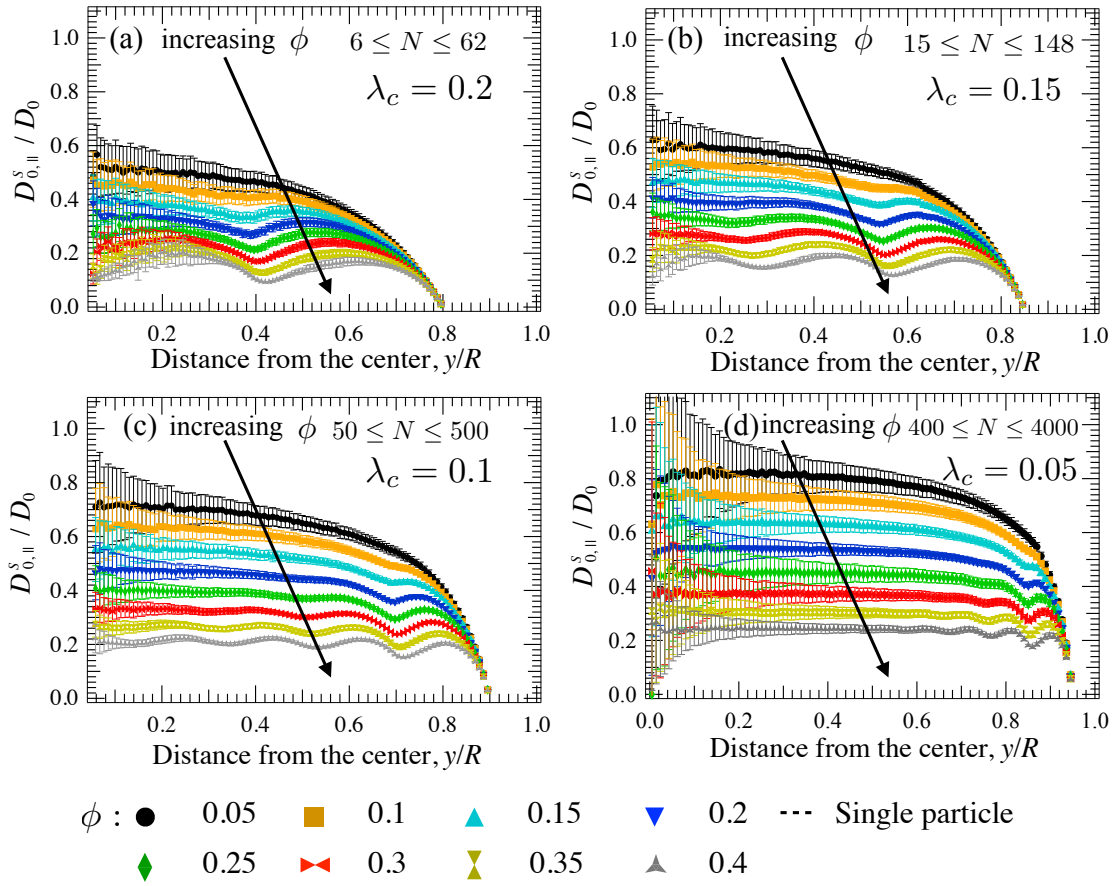

Figure B.5: Radial component of the short-time self-diffusivity in confined suspensions as a function of normalized distance from the center y/R for particle-to-cavity size ratios (a) $\lambda_c = 0.2$, (b) $\lambda_c = 0.15$, (c) $\lambda_c = 0.1$, and (d) $\lambda_c = 0.05$. Number of particles per simulation varies with volume fraction as shown in plots. Error bars are larger for particles near the center of the cavity, due to lower sampling of radial bins near the cavity center where the volume of each bin is small.

comes progressively smaller moving radially outward as bins grow in volume. The uncertainty of other position-dependent quantities follows a qualitatively similar trend, wherein error bars are smaller for positions close to the cavity wall than they are for positions close to the cavity center. To mitigate error near the center, the number of simulations was increased until the average relative error obtained in a region from the cavity center to half the cavity radius was

5 – 18%; relative errors near the wall are small due to better sampling in bins of higher volume.

Time-dependent quantities, such as the mean-square displacement and the excess kurtosis, are computed as a function of simulation lagtime. Simulation snapshots are taken by tracking particle positions over a time interval Δt in a simulation with a total time t_f, with samples obtained from all of the particles. The total number of snapshots is thus given by $N_s = t_f/\Delta t$, which is directly proportional to the simulation time but inversely proportional to the time interval Δt. Thus, in the calculation of all time-dependent quantities, a smaller time interval produces more snapshots for averaging. As a result, the uncertainty is smaller at short times, and increases as the value of the time interval increases. This behavior is illustrated in figures 5.10 and 5.11, where the noise increases as the time interval of interest increases. For each volume fraction and particle-to-cavity size ratio, at least three simulations were carried out for a total of 200 diffusive time steps, to observe the long-time plateau for all particle-to-cavity relative sizes. These simulations provided enough samples to obtain a relative standard error less than 0.5% for the mean-square displacement at short and intermediate times, as evidence by the nearly indistinguishable noise in figure 5.10. Only for time intervals comparable to the total simulation time does the standard error of the mean-square displacement lead to noticeable statistical noise in figure 5.10. Noise becomes more observable in the excess kurtosis (figure 5.11) owing to the small magnitude of the measurement itself,, which results in a smaller 'signal-to-noise' ratio.

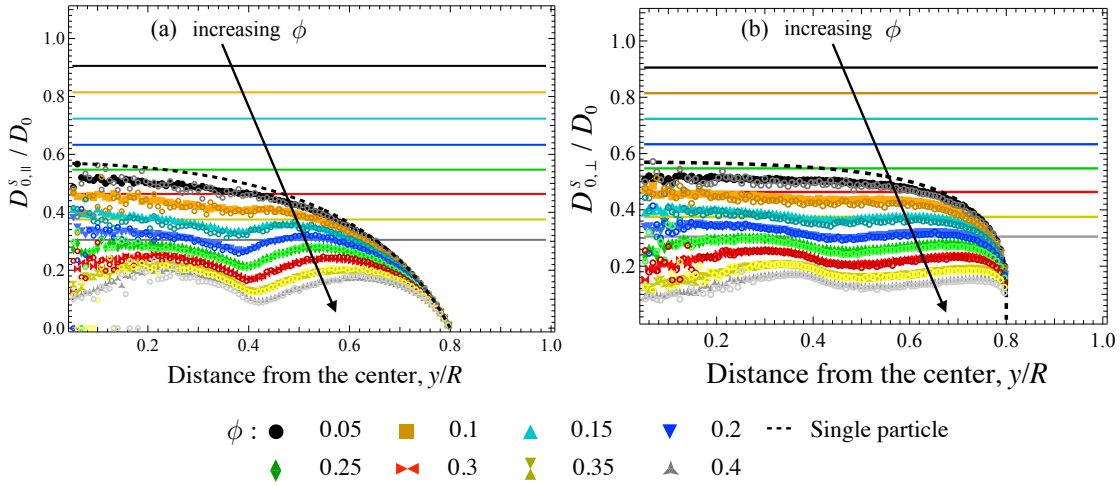

Figure B.6: Short-time self diffusivity in the (a) radial and (b) perpendicular directions as a function of normalized distance from the center y/R. Solid symbols represent the short-time self diffusivity from force-torque simulations, hollow circles represent the short-time self diffusivity from force-torque-stresslet simulations at matching volume fractions, and solid lines represent the short-time self diffusivity in unbound suspensions at matching volume fractions. Particles are 1/5 the cavity size and several volume fractions are plotted as shown in the legend.

B.6 Effects of truncating at the force-torque level

In this section, we discuss the effect of truncating the far-field mobility matrix Figure B.6 presents a comparison of the short-time self-diffusion coefficients for the force/torque only calculation and for the force/torque/stresslet calculation. The radial and perpendicular short-time self diffusivities for particles that are 1/5 the cavity size are plotted as a function of particle distance to the cavity center in figures B.6(a) and B.6(b), respectively. Solid symbols correspond to the radial short-time self diffusivity predicted by force-torque simulations, hollow circles correspond to the short-time self diffusivity obtained from force-torque-stresslet simulations, and solid lines correspond to the short-time diffusivity of particles in an unbound domain. Solid symbols, hollow circles, and solid lines

of equal color correspond to simulations at matching volume fractions. As seen in the figure, the results are nearly indistinguishable, demonstrating that the weak contribution of the stresslet at equilibrium can be neglected.

APPENDIX C

APPENDICES RELATED TO CHAPTER 5

C.1 Effect of particle to cavity relative size

Here, we analyze the dependence on particle-to-cavity relative size of the concentrated pair mobility in the confined domain. The same qualitative behaviors observed in chapter 6 are observed for the different particle-to-cavity relative sizes. As expected, the prediction obtained from using the spherically confined Green's function performs worse for larger particle-to-cavity relative sizes.

C.2 Concentrated pair mobility along the line of centers

In figures C.1, C.2, and C.3, the concentrated pair mobility along the particle line of centers is plotted as a function of separation distance between the particles for suspensions where the particle-to-cavity relative is 0.1, 0.15, and 0.2, respectively. Plots labeled (a)-(d) in figures C.1, C.2, and C.3, present data for particles in different locations inside the cavity, where the distance to the cavity center increases from (a) to (d) in each plot. Data from dilute to concentrated is presented in each plot, as shown in the legends.

As with the concentrated pair mobility along the line of centers in suspensions where the particle-to-cavity relative size is 0.05 (cf. chapter 6), the presence of the confining boundary leads to a faster decay of entrainment with inter-particle separation distance. As particles become larger, the decay be-

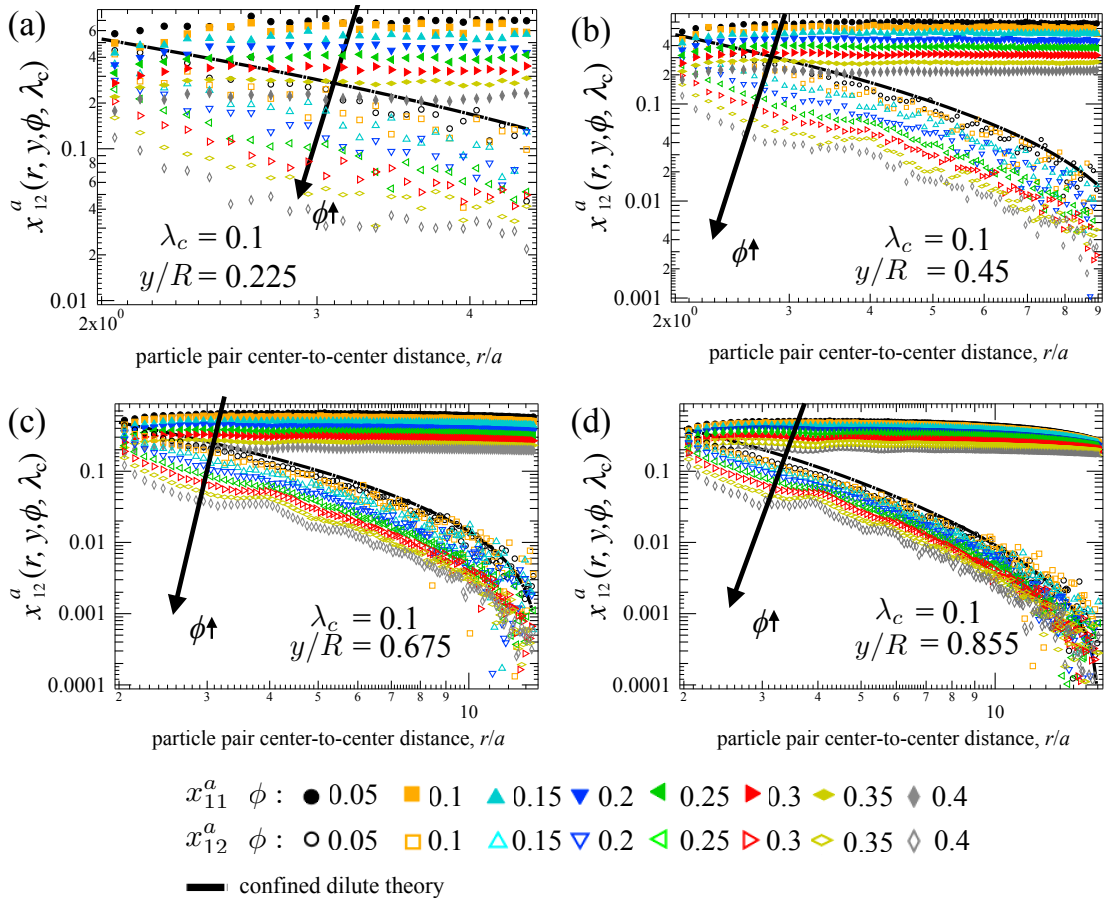

Figure C.1: Self and entrained concentrated pair mobility along the line of centers for spherically confined particles in suspension of varying concentrations as a function of particle separation distance. The particle-to-cavity relative size is $a/R = 0.1$

comes faster, meaning the effects of confinement become more pronounced, as expected. As with smaller particles, increasing volume fractions only leads to an $O(1)$ suppression of entrainment, and does not further alter the dependence of particle entrainment with inter-particle separation distance. Next, we analyze how changing particle-to-cavity relative size impacts the concentrate pair mobility perpendicular to the line of centers.

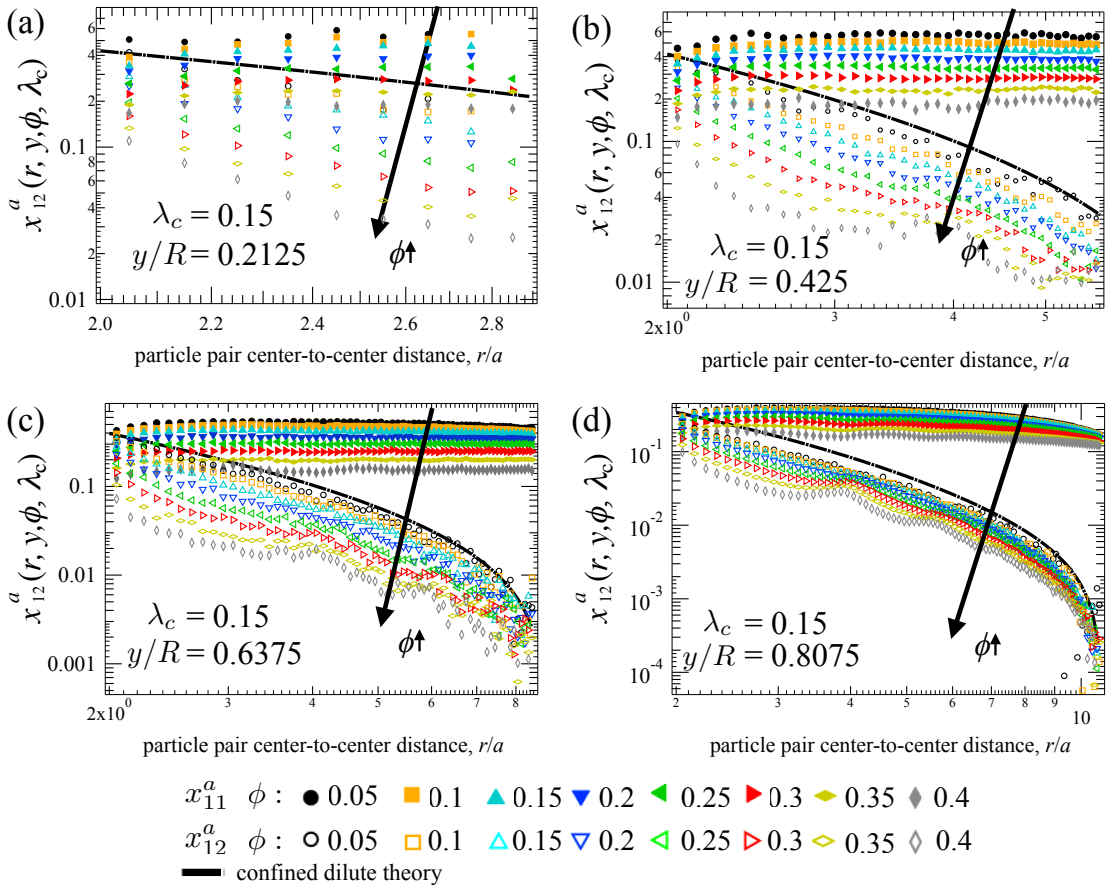

Figure C.2: Self and entrained concentrated pair mobility along the line of centers for spherically confined particles in suspension of varying concentrations as a function of particle separation distance. The particle-to-cavity relative size is $a/R = 0.15$

C.3 Concentrated pair mobility perpendicular to the line of centers

In figures C.4, C.5, and C.6, the concentrated pair mobility perpendicular to the particle line of centers is plotted as a function of separation distance between the particles for suspensions where the particle-to-cavity relative is 0.1, 0.15, and 0.2, respectively. Plots labeled (a)-(d) in figures C.4, C.5, and C.6, present data for particles in different locations inside the cavity, where the distance to the

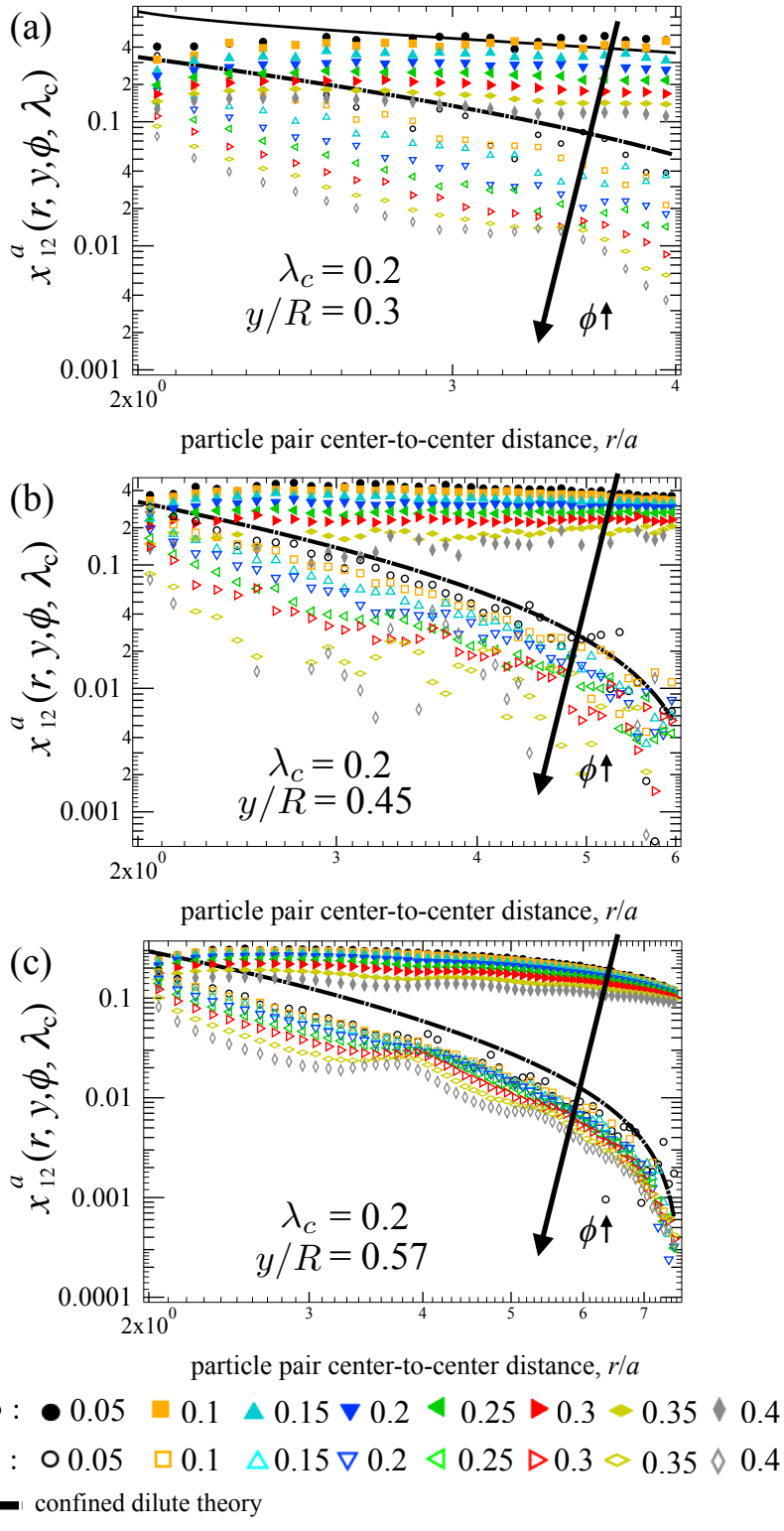

Figure C.3: Self and entrained concentrated pair mobility along the line of centers for spherically confined particles in suspension of varying concentrations as a function of particle separation distance. The particle-to-cavity relative size is $a/R = 0.2$

cavity center increases from (a) to (d) in each plot. Data from dilute to concentrated is presented in each plot, as shown in the legends.

As with particles with a particle-to-cavity relative size of 0.05, confinement induces a sign change in the concentrated pair mobility perpendicular to the line of centers. The separation distance at which the sign change is observed varies with the position of the interacting pair inside the spherical cavity. Although for particles near the center the sign change may be predicted from the functional form of the spherically confined Green's function, the prediction becomes increasingly worse as with increasing particle size and increasing proximity to the cavity wall. This is expected, as larger particles or particles close to the cavity wall are not able to interact with each other or with the cavity as points.

For very large particles close to the cavity wall, plots C.6(b) and C.6(c), the entrainment pair mobility is exclusively negative. For such large particles near the cavity wall, a forced particle will induce a recirculation flow that entrains any particle found at the same radial position in the opposite direction of the forced particle. This reflects that confinement induced effects become more pronounced as particle-to-cavity relative size increases.

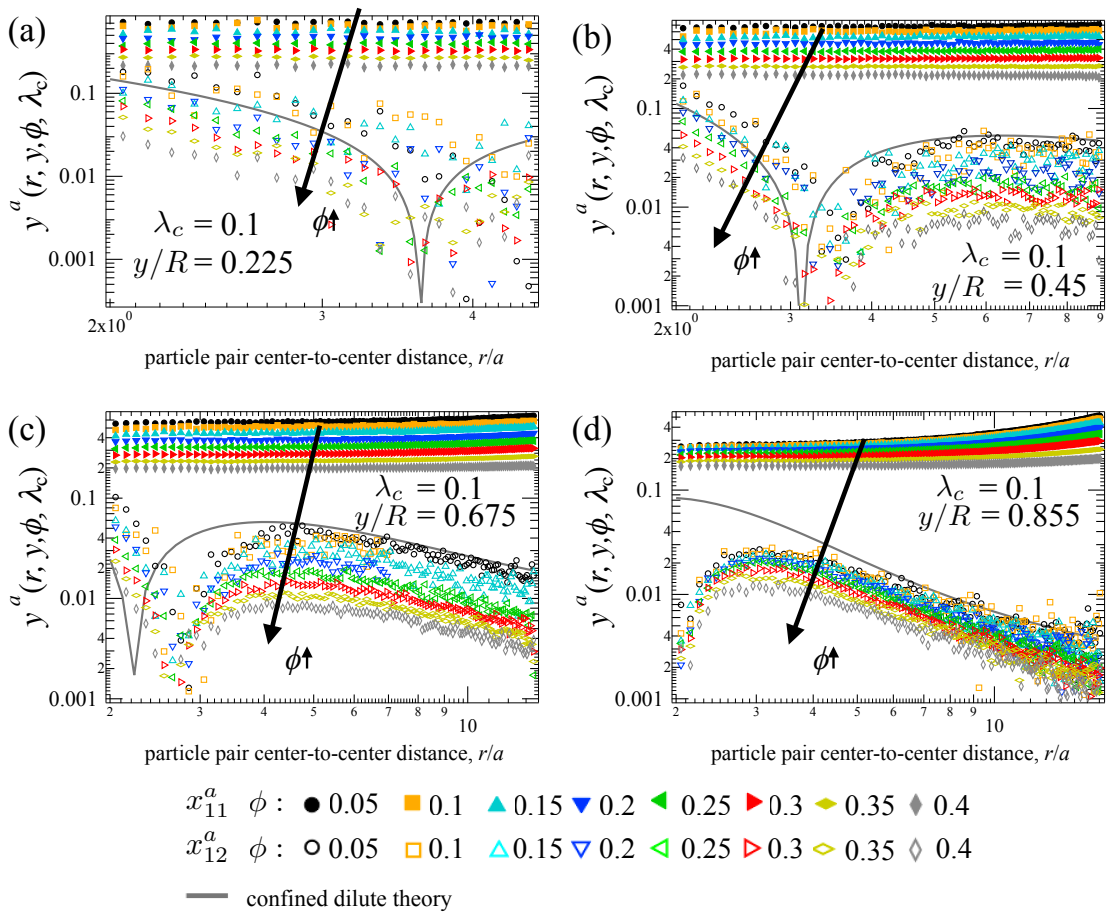

Figure C.4: Self and entrained concentrated pair mobility perpendicular to the line of centers for spherically confined particles in suspension of varying concentrations as a function of particle separation distance. The particle-to-cavity relative size is $a/R = 0.1$

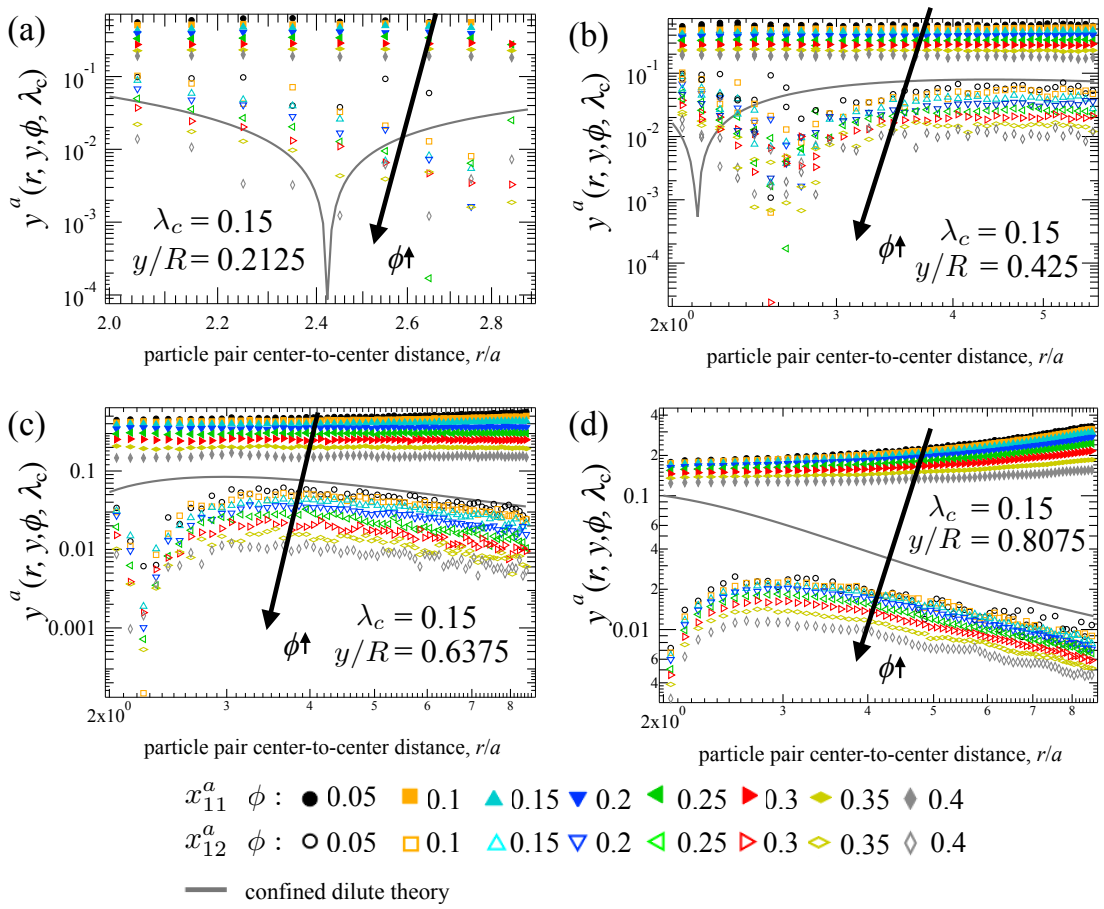

Figure C.5: Self and entrained concentrated pair mobility perpendicular to the line of centers for spherically confined particles in suspension of varying concentrations as a function of particle separation distance. The particle-to-cavity relative size is $a/R = 0.15$

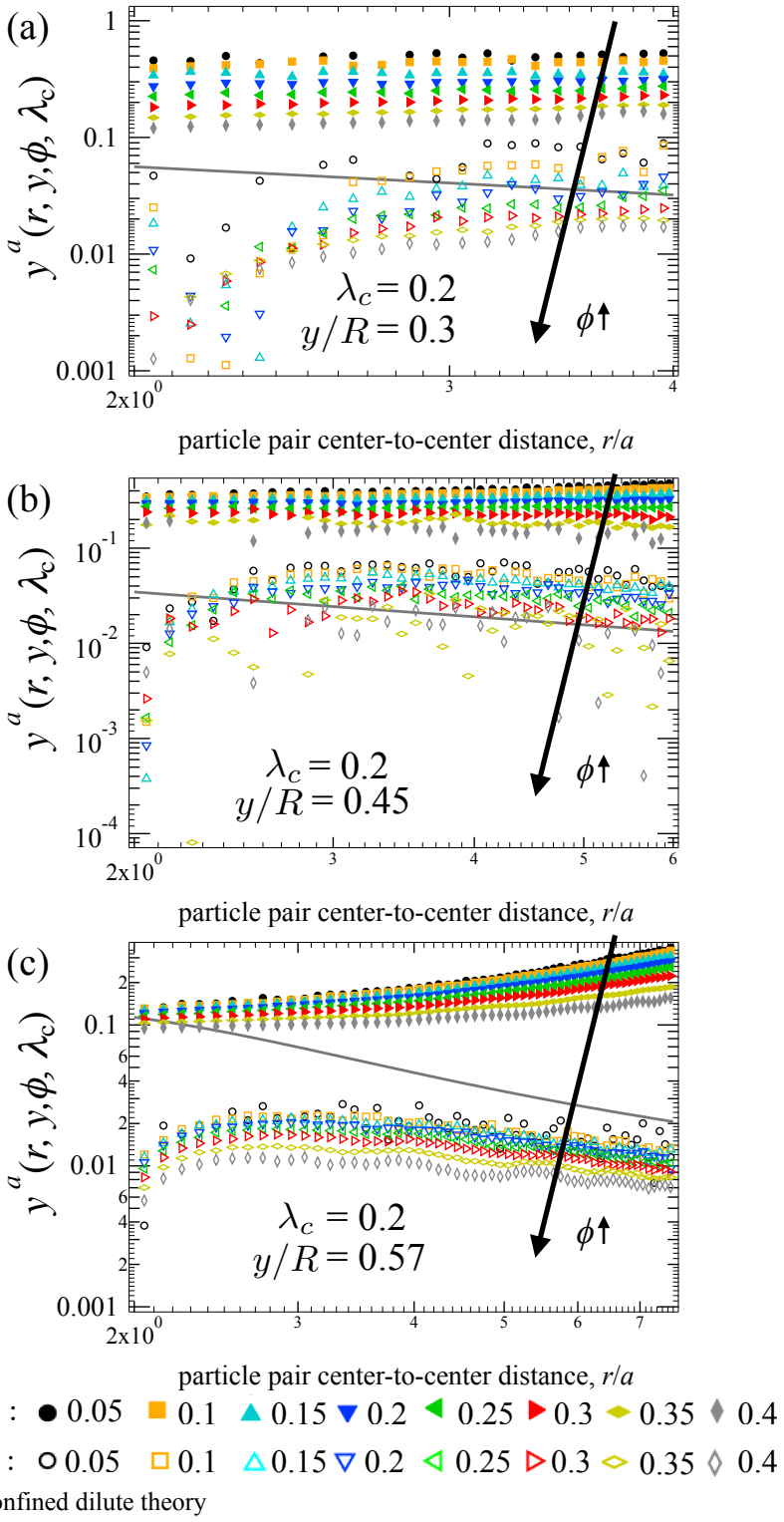

Figure C.6: Self and entrained concentrated pair mobility perpendicular to the line of centers for spherically confined particles in suspension of varying concentrations as a function of particle separation distance. The particle-to-cavity relative size is $a/R = 0.2$

C.4 Components connecting a radial force to a perpendicular velocity and a perpendicular force to a radial velocity

Whereas in an unbound domain a force along (perpendicular to) the line of center between the particles will lead to motion only in that direction, the presence of a boundary results in a coupling between force along (perpendicular to) the line of centers and motion perpendicular to (along) it. However, the strength of this coupling is very weak, with a magnitude smaller than $\leq O(10^{-2})$ for all particle-to-cavity relative sizes considered in this work. As a consequence, the concentrated pair mobility for this coupling obtained from the simulation is not distinguishable from simulation noise. Here, we consider the concentrated pair mobility predicted by the leading order Green's function in the confined domain, in order examine the behavior of this coupling as a function of inter-particle separation distance, radial position in the cavity and particle-to-cavity relative size.

In figure C.7(a)-(b), the leading order entrainment mobility coupling a force perpendicular to the particle line of centers to a velocity along the line of centers is plotted for particles that are 1/20, 1/10, 1.5/10, and 1/5 the cavity size, respectively, as a function of separation distance between the particles. Different curves correspond to particles at different radial positions within the cavity, as shown in the legends. A coupling between a perpendicular force and a radial velocity would be zero in an unbound domain and thus it is an effect arising due to confinement. The magnitude of the coupling is the smallest for positions near the cavity center, where confinement effects are weakest, and increases in magnitude near the cavity wall (blue, green and yellow orange curves), where

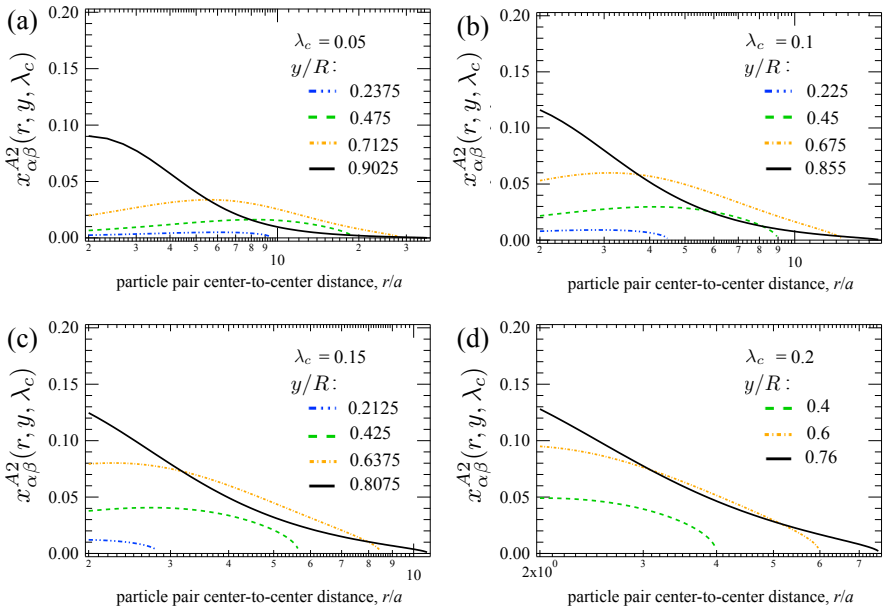

Figure C.7: Entrained mobility coupling a force perpendicular to the line of centers between the particles to velocity along the line of centers. Particle to cavity size ratios and particle radial positions inside the cavity are as shown in each legend.

confinement effects are strongest. For the position closest to the wall (black line), the coupling for particles close together (far left of the plot) is predicted to have the highest magnitude. However, the value of the coupling quickly decays with particle separation distance, making it smaller than the corresponding coupling for particles found closer to the cavity center. This reflects that although confinement effects are strongest near the wall, leading to a stronger coupling when particles are close together, motion is strongly hindered, leading to a fast decay of the coupling with particle separation distance. The positive value of the coupling implies that when the forced particle is acted on by a perpendicular force, the radial motion of the entrained particle would move it away from the forced particle.

In figure C.8(a)-(b), the leading order entrainment mobility coupling a force along the particle line of centers to a velocity perpendicular to the particle line of

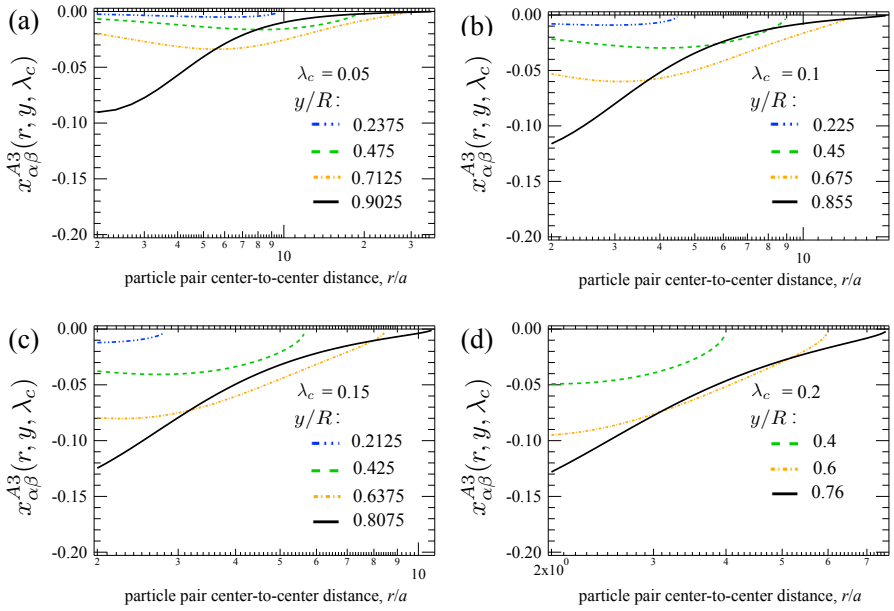

Figure C.8: Entrained mobility coupling a force along the line of centers between the particles to velocity perpendicular to the line of centers. Particle to cavity size ratios and particle radial positions inside the cavity are as shown in each legend.

centers is plotted for particles that are 1/20, 1/10, 1.5/10, and 1/5 the cavity size, respectively, as a function of separation distance between the particles. Similar behaviors to those obtained for the coupling between a perpendicular force and a radial velocity are observed, the strength of the coupling increases with proximity to the cavity wall and for the position closest to the wall the coupling has a fast decay with particle separation distance. However, this coupling is found to have a negative value, meaning that when a forced particle is acted on by a radial force, the motion of the entrained particle a radial force acting on a forced particle the perpendicular motion of the entrained particle would move it away from the cavity wall.

BIBLIOGRAPHY

[1] P Ahlrichs, R Everaers, and B Dünweg. Screening of hydrodynamic interactions in semidilute polymer solutions: a computer simulation study. *Physical review. E, Statistical, nonlinear, and soft matter physics*, 64(4 Pt 1): 040501, 2001. ISSN 1539-3755. doi: 10.1103/PhysRevE.64.040501. URL http://www.ncbi.nlm.nih.gov/pubmed/11689999.

[2] Cyrus K Aidun, Jonathan R Clausen, and G W Woodruff. Lattice-Boltzmann Method for Complex Flows. *Annu. Rev. Fluid Mech*, 42:439–72, 2010. ISSN 0066-4189. doi: 10.1146/annurev-fluid-121108-145519.

[3] B Alder and T Wainwright. Phase Transition for a Hard Sphere System. *Journal of Chemical Physics*, 27:1208–1211, 1957. ISSN 00219606. doi: 10.1063/1.1743957. URL papers://df790107-00bb-4d1a-a7c1-3a1abd474f6d/Paper/p7947.

[4] Tadashi Ando and Jeffrey Skolnick. Crowding and hydrodynamic interactions likely dominate in vivo macromolecular motion. *Proceedings of the National Academy of Sciences of the United States of America*, 107(43): 18457–62, oct 2010. ISSN 1091-6490. doi: 10.1073/pnas.1011354107. URL http://www.pubmedcentral.nih.gov/articlerender.fcgi?artid=2973006{&}tool=pmcentrez{&}rendertype=abstract.

[5] M. J. Andrews and P. J. O'Rourke. The multiphase particle-in-cell (MP-PIC) method for dense particulate flows. *International Journal of Multiphase Flow*, 22(2):379–402, 1996. ISSN 03019322. doi: 10.1016/0301-9322(95)00072-0.

[6] Christian Aponte-Rivera and Roseanna N. Zia. Simulation of hydrodynamically interacting particles confined by a spherical cavity. *Phys-*

ical Review Fluids, 1(2):023301, 2016. ISSN 2469-990X. doi: 10.1103/PhysRevFluids.1.023301.

[7] Christian Aponte-Rivera and Roseanna N. Zia. Hydrodynamic entrainment in spherically confined suspensions and its implications. *In preparation*, 2017.

[8] Christian Aponte-Rivera, Yu Su, and Roseanna N. Zia. Equilibrium structure and diffusion in concentrated, hydrodynamically interacting suspensions confined by a spherical cavity. *Journal of Fluid Mechanics*, In press, 2017.

[9] Adolfo J. Banchio and John F. Brady. Accelerated Stokesian dynamics: Brownian motion. *The Journal of Chemical Physics*, 118(22):10323, 2003. ISSN 00219606. doi: 10.1063/1.1571819. URL http://scitation.aip.org/content/aip/journal/jcp/118/22/10.1063/1.1571819.

[10] G. K. Batchelor. The stress system in a suspension of force-free particles. *Journal of Fluid Mechanics*, 41(03):545, mar 1970. ISSN 0022-1120. doi: 10.1017/S0022112070000745. URL http://www.journals.cambridge.org/abstract{_}S0022112070000745.

[11] G. K. Batchelor. Brownian diffusion of particles with hydrodynamic interaction. *Journal of Fluid Mechanics*, 74(01):1, mar 1976. ISSN 0022-1120. doi: 10.1017/S0022112076001663. URL http://www.journals.cambridge.org/abstract{_}S0022112076001663.

[12] GK Batchelor. Sedimentation in a dilute polydisperse system of interacting spheres. Part 1. General theory. *Journal of Fluid Mechan-*

ics, 119:379–408, 1982. URL http://journals.cambridge.org/abstract{_}S0022112082001402.

[13] CWJ Beenakker and P Mazur. Many-sphere hydrodynamic interactions: IV. Wall-effects inside a spherical container. *Physica A: Statistical Mechanics and its Applications*, 131A:311–328, 1985. URL http://www.sciencedirect.com/science/article/pii/0378437185900019.

[14] C Berdan and L.G Leal. Motion of a sphere in the presence of a deformable interface. *Journal of Colloid and Interface Science*, 87(1):62–80, may 1982. ISSN 00219797. doi: 10.1016/0021-9797(82)90372-1. URL http://linkinghub.elsevier.com/retrieve/pii/0021979782903721.

[15] J. Bergenholtz, J. F. Brady, and M. Vicic. The non-Newtonian rheology of dilute colloidal suspensions. *Journal of Fluid Mechanics*, 456:239–275, apr 2002. ISSN 0022-1120. doi: 10.1017/S0022112001007583. URL http://www.journals.cambridge.org/abstract{_}S0022112001007583.

[16] Sukalyan Bhattacharya. Cooperative motion of spheres arranged in periodic grids between two parallel walls. *Journal of Chemical Physics*, 128(7):074709, 2008. ISSN 00219606. doi: 10.1063/1.2830713.

[17] Sukalyan Bhattacharya, Columbia Mishra, and Sonal Bhattacharya. Analysis of general creeping motion of a sphere inside a cylinder. *Journal of Fluid Mechanics*, 642:295–328, 2010. ISSN 0022-1120. doi: 10.1017/S0022112009991789. URL http://www.journals.cambridge.org/abstract{_}S0022112009991789.

[18] Thomas Bickel. A note on confined diffusion. *Physica A: Statistical Mechanics and its Applications*, 377(1):24–32, 2007. ISSN 03784371. doi: 10.1016/j.physa.2006.11.008.

[19] J. R. Blake. A note on the image system for a stokeslet in a no-slip boundary. *Mathematical Proceedings of the Cambridge Philosophical Society*, 70(02):303, oct 1971. ISSN 0305-0041. doi: 10.1017/S0305004100049902. URL http://www.journals.cambridge.org/abstract{_}S0305004100049902.

[20] Dan S. Bolintineanu, Gary S. Grest, Jeremy B. Lechman, Flint Pierce, Steven J. Plimpton, and P. Randall Schunk. Particle dynamics modeling methods for colloid suspensions. *Computational Particle Mechanics*, pages 321–356, 2014. ISSN 2196-4378. doi: 10.1007/s40571-014-0007-6. URL http://link.springer.com/10.1007/s40571-014-0007-6.

[21] G. Bossis and J. F. Brady. The rheology of Brownian suspensions. *The Journal of Chemical Physics*, 91(3):1866, 1989. ISSN 00219606. doi: 10.1063/1.457091. URL http://scitation.aip.org/content/aip/journal/jcp/91/3/10.1063/1.457091.

[22] J F Brady and G Bossis. Stokesian Dynamics. *Annual Review of Fluid Mechanics*, 20(1):111–157, jan 1988. ISSN 0066-4189. doi: 10.1146/annurev.fl.20.010188.000551. URL http://www.annualreviews.org/doi/abs/10.1146/annurev.fl.20.010188.000551.

[23] John F. Brady. Brownian motion, hydrodynamics, and the osmotic pressure. *The Journal of Chemical Physics*, 98(4):3335, 1993. ISSN 00219606. doi: 10.1063/1.464105. URL http://link.aip.org/link/JCPSA6/v98/i4/p3335/s1{&}Agg=doi.

[24] John F. Brady. The long-time self-diffusivity in concentrated colloidal dispersions. *Journal of Fluid Mechanics*, 272(-1):109, 1994. ISSN 0022-1120. doi: 10.1017/S0022112094004404.

[25] John F. Brady and Georges Bossis. The rheology of concentrated suspensions of spheres in simple shear flow by numerical simulation. *Journal of Fluid Mechanics*, 155:105, 1985. ISSN 0022-1120. doi: 10.1017/S0022112085001732.

[26] John F. Brady and Jeffrey F. Morris. Microstructure of strongly sheared suspensions and its impact on rheology and diffusion. *Journal of Fluid Mechanics*, 348:103–139, 1997. ISSN 00221120. doi: 10.1017/S0022112097006320.

[27] John F. Brady and M Vicic. Normal stresses in colloidal dispersions. *Journal of Rheology*, 39(3):545, 1995. ISSN 01486055. doi: 10.1122/1.550712.

[28] Clifford P Brangwynne, Gijsje H Koenderink, Frederick C MacKintosh, and David a Weitz. Cytoplasmic diffusion: molecular motors mix it up. *The Journal of cell biology*, 183(4):583–587, nov 2008. ISSN 1540-8140. doi: 10.1083/jcb.200806149. URL http://www.pubmedcentral.nih.gov/articlerender.fcgi?artid=2582900{&}tool=pmcentrez{&}rendertype=abstract.

[29] Clifford P Brangwynne, Christian R Eckmann, David S Courson, Agata Rybarska, Carsten Hoege, Jöbin Gharakhani, Frank Jülicher, and Anthony a Hyman. Germline P granules are liquid droplets that localize by controlled dissolution/condensation. *Science (New York, N.Y.)*, 324(5935):1729–32, jun 2009. ISSN 1095-9203. doi: 10.1126/science.1172046. URL http://www.ncbi.nlm.nih.gov/pubmed/19460965.

[30] Clifford P Brangwynne, Gijsje H Koenderink, Frederick C MacKintosh, and David a Weitz. Intracellular transport by active diffusion. *Trends in cell biology*, 19(9):423–427, sep 2009. ISSN 1879-3088. doi: 10.1016/j.tcb.2009.04.004. URL http://www.ncbi.nlm.nih.gov/pubmed/19699642.

[31] Howard Brenner. The slow motion of a sphere through a viscous fluid towards a plane surface. *Chemical Engineering Science*, 16(3-4):242–251, 1961. ISSN 00092509. doi: 10.1016/0009-2509(61)80035-3.

[32] Howard Brenner and Michael E. O'Neill. On the Stokes resistance of multiparticle systems in a linear shear field. *Chemical Engineering Science*, 27: 1421–1439, 1972. ISSN 00092509. doi: 10.1016/0009-2509(72)87060-X.

[33] A. E. Cervantes-Martínez, A. Ramírez-Saito, R. Armenta-Calderón, M. a. Ojeda-López, and J. L. Arauz-Lara. Colloidal diffusion inside a spherical cell. *Physical Review E*, 83(3):030402, mar 2011. ISSN 1539-3755. doi: 10.1103/PhysRevE.83.030402. URL http://link.aps.org/doi/10.1103/PhysRevE.83.030402.

[34] E Chow and J Skolnick. Effects of confinement on models of intracellular macromolecular dynamics. *Proceedings of the National Academy of Sciences of the United States of America*, 112(48):14846–14851, 2015. ISSN 0027-8424. doi: 10.1073/pnas.1514757112.

[35] Henry C.W. Chu and Roseanna N. Zia. The non-Newtonian rheology of hydrodynamically interacting colloids via active, nonlinear microrheology. *Journal of Rheology*, page In preparation, 2016.

[36] Henry C.W. Chu and Roseanna N. Zia. Active microrheology of hydrody-

namically interacting spheres: Normal stresses. *Journal of Rheology*, page In review, 2016.

[37] Ralph H. Colby. Structure and linear viscoelasticity of flexible polymer solutions: Comparison of polyelectrolyte and neutral polymer solutions. *Rheologica Acta*, 49(5):425–442, 2010. ISSN 00354511. doi: 10.1007/s00397-009-0413-5.

[38] M. D. a. Cooley and M. E. O'Neill. On the slow motion generated in a viscous fluid by the approach of a sphere to a plane wall or stationary sphere. *Mathematika*, 16:37, feb 1969. ISSN 0025-5793. doi: 10.1112/S0025579300004599. URL http://www.journals.cambridge.org/abstract{_}S0025579300004599.

[39] Carrie R Cowan and Anthony a Hyman. Acto-myosin reorganization and PAR polarity in C. elegans. *Development (Cambridge, England)*, 134(6):1035–43, mar 2007. ISSN 0950-1991. doi: 10.1242/dev.000513. URL http://www.ncbi.nlm.nih.gov/pubmed/17287245.

[40] John C Crocker and Brenton D Hoffman. Multiple-particle tracking and two-point microrheology in cells. *Methods in cell biology*, 83(07):141–178, jan 2007. ISSN 0091-679X. doi: 10.1016/S0091-679X(07)83007-X. URL http://www.ncbi.nlm.nih.gov/pubmed/17613308.

[41] John C. Crocker, M. T. Valentine, Eric R. Weeks, T. Gisler, P. D. Kaplan, a. G. Yodh, and D. a. Weitz. Two-point microrheology of inhomogeneous soft materials. *Physical Review Letters*, 85(4):888–891, 2000. ISSN 00319007. doi: 10.1103/PhysRevLett.85.888.

[42] E. Cunningham. On the Velocity of Steady Fall of Spherical

Particles through Fluid Medium. *Proceedings of the Royal Society A: Mathematical, Physical and Engineering Sciences*, 83(563):357–365, mar 1910. ISSN 1364-5021. doi: 10.1098/rspa.1910.0024. URL http://rspa.royalsocietypublishing.org/cgi/doi/10.1098/rspa.1910.0024.

[43] Brian R Daniels, Byron C Masi, and Denis Wirtz. Probing single-cell micromechanics in vivo: the microrheology of C. elegans developing embryos. *Biophysical journal*, 90(12):4712, jun 2006. ISSN 0006-3495. doi: 10.1529/biophysj.105.080606. URL http://www.pubmedcentral.nih.gov/articlerender.fcgi?artid=1471839{&}tool=pmcentrez{&}rendertype=abstract.

[44] P. G. de Gennes. Dynamics of Entangled Polymer Solutions. II. Inclusion of Hydrodynamic Interactions. *Macromolecules*, 9(4):594–598, 1976. ISSN 0024-9297. doi: 10.1021/ma60052a012.

[45] WR Dean and ME O'Neill. A slow motion of viscous liquid caused by the rotation of a solid sphere. *Mathematika*, 10(01):13–24, 1963. URL http://journals.cambridge.org/abstract{_}S0025579300003314.

[46] R. E. DeWames, W. F. Hall, and M. C. Shen. On the Molecular Theories of Polymer Solutions. *The Journal of Chemical Physics*, 46(7):2782–2794, 1967. ISSN 00219606. doi: 10.1063/1.1841114.

[47] L Durlofsky and J. F. Brady. Analysis of the Brinkman equation as a model for flow in porous media. *Physics of Fluids*, 30(11):3329–3341, 1987. ISSN 00319171. doi: 10.1063/1.866465. URL http://link.aip.org/link/PFLDAS/v30/i11/p3329/s1{&}Agg=doi.

[48] L. Durlofsky, J. F. Brady, and G. Bossis. Dynamic simulation of hydrodynamically interacting particles. *Journal of Fluid Mechanics*, 180:21–49, apr 1987. ISSN 0022-1120. doi: 10.1017/S002211208700171X. URL http://www.journals.cambridge.org/abstract{_}S002211208700171X.

[49] B U Felderhof and A Sellier. Mobility matrix of a spherical particle translating and rotating in a viscous fluid confined in a spherical cell, and the rate of escape from the cell. *The Journal of chemical physics*, 136 (5):054703, feb 2012. ISSN 1089-7690. doi: 10.1063/1.3681368. URL http://www.ncbi.nlm.nih.gov/pubmed/22320755.

[50] David R. Foss and John F. Brady. Brownian Dynamics simulation of hard-sphere colloidal dispersions. *Journal of Rheology*, 44(3):629, 2000. ISSN 01486055. doi: 10.1122/1.551104.

[51] DR Foss and JF Brady. Structure, diffusion and rheology of Brownian suspensions by Stokesian dynamics simulation. *Journal of Fluid Mechanics*, 407:167–200, 2000. URL http://journals.cambridge.org/abstract{_}S0022112099007557.

[52] AS Geller, SH Lee, and LG Leal. The creeping motion of a spherical particle normal to a deformable interface. *Journal of Fluid Mechanics*, 169:27–69, 1986. URL http://journals.cambridge.org/abstract{_}S0022112086000538.

[53] A Golden. Cytoplasmic flow and the establishment of polarity in C. elegans 1-cell embryos. *Current opinion in genetics & development*, 10(4):414–420, aug 2000. ISSN 0959-437X. URL http://www.ncbi.nlm.nih.gov/pubmed/10889063.

[54] Ido Golding and Edward Cox. Physical Nature of Bacterial Cytoplasm. *Physical Review Letters*, 96(9):098102, mar 2006. ISSN 0031-9007. doi: 10.1103/PhysRevLett.96.098102. URL http://link.aps.org/doi/10.1103/PhysRevLett.96.098102.

[55] Raymond E Goldstein, Idan Tuval, and Jan-willem Van De Meent. Microfluidics of cytoplasmic streaming and its implications for intracellular transport. *Proceedings of the National Academy of Sciences of the United States of America*, 105(10):3663–3667, 2008.

[56] Pierre Gönczy and Lesilee S Rose. *Asymmetric cell division and axis formation in the embryo*. WormBook Ed. The C. Elegans Research Community, 2005.

[57] A. González, J. A. White, F. L. Román, and R. Evans. How the structure of a confined fluid depends on the ensemble: Hard spheres in a spherical cavity. *Journal of Chemical Physics*, 109(9):3637–3650, 1998. ISSN 00219606. doi: 10.1063/1.476961.

[58] David Goulding and Jean-Pierre Hansen. Effective interaction between charged colloidal particles near a surface. *Molecular Physics*, 95(3):649–655, oct 1998. ISSN 0026-8976. doi: 10.1080/00268979809483198. URL http://www.tandfonline.com/doi/abs/10.1080/00268979809483198.

[59] J T Green and G. K. Batchelor. The hydrodynamic interaction of two small freely-moving spheres in a linear flow field. *Journal of Fluid Mechanics*, 56:375, 1972.

[60] Elisabeth Guazzelli and Jeffrey F. Morris. *A physical introduction to suspension dynamics*. Cambridge University Press, New York, NY, 2012.

[61] S. Haber and H. Brenner. Hydrodynamic interactions of spherical particles in quadratic Stokes flows. *International Journal of Multiphase Flow*, 25(6-7):1009–1032, 1999. ISSN 03019322. doi: 10.1016/S0301-9322(99)00039-7.

[62] John Happel. Viscous flow in multiparticle systems: Slow motion of fluids relative to beds of spherical particles. *AIChE Journal*, 4(2):197–201, jun 1958. ISSN 0001-1541. doi: 10.1002/aic.690040214. URL `http://doi.wiley.com/10.1002/aic.690040214`.

[63] John Happel and Howard Brenner. *Low Reynolds number Hydrodynamics with special applications to particulate media*. Martinus Nijhoff Publishers, Hingham, MA, 2nd edition, 1983. ISBN 90-247-2877-0.

[64] Gregory P. Henderson, Lu Gan, and Grant J. Jensen. 3-D ultrastructure of O. tauri: Electron cryotomography of an entire Eukaryotic cell. *PLoS ONE*, 2(8):e749, 2007. ISSN 19326203. doi: 10.1371/journal.pone.0000749.

[65] a. G. Hendricks, Bogdan I. Epureanu, and Edgar Meyhöfer. Collective dynamics of kinesin. *Physical Review E - Statistical, Nonlinear, and Soft Matter Physics*, 79(3):1–12, 2009. ISSN 15393755. doi: 10.1103/PhysRevE.79.031929.

[66] Brenton D Hoffman and John C Crocker. Cell mechanics: dissecting the physical responses of cells to force. *Annual review of biomedical engineering*, 11:259–288, jan 2009. ISSN 1545-4274. doi: 10.1146/annurev.bioeng.

10.061807.160511. URL http://www.ncbi.nlm.nih.gov/pubmed/19400709.

[67] Brenton D Hoffman, Gladys Massiera, Kathleen M Van Citters, and John C Crocker. The consensus mechanics of cultured mammalian cells. *Proceedings of the National Academy of Sciences of the United States of America*, 103 (27):10259–10264, 2006. ISSN 0027-8424. doi: 10.1073/pnas.0510348103.

[68] Nicholas J Hoh and Roseanna Zia. The impact of probe size on measurements of diffusion in active microrheology. *Lab Chip*, 16:3114–3129, 2016. ISSN 1473-0197. doi: 10.1039/C6LC00476H. URL http://pubs.rsc.org/en/Content/ArticleLanding/2016/LC/C6LC00476H.

[69] Nicholas J Hoh and Roseanna N. Zia. Hydrodynamic diffusion in active microrheology of non-colloidal suspensions: the role of interparticle forces. *Journal of Fluid Mechanics*, 785:189–218, 2015.

[70] Nicholas J. Hoh and Roseanna N. Zia. Force-induced diffusion in suspensions of hydrodynamically interacting colloids. *Journal of Fluid Mechanics*, 795:739–783, 2016.

[71] P. J Hoogerbrugge and J. M. V. a Koelman. Simulating Microscopic Hydrodynamic Phenomena with Dissipative Particle Dynamics. *Europhysics Letters (EPL)*, 19(3):155–160, 1992. ISSN 0295-5075. doi: 10.1209/0295-5075/19/3/001.

[72] JP Hsu, WL Hsu, and ZS Chen. Boundary effect on diffusiophoresis: spherical particle in a spherical cavity. *Langmuir*, 25(3):1772–1784, 2009. doi: 10.1021/la803334a. URL http://pubs.acs.org/doi/abs/10.1021/la803334a.

[73] Jyh-Ping Hsu and Zheng-Syun Chen. Effects of double-layer polarization and electroosmotic flow on the electrophoresis of an ellipsoid in a spherical cavity. *The journal of physical chemistry. B*, 112(36):11270–7, sep 2008. ISSN 1520-6106. doi: 10.1021/jp8043863. URL http://www.ncbi.nlm.nih.gov/pubmed/18707074.

[74] Jyh-ping Hsu, Shih-hsing Hung, and Chen-yuan Kao. Electrophoresis of a Sphere at an Arbitrary Position in a Spherical Cavity. *Langmuir*, 18: 8897–8901, 2002.

[75] Jyh-Ping Hsu, Zheng-Syun Chen, Ming-Hong Ku, and Li-Hsien Yeh. Effect of charged boundary on electrophoresis: Sphere in spherical cavity at arbitrary potential and double-layer thickness. *Journal of colloid and interface science*, 314(1):256–63, oct 2007. ISSN 0021-9797. doi: 10.1016/j.jcis.2007.05.042. URL http://www.ncbi.nlm.nih.gov/pubmed/17583719.

[76] Jyh-Ping Hsu, Li-Hsien Yeh, and Zheng-Syun Chen. Effect of a charged boundary on electrophoresis: a sphere at an arbitrary position in a spherical cavity. *Journal of colloid and interface science*, 310(1):281–91, jun 2007. ISSN 0021-9797. doi: 10.1016/j.jcis.2007.01.030. URL http://www.ncbi.nlm.nih.gov/pubmed/17306286.

[77] Gary L. Hunter, Kazem V. Edmond, and Eric R. Weeks. Boundary Mobility Controls Glassiness in Confined Colloidal Liquids. *Physical Review Letters*, 112(21):218302, may 2014. ISSN 0031-9007. doi: 10.1103/PhysRevLett.112.218302. URL http://link.aps.org/doi/10.1103/PhysRevLett.112.218302.

[78] Steffen Jaensch, Markus Decker, Anthony a. Hyman, and Eugene W. My-

ers. Automated tracking and analysis of centrosomes in early Caenorhabditis elegans embryos. *Bioinformatics*, 26(12):13–20, 2010. ISSN 13674803. doi: 10.1093/bioinformatics/btq190.

[79] G. B. Jeffery. On a Form of the Solution of Laplace's Equation Suitable for Problems Relating to Two Spheres. *Proceedings of the Royal Society A: Mathematical, Physical and Engineering Sciences*, 87(593): 109–120, aug 1912. ISSN 1364-5021. doi: 10.1098/rspa.1912.0063. URL http://rspa.royalsocietypublishing.org/cgi/doi/10.1098/rspa.1912.0063.

[80] G. B. Jeffery. On the steady rotation of a solid of revolution in a viscous fluid. *Proceedings of the London Mathematical Society*, s2-14(1):327–338, 1915. ISSN 1460244X. doi: 10.1112/plms/s2_14.1.327. URL http://plms.oxfordjournals.org/content/s2{_}14/1/327.extract.

[81] D. J. Jeffrey. The calculation of the low Reynolds number resistance functions for two unequal spheres. *Physics of Fluids A: Fluid Dynamics*, 4(1):16–29, jan 1992. ISSN 0899-8213. doi: 10.1063/1.858494. URL http://scitation.aip.org/content/aip/journal/pofa/4/1/10.1063/1.858494.

[82] D. J. Jeffrey and Y. Onishi. Calculation of the resistance and mobility functions for two unequal rigid spheres in low-Reynolds-number flow. *Journal of Fluid Mechanics*, 139:261–290, apr 1984. ISSN 0022-1120. doi: 10.1017/S0022112084000355. URL http://www.journals.cambridge.org/abstract{_}S0022112084000355.

[83] D J Jeffrey, J F Morris, and J F Brady. The pressure moments for two rigid spheres in low Reynolds number flow. *Physics of Fluids A*, 5(10):

2317–2325, 1993. ISSN 08998213. doi: 10.1063/1.858795. URL http://authors.library.caltech.edu/9998/.

[84] DJ Jeffrey. Stresslet resistance functions for low Reynolds number flow using deforming spheres. *Zeitschrift für angewandte Mathematik und Physik ZAMP*, 40(2):163–171, 1989. URL http://link.springer.com/article/10.1007/BF00944996.

[85] R. B. Jones. Chapter 4: Dynamics of a colloid in a spherical cavity. In F. Feuillebois and A. Sellier, editors, *Theoretical Methods for Micro Scale Viscous Flows*, chapter 4, pages 61–104. Transworld Research Network, Kerala, India, 2009. ISBN 978-81-7895-400-4.

[86] Huan J Keh and Jih H Chang. Boundary effects on the creeping-flow and thermophoretic motions of an aerosol particle in a spherical cavity. *Chemical Engineering Science*, 53(13):2365–2377, 1998.

[87] Huan J Keh and Tzu H Hsieh. Electrophoresis of a colloidal sphere in a spherical cavity with arbitrary zeta potential distributions. *Langmuir : the ACS journal of surfaces and colloids*, 23(15):7928–35, jul 2007. ISSN 0743-7463. doi: 10.1021/la7004002. URL http://www.ncbi.nlm.nih.gov/pubmed/17569547.

[88] Huan J Keh and Tzu H Hsieh. Electrophoresis of a colloidal sphere in a spherical cavity with arbitrary zeta potential distributions and arbitrary double-layer thickness. *Langmuir : the ACS journal of surfaces and colloids*, 24(2):390–8, jan 2008. ISSN 0743-7463. doi: 10.1021/la702399u. URL http://www.ncbi.nlm.nih.gov/pubmed/18085803.

[89] Huan J. Keh and Tai C. Lee. Axisymmetric creeping motion of a slip

spherical particle in a nonconcentric spherical cavity. *Theoretical and Computational Fluid Dynamics*, 24(5):497–510, jan 2010. ISSN 0935-4964. doi: 10.1007/s00162-010-0181-y. URL http://link.springer.com/10.1007/s00162-010-0181-y.

[90] Aaron S. Keys, Christopher R. Iacovella, and Sharon C. Glotzer. Characterizing complex particle morphologies through shape matching: Descriptors, applications, and algorithms. *Journal of Computational Physics*, 230(17):6438–6463, 2011. ISSN 00219991. doi: 10.1016/j.jcp.2011.04.017. URL http://dx.doi.org/10.1016/j.jcp.2011.04.017.

[91] Aditya S. Khair and John F. Brady. Single particle motion in colloidal dispersions: a simple model for active and nonlinear microrheology. *Journal of Fluid Mechanics*, 557:73, jun 2006. ISSN 0022-1120. doi: 10.1017/S0022112006009608. URL http://www.journals.cambridge.org/abstract{_}S0022112006009608.

[92] S H Kim, J G Park, T M Choi, V N Manoharan, and D a Weitz. Osmotic-pressure-controlled concentration of colloidal particles in thin-shelled capsules. *Nature Communications*, 5:3068, 2014. ISSN 2041-1723. doi: 10.1038/ncomms4068. URL http://www.ncbi.nlm.nih.gov/pubmed/24394965.

[93] Sangtae Kim and Seppo Karrila J. *Microhydrodynamics: Principles and Selected Applications*. Dover Publications, Inc., Mineola, NY, 2005. ISBN 0-486-44219-5.

[94] Sangtae Kim and Richard T. Mifflin. The resistance and mobility functions of two equal spheres in low-Reynolds-number flow. *Physics of Fluids*, 28(7):2033, 1985. ISSN 00319171. doi:

10.1063/1.865384. URL http://scitation.aip.org/content/aip/journal/pof1/28/7/10.1063/1.865384{%}5Cnhttp://link.aip.org/link/PFLDAS/v28/i7/p2033/s1{&}Agg=doi.

[95] Rainer Klages, Gunter Radons, and Igor M Sokolov. *Anomalous Transport: Foundations and Applications*. Wiley-VCH, Weinheim, 2008.

[96] Rajan P Kulkarni, David D Wu, Mark E Davis, and Scott E Fraser. Quantitating intracellular transport of polyplexes by spatio-temporal image correlation spectroscopy. *Proceedings of the National Academy of Sciences of the United States of America*, 102(21):7523–8, may 2005. ISSN 0027-8424. doi: 10.1073/pnas.0501950102. URL http://www.pubmedcentral.nih.gov/articlerender.fcgi?artid=1140437{&}tool=pmcentrez{&}rendertype=abstract.

[97] A J C Ladd. Numerical simulations of particulate suspensions via a discretized Boltzmann equation. Part 1. Theoretical foundation. *Journal of Fluid Mechanics*, 271:285–309, 1994.

[98] A J C Ladd. Numerical simulations of particulate suspensions via a discretized Boltzmann equation. Part 2 . Numerical results. *Journal of Fluid Mechanics*, 271:311–339, 1994.

[99] O. A. Ladyzhenskaya. *The Mathematical Theory of Viscous Incompressible Flow*. Gordon and Breach Science Publishers, New York London Paris, second edi edition, 1969.

[100] A. Lau, B. Hoffman, A. Davies, J. Crocker, and T. Lubensky. Microrheology, Stress Fluctuations, and Active Behavior of Living Cells. *Physical Review Letters*, 91(19):198101, nov 2003. ISSN 0031-9007. doi: 10.1103/

PhysRevLett.91.198101. URL http://link.aps.org/doi/10.1103/PhysRevLett.91.198101.

[101] E Lee, Jw Chu, and Jp Hsu. Electrophoretic Mobility of a Spherical Particle in a Spherical Cavity. *Journal of colloid and interface science*, 196(2):316–320, dec 1997. ISSN 1095-7103. doi: 10.1006/jcis.1997.5220. URL http://www.ncbi.nlm.nih.gov/pubmed/9792757.

[102] E Lee, Jw Chu, and Jp Hsu. Electrophoretic Mobility of a Sphere in a Spherical Cavity. *Journal of colloid and interface science*, 205(1):65–76, sep 1998. ISSN 1095-7103. doi: 10.1006/jcis.1998.5595. URL http://www.ncbi.nlm.nih.gov/pubmed/9710500.

[103] Eric Lee, YP Tang, and JP Hsu. Electrophoresis of a membrane-coated sphere in a spherical cavity. *Langmuir*, 20(21):9415–9421, 2004. URL http://pubs.acs.org/doi/abs/10.1021/la048329b.

[104] Eric Lee, Tzu-hao Huang, and Jyh-ping Hsu. Sedimentation of a Composite Particle in a Spherical Cavity. *Langmuir*, 21(5):1729–1737, 2005.

[105] Eric Lee, Wei-lun Min, and Jyh-ping Hsu. Dynamic Electrophoresis of a Droplet in a Spherical Cavity. *Langmuir*, 22(11):3920–3928, 2006.

[106] Hsin-min Lee. *A modification of Stoke's Law to account for boundary influence*. PhD thesis, State University of Iowa, 1947.

[107] Jerry S H Lee, Porntula Panorchan, Christopher M Hale, Shyam B Khatau, Thomas P Kole, Yiider Tseng, and Denis Wirtz. Ballistic intracellular nanorheology reveals ROCK-hard cytoplasmic stiffening response to fluid flow. *Journal of Cell Science*, 119(9):1760–1768, 2006. ISSN 0021-

9533. doi: 10.1242/jcs.02899. URL http://jcs.biologists.org/content/119/9/1760.abstract.

[108] S. H. Lee and L. G. Leal. Motion of a sphere in the presence of a plane interface. Part 2. An exact solution in bipolar co-ordinates. *Journal of Fluid Mechanics*, 98(01):193–224, apr 1980. ISSN 0022-1120. doi: 10.1017/S0022112080000109. URL http://www.journals.cambridge.org/abstract{_}S0022112080000109.

[109] S. H. Lee, R. S. Chadwick, and L. G. Leal. Motion of a sphere in the presence of a plane interface. Part 1. An approximate solution by generalization of the method of Lorentz. *Journal of Fluid Mechanics*, 93(04):705, apr 1979. ISSN 0022-1120. doi: 10.1017/S0022112079001981. URL http://www.journals.cambridge.org/abstract{_}S0022112079001981.

[110] Tai C. Lee and Huan J. Keh. Electrophoresis of a spherical particle in a spherical cavity. *Microfluidics and Nanofluidics*, 16(6):1107–1115, oct 2014. ISSN 1613-4982. doi: 10.1007/s10404-013-1276-8. URL http://link.springer.com/10.1007/s10404-013-1276-8.

[111] David Leighton and Andreas Acrivos. The shear-induced migration of particles in concentrated suspensions. *Journal of Fluid Mechanics*, 181:415–439, 1987. ISSN 0022-1120. doi: 10.1017/S0022112087002155.

[112] Pushkar P. Lele, James W. Swan, John F. Brady, Norman J. Wagner, and Eric M. Furst. Colloidal diffusion and hydrodynamic screening near boundaries. *Soft Matter*, 7(15):6844, 2011. ISSN 1744-683X. doi: 10.1039/c0sm01466d. URL http://xlink.rsc.org/?DOI=c0sm01466d.

[113] Jennifer I Linderman and Douglas A. Lauffenburger. *Receptors: Models for Binding, Trafficking, and Signalling*. Oxford University Press, New York, N.Y., 1993.

[114] Karen Lipkow and David J Odde. Model for Protein Concentration Gradients in the Cytoplasm. *Cellular and molecular bioengineering*, 1(1): 84–92, mar 2008. ISSN 1865-5025. doi: 10.1007/s12195-008-0008-8. URL http://www.pubmedcentral.nih.gov/articlerender.fcgi?artid=2996619{&}tool=pmcentrez{&}rendertype=abstract.

[115] Shih-Han Lou, Eric Lee, and Jyh-Ping Hsu. Dynamic electrophoresis of a sphere in a spherical cavity: arbitrary surface potential. *Journal of colloid and interface science*, 285(2):865–71, may 2005. ISSN 0021-9797. doi: 10.1016/j.jcis.2004.12.013. URL http://www.ncbi.nlm.nih.gov/pubmed/15837506.

[116] Enkeleida Lushi, Hugo Wioland, and Raymond E Goldstein. Fluid flows created by swimming bacteria drive self-organization in confined suspensions. *Proceedings of the National Academy of Sciences of the United States of America*, 111(27):9733–9738, jul 2014. ISSN 1091-6490. doi: 10.1073/pnas.1405698111. URL http://www.ncbi.nlm.nih.gov/pubmed/24958878.

[117] S. R. Majumdar. Slow motion of an incompressible viscous liquid generated by the rotation of two spheres in contact. *Mathematika*, 14(01):43–46, feb 1967. ISSN 0025-5793. doi: 10.1112/S0025579300007993. URL http://www.journals.cambridge.org/abstract{_}S0025579300007993.

[118] W F Marshall, A Straight, J F Marko, J Swedlow, A Dernburg, A Belmont,

a W Murray, D a Agard, and J W Sedat. Interphase chromosomes undergo constrained diffusional motion in living cells. *Current biology : CB*, 7(12): 930–939, 1997. ISSN 09609822. doi: 10.1016/S0960-9822(06)00412-X.

[119] Christine Maul and Sangtae Kim. Image systems for a Stokeslet inside a rigid spherical container. *Physics of Fluids*, 6:2221, 1994. ISSN 10706631. doi: 10.1063/1.868223. URL `http://link.aip.org/link/PHFLE6/v6/i6/p2221/s1{&}Agg=doi`.

[120] Christine Maul and Sangtae Kim. Image of a point force in a spherical container and its connection to the Lorentz reflection formula. *Journal of Engineering Mathematics*, 30(1-2):119–130, mar 1996. ISSN 0022-0833. doi: 10.1007/BF00118826. URL `http://www.springerlink.com/index/10.1007/BF00118826`.

[121] P Mazur and W V A N Saarloos. Many-Sphere Hydrodynamic Interactions and Mobilities in a Suspension. *Physica*, 115A:21–57, 1982.

[122] Sean R. McGuffee and Adrian H. Elcock. Diffusion, crowding & protein stability in a dynamic molecular model of the bacterial cytoplasm. *PLoS Computational Biology*, 6(3):e1000694, 2010. ISSN 1553734X. doi: 10.1371/journal.pcbi.1000694.

[123] Guy R. McNamara and Gianluigi Zanetti. Use of the boltzmann equation to simulate lattice-gas automata. *Physical Review Letters*, 61(20):2332–2335, 1988. ISSN 00319007. doi: 10.1103/PhysRevLett.61.2332.

[124] V. Michailidou, G. Petekidis, J. Swan, and J. Brady. Dynamics of Concentrated Hard-Sphere Colloids Near a Wall. *Physical Review Letters*, 102 (6):068302, feb 2009. ISSN 0031-9007. doi: 10.1103/PhysRevLett.102.

068302. URL http://link.aps.org/doi/10.1103/PhysRevLett.102.068302.

[125] AP Minton. The Effective Hard Particle model provides a simple, robust, and broadly applicable description of nonideal behavior in concentrated solutions of bovine serum albumin and other nonassociating proteins. *Journal of pharmaceutical sciences*, 96(12):3466–3469, 2007. doi: 10.1002/jps. URL http://onlinelibrary.wiley.com/doi/10.1002/jps.20964/full.

[126] Shahin Navardi and Sukalyan Bhattacharya. A new lubrication theory to derive far-field axial pressure difference due to force singularities in cylindrical or annular vessels. *Journal of Mathematical Physics*, 51(4):043102, 2010. ISSN 00222488. doi: 10.1063/1.3321580.

[127] Shahin Navardi, Sukalyan Bhattacharya, and Hanyan Wu. Stokesian simulation of two unequal spheres in a pressure-driven creeping flow through a cylinder. *Computers and Fluids*, 121:145–163, 2015. ISSN 00457930. doi: 10.1016/j.compfluid.2015.07.027. URL http://dx.doi.org/10.1016/j.compfluid.2015.07.027.

[128] Z T Németh and H Löwen. Freezing and glass transition of hard spheres in cavities. *Physical review. E, Statistical physics, plasmas, fluids, and related interdisciplinary topics*, 59(6):6824–6829, 1999. ISSN 1063-651X. doi: 10.1103/PhysRevE.59.6824.

[129] Ritsuya Niwayama, Kyosuke Shinohara, and Akatsuki Kimura. Hydrodynamic property of the cytoplasm is sufficient to mediate cytoplasmic streaming in the Caenorhabditis elegans embryo. *Proceedings of the Na-*

tional Academy of Sciences of the United States of America, 108(29):11900–5, jul 2011. ISSN 1091-6490. doi: 10.1073/pnas.1101853108.

[130] M. E. O'Neill and K. Stewartson. On the slow motion of a sphere parallel to a nearby plane wall. *Journal of Fluid Mechanics*, 27(04):705–724, mar 1967. ISSN 0022-1120. doi: 10.1017/S0022112067002551. URL http://www.journals.cambridge.org/abstract{_}S0022112067002551.

[131] ME O'Neill and R Majumdar. Asymmetrical slow viscous fluid motions caused by the translation or rotation of two spheres. Part I: The determination of exact solutions for any values of the ratio of radii and separation parameters. *Zeitschrift für angewandte Mathematik und Physik ZAMP*, 21:164–179, 1970. doi: 10.1007/BF01590641. URL http://link.springer.com/article/10.1007/BF01590641http://dx.doi.org/10.1007/BF01590641.

[132] ME O'Neill and R Majumdar. Asymmetrical slow viscous fluid motions caused by the translation or rotation of two spheres. Part II: Asymptotic forms of the solutions when the minimum clearance. *Zeitschrift für angewandte Mathematik und Physik ZAMP*, 21:180–187, 1970. URL http://link.springer.com/article/10.1007/BF01590642.

[133] Steven A. Orszag and G. S. Patterson. Numerical simulation of three-dimensional homogeneous isotropic turbulence. *Physical Review Letters*, 28(2):76–79, 1972. ISSN 00319007. doi: 10.1103/PhysRevLett.28.76.

[134] C.W Oseen. *Neuere methoden und ergebnisse in der hydrodynamik*. Akademische verlagsgesellschaft M.B.H., Leipzig, 1927. URL http://newcatalog.library.cornell.edu/catalog/405051.

[135] Y. Peng, W. Chen, Th. M. Fischer, D. a. Weitz, and P. Tong. Short-time self-diffusion of nearly hard spheres at an oilwater interface. *Journal of Fluid Mechanics*, 618:243–261, 2009. ISSN 0022-1120. doi: 10.1017/S0022112008004114.

[136] Jerome K. Percus and George J. Yevick. Analysis of Classical Statistical Mechanics by Means of Collective Coordinates. *Physical Review*, 110(1): 1–13, 1958. ISSN 0031899X. doi: 10.1103/PhysRev.110.1.

[137] C S Peskin. Numerical analysis of blood flow in the heart. *Journal of Computational Physics*, 25(3):220–252, 1977. ISSN 00219991. doi: 10.1016/0021-9991(77)90100-0. URL http://www.sciencedirect.com/science/article/pii/0021999177901000.

[138] CS Peskin. The immersed boundary method. *Acta numerica*, 11(January 2002):479–517, 2002. ISSN 0962-4929. doi: 10.1017/S0962492902000077. URL http://www.journals.cambridge.org/abstract{_}S0962492902000077{%}5Cnhttp://journals.cambridge.org/abstract{_}S0962492902000077.

[139] Thanh N. Phung, John F. Brady, and Georges Bossis. Stokesian Dynamics simulation of Brownian suspensions. *Journal of Fluid Mechanics*, 313:181–207, apr 1996. ISSN 0022-1120. doi: 10.1017/S0022112096002170. URL http://www.journals.cambridge.org/abstract{_}S0022112096002170.

[140] Narahari S. Pujar and Andrew L. Zydney. Boundary effects on the sedimentation and hindered diffusion of charged particles. *AIChE Journal*, 42(8):2101–2111, aug 1996. ISSN 0001-1541. doi: 10.1002/aic.690420802. URL http://doi.wiley.com/10.1002/aic.690420802.

[141] Bhargav Rallabandi, Sascha Hilgenfeldt, and Howard A. Stone. Hydrodynamic force on a sphere normal to an obstacle due to a non-uniform flow. *Journal of Fluid Mechanics*, 818:407–434, 2017. ISSN 0022-1120. doi: 10.1017/jfm.2017.135. URL https://www.cambridge.org/core/product/identifier/S0022112017001355/type/journal{_}article.

[142] J.M. Rallison and E.J. Hinch. The effect of particle interactions on dynamic light scattering from a dilute suspension. *Journal of Fluid Mechanics*, 167: 131–168, 1986.

[143] J Rotne and S Prager. Variational treatment of hydrodynamic interaction in polymers. *The Journal of Chemical Physics*, 50(11):4831, 1969. URL http://onlinelibrary.wiley.com/doi/10.1002/cbdv.200490137/abstracthttp://link.aip.org/link/?JCPSA6/50/4831/1.

[144] A Sellier. Slow viscous motion of a solid particle in a spherical cavity. *Computer modeling in engineering & sciences*, 25(3):165–179, 2008. URL http://www.techscience.com/doi/10.3970/cmes.2008.025.165.pdf.

[145] Tamar Shinar, Miyeko Mana, Fabio Piano, and Michael J Shelley. A model of cytoplasmically driven microtubule-based motion in the single-celled Caenorhabditis elegans embryo. *Proceedings of the National Academy of Sciences of the United States of America*, 108(26):10508–10513, 2011. ISSN 0027-8424. doi: 10.1073/pnas.1017369108. URL http://www.pnas.org/content/108/26/10508.short.

[146] A. Sierou and J. F. Brady. Rheology and microstructure in concentrated noncolloidal suspensions. *Journal of Rheology*, 46(5):1031, 2002. ISSN

01486055. doi: 10.1122/1.1501925. URL http://scitation.aip.org/content/sor/journal/jor2/46/5/10.1122/1.1501925.

[147] Asimina Sierou and John F. Brady. Accelerated Stokesian Dynamics simulations. *Journal of Fluid Mechanics*, 448:115–146, nov 2001. ISSN 0022-1120. doi: 10.1017/S0022112001005912. URL http://www.journals.cambridge.org/abstract{_}S0022112001005912.

[148] Ik Snook and D Henderson. Monte Carlo study of a hardsphere fluid near a hard wall. *The Journal of Chemical Physics*, 68(5):2134–2139, 1978. ISSN 00219606. doi: 10.1063/1.436036. URL http://scitation.aip.org/content/aip/journal/jcp/68/5/10.1063/1.436036.

[149] Todd M. Squires and John F. Brady. A simple paradigm for active and nonlinear microrheology. *Physics of Fluids*, 17(7):073101, 2005. ISSN 10706631. doi: 10.1063/1.1960607. URL http://link.aip.org/link/PHFLE6/v17/i7/p073101/s1{&}Agg=doi.

[150] Paul J. Steinhardt, David R. Nelson, and Marco Ronchetti. Bond-orientational order in liquids and glasses. *Physical Review B*, 28(2):784–805, 1983. ISSN 01631829. doi: 10.1103/PhysRevB.28.784.

[151] M. Stimson and G. B. Jeffery. The Motion of Two Spheres in a Viscous Fluid. *Proceedings of the Royal Society A: Mathematical, Physical and Engineering Sciences*, 111(757):110–116, may 1926. ISSN 1364-5021. doi: 10.1098/rspa.1926.0053. URL http://rspa.royalsocietypublishing.org/cgi/doi/10.1098/rspa.1926.0053.

[152] Yu Su, James W. Swan, and Roseanna N. Zia. Pair mobility functions for rigid spheres in concentrated colloidal dispersions: Stresslet and straining

motion couplings. *The Journal of Chemical Physics*, 146:124903, 2017. ISSN 00219606. doi: 10.1063/1.4936664.

[153] Junghae Suh, Denis Wirtz, and Justin Hanes. Efficient active transport of gene nanocarriers to the cell nucleus. *Proceedings of the National Academy of Sciences of the United States of America*, 100(7):3878–3882, apr 2003. ISSN 0027-8424. doi: 10.1073/pnas.0636277100. URL http://www.pubmedcentral.nih.gov/articlerender.fcgi?artid=153016{&}tool=pmcentrez{&}rendertype=abstract.

[154] Jian Sun and Harel Weinstein. Toward realistic modeling of dynamic processes in cell signaling: quantification of macromolecular crowding effects. *The Journal of chemical physics*, 127(15):155105, oct 2007. ISSN 0021-9606. doi: 10.1063/1.2789434. URL http://www.ncbi.nlm.nih.gov/pubmed/17949221.

[155] James W. Swan and John F. Brady. Simulation of hydrodynamically interacting particles near a no-slip boundary. *Physics of Fluids*, 19(11):113306, 2007. ISSN 10706631. doi: 10.1063/1.2803837. URL http://link.aip.org/link/PHFLE6/v19/i11/p113306/s1{&}Agg=doi.

[156] James W. Swan and John F. Brady. Particle motion between parallel walls: Hydrodynamics and simulation. *Physics of Fluids*, 22(10):103301, 2010. ISSN 10706631. doi: 10.1063/1.3487748.

[157] James W. Swan and John F. Brady. The hydrodynamics of confined dispersions. *Journal of Fluid Mechanics*, 687:254–299, 2011. ISSN 0022-1120. doi: 10.1017/jfm.2011.351.

[158] James W Swan and John F Brady. Anisotropic diffusion in confined col-

loidal dispersions: The evanescent diffusivity. *Journal of chemical physics*, 135:014701, jul 2011. ISSN 1089-7690. doi: 10.1063/1.3604530. URL http://www.ncbi.nlm.nih.gov/pubmed/21744908.

[159] James W. Swan and Roseanna N. Zia. Active microrheology: Fixed-velocity versus fixed-force. *Physics of Fluids*, 25(8):083303, 2013. ISSN 10706631. doi: 10.1063/1.4818810. URL http://scitation.aip.org/content/aip/journal/pof2/25/8/10.1063/1.4818810.

[160] S M Ali Tabei, Stanislav Burov, Hee Y Kim, Andrey Kuznetsov, Toan Huynh, Justin Jureller, Louis H Philipson, Aaron R Dinner, and Norbert F Scherer. Intracellular transport of insulin granules is a subordinated random walk. *Proceedings of the National Academy of Sciences of the United States of America*, 110(13):4911–4916, mar 2013. ISSN 1091-6490. doi: 10.1073/pnas.1221962110. URL http://www.pubmedcentral.nih.gov/articlerender.fcgi?artid=3612641{&}tool=pmcentrez{&}rendertype=abstract.

[161] Erin G Teich, Greg van Anders, Daphne Klotsa, Julia Dshemuchadse, and Sharon C. Glotzer. Clusters of polyhedra in spherical confinement. *Proceedings of the National Academy of Sciences*, 113(6):E669–E678, 2016. ISSN 0027-8424. doi: 10.1073/pnas.1524875113. URL http://www.pnas.org/content/early/2016/01/21/1524875113{%}5Cnhttp://www.pnas.org/lookup/doi/10.1073/pnas.1524875113.

[162] RJA Tough and C van den Broeck. Diffusion within a sphere; a non-Gaussian statistical model for particle displacements in a dense colloidal suspension. *Physica A: Statistical Mechanics and its Applications*, 157:

769–796, 1989. URL http://www.sciencedirect.com/science/article/pii/0378437189900666.

[163] Cheng-Pang Tung, Eric Lee, and Jyh-Ping Hsu. Dynamic electrophoretic mobility of a sphere in a spherical cavity. *Journal of Colloid and Interface Science*, 260(1):118–125, apr 2003. ISSN 00219797. doi: 10.1016/S0021-9797(02)00186-8. URL http://linkinghub.elsevier.com/retrieve/pii/S0021979702001868.

[164] Alan S Verkman. Solute and macromolecule diffusion in cellular aqueous compartments. *Trends in biochemical sciences*, 27(1):27–33, jan 2002. ISSN 0968-0004. URL http://www.ncbi.nlm.nih.gov/pubmed/11796221.

[165] Nicolas Vogel, Stefanie Utech, Grant T England, Tanya Shirman, Katherine R Phillips, Natalie Koay, Ian B Burgess, Mathias Kolle, David A Weitz, and Joanna Aizenberg. Color from hierarchy: Diverse optical properties of micron-sized spherical colloidal assemblies. *Proceedings of the National Academy of Sciences*, 112(35):10845–10850, 2015. ISSN 0027-8424. doi: 10.1073/pnas.1506272112. URL http://www.pnas.org/content/112/35/10845.abstract.

[166] Ekaterina Voronina. The diverse functions of germline P-granules in Caenorhabditis elegans. *Molecular Reproduction and Development*, 80(8):624–631, 2013. ISSN 1040452X. doi: 10.1002/mrd.22136.

[167] M Wachsmuth, W Waldeck, and J Langowski. Anomalous diffusion of fluorescent probes inside living cell nuclei investigated by spatially-resolved fluorescence correlation spectroscopy. *Journal of molecular biology*, 298(4):

677–89, may 2000. ISSN 0022-2836. doi: 10.1006/jmbi.2000.3692. URL http://www.ncbi.nlm.nih.gov/pubmed/10788329.

[168] Norman J. Wagner and John F. Brady. Shear thickening in colloidal dispersions. *Physics Today*, 62(10):27–32, 2009. ISSN 00319228. doi: 10.1063/1.3248476.

[169] S Wakiya. Slow Motions of a Viscous Fluid around Two Spheres. *Journal of the Physical Society of Japan*, 22(4):1101–1109, 1967. URL http://journals.jps.jp/doi/abs/10.1143/JPSJ.22.1101.

[170] Stephanie C. Weber and Clifford P. Brangwynne. Inverse Size Scaling of the Nucleolus by a Concentration-Dependent Phase Transition. *Current Biology*, 25:1–6, 2015. ISSN 09609822. doi: 10.1016/j.cub.2015.01.012. URL http://linkinghub.elsevier.com/retrieve/pii/S0960982215000147.

[171] Stephanie C. Weber, Julie a. Theriot, and Andrew J. Spakowitz. Subdiffusive motion of a polymer composed of subdiffusive monomers. *Physical Review E - Statistical, Nonlinear, and Soft Matter Physics*, 82(1):1–11, 2010. ISSN 15393755. doi: 10.1103/PhysRevE.82.011913.

[172] E. R. Weeks, J. C. Crocker, Andrew L. Levitt, Andrew Schofield, and D. A. Weitz. Three-Dimensional Direct Imaging of Structural Relaxation Near the Colloidal Glass Transition. *Science*, 287(5453):627–631, 2000. ISSN 00368075. doi: 10.1126/science.287.5453.627. URL http://www.sciencemag.org.libproxy.mit.edu/content/287/5453/627.short.

[173] Matthias Weiss, Markus Elsner, Fredrik Kartberg, and Tommy

Nilsson. Anomalous subdiffusion is a measure for cytoplasmic crowding in living cells. *Biophysical journal*, 87(5):3518–3524, 2004. ISSN 0006-3495. doi: 10.1529/biophysj.104.044263. URL http://www.pubmedcentral.nih.gov/articlerender.fcgi?artid=1304817{&}tool=pmcentrez{&}rendertype=abstract.

[174] Denis Wirtz. Particle-tracking microrheology of living cells: principles and applications. *Annual review of biophysics*, 38:301–26, jan 2009. ISSN 1936-122X. doi: 10.1146/annurev.biophys.050708.133724. URL http://www.ncbi.nlm.nih.gov/pubmed/19416071.

[175] Andreas Wodarz. Establishing cell polarity in development. *Nat Cell Biol*, 4(2):39–44, 2002. URL http://mi.img.cas.cz/Teaching/Molekul{\unhbox\voidb@x\bgroup\let\unhbox\voidb@x\setbox\@tempboxa\hbox{a\global\mathchardef\accent@spacefactor\spacefactor}\accent19a\egroup\spacefactor\accent@spacefactor}rn{\unhbox\voidb@x\bgroup\let\unhbox\voidb@x\setbox\@tempboxa\hbox{\OT1\i\global\mathchardef\accent@spacefactor\spacefactor}\accent19\OT1\i\egroup\spacefactor\accent@spacefactor}mechanizmymorfogeneze-{\unhbox\voidb@x\bgroup\let\unhbox\voidb@x\setbox\@tempboxa\hbox{C\global\mathchardef\accent@spacefactor\spacefactor}\accent20C\egroup\spacefactor\accent@spacefactor}erm{\unhbox\voidb@x\bgroup\let\unhbox\voidb@x\setbox\@tempboxa\hbox{a\global\mathchardef\accent@spacefactor\spacefactor}\accent19a\egroup\spacefactor\accent@spacefactor}k(zimn{\unhbox\

voidb@x\bgroup\let\unhbox\voidb@x\setbox\
@tempboxa\hbox{\OT1\i\global\mathchardef\
accent@spacefactor\spacefactor}\accent19\OT1\i\
egroup\spacefactor\accent@spacefactor}semestr)
/DrosophilaoogenesisA{_}Passymetry/Articles/
Establishingcellpolarityindevelopment.pdf.

[176] E. Yariv and H. Brenner. Near-contact electrophoretic motion of a sphere parallel to a planar wall. *Journal of Fluid Mechanics*, 484:85–111, jun 2003. ISSN 00221120. doi: 10.1017/S002211200300418X. URL http://www.journals.cambridge.org/abstract{_}S002211200300418X.

[177] R. N. Zia and J. F. Brady. Microviscosity, microdiffusivity, and normal stresses in colloidal dispersions. *Journal of Rheology*, 56(5):1175, 2012. ISSN 01486055. doi: 10.1122/1.4722880. URL http://link.aip.org/link/JORHD2/v56/i5/p1175/s1{&}Agg=doi.

[178] R. N. Zia and J. F. Brady. Stress development, relaxation, and memory in colloidal dispersions: Transient nonlinear microrheology. *Journal of Rheology*, 57(2):457, 2013. ISSN 01486055. doi: 10.1122/1.4775349. URL http://link.aip.org/link/JORHD2/v57/i2/p457/s1{&}Agg=doi.

[179] Roseanna N. Zia and John F. Brady. Single-particle motion in colloids: force-induced diffusion. *Journal of Fluid Mechanics*, 658:188–210, jun 2010. ISSN 0022-1120. doi: 10.1017/S0022112010001606. URL http://www.journals.cambridge.org/abstract{_}S0022112010001606.

[180] Roseanna N Zia, James W Swan, and Yu Su. Pair mobility functions for rigid spheres in concentrated colloidal dispersions: force, torque, trans-

lation, and rotation. *Journal of Chemical Physics*, 143:224901, 2015. ISSN 0021-9606. doi: 10.1063/1.4936664.

[181] R Zwanzig, J Kiefer, and G H Weiss. On the Validity of the Kirkwood-Riseman Theory. *Proceedings of the National Academy of Sciences*, 60(2):381, 1968. ISSN 0027-8424.

[182] AL Zydney. Boundary effects on the electrophoretic motion of a charged particle in a spherical cavity. *Journal of colloid and interface science*, 169: 476–485, 1994. URL `http://www.sciencedirect.com/science/article/pii/S0021979785710582`.